Università degli Studi di Ferrara

PhD course in
"PHYSICS"

CYCLE XXXIV

COORDINATOR Prof. Eleonora Luppi

Electron Beam Lithography and Focused Ion Beam Techniques for the Development of Low Power Consumption Microelectromechanical Systems-based Chemiresistive Gas Sensors

Disciplinary Scientific Sector FIS/01

Candidate
Dott. Feng - Zhifu

Supervisor
Prof. Vincenzo Guidi

Second supervisor
Dr. Andrea Gaiardo

Years 2018/2023

Index

Abstract 7

Acknowledgements 11

Declarations 13

List of Symbols 15

List of Abbreviations and Acronyms 18

1. Gas Sensor Overview 20

1.1 Gas Sensor Types 21

1.1.1 Acoustic Gas Sensors 21

1.1.2 Optical Gas Sensors 23

1.1.3 Electrochemical Sensors 27

1.1.4 Chemi-Resistive Solid Gas Sensor 28

1.2 Comparison of Different Types of Gas Sensors 31

1.3 Sensing Mechanism of SMO Gas Sensors 33

1.4 Approaches to Enhancing SMO Gas Sensing Materials Properties 38

1.5 Main Elements of MEMS Based SMO Gas Sensor Devices and Fabrication Routines. 40

1.5.1 Gas Sensing Films Deposition 41

1.5.2 Substrate Materials Introduction 43

1.5.3 Hotplate Introduction 44

1.6 Application of Semiconductor Gas Sensors 48

References 50

2. Fabrication Techniques and Characterization Methods 58

2.1 Fabrication Tools 58

2.1.1 EBL Technique 58

2.1.2 FIB Machine 64

2.2 Physical and Chemical Analysis Techniques 67

2.3 Gas Sensor Test System 76

References 77

3. Micro/Nano Hotplates Simulation and Fabrication 79

3.1 Hotplate Introduction 79

3.2 Hotplate Design and General Fabrication Process 81

3.3 Heat Dissipation Theory 85

3.4 Micro/Nano Hotplate Simulation 88

3.4.1 Model and Boundaries Setting for the Simulation 88

3.4.2 Calibration of Simulation Results with the Experiment Data by Using MHP1 Model 90

3.4.3 MHP2 Simulation Results 92

3.4.4 NHP1 Simulation Results 96

3.4.5 NHP2 Simulation Results 99

3.5 Micro Hotplate Fabrication Process and Results Discussion 102

3.5.1 NHP2 Fabrication by Combining EBL and FIB Techniques. 102

3.5.2 NHP1 Fabrication in Two-step by EBL and Results Discussion 121

3.5.3 MHP2 Fabrication in Two-step by EBL and Results Discussion 131

3.5.4 ZnO Self-heating Gas Sensor Fabrication by EBL and Results Discussion 133

Conclusion 134

Reference 137

4. MEMS-based Thin Film SMO ZnO Gas Sensor 140

4.1 Introduction 140

4.2 Fabrication Process 143

4.3 Results and Discussion. 144

4.3.1 Morphological and Elemental Studies 144

4.3.2 Resistance Measurement 152

4.3.3 Gas Sensing Test 154

4.4 Sensing Mechanism. 156

Conclusion 157

References 158

5. Thick Film Gas Sensor of SMO SnO_2 Doped by Antimony Deposited on MEMS-based MHP1 161

5.1 Introduction 161

5.2 Sensing Materials and Sensor Devices Preparation 163

5.3. Results and Discussion 165

5.3.1 Morphological and Elemental Studies 165

5.3.2 Gas Sensing Characterization 173

5.4 Gas Sensing Mechanism Discussion 175

Conclusion 178

References 179

6. Conclusion and Outlook 186

6.1 Conclusion 186

6.2 Outlook 190

Appendix A: List of Figures and Tables 192

Appendix B: Materials Properties Used in COMSOL Simulation. 197

Abstract

Gas sensors are widely used for detecting toxic gases for environmental protection, industrial monitoring, household safety, breath analysis and food deterioration. Apart from the electrochemical gas sensors, which have a short lifetime, and optical gas sensors with large volume size with high cost, semiconductor metal oxide (SMO) gas sensors as one of the chemiresistive type gas sensors are now developing fast owing to its low production cost, stable physical properties and chemical versatility. However, regarding the high operational temperature of SMO gas sensors, reduction of power consumption is extremely important for its application in smartphones and other portable devices. For this purpose, miniaturization of SMO gas sensor devices, primarily for the hotplate part acting as mechanical support of the sensing material and heater/electrode part, is an effective way to improve the power efficiency. Microelectromechanical systems (MEMS) offer an opportunity to achieve such goal. This dissertation addressed to miniaturization of the hotplate, was focused on hotplate fabrication by using Electron Beam Lithography (EBL) and Focused Ion Beam (FIB).

Firstly, through simulation software COMSOL, the operational temperature and power consumption of the hotplate with three different sizes were investigated. In the first case, micro size hotplate (MPH1) was designed and simulated with heater circuit width of 100 μm and heat area of 1300 μm x 1300 μm, then the geometry of MHP1 was downsized by 50 times into MHP2 device to decrease the power consumption. NHP1 devices were obtained with 1 μm wide heater circuit and 500 nm wide heater circuit gap. Thermal and mechanical simulations, through finite element analysis, were carried out for optimizing MHP and NHP layouts. Simulation results highlighted that the development of suspended membrane structure of the hotplate could improve the working temperature and power efficiency, also reduce stress concentration and displacement at high temperature compared to the bulk silicon structure substrate. In addition, it was found that the thickness of the insulation layer between the electrode/heater circuit and silicon wafer affected both the temperature uniformity and power efficiency.

Then two different approaches were studied and used at Bruno Kessler Foundation facilities to microfabricate the hotplates. First method combined EBL and FIB techniques to define the layout. EBL was used to exposure the micro-level size electrode part (or pad part), and FIB was used to mill the heater circuit part with fine and dense structure. The patterned

hotplate structure was characterized by Scanning Electron Microscope (SEM), and the milling result was analyzed by Secondary-ion Mass Spectrometry (SIMS). By studying these results, the optimized parameters for EBL and FIB were selected. The second method used two-step EBL exposure. Low energy of electron beam with low dose and large writing field for the electrode part exposure and high energy of electron beam with high dose and small writing field for the dense heater circuit patterning.

After these hotplates were fabricated, their electrical and thermal properties were experimentally evaluated. Subsequently, chemiresistive sensors based on the developed hotplates were developed. In particular, n-type sensing material ZnO nano film was deposited on MHP2 and NHP1 by magnetron sputtering technique. SEM revealed the nano size of ZnO particle, and the calcination condition effect on the size of ZnO. ZnO crystal structure was characterized by X-ray Powder Diffraction (XRD), and X-Ray Photoelectron Spectroscopy (XPS) proved the atom ratio of Zn and O. ZnO nanofilm did not show strong response to humidity, but humidity could decrease the response toward NO_2, and increase the response toward ethanol.

Thick films of SnO_2 highly doped by antimony with concentration of 10 wt% (ATO1) and 15wt% (ATO2) were drop coated on MHP1. These materials were characterized by SEM, XRD and XPS. It suggested that antimony doping modified the morphology of SnO_2 powder by preventing the growth of powder particles. The results of the XPS experiment demonstrated that the concentration of antimony was higher on the surface of SnO_2 than its inside. It was found that ATO sensors led to a particularly high selectivity and sensitivity to NO_2 when compared to the other gases at 400 °C in dry air. Additionally, the sensing response of ATO1 and ATO2 was only moderately affected by humidity, which made them ideal candidates to detect NO_2 in the actual atmosphere.

Abstract

I sensori di gas sono ampiamente utilizzati per rilevare gas tossici per la protezione ambientale, il monitoraggio industriale, la sicurezza domestica, l'analisi del respiro e il deterioramento degli alimenti. A parte i sensori di gas elettrochimici, che hanno una breve durata, e i sensori di gas ottici di grandi dimensioni con un costo elevato, i sensori di gas chemiresistivi basati su ossidi metallici semiconduttori (OMS) risultano essere una soluzione tecnologica estremamente interessante, grazie alla sua bassa produzione costo, proprietà fisiche stabili e versatilità chimica. Tuttavia, per via dell'elevata temperatura operativa dei sensori di gas OMS, la riduzione del consumo energetico è di fondamentale importanza per una loro futura integrazione su dispositivi portatili, quali gli smartphones. A tale scopo, la miniaturizzazione dei sensori di gas OMS, principalmente per quanto riguarda il microriscaldatore, che funge da supporto meccanico del materiale di rilevamento e della parte riscaldatore/elettrodo, è un modo efficace per migliorare l'efficienza energetica. I sistemi microelettromeccanici (MEMS) offrono l'opportunità di raggiungere tale obiettivo. Questa dissertazione, focalizzata principalmente alla miniaturizzazione del microriscaldatore, si è concentrata sulla simulazione della dissipazione del calore del microriscaldatore mediante analisi agli elementi finiti, e sulla fabbricazione degli stessi utilizzando la litografia a fascio di elettroni (EBL) e il fascio di ioni focalizzati (FIB) per lo sviluppo di sensori di gas a bassissimo consumo energetico.

In primo luogo, attraverso il software di simulazione COMSOL, sono stati studiati la temperatura operativa e il consumo energetico dei microriscaldatori. Inizialmente, è stata progettata e simulato un microriscaldatore con caratteristiche micrometriche (MHP1), posto su una membrana sospesa isolante di area 1300 µm x 1300 µm, e con una larghezza della pista del circuito riscaldante di 100 µm. Successivamente, la dimensione della geometria di MHP1 è stata ridimensionata di 50 volte per ottenere il dispositivo MHP2. In secondo luogo, sono stati realizzati microriscaldatori con caratteristiche nanometriche (NHP1 e NHP2), progettati con un circuito del riscaldatore con larghezza della pista <1 µm, e un gap tra le serpentine del circuito riscaldante di 500 nm. Per quanto concerne gli elettrodi, sia per i dispositivi MH che NH sono state mantenute caratteristiche micrometriche, in quanto non vanno ad impattare in maniera significativa sul consumo finale del dispositivo. I risultati della simulazione hanno evidenziato che la struttura della membrana sospesa del microriscaldatore migliora l'efficienza energetica, riducendo anche lo stress e le sollecitazioni rispetto ad un substrato sviluppato su silicio bulk, senza membrana. Inoltre, è

stato riscontrato che lo spessore dello strato isolante tra il circuito elettrodo/riscaldatore e il wafer di silicio influenza l'uniformità della distribuzione della temperatura.
Quindi sono stati studiati e utilizzati due diversi approcci presso le strutture della Fondazione Bruno Kessler per fabbricare i microriscaldatori. Il primo metodo ha combinato le tecniche EBL e FIB per definire il layout del riscaldatore stesso. EBL è stato utilizzato per esporre la parte dell'elettrodo di dimensioni micrometriche, mentre il FIB è stato utilizzato per fresare la parte del circuito del riscaldatore con caratteristiche nanometriche. Nel secondo metodo, è stata utilizzata un'esposizione EBL in due fasi, senza utilizzo del FIB: i) bassa energia del fascio di elettroni con bassa dose e ampia area di scrittura per la definizione della struttura degli elettrodi; ii) alta energia del fascio di elettroni con dose elevata e piccolo campo di scrittura per la definizione del circuito del riscaldatore.
Dopo che questi microriscaldatori sono stati fabbricati, le loro proprietà elettriche e termiche sono state valutate sperimentalmente. Successivamente sono stati sviluppati sensori chemiresistivi sfruttando i microriscaldatori sviluppati. In particolare, il nanofilm ZnO di materiale sensibile di tipo n è stato depositato su MHP2 e NHP1 mediante magnetron sputtering. Il SEM ha rivelato le dimensioni nanometriche delle particelle di ZnO. La struttura cristallina di ZnO è stata caratterizzata dalla diffrazione della polvere di raggi X (XRD) e la spettroscopia fotoelettronica a raggi X (XPS) ha dimostrato il rapporto atomico di Zn e O. Il nanofilm di ZnO non ha mostrato una forte risposta all'umidità, mentre ha mostrato una buona sensibilità nei confronti del NO_2.
Successivamente, i microriscaldatori MHP1 sono stati testati anche come substrati per sensori chemiresistivi a film spesso, utilizzando come materiale sensibile SnO_2 altamente drogate con antimonio (ATO), concentrazione atomica del 10% e 15% in peso. Questi materiali sono stati caratterizzati da SEM, XRD e XPS, il che ha suggerito che il drogaggio di antimonio ha modificato la morfologia rispetto alla polvere di SnO_2 non drogata, prevenendo la crescita delle particelle di polvere e diminuendo quindi la dimensione media delle nanoparticelle. La caratterizzazione XPS ha dimostrato che la concentrazione di antimonio era maggiore sulla superficie delle nanoparticelle di SnO_2 rispetto al bulk. È stato riscontrato che i sensori ATO hanno portato a un’alta selettività e sensibilità all'NO_2, specialmente ad una temperatura di 400 °C in aria secca.

Key words

Gas sensor, electron beam lithography, focused ion beam, microelectromechanical system, micro hotplate, power consumption

Acknowledgements

Firstly, the greatest gratitude should be given to my supervisors Prof. Vincenzo Guidi. Thank you for offering me such precious opportunity to study semiconductor physics, gas sensor and nanofabrication methods. You helped me solve the official formalities with our University of Ferrara and Fondazione Bruno Kessler institute, I am also appreciating that you provide me with sophisticated suggestions for my work all the time during my PhD period.

I still remembered that when I arrived in Ferrara in the first time, you picked me up in the train station, and you helped me find a flat, you introduced me the local life, you took me to the supermarket, you explained me the theory of semiconductor and gas sensor work mechanisms. All the favors will stay in my mind forever, and without your marvelous and generous guidance in gas sensor field and life, I could not make any further steps. No enough words can express how much I am grateful for your supports, my second supervisor, Dr. Andrea Gaiardo. The most important things you gave to me I think are your opinions about how to be a good researcher, you suggest me what I should do during a new research topic, that is changing my scientific career.

I would like to thank my colleagues in Ferrara University, Dr. Barbara Fabbri, Dr. Matteo Valt and Dr. Soufiane Krik. You helped me a lot during working time and life time, with your kindness I can get used to this new world quickly.

I feel so grateful for the introduction of nanofabrication from Damiano Giubertoni and Alessandro Cian, you taught me how to use FIB and EBL in FBK clean room patiently from 0 level. You led me into this nanofabrication world, by this chance, I find out there were a lot of state-of-art works to do to improve gas sensor device performances.

I also want to thank my colleagues in MNF FBK, who helped me to finish my nanofabrication works, they are Dr. Alvise Bagolini, Dr. Papardela Laura, Dr. Anze Sitar, Dr. Demenev Evgeny, Dr. Nawaz Ali, Dr. Novel David, Tosato Pietro, Ferrari Sara, Mattevi Paolo, Fioravanti Simona, Lacob Erica, Marinelli Stefano, Michele Fedrizzi, Flavio Giacomozzi and PhD students Elia Scattolo, Nicolo Di Novo, Naga Manikanta and Teferi Sitotaw Yallew.

The reason I am so enjoying the life time in Trento is because of my dear friend Alessia Frapporti and her mom, who care me a lot and have taken me to tour this beautiful area of

Trentino, we had much great time together during the weekend life. You make my life more colorful, and you don’t know how lucky I am to have you in my life.

For the last, I want to thank my family for the support, especially my girlfriend Dr. Lyuye Lin, who supports me all the time. Difficulties I have met in my life never knocked me down because of your presence in my life, I don’t know how I can deliver my full appreciate to you, my gratitude is beyond words.

Declarations

The work described in this thesis is entirely original and my own, except where otherwise indicated.

Parts of this work have been published in the scientific literature:

1. Zhifu Feng, Andrea Gaiardo, Soufine Krik, Vincenzo Guidi, Giancarlo Pepponi, Cesare Malagù, Pierluigi Bellutti, Barbara Fabbri, Matteo Valt and Stefano Caramori. Gas Sensing Properties Comparison between SnO_2 and Highly Antimony-doped SnO_2 Materials. 18th International Meeting on Chemical Sensors, Virtual Meeting, USA, May 30th – June 3rd 2021.

2. Z. Feng, D. Giubertoni, A. Gaiardo, A. Cian, M. Valt, M. Barozzi, V. Guidi. Nano hotplate fabrication for metal oxide-based gas sensor by combining electron beam and focused ion beam lithography. Micro and Nano Engineering, MNE-D-22-00173. (In review).

3. Z. Feng, D. Giubertoni, A. Gaiardo, A. Cian, M. Valt, M. Barozzi, V. Guidi. Fabrication of ZnO nanofilm based gas sensor pattern by two-step electron beam lithography and lift off techniques. Sensors and Actuators B. (In writing)

4. Zhifu Feng, Andrea Gaiardo, Damiano Giubertoni, Alessandro Cian, Pierluigi Bellutti, Vincenzo Guidi. Nano hotplate fabrication by combining EBL and FIB techniques. MNE 2021 – Micro and Nano Engineering Conference, Turin, Sept. 20th – 23rd, 2021.

5. Z. Feng, A. Cian, D. Giubertoni, A. Gaiardo, M. Valt, P. Bellutti, V. Guidi, J. Fiala, J. Babocký, M. Hrabovský. Nano-heater implementation in gas sensing devices by Electron Beam Lithography. The 65th International Conference on Electron, Ion, and Photon Beam Technology and Nanofabrication, New Orleans, May 31st – June 3rd, 2022.

6. Zhifu Feng, Andrea Gaiardo, Alessandro Cian, Damiano Giubertoni, Matteo Valt, Jiri Fiala, Jiri, Babocký, Milos Hrabovsky, Pierluigi Bellutti, Vincenzo Guidi. Micro gas sensor device fabrication with ZnO sensing nanofilms by electron beam lithography, Micro & Nano Engineering (MNE), Leuven, Sept. 19th – 23rd, 2022.

7. Zhifu Feng, Andrea Gaiardo, Matteo Valt, Barbara Fabbri, Davide Casotti, Soufiane Krik, Lia Vanzetti, Michele Della Ciana, Simona Fioravanti, Stefano Caramori, Alberto

Rota and Vincenzo Guidi. Investigation on Sensing Performance of Highly Doped Sb/SnO_2. SENSORS, 2022, 22(3), 1233.

List of Symbols

Symbol	Description
m	diffraction order
λ	diffraction wavelength of light
n	effective refractive index
d	the distance between adjacent periodic patterns on the lattice
I	the light that transmitted through the gas sample
I_0	light incident on the sample
z	sample absorption coefficient
l	optical pathlength of the cell
L_D	Debyee length
q	elementary charge
ε	dielectric constant
k_B	Boltzmann constant
T	absolute temperature
N_d	the density of dopants
T(t)	the temperature of the microheater
T_{amb}	temperature of the surrounding environment
P_{el}	heating power
R_{therm}	overall thermal resistance
C	overall thermal capacity
G_m	geometry factors
G_{air}	geometry factors
G_{rad}	geometry factors
T_{hot}	temperature of the hot active area
T_{amb}	temperature of the ambient
λ_m	thermal conductivity of the membrane

λ_{air}	thermal conductivity of surrounding atmosphere
ε	emissivity
σ	Stefan-Boltzmann constant
r_a	width of the membrane
r_i	width of the suspension beams
R	the resistance at real temperature
R_0	resistance value of Pt at 0°C
T_0	temperature of 0°C
T	the real temperature
α	temperature coefficient
k	spinner constant
p	resist solids content in percent
ω	spinner rotational speed in rpm/1000
t	resist thickness
λ	radiation wavelength
n	integer number
θ	the angle between the lattice planes and the incident beam
Φ_{spec}	the work function of the spectrometer
E	electrical field
V	potential difference between the two sides of the micro heater
J	current density
Q_j	Joule heating power
σ	electrical conductivity
C_p	heat capacity of the heater material
k	thermal conductivity of the heater material
ε	strain
ε_T	initial thermal strain
E	Young's Modulus matrix

α	thermal expansion coefficient
T	differential temperature
H	Sputtered thickness
IF	Ion fluence
SY	Sputtering yield
M	Pt atom molar mass
ρ	Pt density
N_A	Avogadro Constant

List of Abbreviations and Acronyms

Term	Definition
WHO	World Health Organization
MEMS	Micro-electromechanical Systems
CMOS	Complementary metal-oxide semiconductor
SMO	Semiconductor metal oxide
PL	Photoluminescence
DC	Direct current
QCM	quartz crystal micro-balance
SAW	surface acoustic waves
FPW	flexural plate wave
VOCs	volatile organic compounds
PWM	Pulse-width modulation
PhC	Photonic crystal
UV	Ultraviolet
NDIR	non-dispersive infrared
Ppy	polypyrrole
IDE	interdigitated electrodes
TNT	Trinitrotoluene
CNTs	Carbon nanotubes
SWCNTs	Single-walled carbon nanotubes
MWCNTs	multi-walled carbon nanotubes
HAL	hole accumulation layer
PVD	physical vapour deposition
PET	polyethylene terephthalate
PEN	polyethylene naphthalate
PI	polyimide

LPG	liquefied petroleum gas
EBL	Electron Beam Lithography
LPCVD	low pressure chemical vapor deposition
TEOS	tetraethyl orthosilicate
SEM	scanning electron microscope
FIB	focused ion beam
IMM	Integrated Micro Materials
TMAH	Tetra Methyl Ammonium Hydroxide
LMIS	liquid-metal ion source
GIS	gas injection systems
EDS	Energy Dispersive Spectrometer
XRD	X-ray Diffraction
XPS	X-ray photoelectron spectroscopy
KE	electron kinetic energy
BE	Binding energy
TOF-SIMS	Time-Of-Flight Secondary Ion Mass Spectrometry
UV/VIS	ultraviolet–visible
MHP	Micro hotplate
TCR	temperature coefficient of resistance
FEA	Finite Element Analysis
ONO	SiO2/Si3N4/SiO2
PECVD	Plasma Enhanced Chemical Vapor Deposition
ATO	SnO2 doped by antimony

1. Gas Sensor Overview

Environmental protection is an extremely significant topic for sustainable development of society. While with the rise in human population and advancements in technology, the release of toxic gases, such as NO_x, CO_x, NH_3, SO_x from pollution, vehicles, and industrial waste has become a cause for concern of all living creatures due to global warming, acid rain, sick house syndrome and destruction of ozone layer [1, 2]. Based on the reports from World Health Organization (WHO) official website, it says almost all of the global population (99%) are exposed to air pollution (household air pollution and ambient air pollution), which are keeping us at risk for diseases including heart disease, stroke, chronic obstructive pulmonary disease, cancer and pneumonia [1, 3, 4]. Every year 3.2 million people die of household smoke from dirty cookstoves and fuels, 4.2 million die because of outdoor air pollution, and 90% people are living in places where air quality exceeds WHO guideline limits. Monitoring the harmful gases in the air is primary precondition for environment preservation and health concerns. For example, NO_2 is an important gas because of its health effects, and it can also absorb visible solar radiation and contribute to impaired atmospheric visibility, which plays a critical role in global climate change and determining ozone concentrations. The Air Quality Guidelines (AGQ) value of NO_2 is hourly 200 $\mu g/m^3$ based on WHO guideline values, and for other pollutant gases, such as SO_2, CO and O_3, the AGQ level are 40 $\mu g/m^3$, 4 $\mu g/m^3$ during 24-hour averaging period and 100 $\mu g/m^3$ during 8-hour averaging period. To monitor these pollutant gases, there are several precise techniques applied to measure target gases concentrations, such as spectroscopy, chemiluminescence detection and photoluminescence detection, which function according to the luminescent phenomena, and can be defined as the emission (ultraviolet, visible, or infrared radiation) produced by a chemical reaction [5, 6].

Gas sensors are more and more used to detect the gases not only from the surrounding environment, but also from the exhaled gases of human beings and food. Based on Grandviewresearch report, the global gas sensor market size was valued at USD 2.5 billion in 2021, and expected to expand at a compound annual growth rate of 8.9% from 2022 to 2030 (https://www.grandviewresearch.com/industry-analysis/gas-sensors-market). To satisfy the need of nowadays improving life quality, only these spectroscopy, chemiluminescence detection and photoluminescence detection gas sensing ways with huge

cost and tremendous volume are far not enough, more new types of gas sensors should be investigated with low-cost, high-power efficiency and portable size.

1.1 Gas Sensor Types

A gas sensor detects analytes through the interaction of the analyte with the detecting material. In response to their concentration, a proportional electrical or optical signal is generated and displayed by sensing devices. Depending on the gas detection mechanism, this is achieved using a range of sensor types, including chemoresistive, thermoelectric, electrochemical, photoionization, ultrasonic, and infrared type. These different gas sensors function based on sensing materials and methods, such as mass spectrometers, gas chromatographs, optical spectroscopies, electrochemical method, surface acoustic and Fourier Transform Infrared Spectrometers [1, 7]. Ananya Dey has classified these gas sensors as catalytic combustion, electrochemical, thermal conductive, infrared absorption, paramagnetic, solid electrolyte and semiconductor metal oxide (SMO) sensors gas sensor [8]. Comini categorized all gas sensors into DC conductometric gas sensors, field effect transistors based gas sensor and photoluminescence (PL) based gas sensors [9].

1.1.1 Acoustic Gas Sensors

Acoustic sensors respond to the absorption of analytes in the sensing film and detect trapped gas molecules on the device surface. Acoustic gas sensors include quartz crystal micro-balance (QCM), surface acoustic waves (SAW), flexural plate wave (FPW), and thin rod sensors. With these sensors, analytes with stronger chemical interactions can be detected at lower concentrations. There have been reports of acoustic sensors with a minimum detection threshold of ppm to ppb. However, one of the most frequently observed issues with acoustic sensors is their weak selectivity, which is attributed to the commonly employed sensing materials. Several methods have been reported for increasing the selectivity of these sensors, including the use of an array of sensors with different chemical interfaces and a pattern recognition algorithm for identifying analytes, as well as the addition of a chromatographic column to the sensor for separating the various absorbed analytes [7].

The operating principle of QCM is based on the fact that the oscillation frequency of a quartz crystal is dependent on the change in crystal surface mass [10]. When Quartz or a similar piezoelectric crystal is subjected to electrical or mechanical stress, the piezoelectric crystal produces a voltage proportionate to the amount of stress. A piezoelectric quartz crystal is

placed between two electrodes and covered with the sensing material in QCM sensors. QCM sensors detect the change in mass of the sensing layer by detecting the quartz resonance frequency shift. When an external electric field is supplied to quartz via the two electrodes, an imbalance in the dipole moments of the crystal structure results in deformation of the quartz. Consequently, this ability can be utilized to generate a standing wave between two electrodes by applying alternating current at the resonance frequency of the device. When the crystal surface mass shifts due to analyte adsorption, and the crystal resonant frequency shifts, which can be connected with the gas characteristics and concentrations.

The first generation of SAW gas sensors with an extremely high resonant frequency of 400 MHz was introduced decades ago [11]. These sensors detect environmental changes based on the modification of the physical characteristics and amplitude of surface waves. SAW sensors consist of two SAW reflector arrays on a crystal substrate that are separated by a cavity containing a pair of electrodes. The maximum length of a sensor is several millimeters. Figure 1.1 depicts a schematic representation of a SAW gas sensor.

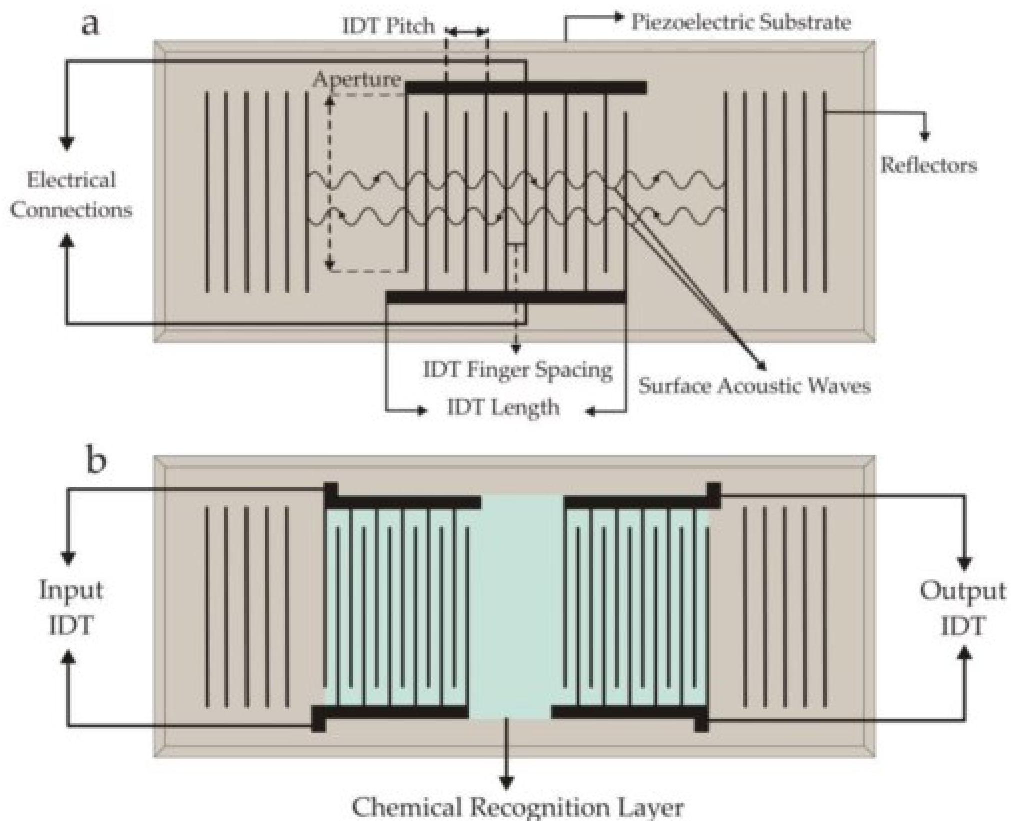

Figure 1.1 (a) A typical design of a one-port SAW resonator; (b) A two-port SAW device having a chemical recognition layer [11]. This figure has been reproduced with permission from [11].

CMUTs have been developed as an alternative to conventional piezoelectric transducers with enhanced features, such as a wider bandwidth and greater acoustic matching [12]. CMUT arrangement can also be utilized in the field of gas sensors by functionalizing a sensing material to detect volatile organic compounds (VOCs) and other gases. Moreover, good sensitivity, low LOD, reversibility, and a high-quality factor are cited as benefits of this type sensors [13]. A CMUT gas sensor is comprised of a thin, flexible membrane coated with a sensing substance and suspended over a fixed bottom electrode. In this configuration, the upper membrane and the lower electrode function as a capacitor, in which the changes in the device-sensing material can affect the capacitance of the device. Figure 1.2 shows a schematic depiction of a CMUT sensor [13]. By exposing the top membrane to the gas, it will absorb analytes, resulting in a change in the mass of the flexible membrane. This mass change results in a shift in the center resonant frequency, which is proportional to the analyte concentration.

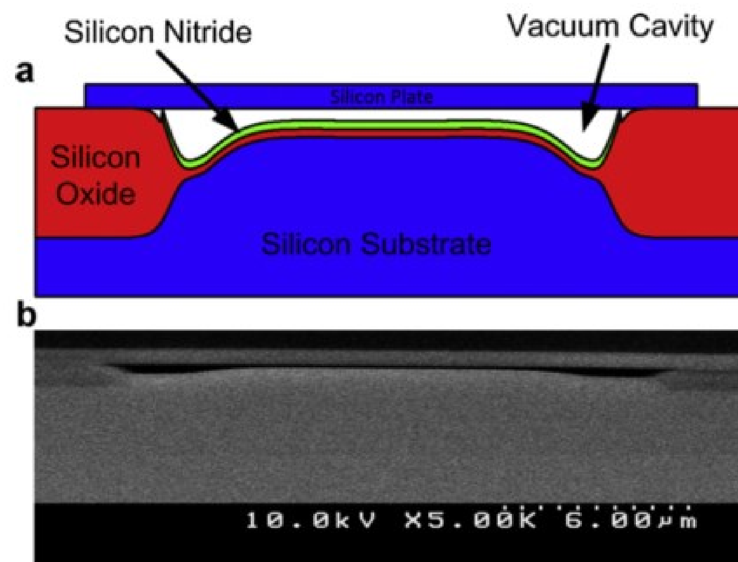

Figure 1.2 (a) Cross-sectional schematic of a unit resonator of a CMUT. (b) SEM cross-section picture of a unit resonator [13]. This figure has been reproduced with permission from [13].

1.1.2 Optical Gas Sensors

Optical sensors rely on the control, modification, or detection of the propagation of light in an active region, where the detection of photons immediately results in the transmission of electrical signals. Fiber-optic gas sensors and photonic crystal gas sensors are two typical optical sensors.

As shown in Fig. 1.3, fiber-optic sensors consist of a sensing layer, an optical fiber and a substrate [14]. The optical fiber is held on the substrate so that the sensing layer is partially exposed to light. The sensor membrane is positioned above the polished fiber, where the interaction between the analyte and sensing layer creates physical and chemical changes, such as a change in the refractive index. Consequently, fiber-optic sensors are able to detect analytes that induce detectable optical or optoelectrical changes in the sensing layer. Pulse-width modulation (PWM) and analytes-sensing layer interaction can explain the working mechanism of fiber-optic sensors. In PWM-based fiber-optic gas sensors, the pulse width varies with the change in sensing layer properties when exposed to the target analytes [62].

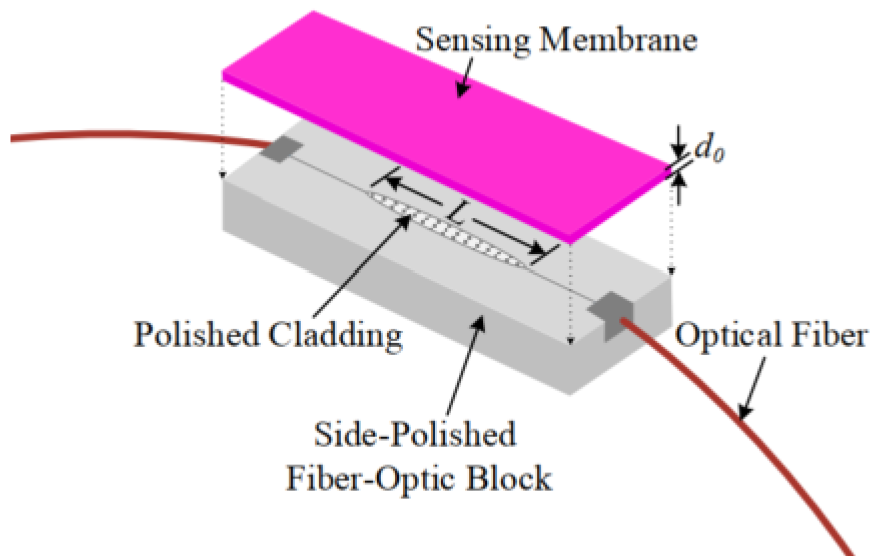

Figure 1.3 Schematic diagram of the side-polished optical fiber with a sensing membrane [14]. This figure has been reproduced with permission from [14].

Photonic crystal (PhC) sensors utilize periodic arrangements of dielectric materials with varying refractive indices for detection [15]. Figure 1.4 depicts the structure of PhC gas sensor devices [16]. In gas-sensing applications, PhC sensors are utilized to detect analytes by measuring the change in diffraction wavelength produced by two factors: variation in effective refractive index and variation in lattice distance of periodic structure [15]. These sensors have been proposed as potential candidates for achieving high sensitivity with the capability of detecting nanometer-sized chemical compounds, detecting environmental parameters such as temperature, pressure, and humidity [16, 17]. Dielectric materials with highly periodic micro- or nano-structures or patterns are utilized in PhC gas sensors. The periodic arrangement of the utilized dielectric materials can provide a photonic bandgap that permits some wavelengths of light to propagate through the PhC while preventing the

propagation of other wavelengths [16]. Using different PhC materials and patterning, this photonic feature can be tailored to the characteristics of the target light. As CO_2, CH_4, and CO gases exhibit absorption lines in the mid-infrared region, these mid-infrared samples of will be detected by these sensor devices [16].

Bragg's law helps explain both the diffraction of light in PhCs and the sensing mechanism [7]:

$$m\lambda = 2nd \cdot \sin \theta \qquad \textbf{1-1}$$

where m is the diffraction order, λ is the diffraction wavelength of light, n is the effective refractive index, d is the distance between adjacent periodic patterns on the lattice, and θ is the incidence angle. Assuming that the position of the incident light and the PhC layer are fixed, the effective refractive index is the sole variable that can affect the permitted wavelength of light. In the majority of instances, the refractive index of analytes differs from PhC substances. This difference in index of refraction alters the effective index of refraction, n, at the boundary between periodic structures and gaseous analytes. There are instances in which some analytes can alter the physical properties of photonic materials, such as swelling, which can contract or extend the PhC and consequently alter the lattice distance d. The consequent diffraction wavelength of probe light can be affected by both changes in refractive index and lattice distance, allowing for the identification of analytes [15].

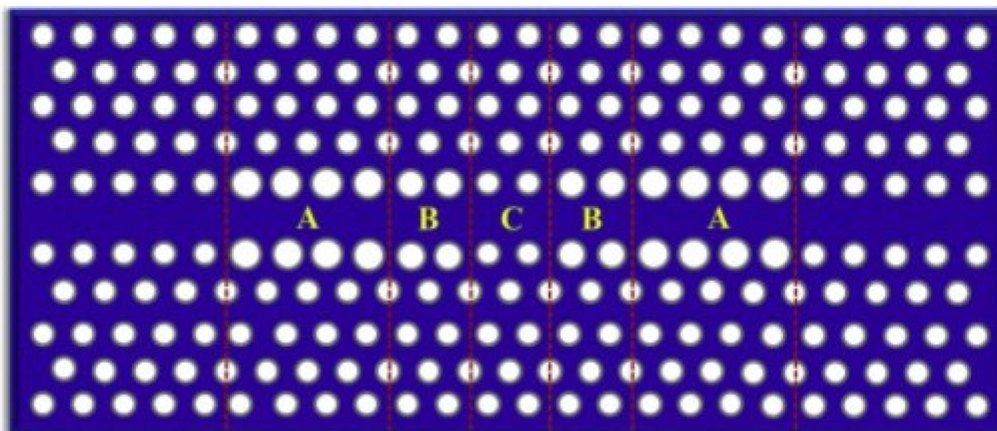

Figure 1.4 Structure of heterostructure photonic crystal cavity for gas sensor [16]. This figure has been reproduced with permission from [16].

In the UV/visible, near-infrared and mid-infrared areas of the electromagnetic spectrum, a great number of chemical species exhibit high absorption [18]. The absorption lines or bands

are unique to each species and serve as the basis for detecting and measuring them. Absorption spectra in the various spectral ranges exhibit distinct properties [17]. Optical gas detection with absorption spectroscopy relies on the Beer–Lambert Law:

$$I = I_0 \ exp\,(-\alpha\ell) \qquad \textit{1-2}$$

In which I is the light that is transmitted through the gas sample, I_0 is the light incident on it, α is the sample absorption coefficient, and ℓ is the optical pathlength of the cell. The absorption coefficient α is related to the gas concentration and the specific absorptivity of the gas. Figure 1.5 shows the common gases absorption coefficient [17]. Optical absorption gas sensors provide rapid response, minimum drift, and great gas selectivity, but it has very complicated light source and receiver equipment.

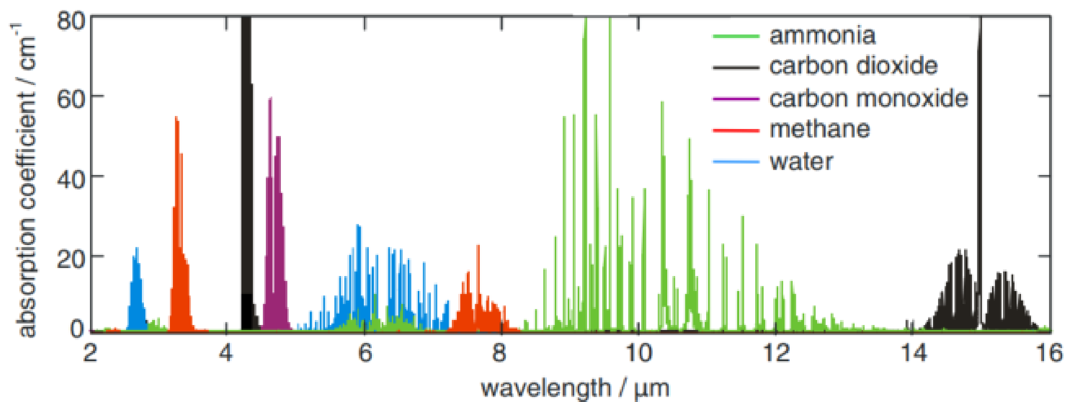

Figure 1.5 Absorption spectra for five gases in the mid IR region of the spectrum (all at 100% vol), taken from the PNNL database [17]. This figure has been reproduced with permission from [17].

Similar measurements can be conducted in the mid infrared (in classic non-dispersive infrared, or NDIR), near infrared, and UV/visible areas of the electromagnetic spectrum. Emission from a broadband source is often routed via two filters, one spanning the whole absorption band of the target gas (in the active channel) and the other covering a neighboring non-absorbed region, as shown in Fig. 1.6.

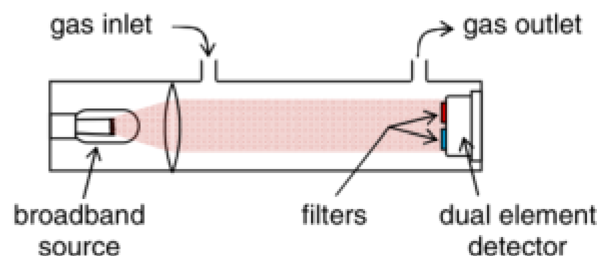

Figure 1.6 Schematic diagram of a typical non-dispersive gas sensor with optical pathlength in the range 3–20 cm. The source and detector are usually placed inside the cell to avoid baseline drifts caused by variations in the background concentration, which are particularly important in the case of CO_2 measurements [17]. This figure has been reproduced with permission from [17].

In contrast to the non-dispersive approaches discussed previously, spectrophotometry is dispersive in the sense that a wavelength selective element, such as a grating, disperses the spectrum of a broadband source. Multiple gases can be identified if their absorption lines lie within the wavelength range of the spectrometer, and regions with little or no absorption can often be located to serve as a reference, similar to the way the reference measurement in NDIR works. The ability to screen for the presence of a large number of unknown substances, as well as to identify and measure their quantities, can be useful for first responders in security applications.

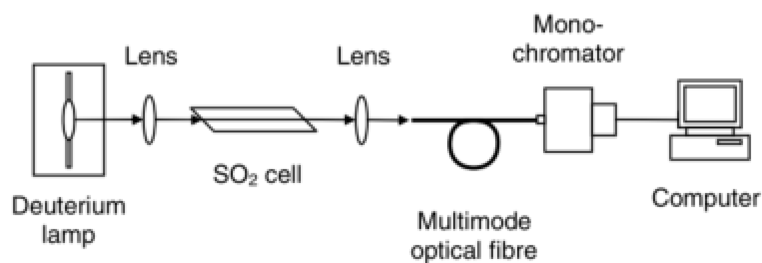

Figure 1.7 Simple configuration for spectrophotometric gas sensing using a fixed pathlength gas cell [19]. This figure has been reproduced with permission from [19].

1.1.3 Electrochemical Sensors

Electrochemical sensors are divided three types based on the operating principles for the potentiometric electrochemical [20, 21]:

Type I: Two electrodes are attached on either side of the electrolyte. In this case, the difference in chemical potential between neutral components that correspond to the mobile species in the electrolyte is directly measured by the electromotive force.

Type II: In order to offer versatility in the detection of chemical species besides the mobile species in the electrolyte, type II sensors employ both the electrode of the first kind and the electrode of the second kind, as shown in Fig.1.8. The conjugate component of the electrolyte chemical potential can be determined in this configuration.

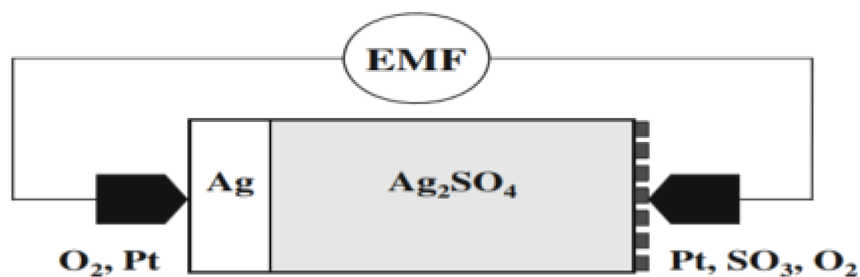

Figure 1.8 Schematic representation of type II potentiometric sensor. (-) Ag, O2, |Ag2SO4|Pt, SO3, O2 (+) [21]. This figure has been reproduced with permission from [21].

Type III: As illustrated in Fig. 1.9, the Type III sensor is made up of the second kind electrode and an ionic junction between the electrolyte and auxiliary phase to address this issue. The concentration of the chemical species that is absent from the electrolyte can be measured thanks to the ionic junction. For the chemical activity of the neutral component corresponding to the mobile ion to be constant throughout the continuous auxiliary phase, it is necessary for it to have ionic and electronic conductivity. If the auxiliary phase is porous or dispersed into a two-phase mixture with the electrolyte, either of which provides the necessary contact for chemical equilibrium between the electrolyte and the auxiliary phase, in this case this constraint is eased.

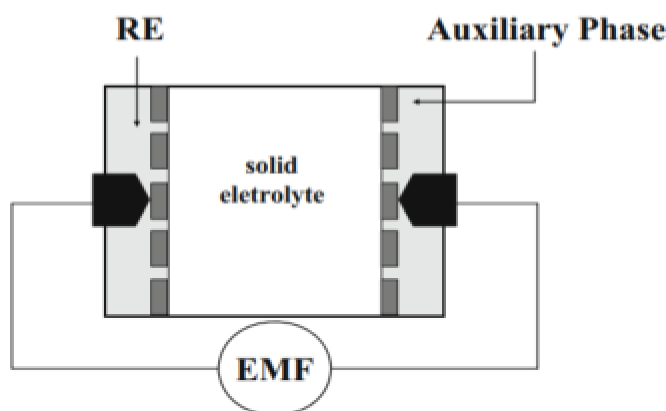

Figure 1.9 The schematic structure of type III arrangement. (-) $Na_2ZrO_3 + ZrO_2$, Au|Na^+|Au, $NaNO_3$ (+) [21]. This figure has been reproduced with permission from [21].

1.1.4 Chemiresistive Solid Gas Sensor

Organic-Based Chemiresistive Gas Sensor

Chemiresistive sensors constitute a newly emerging class of electrochemical sensors [1, 22]. They function on the basis of the change in electrical resistance of the materials caused by their chemical interaction with the analytes. These devices can utilize a variety of sensing

materials, including conductive polymers, organic semiconductors, and carbon-based substances. In comparison to SMO sensors, organic-based chemiresistive gas sensors have a comparatively simple structure that eliminates the requirement for a micro-heater. The geometry of these sensors comprises of a sensing material coated on a thin insulation layer such as SiO_2 on a silicon substrate, which bridges the gap between two electrodes.

Organic chemiresistive gas sensors assess variations in the electrical resistance of the sensing material in response to environmental changes. When the sensor is subjected to particular analytes, a direct interaction takes place between the sensing material and the analytes, resulting in a change in the sensing material properties, such as an increase in material volume or a decrease in material conductivity. There is a correlation among sensor resistance change, analyte characteristics and concentration of target gases. Changes in material characteristics are determined by the mechanism of interaction between the analytes and the sensing material. This can vary depending on the employed materials; for instance, highly sensitive nano-structured dye-doped polypyrrole (PPy) electrosynthesis has been fabricated on gold interdigitated electrodes (IDE) with a reported detection limit of 0.2 ppb and a dynamic range of 9.7–827 ppb for 2,4,6 Trinitrotoluene (TNT) detection [7].

Carbon nanotubes (CNTs) sensors are beneficial from the development of advanced micro- and nanofabrication techniques [23]. Single-walled carbon nanotubes (SWCNT) and multi-walled carbon nanotubes (MWCNT) are the two types of carbon nanotubes. CNTs are distinguished by their high aspect ratio, extremely strong intermolecular interactions, and low density, which results in increased sensitivity, a low detection limit, and a quick response time. On the basis of their operating principle, these sensors can be classified as gas sorption sensor, gas ionization sensor and capacitive gas sensors:

Chemosorbing gas sorption CNT sensors exposes CNTs to the target gas resulting in the transfer of charge between the CNT and the target gas. This process causes the conductivity of the CNT sensing material to shift. Changes in the conductivity of the device are proportional to the gas characteristics and concentration. The recovery time of these sensors can be improved by heating the sensing film. Using different chemical functional groups, for example, oxygen on the surface of CNTs can lead to selective interaction with desirable analytes, such as hydrogen-containing molecules, hence modifying the detecting property of sorption-based CNT gas sensors. Nonetheless, this can reduce the accessibility of analytes to the CNT surface, hence decreasing the sensitivity. Long recovery time, irreversibility of

CNT conductivity, and lower sensitivity for low gas energy levels are common shortcomings of these sensors [23].

The structure of CNTs with a high aspect ratio is perfect for creating an electrical field by applying voltage. CNTs are employed for both the anode and cathode electrodes to generate an electric field in ionization CNT gas sensors. By accelerating electrons from the electrode, analytes are ionized into a plasma state. The ionization energy and plasma current can be measured to determine the characteristics and concentration of a gas. This technique can detect gases with low sorption energies. Common gas ionization sensors are bulky and have high energy consumption; however, the use of CNTs can considerably reduce the size and ionization energy of gas due to the sharp tip structure and low work function of CNTs [24].

CNTs can also act as the sensing element of capacitive-based gas sensors. In this construction, one capacitor plate is constructed of silicon while the second plate is silicon covered with carbon nanotubes. By placing a voltage across the capacitor, CNT generates a strong electric field, resulting in the polarization of the gas molecules and, consequently, a change in capacitance. The shift in capacitance of the sensor is caused by the change in dielectric constant of CNT, which is associated with the desired gas concentration. This CNT sensor dielectric change can also be used in a resonance frequency sensor arrangement, which monitors the frequency shift associated with gas characteristics and concentrations [25].

Semiconductor metal oxide (SMO) gas sensors, including n-type sensing materials, such as TiO_2, ZnO, SnO_2, and WO_3, and p-type sensing materials, such as NiO, Mn_3O_4, and Cr_2O_3 properties are greatly dependent on the interaction with the adsorption gases, which is a magnificent material for gas sensing application, and feature a universal sensing mechanism using chemisorbed oxygen species and gas (analyte) molecules with two operational roles: receptor and transducer [26-30]. The receptor identifies the target gas through the material/gas interface, causing a change in the material electronic characteristics, whereas the transducer converts surface phenomena into a change in the electrical resistance of the tested sensor. In addition, the progressive rate of resistance change of the sensor is proportional to the concentration of the target gas, allowing for a rapid determination of the concentration of the target gas. The electrical conductivity of these semiconductors will increase when exposed to reducing gases, whilst oxidizing gases will have the opposite effect. When a heterojunction is produced by depositing metal (Pd or Pt) nanoparticles over pure

metal oxide semiconductors, the proposed mechanism is extremely complex. In general, the sensitivity of the SMO sensor is determined by the thickness of the receptor layer, the catalytic metal particles placed within it, and the receptor layer operational temperature [31].

1.2 Comparison of Different Types of Gas Sensors

The acoustic gas sensors and optical sensors do have very high gas detection precision and fast response, but they require huge volume or high preparation cost [32, 33]. Electrochemical gas sensors can be relatively selective to individual gases and sensitive to ppm or ppb levels, but they have limited lifetimes and are prone to cross-response problems, such as to humidity. SMO gas sensor are more and more widely studied and used due to its physical and chemical stability, low fabrication cost and easy integration [22, 26, 27, 29, 34]. Furthermore, SMO gas sensors is the most suitable to develop portable instrumentation because of its compatibility with silicon technology [35]. In our work, we focused on SMO gas sensors fabrication and characterization.

Table 1-1 Comparison of various types of gas sensors [34]

Parameter	Type of gas sensors				
	Semi-conductor	Catalytic combustion	Electro-chemical	Thermal conductive	Infrared absorption
Sensitivity	e	g	g	b	e
Accuracy	g	g	g	g	e
Selectivity	p	b	g	b	e
Response time	e	g	p	g	p
Stability	g	g	b	g	g
Durability	g	g	p	g	e
Maintenance	e	e	g	g	p
Cost	e	e	g	g	p
Suitability to portable instruments	e	g	p	g	b

e: excellent; g: good; p: poor; b: bad.

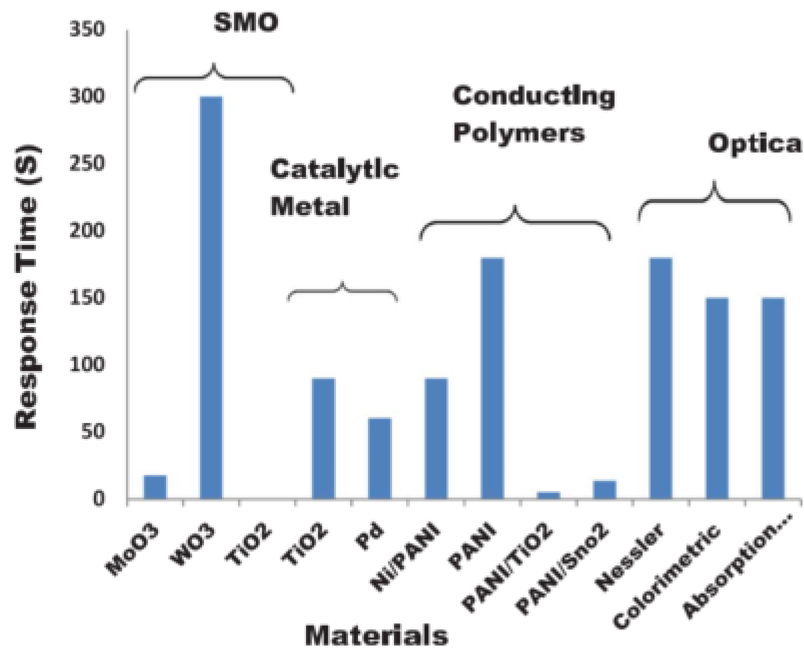

Figure 1.10 Comparison of different sensor materials according to their response time for NH_3 sensing [8]. This figure has been reproduced with permission from [8].

SMO gas sensors development was with discovery of semiconductor materials properties and the improvement of MEMS technologies. Brattain and Bardeen observed in 1952 that the semiconducting characteristics of germanium changed when the oxygen partial pressure in the surrounding atmosphere varied [36]. Seiyama published the results of his research that demonstrated the gas sensing impact on metal oxides [37]. Taguchi was the first person to commercialize SMO gas sensors by employing an alumina ceramic tube installed with the metal oxide and electrodes, and a heater coil that passed through the middle of the tube [N. Taguchi, Japan. Patent 45-38200 (1962)]. In today market, the majority of the commercially available devices are produced by screen printing on thin ceramic substrates. Then the first patent based on a micromachined silicon substrate demonstrated the first thin-film metal oxide gas sensors. A thermally insulating silicon oxide membrane was utilized in the construction of the micro hotplate [38-41]. Advanced micromachining of silicon technologies significantly results in the development of novel MEMS devices [42, 43]. In contrast to miniaturization, the employment of microfabrication techniques to create microsensors and MEMS devices has brought forth novel modes of operation, array formation, batch processing, and lower power consumption [44, 45]. Anodic alumina has been micromachined for some tasks, but silicon micromachining is the basis for substantial development. Micromachined thick-film semiconductor gas sensors were introduced by drop-coating the metal oxide materials on a thin dielectric membrane with platinum used

both for heaters and electrodes, offering improved performances and robustness [46]. Temperature modulation was introduced as a mode of operation due to the low thermal mass of the micro hotplates. This mode of operation is now mainly applied to minimize power consumption. Since 2000, the field has been evolving toward the use of Silicon On Insulator structure (SOI) wafers, the implementation of these sensors is in complementary with CMOS technology and on polymeric substrates, and the identification of suitable modes of operation for different applications [47, 48]. The field is now strongly focusing on nanomaterials, especially nanostructured metal oxides, but one can question whether this would be the solution to the main problems remaining with thin-film and thick-film gas sensor devices, which has transferred to and been exploited by industry so far since the extensive work carried out in this regard. Micro hotplates being a mature and robust technology, the main issue remains of the synthesis of performing materials and their effective integration into a robust manufacturing process [49, 50].

1.3 Sensing Mechanism of SMO Gas Sensors

Chemiresistive gas sensors have been extensively utilized based on their change of electrical properties to detect environmental analytes, such as CO_x, NO_x, SO_x and organic gases [33]. Researchers have developed a mount of materials for chemiresistive gas sensor over these years, SMO, polymers and metallic nanoparticles are mostly used as chemiresistive gas sensing materials. Among of them, SMO is now developing fast due to its low production cost, stable physical properties and chemical versatility including SnO_2, ZnO, WO_3, CuO, In_2O_3 and so on [51].

The evaluation criterions of gas sensor behaviors are decided by the parameters of sensitivity, selectivity, stability, detect limit, life cycle, response and recovery time [52]. Sensitivity is defined by the resistance changing ratio of sensing materials before and after detecting the target gases, selectivity states how much the sensor is disturbed by interfering gases from target gases, which can reflect the ability of sensor devices to differentiate among mixture gases. Stability refers to the capacity of a sensor material to keep producing the same output signal over an extended period of time towards target analyte gases with varying concentrations. The recovery time (τ) means the time period for reaching 90% of the stable maximum response between gas in and out, which also logarithmically depends on partial pressure. To enhance the gas sensor performance, researchers have tried thousands and thousands of solutions, such as optimizing the working temperatures, controlling the material

powder grain size and morphology, doping, heterostructure and novel devices [22]. In order to develop the capabilities of gas sensor, it is fundamental to understand the SMO work mechanism.

SMO typically consists functionally of a receptor and a transducer. The former has a material or a system interacting with gases that causes a change in their own properties (work function, dielectric constant, electrode potential, mass, etc.) [53, 54]. The transducer is a tool that converts a phenomenon into an electrical signal (sensor response). The type of transducer with the receptor appearing to be implanted within it, can determine how SMOs are classified, such as resistor sensor, diode type, metal insulator semiconductor capacitor type field effect transistor type [53, 55].

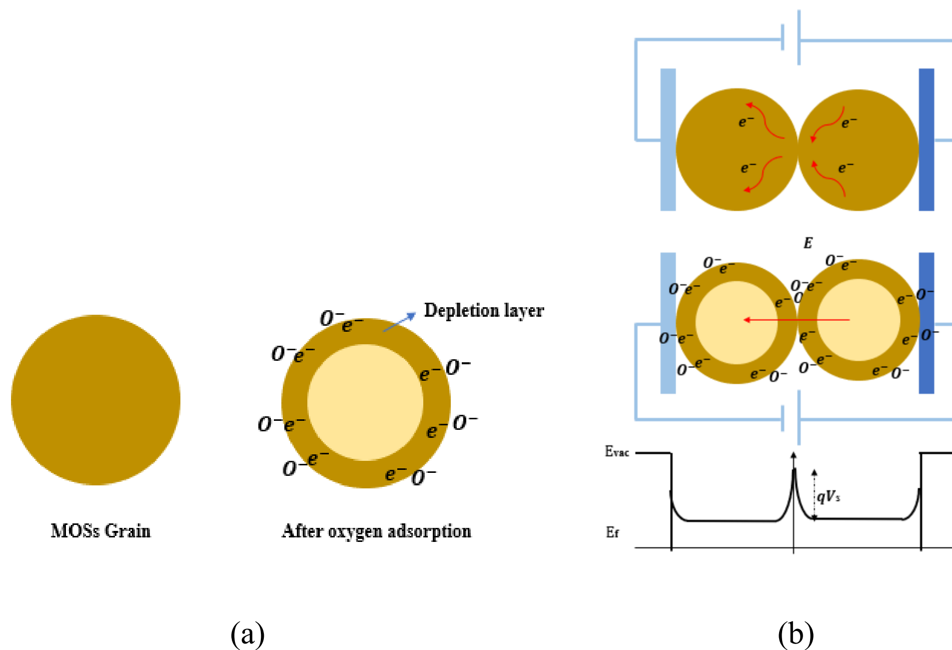

Figure 1.11 (a) Receptor function: oxygen adsorption on SMOs particle surface model; (b) Transducer function: surface conductive grains contact model. Idea from [56].

SMOs physicochemical properties are evaluated in large part by the resistance changing of semiconductors, which either rises or decreases depending on the physical properties of the metal oxides and the gaseous analytes. As we all know, semiconductor material physical properties are easily affected by the environments, such temperature and surface conditions. The primary cause of the resistance fluctuation occurs when host materials are exposed to an atmosphere containing target gases, which is the detecting mechanism of gas sensors based on metal oxide semiconductors [56-58]. During the gas sensing progress, loosely sintered sensing material grains play the role of receptor, and the contact parts among grains

act as transducer, which is the most resistive part in the materials. The formation of an electronic core-shell structure by oxygen adsorption is responsible for the gas sensing properties of metal oxide semiconductors. In more detail of n-type SMOs as shown in Fig.1.11, in which electrons are the current primary carrier, oxygen molecules are adsorbed onto the surfaces of n-type sensing material (such as SnO_2 and ZnO) at high temperatures (>100 °C), where they then take electrons from the surfaces to ionize oxygen species like O^{2-}, O^-, and O_2^- as shown in equations of 1-3,1-4,1-5 and 1-6, decreasing electron density and raising resistance when exposed to ambient air. These ionosorption species (O^{2-}, O^-, and O_2^-) are generally known to be dominant at 150 °C, 150 °C to 400 °C, and >400 °C, respectively [56]. This induces the formation of an electronic core-shell structure, where an n-type semiconducting region exists in the cores and resistive electron depletion layer at the shells of the particles.

$$O_2(gas) \rightarrow O_2(ads) \qquad \textbf{1-3}$$

$$O_2(ads) + e^- \rightarrow O_2(ads)^- \qquad \textbf{1-4}$$

$$O_2(ads)^- + e^- \rightarrow 2O(ads)^- \qquad \textbf{1-5}$$

$$O(ads)^- + e^- \rightarrow O(ads)^{2-} \qquad \textbf{1-6}$$

The adsorbed oxygen species can only have a small and localized impact on the semiconductor electron distribution close to the surface. Debye length (L_D), which is typically several nanometers, is used to define the depletion layer depth. Equation 1-7 calculates the Debye length of a semiconductor, where q is the elementary charge, ε is the dielectric constant, k_B is the Boltzmann constant, T is the absolute temperature in Kelvins, and N_d is the density of dopants (either donors or acceptors) [53]. Based on Debye length equation, it clear that the depletion layer thickness is decided by the material intrinsic parameter ε, temperature and doping level.

$$L_D = \frac{\sqrt{\varepsilon k_B T}}{q^2 N_d} \qquad \textbf{1-7}$$

When this n-type SMOs is exposed to reductive gases, the surface reaction between negative oxygen species and reductive gases causes electrons to flow back to bulk materials, which can reduce the resistance of SMOs.

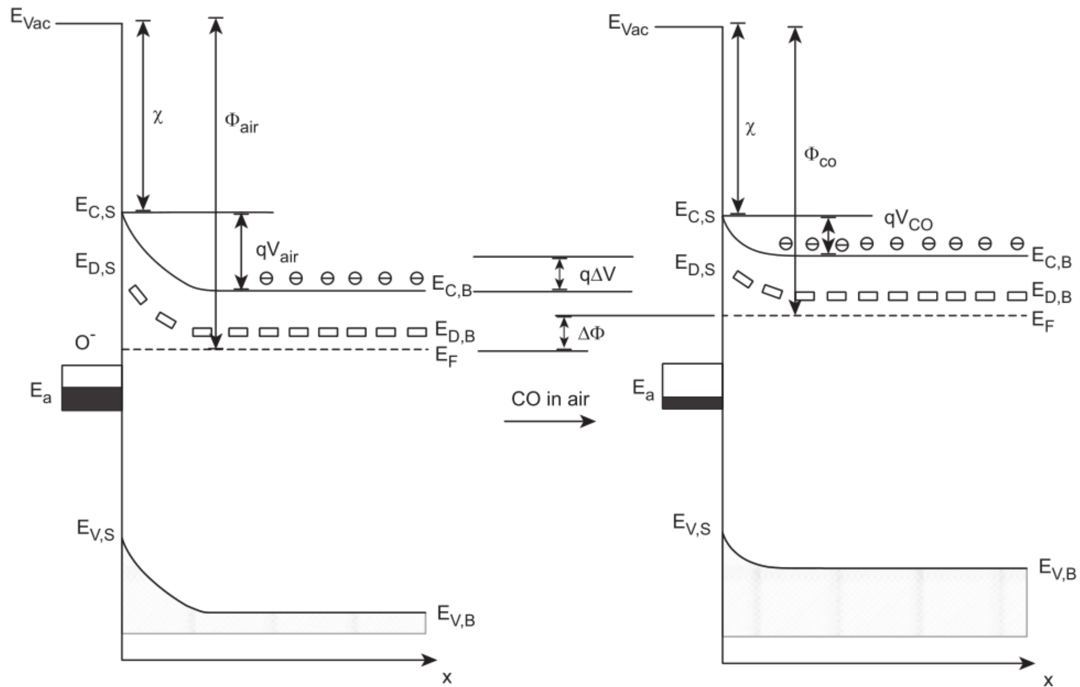

Figure 1.12 Energy band representation of n-type SMO material before and after exposure towards reducing gas. Reprinted permission [53].

From the energy band bending point of view for n-type materials, the formation of depletion layer indicates energy band upward bending, meaning that the electrons need more energy to reach the surface. Hence electrons need more energy to flow from one grain to another grain, resulting in higher resistance due to Schottky barriers among grains. When reduced gases react with preabsorbed oxygen, the grabbed electrons on the surface will be released to the conduction band of the sensing material again, which decrease the energy band barrier height, and increase the concentration of electrons and conductivity of n-type sensing materials, as shown in Fig.1.12.

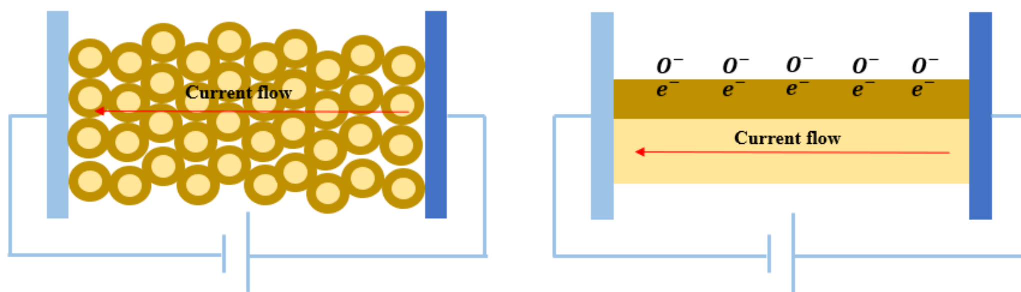

Figure 1.13 Schematic of gas sensing process of porous sensing film and compact film. Idea from [53, 59].

Based on utility level of SMO, there are two types of sensing material films: the porous sensing film and compact film, the distinction between them is depicted in Fig.1.13. The porous film sensing process is explained above, the grains that make up the sensing layer are only loosely adhered to one another. For the compact film sensing film, it is assumed that any influence exerted by the surface does not permeate the entire grain, the gases cannot reach the deep position, and only interact on the geometric surface. The concentration of electrons changing occurs near the film surface, and resistance of the deep bulk part is hardly affected by the gas chemical reaction. In this case, the signal for this kind of film is very weak. Consequently, it is possible to think of the sensing layer as having two distinct areas: a space charge layer that is located on the surface, and the bulk, which is unaffected by the presence of gas. When ambient oxygen reacts with the surface of stannous dioxide in dry air, acceptor levels are formed. The electrons from the conduction band are then trapped at these levels, which results in the formation of molecular and/or atomic oxygen ions.

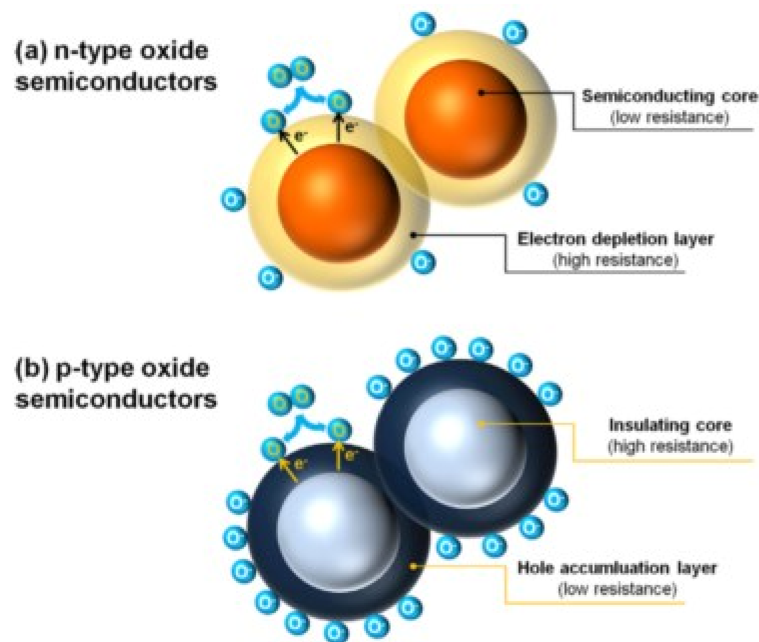

Figure 1.14 Gas interaction with n-type and p-type SMOs model. Reprinted with permission [30].

As opposed to n-type semiconductors, the majority carrier in p-type metal oxides is the holes (h^+), and the change of resistance toward reductive gases and oxidizing gases is completely reverse, as shown in Fig.1.14 [30, 57, 58]. The adsorption of oxygen species in p-type metal oxide semiconductors results in the formation of a hole accumulation layer (HAL) at SMOs

surface as a result of the electrostatic interaction between the species with opposing charges, which once more creates an electronic core-shell configuration and results in the formation of an insulating region at the cores and semiconducting HALs near the surface of these particles.

1.4 Approaches to Enhancing SMO Gas Sensing Materials Properties

There are several parameters of the gas sensors to be optimized, such as sensitivity, selectivity and stability except for detection limit, response/recovery time [60]. Plenty of research works have been conducted to improve these parameters, such as synthesizing sensing materials with different morphologies, changing crystal structure, noble metal doping, grain size adjusting and heterojunction and so on.

Morphology of sensing materials design and synthesizing is one of the easiest ways to improve the sensitivity of gas sensors mainly due to specific surface area changing, such as nanoparticle, nanowire, nanosheet and nanoclusters [61]. Different fabrication methods have been developed, such as sol-gel method, hydrothermal method, sputtering and ball milling method. The grain size has a huge effect on the response, especially when the space-charge layer of crystallite is smaller than the practical crystallite sizes [62].

Noble metal decoration such as Pt, Au and Pd doping can hugely improve the sensitivity and selectivity of SMO gas sensors by changing their microstructure, morphology, activation energy, electronic structure or band gap of the metal oxide [8, 63]. For example, Anmona Shabnam Pranti et al. have investigated that Pt nanoparticles can exceedingly improve sensitivity of the sensor toward hydrogen with concentrations as low as 0.001% (10 ppm) with an average response time of 650 ms [63]. Wenhao Jiang et al. designed highly sensitive and selective xylene gas sensor of MoO_3 nano-pompon doped by Ni metal, and they found that with different doping concentration of Ni^{2+} by one-step solvothermal method, the morphology could be changed. During their measurement process, they obtained increased 18 times response on xylene due to the increases of surface-active sites and the improvement of micro-morphology caused by Ni^{2+} doping [64]. Vasile Postica et al. created a new strategy based on surface functionalization and doping of semiconducting oxides for tuning device properties of ZnO:Fe sensors via surface decoration with oxidized silver nanoparticles with a diameter of 7-10nm. Ago/Ag decorated ZnO:Fe samples exhibited ultra-high sensitivity to

ethanol vapor versus CH_4 and H_2 gases. They found that the transition metal oxide clusters modify the surface chemistry of the doped ZnO surface by quantum mechanical simulations. Compared to Fe doping, (AgO)m nanoparticles on the surface with different sizes was more favorable to contribution of the gas sensitivity [65]. Ying Chen et al. modified mesoporous-In_2O_3 by loading Pd nanodots, which showed super high response to H_2 as with concentrations in the range of 0.5-100 ppm [66].

When the grain size is compatible to the depletion layer, the sensitivity of gas sensor is heterojunction structure creation can enhance the gas sensor performance, which refers to the interface region formed between two semiconductors with different band gap widths. A heterojunction can be categorized as either homogeneous (n-n heterojunction and p-p heterojunction) or heteromorphic (p-n heterojunction). Due to the different chemical and physical parameters of the two materials, such as band structure, dielectric constant, lattice constant, and electron affinity, etc., the mismatch phenomenon at the interface endows the heterojunction with a number of novel properties, which have attracted a great deal of research on heterogeneous materials and devices. when the junction interacts with gas analytes, it modifies the interface potential energy barriers and regulates the transfer and/or injection of electrons and holes in a precise manner [67].

Micro-electromechanical Systems (MEMS) applied in SMO gas sensor field can significantly enhance the sensing performances, such as improving the power efficiency, increasing integration and sensitivity [68]. For example, Vijay V. Kondalkar et al. designed customized, compact and portable MEMS gas sensor arrays for dissolved hydrogen gas analysis with a specially designed system, which had a Wheatstone bridge circuitry with two pairs of resistors. They also integrated an in-plane microheater and a temperature sensor on it, and the sensing results were quite similar to those measured with a digital multimeter, which was very promising for long term monitoring of the operational status of transformers [42]. Sirui Tang et al. they developed an MEMS sensor array composed by eight SECNTs-based sensing units to detect gases of H_2, CO and C_2H_2, and they found the accuracy and reliability of this sensor array was higher than the traditional BPNN model [44]. Wonjun Shin et al. investigated the Si metal-oxide-silicon field effect transistor type gas sensor with a localized embedded micro-heater, and the sense material was 12 nm thick In_2O_3 deposited by radio frequency magnetron sputtering to detect target gas NO_2. They found that the limit of the detection of the gas sensor toward NO_2 gas could be improved from 0.55 ppb to 0.27 ppb by applying a forward voltage of 0.5 V [45].

1.5 Main Elements of MEMS Based SMO Gas Sensor Devices and Fabrication Routines.

MEMS and complementary metal-oxide semiconductor (CMOS) development and application in gas sensor field has driven the gas sensors market overwhelmingly [4, 7]. The components of a MEMS-based SMO gas sensor device include three main parts: a microheater element embedded in the substrate layer (suspension), a dielectric layer or insulation layer (oxides) and sensing film, as shown in Fig. 1.15 (a).

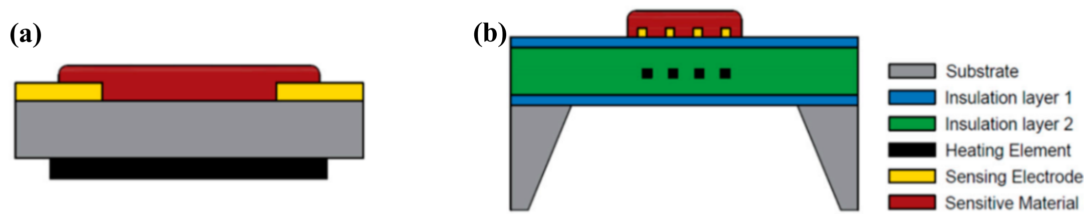

Figure 1.15 Models of (a) a traditional SMO gas sensor and (b) a micro hotplate SMO gas sensor. Reprinted with permission [69].

MEMS based micro/nano heater has a low power consumption at same temperature compared to conventional SMO gas sensors, which can play a significant part in finding a solution to the problem described above. The latest developments in a variety of fabrication processes have led to the downsizing of sensing chips and heater resistors, which has resulted in the creation of miniature gas sensors that require significantly less power [59]. Specifically, MEMS has made it possible to create SMO gas sensors that are very small, consuming very little power (just a few tens of milliwatts) [70]. It is possible to develop tiny, portable, and extremely low power consumption sensing devices by integrating gas sensors based on SMO materials into MEMS platforms. MEMS based micro/nano heater are fabricated on platforms made of silicon wafers by the use of microelectronic fabrication processes, specifically photolithography and post-processing procedures. Furthermore, these technologies make it possible for designers to combine multiple sensor arrays onto a single sensor platform, which then enables the platform to be used in mass manufacturing at a reduced cost. as shown in Fig. 1.15 (b) shows the cross section of MEMS based micro hotplate structure, clearly SMO devices compose of three main parts: sensing material film acting as receptor and transducer, interdigitated electrode to readout of the resistance changing signal of sensing material, and heater system offering required operation temperature. These three main parts are fabricated on insulating substrate, which acts as

mechanical support for the sensor devices (typically Si_3N_4 and SiO_2) [33]. Techniques to deposit sensing film, design of electrode and heater system, and selection of substrate materials can intrinsically affect the response of SMO sensor devices.

1.5.1 Gas Sensing Films Deposition

A gas sensor must meet a number of specifications before it can be put to use, which are determined by the goals, environments, and circumstances under which the sensor will operate. The requirements that relate to sensing performance (such as sensitivity, selectivity, and speed of response) and reliability (such as signal drift, stability, and interfering gases) are those that are most crucial. The selection and processing of the sensing materials (materials design) are critical in research and development because they are all connected to the used sensing materials. the creation of gas sensors. Thick film-based SMO sensors were firstly commercialized regarding the stability and reproducibility before the burst of MEMS technologies. Deposition technologies like dipping, drop coating and screen printing are mainly used to make the thick sensing film. While if the SMO is micro/nano-level size fabricated by MEMS fabrication process, it is hard to deposit the sensing film on the small chips by using the traditional depositing methods. Micromachining of silicon offer a way to deposit the thin film on micro/nano devices, which has brought different advantages not only for miniaturization, but also for batch process, gas sensor arrays fabrication and power consumption reduction.

The techniques to deposit thin SMOs thin film are widely used in the clean room, such as chemical vapour deposition (CVD) and physical vapour deposition (PVD). CVD is a form of vacuum deposition, which can produce of high-quality and high-performance solid materials. The production of thin films is a common use of the method in the semiconductor sector. In a conventional chemical vapor deposition process, the wafer (the substrate) is subjected to one or more volatile precursors, which then react and/or decompose on the surface of the substrate to generate the desired deposit. The production of volatile by-products is common, and these by-products are often eliminated by the flow of gas through the reaction chamber. This technique can be used to deposit materials in a variety of morphologies, including monocrystalline, polycrystalline, amorphous, and epitaxial. These materials consist of carbon (fiber, nanofibers, nanotubes, diamond, and graphene), silicon (dioxide, carbide, nitride, and oxynitride), fluorocarbons, filaments, tungsten, titanium

nitride. The most common CVD formats are Low-pressure CVD (LPCVD), Plasma-enhanced CVD (PECVD) and Microwave plasma-assisted CVD (LPCVD).

Using a MEMS-based sensor platform, sputtering is a promising candidate PVD approach to produce oxide semiconductor gas sensor with various compositions and catalysts. Sputtering has been used to deposit the majority of sensing materials with a high melting point or a mixture of materials. By depositing the atoms that become separated from the targets, sputtering creates a thin film due to the bombardment of Ar ions. Metals, oxides, nitrides, and alloys can be deposited using sputtering to create a wide range of thin films. It is desirable to use direct current (DC) sputtering to create metal films with high conductivity. In contrast, radio frequency (RF) sputtering delivers reactive sputtering, which is the production of a thin film by the reaction between the target material and reactant gas in the chamber. RF sputtering is typically used to deposit oxide semiconductors. The ability to easily regulate composition, thickness, and catalyst loading are the key benefits of using sputtering to create films for gas sensors. Certain processes will benefit from enhanced film adhesion as a result of an increase in impact energy. However, it can be challenging to deposit porous thin films and fine-tune the microstructure of the films.

An important PVD tool for creating thin films of metals, oxides, and semiconductors in a high-vacuum setting is electron beam evaporation. A vacuum chamber is filled with ultra-high purity coating material, usually in the form of pellets in a crucible. These pellets are heated by electron energy, which causes the coating material to transition into the gas phase. The evaporated particles can move to the substrate without running into any outside particles thanks to the vacuum environment. They then form a thin film and condense on the substrate surface.

Resistive thermal evaporation as another type of PVD can be used to deposit metals as well as organic and inorganic polymers. In this technique, electrical energy is employed to heat a filament, which then heats the deposition material to the point of evaporation. The process can be carried out at extremely high levels of vacuum to minimize collisions with extraneous particles and, hence, reduce the likelihood of film impureness. It is possible to obtain high deposition speeds, and particles with lower energies can limit substrate damage. The thermal evaporation process permits both sequential and concurrent deposition of thin films. In the evaporation process, the substance to be deposited is heated to its melting point to generate sufficient vapour pressure, and the necessary evaporation or condensation period is

established. The simplest sources utilized in this evaporation include wire filaments with a higher melting point, metal boats, and ceramics that are heated by putting a transient electrical current across them.

1.5.2 Substrate Materials Introduction

Substrate acts as the mechanical support for gas sensor devices, with heater element and interdigitated electrodes on top of it. There are several kinds of substrate materials: ceramic, plastic, paper, textiles and silicon wafer.

Plastic materials are used for flexible sensor substrate, such as polyethylene terephthalate (PET), polyethylene naphthalate (PEN), parylene, nylon, PDMS polystyrene and polyimide (PI) [71-75]. For example, Jose V. Anguita et al. have used a new sputtering technology to reactively sputter-deposit good quality ITO on a flexible polymer substrate that was maintained at less than 50°C, achieving electrical resistivity and optical absorption coefficients of 5×10^{-4} Ω·cm and 4000 cm^{-1} [73]. Even these materials are highly thermal and electrical constraints, they cannot operate at high temperature, which will limit the application for SMO gas sensors. Furthermore, plastic materials own high thermal expansion coefficients, it is difficult to deposit sensing materials with low thermal expansion coefficient and easily result in disturbance of the response measurement. Paper is another substrate material, enabling low-cost development of sensor devices due to its recyclable and environmentally friendly properties. Paper can be fold and unfolded to support sensor devices and used in some uncommon conditions where it requires less rigid substrates. For example, Gwangseok Yang et al. has developed Graphene-based flexible NO_2 sensors on paper substrates, which showed an immediate response (32-39%) exposed to 200 ppm NO_2 [76]. J. Sarfraz et al. printed polyaniline composite material on paper substrate to make the gas sensor to detect hydrogen sulfide gas [77]. But the roughness and absorptiveness of paper have declined the application cases [76, 77]. Textiles material can both play the role of substrate and sensing material, JinWoo Han et al have implemented single-wall nanotube based material on cotton textile to detect ammonia gas [78]. But the drawback for textile substrate is that this material has high bending strain.

Single crystal silicon wafer can serve as a wonderful substrate for SMO micro/nano system, which can also make it possible to apply highly developed and sophisticated batch-production methods of integrated circuits to the sensor field, feasible to combine sensors with other electronic products on a small chip. However, silicon wafer cannot be used

directly for SMO sensor substrate due to its high electrical conductivity. SiO_2 and Si_3N_4 are easily deposited on silicon wafers with excellent thermal and electrical isolation, and high resistance to oxidation or many etchants. These two materials can be utilized to inhibit the diffusion of numerous undesirable contaminants or the implantation of ions during depositing sensing materials on silicon wafer. The mechanical and electrical advantages at the silicon-silicon dioxide interface make it possible to develop tiny size geometries devices on them [79]. They are wonderful insulator because of its strong dielectric strength and relatively broad band gap, which even can withstand high temperatures of up to 1600 °C, making them useful materials for integrating processes and devices. SiO_2 can be easily grown thermally under O_2 environment, and Si_3N_4 is formed by the reaction between $SiCl_2H_2$ and NH_3. These two materials are perfect for MEMS SMO substrate [80, 81].

1.5.3 Hotplate Introduction

One of the key elements that affects the sensitivity, selectivity, and reaction time of SMO sensors is operational temperature. A hotplate on SMO gas sensors can initiate the sensing reaction between the target gas and the sensing material surface. A significant number of SMO based commercial gas sensors make use of this heater resistors to obtain the operation temperature up to the necessary value.

Most SMO gas sensors work at high temperature, and the necessary operate temperature is provided by a hotplate. The reaction rates during sensing process between various absorbate gases on the sensing layer surface can be driven by activation energy through heating temperatures, besides several other factors like the conductance of the sensing layer and the capacity of a particular gas absorbed [82, 83]. Ceramic hotplates such as alumina are widely used in market, but for the fabrication of nanoscale electrodes, which requires an extremely smooth surface, it seems very difficult for ceramic surface. Additionally, ceramic based hotplate consumes high power and requires complicated mounting technology [83]. Due to its high-power consumption that conventional SMO gas sensors require, their application is restricted to mobile phones and other portable electronic equipment.

Silicon wafer with an oxide or nitride insulating layer on top offers a chance to miniaturization of the sensor devices and reduction of the power consumption. Moreover, an MEMS micro/nano heater is essentially a tiny structure fabricated by using a CMOS-compatible fabrication technique [84]. The design of a microheater structure is extremely important since it must consider concerns with temperature distribution and power usage

[85]. To achieve the best outcome, various membrane dimensions and microheater structure geometries must be taken into account. The following are the crucial aspects of a micro hotplate design: (1) quick thermal response, (2) low power consumption, and (3) temperature homogeneity. Factors must be optimized according to the necessity by selecting the right materials, designing the proper geometry and developing new fabrication skills [81, 82].

There are mainly three structure configurations adopted for SMO devices: closed membrane, suspended membrane and bridge structure, as shown in Fig.1.17. On the other hand, suspended membranes are more common in research due to the fact that it is able to push the power consumption performance to its absolute maximum. Furthurmore, suspended structure can also increase the temperature response. For example, Qin Zhou et al. have developed MEMS microheaters for WO_3 gas sensors by making the supporting beam conduction equal to heat loss through the air conduction. When the operated temperature continuously was 300 °C, the poswer consumption was 2 mW with an ultra-fast thermal response time of 33 μs via a transient temperature-resistivity response method [86]. In addition, it has a low thermal inertia, which contributes to its quick response and recovery time and enables it to reliably modulate temperature. Usually planar-type hotplate can provide larger active heating areas than suspended type hotplate [87].

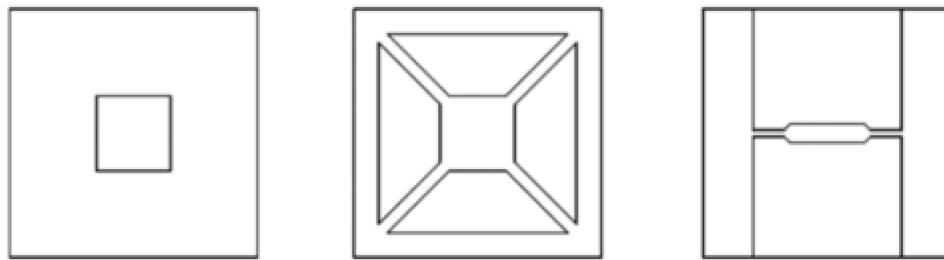

Figure 1.17. Top view of hotplates with different geometry structures closed membrane, suspended membrane and bridge structure. Reprinted with permission [69].

Heater circuit material is one of the most important factors, which can affect the thermal response of hotplate. Finding the ideal material for the microheater is difficult for the gas sensor to operate better [81]. The selection of an appropriate heating material must take into account a variety of factors, including cost, ease of fabrication, electrical resistance, low thermal conductivity, low thermal expansion coefficient, low thermal conductivity, high Young's modulus, and, most importantly, compatibility with standard silicon fabrication technology. Platinum, NiCr, silver, Mo, gold, polysilicon, Al and tungsten have been cited by a number of authors as the heating element [84, 88-95]. Electrodes of semiconductor gas

sensors serve not only as contact materials and conductors to an external circuit, but also in some circumstances, the electrode-oxide semiconductors created contact resistance may significantly affect how the sensors react. In the operation of the sensor, electrode materials are also used as catalytic activators. In some cases, electrode materials must withstand temperatures of up to 600 ° C in order to operate at high temperatures in the automotive and aerospace industries. Platinum appears to be the most common electrode material in both practical and experimental sensors due to its physical and chemical properties, such as high Young's modulus, low thermal expansion coefficient, corrosion resistance, humidity resistance, and non-magnetic property [38]. Additionally, because of Pt positive temperature coefficient, the temperature can be calculated based on resistance value [88, 96].

$$R = R_0 (1 + \alpha (T - T_0)) \quad (1\text{-}11)$$

In which T_0 is the temperature of 0°C, R_0 is the resistance value of Pt at 0°C, α is the temperature coefficient, T is the real temperature and R is the resistance at real temperature. By this chance, the temperature of the hotplate can me calculated from the resistance changing by using this equation. Pt film cannot be deposited on SiO_2 or Si_3N_4 directly due to the poor adhesion force between them, generally titanium (Ti) with nanometers thickness is formed between Pt and insulating layer. While above 500°C, Ti will diffuse into the platinum layer and form precipitates on the grain boundaries, which affects Pt resistance behaviors [97]. In this case, tantalum shows better diffusion barrier but with high cost [98]. Many researchers also studied other micro heater circuit materials, such as aluminum and polysilicon. For example, Gyuweon Jung et al. proposed a new design guideline of the FET-type gas sensor platform to improve the power efficiency of the embedded poly-Si microheater [88]. Ruizhen Xie et al. sputtered nichrome heater on bridge region [99]. Ting-Jen Hsueh et al. developed an ITO micro heater for a transparent ZnO nanowire MEMS gas sensor [91].

By designing suitable heater circuit layout, the temperature uniformity can be optimized. The heater geometry can be broadly classified into five categories: rectangular, square, circular, irregular and 3D structure [83], as shown in Fig.1.18. The temperature distribution using meander shaped resistors causes nonuniform condition, the center part is always higher than the edge area. Spiral or double spiral shaped heaters can improve the temperature uniformity with equal or unequal line spacing [100]. Even heater resistor layout structure can affect the temperature time evolution, for example, Souhir Bedoui et al. simulated the

micro hotplate model to compare three geometries of Pt heater influence on temperature profile along different axis spiral model showed the higher working temperature than meander-spiral and meander model by FEM simulation. It was also interesting that the geometry could affect transient temperature peak [101]. To further increase the temperature homogeneous, simulation will be primary choice to consider the materials, structures, geometries, heat dissipation by coupling Joule heating. Woo-Seok Choi simulated four different micro-heater geometries effects on NO_2 gas sensing performance of In_2O_3, afterwards designed and fabricated these co-planar type microheaters, obtaining a minimum power consumption of 41 mW at the operating temperature 250 °C. It turned out that helical type heater showed the highest temperature at the same input voltage, and the power consumption was the lowest at the same working temperature with the highest In_2O_3 sensing response under NO_2 gas [102].

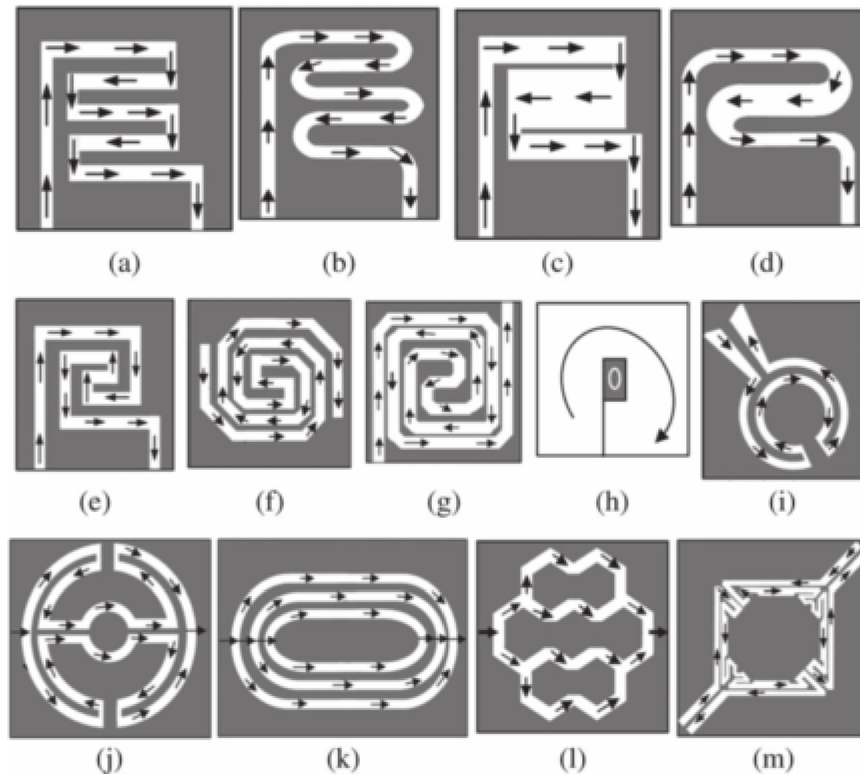

Figure 1.18 Different heater geometry: (a) Meander. (b) Meander with rounded corner. (c) S-shaped. (d) S-shaped rounded corner. (e) Double spiral. (f) Double spiral with rounded corner. (g) Double spiral with irregular spacings. (h) Plane plate with central square hole. (i) Circular. (j) Drive wheel. (k) Elliptical. (l) Honeycomb. (m) Irregular. Reprinted with permission [83].

Temperaturre uniformity can be optimised by using high thermal conductivity material. In addition, heater geometry also has significant impact on the temperature uniformity.

Another essential requirement for SMO sensors is uniform temperature distribution over the active region, since it improves the sensor response because the sensing area directly above the micro hotplate is strongly impacted. Temperature homogeneity reduces heater area, which is crucial for the device downsizing and heater dependability [103]. The materials used for the membrane, the area of the membrane, and the microheater shape all affect temperature uniformity. Making thin, thermally inefficient membranes and adjusting the heater size compared to the membrane can be done to reduce overall power consumption. In a word, to achieve an magnificent hotplate, there are several factors we should consider: plenary shape, thickness, electrodes gap and electrode width [104].

1.6 Application of Semiconductor Gas Sensors

SMO material-based gas sensors have been used extensively in the home, workplace, hospitals, and laboratories in recent years. It offers a potentially effective option for quick and accurate semiquantitative detection. It draws a lot of attention not only because it is inexpensive, easy to make, and small size, but also because of its superior gas sensing qualities and an unfavorable wide range of detectable gases. A good alternative for gas alarm, environmental monitoring, food hygiene quarantine, and medical diagnostics [105]. SMO-based gas sensors can detect volatile organic compounds, hazardous gases, some harmful gases, and specific gases. The current investigation into SMO-based gas sensors is outlined below in accordance with the taxonomy of gas species.

Indoor air quality monitoring is primarily studied, in the beginning of SMO sensor, it was used to detect liquefied petroleum gas (LPG) gases domestically, and protect people from gas leaks and explosion. CO_2 concentration could be used as a marker of indoor air quality. CO_2 does not react with metal oxide surface of SnO_2, while by adding materials like barium or lanthanum, SnO_2 will have a high affinity with CO_2, furthermore, increasing the response. In 2004, the European Union issued a guideline for indoor air quality that identified carbon monoxide, volatile organic compounds (VOCs) formaldehyde, benzene, and naphthalene, as well as the oxidizing gas nitrogen dioxide, as indoor pollutants of highest concern. VOCs may contribute to the development of sick building syndrome. The term is used when multiple occupants of a building experience nonspecific health issues, such as nausea, irritated eyes, nose, skin, and throat [105].

By 2050, the global population is projected to reach 9.7 billion, with food safety posing a significant problem due to limited resources [106]. Convenient and inexpensive food quality detectors can play a key role in optimizing food production by screening for ripening markers (e.g., the plant hormone ethylene), spoiling markers (e.g., NH_3, putrescine, and cadaverine for meat), or dangerous substances (e.g. methanol in alcoholic beverages) [107]. Particularly challenging for food quality detectors is the separation of food indicators, toxicants, and pesticides from unavoidable confounding substances [52]. SMOs are also widely used in food freshness. The rotting process starts as soon as fruits and vegetables are harvested or animals are butchered. Food is now produced, prepared, distributed, sold, and purchased before it is eaten. Companies publish expiration dates in order to guarantee freshness. Food can, however, still be enjoyed after this date if storage circumstances are proper. On the other hand, if circumstances are not ideal, food may spoil before its time. Many people are extremely careful and toss away food excessively. Waste may be reduced as a result of a freshness assessment that is made with more accuracy.

Breath analysis has applications beyond just identifying drunkenness from alcohol. Human breath contains a wealth of physiological data, is always accessible, and may be measured with less invasiveness than blood or urine tests. By tracing related compounds, breath analysis can in theory follow physiological indicators, detect disorders, and monitor their progression. Over 1000 chemicals in breath can now be detected using highly sensitive testing tools [108]. The most difficult aspect of breath analysis is the selective detection of trace analytes (usually at ppb) among more than eight hundred under high humidity (above 90% RH) [105].The requirement for precise and systematic sampling became clear as detection technology advanced. The primary components of exhaled breath are oxygen, CO_2, water, and nitrogen. Biomarker concentrations in breath are typically in the ppm or ppb range. Accurate sampling is highly challenging due to the intricacy of respiration and the low concentration of biomarkers. Simply put, distinct breath fractions are present in exhaled air. The portion of breath has taken part in the exchange of oxygen and carbon dioxide. The physiologic dead space provides the remaining portion of exhaled breath. Different breath samples must be taken depending on where the intended biomarker came from. It is important to take into account the biomarker body of origin as well as any potential sources of contamination. The process of downsizing can start once sampling techniques have been improved for a specific breath biomarker and it is possible to monitor a patient's health using pricey high-end analytical techniques like mass spectrometry. Breath analyzers could be

made more compact, less expensive, and user-friendly by swapping out complex analytical detectors, like SMO-based sensors.

Industrial environment safety such as coal mines are often cited as the origin of gas sensors. A high sample density is required to guarantee the health and safety of coal miners since the tunnels that connect coal mines are typically quite long and deep. In the past, sensors had to be directly connected to the processing server in order for them to function properly. This required a significant quantity of cable and careful coordination. Research on wireless monitoring systems is now being conducted [8]. These would be significantly more adaptable and would make it possible to conduct widespread detection throughout the mine. Because of their portability and low cost, sensors based on SMOs are an excellent choice for this particular application. They are durable and able to withstand the extreme conditions that are found in mines. SMOs sensors for carbon monoxide (CO), methane (CH_4), propane (propane), and butane (butane) are included in the mine detection system prototype that is completely wireless.

References

[1] S. Dhall, B. R. Mehta, A. K. Tyagi, and K. Sood, "A review on environmental gas sensors: Materials and technologies," *Sensors International,* vol. 2, p. 100116, 2021.

[2] X. Wang, H. Feng, T. Chen, S. Zhao, J. Zhang, and X. Zhang, "Gas sensor technologies and mathematical modelling for quality sensing in fruit and vegetable cold chains: A review," *Trends in Food Science & Technology,* vol. 110, pp. 483-492, 2021.

[3] M. A. H. Khan, M. V. Rao, and Q. Li, "Recent Advances in Electrochemical Sensors for Detecting Toxic Gases: NO_2, SO_2 and H_2S," *Sensors (Basel),* vol. 19, Feb 21 2019.

[4] S. Feng, F. Farha, Q. Li, Y. Wan, Y. Xu, T. Zhang*, et al.*, "Review on Smart Gas Sensing Technology," *Sensors (Basel),* vol. 19, Aug 30 2019.

[5] A. Gurlo and R. Riedel, "In situ and operando spectroscopy for assessing mechanisms of gas sensing," *Angew Chem Int Ed Engl,* vol. 46, pp. 3826-48, 2007.

[6] L. Zhang, J. Hu, Y. Lv, and X. Hou, "Recent Progress in Chemiluminescence for Gas Analysis," *Applied Spectroscopy Reviews,* vol. 45, pp. 474-489, 2010.

[7] H. Nazemi, A. Joseph, J. Park, and A. Emadi, "Advanced Micro- and Nano-Gas Sensor Technology: A Review," *Sensors (Basel),* vol. 19, Mar 14 2019.

[8] A. Dey, "Semiconductor metal oxide gas sensors: A review," *Materials Science and Engineering: B,* vol. 229, pp. 206-217, 2018.

[9] E. Comini, "Metal oxide nano-crystals for gas sensing," *Anal Chim Acta,* vol. 568, pp. 28-40, May 24 2006.

[10]T. Addabbo, A. Fort, M. Mugnaini, V. Vignoli, A. Baldi, and M. Bruzzi, "Quartz-Crystal Microbalance Gas Sensors Based on TiO2Nanoparticles," *IEEE Transactions on Instrumentation and Measurement,* vol. 67, pp. 722-730, 2018.
[11]A. Mujahid and F. L. Dickert, "Surface Acoustic Wave (SAW) for Chemical Sensing Applications of Recognition Layers," *Sensors (Basel),* vol. 17, Nov 24 2017.
[12]T. A. Emadi and D. A. Buchanan, "Design and Fabrication of a Novel MEMS Capacitive Transducer With Multiple Moving Membrane," *IEEE Transactions on Electron Devices,* vol. 61, pp. 890-896, 2014.
[13]K. K. Park, H. Lee, M. Kupnik, Ö. Oralkan, J.-P. Ramseyer, H. P. Lang*, et al.*, "Capacitive micromachined ultrasonic transducer (CMUT) as a chemical sensor for DMMP detection," *Sensors and Actuators B: Chemical,* vol. 160, pp. 1120-1127, 2011.
[14]M. R. Khan and S. W. Kang, "A high sensitivity and wide dynamic range fiber-optic sensor for low-concentration VOC gas detection," *Sensors (Basel),* vol. 14, pp. 23321-36, Dec 5 2014.
[15]B. Troia, A. Paolicelli, F. De, and V. M. N. Passaro, "Photonic Crystals for Optical Sensing: A Review," 2013.
[16]Y.-n. Zhang, Y. Zhao, and R.-q. Lv, "A review for optical sensors based on photonic crystal cavities," *Sensors and Actuators A: Physical,* vol. 233, pp. 374-389, 2015.
[17]J. Hodgkinson and R. P. Tatam, "Optical gas sensing: a review," *Measurement Science and Technology,* vol. 24, p. 012004, 2013.
[18]Md. Rajibur Rahaman Khan and Shin-Won Kang, "A High Sensitivity and Wide Dynamic Range Fiber-Optic Sensor for Low-Concentration VOC Gas Detection, " Sensors, vol.12, p.23321-23336, 2014.
[19]F. Xu, Z. Lv, Y. G. Zhang, G. Somesfalean, and Z. G. Zhang, "Concentration evaluation method using broadband absorption spectroscopy for sulfur dioxide monitoring," *Applied Physics Letters,* vol. 88, p. 231109, 2006.
[20]C. O. Park, J. W. Fergus, N. Miura, J. Park, and A. Choi, "Solid-state electrochemical gas sensors," *Ionics,* vol. 15, pp. 261-284, 2009.
[21]C.O. Park, S.A.Akbar and W. Weppner, "Ceramic electrolytes and electrochemical sensors, " *Chemical and Bio-ceramics*, vol. 38, p.4639-4660, 2003.
[22]U. Yaqoob and M. I. Younis, "Chemical Gas Sensors: Recent Developments, Challenges, and the Potential of Machine Learning-A Review," *Sensors (Basel),* vol. 21, Apr 20 2021.
[23]I. V. Zaporotskova, N. P. Boroznina, Y. N. Parkhomenko, and L. V. Kozhitov, "Carbon nanotubes: Sensor properties. A review," *Modern Electronic Materials,* vol. 2, pp. 95-105, 2016.
[24]Z. Hou, D. Xu, and B. Cai, "Ionization gas sensing in a microelectrode system with carbon nanotubes," *Applied Physics Letters,* vol. 89, p. 213502, 2006.
[25]S. Chopra, K. McGuire, N. Gothard, A. M. Rao, and A. Pham, "Selective gas detection using a carbon nanotube sensor," *Applied Physics Letters,* vol. 83, pp. 2280-2282, 2003.
[26]P. Raju and Q. Li, "Review—Semiconductor Materials and Devices for Gas Sensors," *Journal of The Electrochemical Society,* vol. 169, p. 057518, 2022.

[27] D. Zappa, V. Galstyan, N. Kaur, H. M. M. Munasinghe Arachchige, O. Sisman, and E. Comini, ""Metal oxide -based heterostructures for gas sensors"- A review," *Anal Chim Acta,* vol. 1039, pp. 1-23, Dec 18 2018.
[28] P. J. D. Peterson, A. Aujla, K. H. Grant, A. G. Brundle, M. R. Thompson, J. Vande Hey*, et al.*, "Practical Use of Metal Oxide Semiconductor Gas Sensors for Measuring Nitrogen Dioxide and Ozone in Urban Environments," *Sensors (Basel),* vol. 17, Jul 19 2017.
[29] G. Korotcenkov and B. K. Cho, "Metal oxide composites in conductometric gas sensors: Achievements and challenges," *Sensors and Actuators B: Chemical,* vol. 244, pp. 182-210, 2017.
[30] H.-J. Kim and J.-H. Lee, "Highly sensitive and selective gas sensors using p-type oxide semiconductors: Overview," *Sensors and Actuators B: Chemical,* vol. 192, pp. 607-627, 2014.
[31] Nicolae Barsan and Klaus Schierbaum, "Conclusion and outlook Gas Sensors Based on Conducting Metal Oxides," p. 259-262, 2019.
[32] J. Mikołajczyk, Z. Bielecki, T. Stacewicz, J. Smulko, J. Wojtas, D. Szabra*, et al.*, "Detection of Gaseous Compounds with Different Techniques," *Metrology and Measurement Systems,* vol. 23, pp. 205-224, 2016.
[33] S. M. Majhi, A. Mirzaei, H. W. Kim, S. S. Kim, and T. W. Kim, "Recent advances in energy-saving chemiresistive gas sensors: A review," *Nano Energy,* vol. 79, p. 105369, Jan 2021.
[34] G. Korotcenkov, "Metal oxides for solid-state gas sensors: What determines our choice?," *Materials Science and Engineering: B,* vol. 139, pp. 1-23, 2007.
[35] A. Ponzoni, C. Baratto, N. Cattabiani, M. Falasconi, V. Galstyan, E. Nunez-Carmona*, et al.*, "Metal Oxide Gas Sensors, a Survey of Selectivity Issues Addressed at the SENSOR Lab, Brescia (Italy)," *Sensors (Basel),* vol. 17, Mar 29 2017.
[36] Ahmed Al-Jumaili, Kateryna Bazaka and Mohan V. Jacob, " Retention of Antibacterial Activity in Geranium Plasma Polymer Thin Films, " *Nanomaterials* **vol.** 9, p. 270, 2017.
[37] Tetsuro Seiyama, Akio Kato, Kiyoshi Fujiishi, and Masanori Nagatani, "A new detector for gaseous components using semiconnductive thin films, " *Anal. Chem*, vol. 34, 11, p.1502–1503, 1962.
[38] A. Gaiardo, D. Novel, E. Scattolo, M. Crivellari, A. Picciotto, F. Ficorella*, et al.*, "Optimization of a Low-Power Chemoresistive Gas Sensor: Predictive Thermal Modelling and Mechanical Failure Analysis," *Sensors (Basel),* vol. 21, Jan 25 2021.
[39] M. Graf, D. Barrettino, K.-U. Kirstein, and A. Hierlemann, "CMOS microhotplate sensor system for operating temperatures up to 500°C," *Sensors and Actuators B: Chemical,* vol. 117, pp. 346-352, 2006.
[40] A. Friedberger, P. Kreisl, E. Rose, G. Müller, G. Kühner, J. Wöllenstein*, et al.*, "Micromechanical fabrication of robust low-power metal oxide gas sensors," *Sensors and Actuators B: Chemical,* vol. 93, pp. 345-349, 2003.
[41] G. Sberveglieri, W. Hellmich and G. Müller, "Silicon hotplates for metal, " *Microsystem Technologies*, vol. 3, p. 183–190, 1997.

[42] V. V. Kondalkar, J. Park, and K. Lee, "MEMS hydrogen gas sensor for in-situ monitoring of hydrogen gas in transformer oil," *Sensors and Actuators B: Chemical,* vol. 326, p. 128989, 2021.
[43] Isolde Simon, Nicolae Bârsan, Michael Bauer and Udo Weimar, "Micromachined metal oxide gas sensors_ opportunities to improve sensor performance, " *Sensors and Actuators B: Chemical*, Vol.73, p. 1-26, 2001.
[44] S. Tang, W. Chen, L. Jin, H. Zhang, Y. Li, Q. Zhou*, et al.*, "SWCNTs-based MEMS gas sensor array and its pattern recognition based on deep belief networks of gases detection in oil-immersed transformers," *Sensors and Actuators B: Chemical,* vol. 312, p. 127998, 2020.
[45] W. Shin, S. Hong, G. Jung, Y. Jeong, J. Park, D. Kim*, et al.*, "Improved signal-to-noise-ratio of FET-type gas sensors using body bias control and embedded micro-heater," *Sensors and Actuators B: Chemical,* p. 129166, 2020.
[46] S. Hong, M. Wu, Y. Hong, Y. Jeong, G. Jung, W. Shin*, et al.*, "FET-type gas sensors: A review," *Sensors and Actuators B: Chemical,* p. 129240, 2020.
[47] A. Singh, A. Sharma, N. Dhull, A. Arora, M. Tomar, and V. Gupta, "MEMS-based microheaters integrated gas sensors," *Integrated Ferroelectrics,* vol. 193, pp. 72-87, 2019.
[48] S. Z. Ali, F. Udrea, W. I. Milne, and J. W. Gardner, "Tungsten-Based SOI Microhotplates for Smart Gas Sensors," *Journal of Microelectromechanical Systems,* vol. 17, pp. 1408-1417, 2008.
[49] M. Prasad and P. S. Dutta, "Development of micro-hotplate and its reliability for gas sensing applications," *Applied Physics A,* vol. 124, 2018.
[50] L. Kulhari and P. K. Khanna, "Design, simulation and fabrication of LTCC-based microhotplate for gas sensor applications," *Microsystem Technologies,* vol. 24, pp. 2169-2175, 2018.
[51] M. A. Franco, P. P. Conti, R. S. Andre, and D. S. Correa, "A review on chemiresistive ZnO gas sensors," *Sensors and Actuators Reports,* vol. 4, p. 100100, 2022.
[52] A. T. Güntner, N. J. Pineau, and S. E. Pratsinis, "Flame-made chemoresistive gas sensors and devices," *Progress in Energy and Combustion Science,* vol. 90, p. 100992, 2022.
[53] Nicolae Barsan, and Udo Weimar, "Conduction Model of Metal Oxide Gas Sensors, " *Journal of Electroceramics*, vol.7, p.143–167, 2001
[54] Karin Potje-Kamloth, "*Semiconductor Junction Gas Sensors*," Chem, Rev, vol.108, p.367-399, 2008.
[55] Masamichi Ippommatsu and Hirokazu Sasaki, "Sensing mechanism of SnO_2 gas sensors," *JOURNAL OF MATERIALS SCIENCE*, vol.25, p.259-262,1990.
[56] N. Yamazoe, "Toward innovations of gas sensor technology," *Sensors and Actuators B: Chemical,* vol. 108, pp. 2-14, 2005.
[57] N. Barsaan, D. Koziej and U. Weimar, "Metal oxide-based gas sensor research How to?" *Sensors and Actuators B*, vol.121, p.18-35, 2007.
[58] N Barsan and U Weimar, "Understanding the fundamental principles of metal oxide based gas sensors; the example of CO sensing with SnO_2 sensors in the presence of humidity," *J. Phys.: Condens*, vol.15, p. R813–R839, 2003.

[59] Isolde Simon, Nicolae Barsan, Michael Bauer and Udo Weimar, "Micromachined metal oxide gas sensors: Opportunities to improve sensor performance," *Sensors and Actuators B*, vol.73 p.1-26, 2001.
[60] Z. Yuan, R. Li, F. Meng, J. Zhang, K. Zuo, and E. Han, "Approaches to Enhancing Gas Sensing Properties: A Review," *Sensors (Basel),* vol. 19, Mar 27 2019.
[61] D. Nunes, A. Pimentel, A. Gonçalves, S. Pereira, R. Branquinho, P. Barquinha*, et al.*, "Metal oxide nanostructures for sensor applications," *Semiconductor Science and Technology,* vol. 34, p. 043001, 2019.
[62] Noboru Yamazoe, "New approaches for improving semiconductor gas sensors," *Sensors andd Actuators B*, vol.5, p. 7-19, 1991.
[63] A. S. Pranti, D. Loof, S. Kunz, V. Zielasek, M. Bäumer, and W. Lang, "Characterization of a highly sensitive and selective hydrogen gas sensor employing Pt nanoparticle network catalysts based on different bifunctional ligands," *Sensors and Actuators B: Chemical,* vol. 322, p. 128619, 2020.
[64] W. Jiang, L. Meng, S. Zhang, X. Chuai, Z. Zhou, C. Hu*, et al.*, "Design of highly sensitive and selective xylene gas sensor based on Ni-doped MoO_3 nano-pompon," *Sensors and Actuators B: Chemical,* vol. 299, p. 126888, 2019.
[65] V. Postica, A. Vahl, J. Strobel, D. Santos-Carballal, O. Lupan, A. Cadi-Essadek*, et al.*, "Tuning doping and surface functionalization of columnar oxide films for volatile organic compound sensing: experiments and theory," *Journal of Materials Chemistry A,* vol. 6, pp. 23669-23682, 2018.
[66] Y. Chen, P. Xu, X. Li, Y. Ren, and Y. Deng, "High-performance H2 sensors with selectively hydrophobic micro-plate for self-aligned upload of Pd nanodots modified mesoporous In_2O_3 sensing-material," *Sensors and Actuators B: Chemical,* vol. 267, pp. 83-92, 2018.
[67] Y. Jian, W. Hu, Z. Zhao, P. Cheng, H. Haick, M. Yao*, et al.*, "Gas Sensors Based on Chemi-Resistive Hybrid Functional Nanomaterials," *Nanomicro Lett,* vol. 12, p. 71, Mar 11 2020.
[68] S. E. Moon, "Semiconductor-Type MEMS Gas Sensor for Real-Time Environmental Monitoring Applications," *ETRI Journal,* vol. 35, pp. 617-624, 2013.
[69] H. Liu, L. Zhang, K. H. H. Li, and O. K. Tan, "Microhotplates for Metal Oxide Semiconductor Gas Sensor Applications-Towards the CMOS-MEMS Monolithic Approach," *Micromachines (Basel),* vol. 9, Oct 29 2018.
[70] A. Gaiardo, D. Novel, E. Scattolo, A. Bucciarelli, P. Bellutti, and G. Pepponi, "Dataset of the Optimization of a Low Power Chemoresistive Gas Sensor: Predictive Thermal Modelling and Mechanical Failure Analysis," *Data,* vol. 6, p. 30, 2021.
[71] Kyung Hwa Hong,Kyung Wha Oh and Tae Jin Kang, "Polyaniline–nylon 6 composite fabric for ammonia gas sensor," *Journal of Applied Polymer Science*,vol. 92, p.37-42, 2004.
[72] D. Briand, A. Oprea, J. Courbat, and N. Bârsan, "Making environmental sensors on plastic foil," *Materials Today,* vol. 14, pp. 416-423, 2011.
[73] J. V. Anguita, M. Thwaites, B. Holton, P. Hockley, S. Rand, and S. Haughton, "Room Temperature Growth of Indium-Tin Oxide on Organic Flexible Polymer Substrates Using a

New Reactive-Sputter Deposition Technology," *Plasma Processes and Polymers,* vol. 4, pp. 48-52, 2007.
[74] J. Bhadra, N. J. Al-Thani, N. K. Madi, and M. A. Al-Maadeed, "Preparation and characterization of chemically synthesized polyaniline–polystyrene blends as a carbon dioxide gas sensor," *Synthetic Metals,* vol. 181, pp. 27-36, 2013.
[75] G. D. Khuspe, D. K. Bandgar, S. Sen, and V. B. Patil, "Fussy nanofibrous network of polyaniline (PANi) for NH_3 detection," *Synthetic Metals,* vol. 162, pp. 1822-1827, 2012.
[76] G. Yang, C. Lee, J. Kim, F. Ren, and S. J. Pearton, "Flexible graphene-based chemical sensors on paper substrates," *Phys Chem Chem Phys,* vol. 15, pp. 1798-801, Feb 14 2013.
[77] J. Sarfraz, P. Ihalainen, A. Määttänen, J. Peltonen, and M. Lindén, "Printed hydrogen sulfide gas sensor on paper substrate based on polyaniline composite," *Thin Solid Films,* vol. 534, pp. 621-628, 2013.
[78] J.-W. Han, B. Kim, J. Li, and M. Meyyappan, "A carbon nanotube based ammonia sensor on cotton textile," *Applied Physics Letters,* vol. 102, p. 193104, 2013.
[79] W.-Y. Chang and Y.-S. Hsihe, "Multilayer microheater based on glass substrate using MEMS technology," *Microelectronic Engineering,* vol. 149, pp. 25-30, 2016.
[80] W. J. Hwang, K. S. Shin, J. H. Roh, D. S. Lee, and S. H. Choa, "Development of micro-heaters with optimized temperature compensation design for gas sensors," *Sensors (Basel),* vol. 11, pp. 2580-91, 2011.
[81] S. P. Lee, "Electrodes for Semiconductor Gas Sensors," *Sensors (Basel),* vol. 17, Mar 25 2017.
[82] Z. E. Jeroish, K. S. Bhuvaneshwari, F. Samsuri, and V. Narayanamurthy, "Microheater: material, design, fabrication, temperature control, and applications-a role in COVID-19," *Biomed Microdevices,* vol. 24, p. 3, Dec 3 2021.
[83] P. Bhattacharyya, "Technological Journey Towards Reliable Microheater Development for MEMS Gas Sensors: A Review," *IEEE Transactions on Device and Materials Reliability,* vol. 14, pp. 589-599, 2014.
[84] N. X. Thai, N. Van Duy, N. Van Toan, C. M. Hung, N. Van Hieu, and N. D. Hoa, "Effective monitoring and classification of hydrogen and ammonia gases with a bilayer Pt/SnO_2 thin film sensor," *International Journal of Hydrogen Energy,* vol. 45, pp. 2418-2428, 2020.
[85] A. Bagolini, A. Gaiardo, M. Crivellari, E. Demenev, R. Bartali, A. Picciotto*, et al.*, "Development of MEMS MOS gas sensors with CMOS compatible PECVD inter-metal passivation," *Sensors and Actuators B: Chemical,* vol. 292, pp. 225-232, 2019.
[86] Q. Zhou, A. Sussman, J. Chang, J. Dong, A. Zettl, and W. Mickelson, "Fast response integrated MEMS microheaters for ultra low power gas detection," *Sensors and Actuators A: Physical,* vol. 223, pp. 67-75, 2015.
[87] G. Wei, P. Wang, M. Li, Z. Lin, and C. Nai, "Simulation and Optimization of a Planar-Type Micro-Hotplate with Si_3N_4-SiO_2 Transverse Composite Dielectric Layer and Annular Heater," *Micromachines (Basel),* vol. 13, Apr 12 2022.

[88] G. Jung, Y. Hong, S. Hong, D. Jang, Y. Jeong, W. Shin*, et al.*, "A low-power embedded poly-Si micro-heater for gas sensor platform based on a FET transducer and its application for NO_2 sensing," *Sensors and Actuators B: Chemical,* vol. 334, p. 129642, 2021.
[89] K. L. Zhang, S. K. Chou, and S. S. Ang, "Fabrication, modeling and testing of a thin film Au/Ti microheater," *International Journal of Thermal Sciences,* vol. 46, pp. 580-588, 2007.
[90] U. Schmid and H. Seidel, "Enhanced stability of Ti/Pt micro-heaters using a-SiC:H passivation layers," *Sensors and Actuators A: Physical,* vol. 130-131, pp. 194-201, 2006.
[91] T.-J. Hsueh, C.-H. Peng, and W.-S. Chen, "A transparent ZnO nanowire MEMS gas sensor prepared by an ITO micro-heater," *Sensors and Actuators B: Chemical,* vol. 304, p. 127319, 2020.
[92] D. Zappa, A. Bertuna, E. Comini, M. Herold, N. Poli, and G. Sberveglieri, "Tungsten Oxide Nanowires on Micro Hotplates for Gas Sensing Applications," *Procedia Engineering,* vol. 120, pp. 439-442, 2015.
[93] C. Tsamis, A. G. Nassiopoulou, and A. Tserepi, "Thermal properties of suspended porous silicon micro-hotplates for sensor applications," *Sensors and Actuators B: Chemical,* vol. 95, pp. 78-82, 2003.
[94] F. Samaeifar, A. Afifi, and H. Abdollahi, "Simple Fabrication and Characterization of a Platinum Microhotplate Based on Suspended Membrane Structure," *Experimental Techniques,* pp. n/a-n/a, 2014.
[95] A. Mozalev, R. Calavia, R. M. Vázquez, I. Gràcia, C. Cané, X. Correig*, et al.*, "MEMS-microhotplate-based hydrogen gas sensor utilizing the nanostructured porous-anodic-alumina-supported WO_3 active layer," *International Journal of Hydrogen Energy,* vol. 38, pp. 8011-8021, 2013.
[96] T. Schössler, F. Schön, C. Lemier, and G. Urban, "Reliability improvements of thin film platinum resistors on wafer-level and micro-hotplates at stress temperatures in the range of 140–290 °C," *Microelectronics Reliability,* vol. 104, p. 113557, 2020.
[97] A. Ababneh, A. N. Al-Omari, A. M. K. Dagamseh, M. Tantawi, C. Pauly, F. Mücklich*, et al.*, "Electrical and morphological characterization of platinum thin-films with various adhesion layers for high temperature applications," *Microsystem Technologies,* vol. 23, pp. 703-709, 2015.
[98] R. M. Tiggelaar, R. G. P. Sanders, A. W. Groenland, and J. G. E. Gardeniers, "Stability of thin platinum films implemented in high-temperature microdevices," *Sensors and Actuators A: Physical,* vol. 152, pp. 39-47, 2009.
[99] R. Xie, X. Ren, L. Liu, W. Liu, K. Yu, and Y. Xue, "Effect of sputtering on bridge region of thin film nichrome heater," *Journal of Physics: Conference Series,* vol. 2256, p. 012012, 2022.
[100] G. Coppola, V. Striano, P. Ferraro, S. De Nicola, A. Finizio, G. Pierattini*, et al.*, "A Nondestructive Dynamic Characterization of a Microheater Through Digital Holographic Microscopy," *Journal of Microelectromechanical Systems,* vol. 16, pp. 659-667, 2007.

[101] S. Bedoui, S. Gomri, H. Charfeddine Samet, and A. Kachouri, "Design and Simulation of Microelectromechanical Systems (MEMS) for Ozone Gas Sensors," *Transactions on Electrical and Electronic Materials,* vol. 19, pp. 41-46, 2018.
[102] W. S. Choi, B. J. Kim, H. J. Lee, J. W. Choi, S. D. Kim, and N. K. Min, "Study on the micro-heater geometry in In_2O_3 micro electro mechanical systems gas sensor platforms and effects on NO_2 gas detecting performances," *J Nanosci Nanotechnol,* vol. 12, pp. 1170-3, Feb 2012.
[103] P. Kahroba, I. Mirzaee, P. Sharifi, and H. Shirvani, "The microcavity-based micro-heater: an optimum design for micro-heaters," *Microsystem Technologies,* vol. 14, pp. 705-710, 2007.
[104] I. Elmi, S. Zampolli, E. Cozzani, F. Mancarella, and G. C. Cardinali, "Development of ultra-low-power consumption MOX sensors with ppb-level VOC detection capabilities for emerging applications," *Sensors and Actuators B: Chemical,* vol. 135, pp. 342-351, 2008.
[105] A. T. Guntner, S. Abegg, K. Konigstein, P. A. Gerber, A. Schmidt-Trucksass, and S. E. Pratsinis, "Breath Sensors for Health Monitoring," *ACS Sens,* vol. 4, pp. 268-280, Feb 22 2019.
[106] F. Fung, H. S. Wang, and S. Menon, "Food safety in the 21st century," *Biomed J,* vol. 41, pp. 88-95, Apr 2018.
[107] M. I. A. Asri, M. N. Hasan, M. R. A. Fuaad, Y. M. Yunos, and M. S. M. Ali, "MEMS Gas Sensors: A Review," *IEEE Sensors Journal,* vol. 21, pp. 18381-18397, 2021.
[108] G. Zonta, G. Anania, M. Astolfi, C. Feo, A. Gaiardo, S. Gherardi*, et al.*, "Chemoresistive sensors for colorectal cancer preventive screening through fecal odor: Double-blind approach," *Sensors and Actuators B: Chemical,* vol. 301, p. 127062, 2019.

2. Fabrication Techniques and Characterization Methods

2.1 Fabrication Tools

2.1.1 EBL Technique

Electron Beam Lithography (EBL) is one of the fundamental techniques for nanofabrication that not only enables the direct writing of structures with dimensions as small as sub-10 nm, but also enables high volume nanoscale patterning technologies such as deep ultraviolet and extreme ultraviolet optical lithography, as well as nanoimprint lithography through the formation of masks and templates [1]. The ability of EBL to create arbitrary two-dimensional patterns at the nanometer scale makes it one of the most important nanofabrication techniques. In brief, it involves exposing an organic resist with a highly focused electron beam to alter its solubility in an appropriate subsequent development agent. The primary goals of EBL writing are to produce arbitrary patterns in resist films with high resolution, high density, and high reliability. These characteristics are intricately interconnected. The most influential factors are the quality of the electron optics (e.g., the ability to create a finely focused spot), the choice of resist, the wafer substrate (composition and film stack), developer and the process conditions such as electron beam energy and dose (the amount of electrons delivered on the sample surface), as well as development time and temperature [2, 3].

An EBL system equipped with a column able to accelerate electrons to energies usually in the range 10-100 keV and to focus them to 1-10 nm spots. The column is integrated with deflectors controlled by a pattern generator and a beam blanker enabling a direct writing process, scanning the electron beam only demanded by a design file. Optimizations of the tool can be a dedicated software with features like mark detection for alignment and a state movement systems controlled by a laser interferometer enabling accurate nanometric positioning [4, 5]. The mark alignment combined with the interferometric stage, also allows overlay exposures. The area to be written is decomposed in writing fields typically of 200 x 200 μm^2 area, in order to avoid beam focus distortions on large area scans. Therefore, it is crucial to have not only nanometric movement stage but also a precise position control in order to allow a perfect stitching among the several writing fields [6]. In the end EBL enables definition of micromere and nanometric patterns in resist films with high lateral resolution and great flexibility, not requiring any mask [5].

The standard steps for an EBL process like the ones adopted for this thesis are:

1. Surface preparation: cleaning and organic residual removal; 2. Resist deposition, typically spin coating; 3. Prebake (soft bake); 4. Electron exposure; 5. Development; 6. Postbake (hard bake); 7. Inspection.

Once these steps are completed, a pattern transfer process is needed. For instance, in this thesis work a metal film was usually deposited by ultra-high vacuum evaporation and then the resist was removed in an adequate solvent (typically acetone). The solvent enables the removal of all the metal deposited on the resist (lift-off), leasing the metal structures in the areas without the resist.

All the chemical operations are done in the chemical hood, an equipment that captures and filters harmful or undesirable molecules and particles emitted by chemically treated products or substances, as shown in Fig. 2.1. In order to make sure that polymer residue and other contaminations are totally eliminated from the wafer, we use oxygen plasm to clean the wafer, the machine is shown in Fig.2.3.

Figure 2.1 Chemical hood in FBK CRM clean room.

Figure. 2.2 Oxygen plasma dry etch machine in FBK

Before EBL exposure, resist is spin coated on the wafer, and the coating resist thickness is a key parameter for exposure, and decided by resist viscosity and spinner rotational speed, which is given by

$$t = kp^2/\omega^{1/2} \qquad \textbf{2-1}$$

In which k represents spinner constant, typically 80-100, p is the resist solids content in percent, and ω is the spinner rotational speed in rpm/1000. If the coating thickness is too thin, the metal deposition layer cannot be thick. Otherwise, the EBL exposure energy will be large. In general, the polymer resist coating thickness is supposed to be as 3 times big as the metal deposition layer thickness. We used the coating machine in FBK clean room as shown in Fig.2.3.

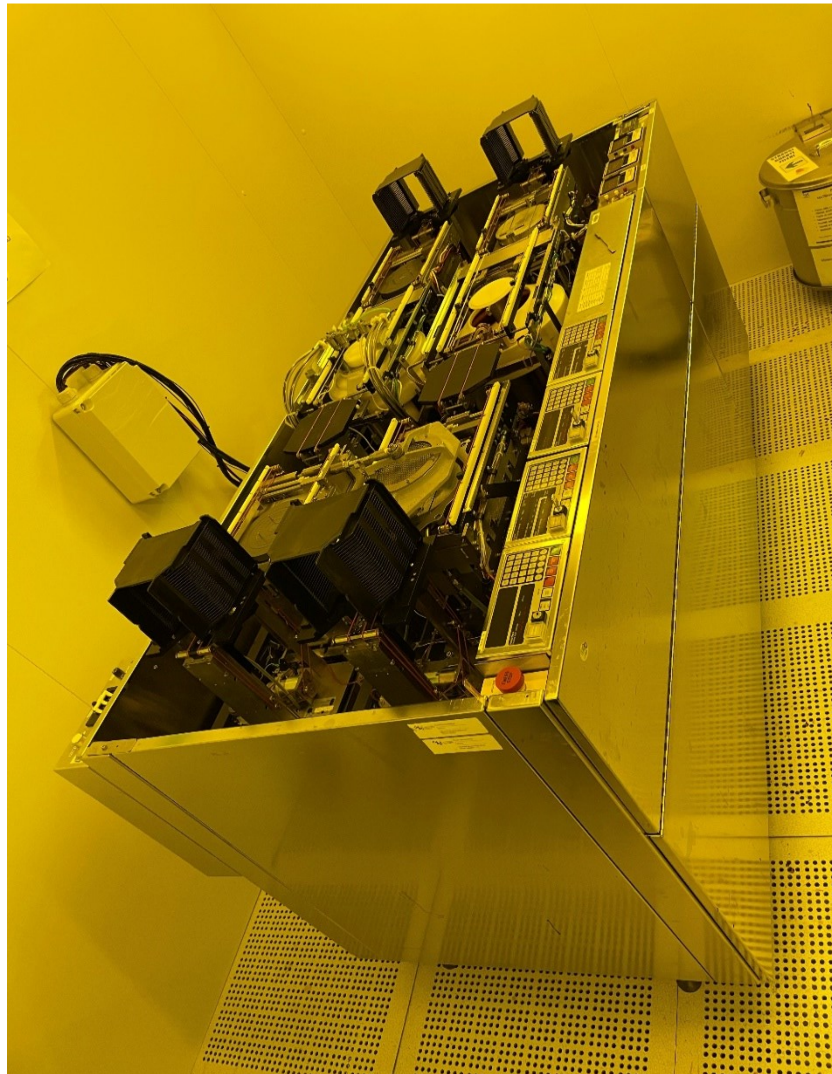

Figure. 2.3 SVG 8600 Photoresist Coating machine in FBK

EBL machine we use in our work is from TESCAN, which is equipped with Essence^{TM} EBL KIT including hardware and software solution. In develop step, we use Methyl Isobuthyl Ketone with solvent isopropanol (MIBK/IPA) as the developer. The stopper agent is pure isopropanol.

During the postbake step, any lingering traces of the coating solvent or developer are eliminated. This prevents the solvent burst effects that can occur during vacuum processing and causes the resist to be subjected to some stress.

In our work, Pt metal was used as electrode and heater circuit material. But it has poor adhesion on the ONO stack structure. Ti adhesion layer was introduced between Pt film and ONO stack structure. Electron beam evaporation technique was used to deposit Pt and Ti,

and magnetic sputtering machine was used to deposit ZnO material in our work. The used tools are shown in Fig. 2.4 and 2.5.

Lift-off by acetone was carried out to leave only the desired pattern on the wafer substrate. To deposit the metal and metal oxide materials, physical vapor deposition (PVD) is one of the typically adopted methods. Evaporation and sputtering are two different kinds of PVD processes. Both processes begin by converting the solid condensed phase into its gaseous or vapour phase. The gaseous source is finally condensed on the substrate, and subsequently film growth occurs. The simplest method of depositing a film by condensing a vapour on a substrate is evaporation, which forms thin films of metals, oxides, and semiconductors in a high-vacuum environment. This approach maintains the substrate temperature below that of the vapour. Any metal will vapourize when heated to a high enough temperature. Coating material of ultra-high purity by E-beam evaporation is deposited in a vacuum chamber, often as pellets in a crucible. These pellets are heated using electron energy, forcing the coating material to enter the gas phase. Due to the vacuum environment, evaporated particles can move onto the substrate without coming into contact with foreign particles. They then form a thin film on the surface of the substrate. This procedure is preferred for deposition of refractory metal and ceramic films due to its ability to deposit materials with a high melting point at a fast deposition rate.

Sputtering is another PVD technique involving the deposition of thin films in a vacuum. A solid substance and a substratum are positioned separately within a vacuum system during this procedure. Targeting the material with a high-energy argon ion plasma stream results in the subject material being ejected and deposited into the substrate, generating a thin film. As this is not an evaporative process, the needed temperatures for sputtering are lower than those required for E-beam evaporation. It is particularly beneficial for depositing materials with a high melting point or a mixture of materials, as compounds that evaporate at different speeds can be sputtered at the same rate. Ions are accelerated towards the surface of the target in ion beam sputtering, where they collide with it. The sputtered material accumulates on a wafer positioned in front of the target. The ion current and energy can be modified independently. Since the target and wafer are placed in a lower-pressure chamber, more target material and fewer contaminations are transmitted to the wafer.

Figure 2.4 Electron beam evaporation machine, PVD Ulvac model EBX-16C with e-gun Ferrotec EV S-6 in FBK

Figure 2.5 Magnetic sputtering machine KS 800C of Kenosistec.

2.1.2 FIB Machine

For the purpose of patterning and drawing nano- and micro-structure without mask, FIB technique can be an excellent choice to make prototypes. It allows the definition of nanometric structures with a direct milling approach avoiding not only the needs of lithographic masks but also a pattern transfer process. The adopted Raith FIB-SEM system VELION is equipped with a normal incidence FIB-column and an oblique SEM, as shown in Fig. 2.6. Furthermore, the instrument is equipped with a laser interferometric stage that allows nanometric positioning of patterning.

(a)

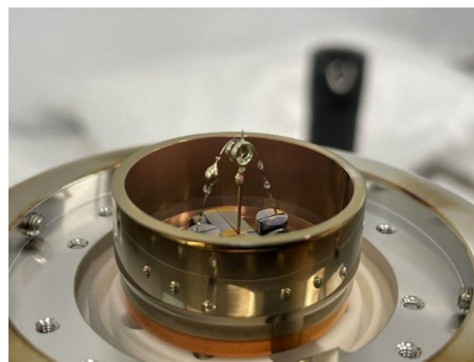

(b)

Figure 2.6 Raith focused ion beam system (a) and the LMIS (b).

The ion column in FIB makes use of a liquid-metal alloy ion source (LMAIS) able to generate focused beams of Au and Si ions from a reservoir loaded with an Au-Si eutectic alloys, as shown in Fig.2.6. The generated ions are typically accelerated with a 35 keV potential and focused onto sample surface for either patterning structure by milling, as well as for imaging exploiting the emission of secondary electrons by ion impact.

The utilization of relatively heavy ions within the beam makes milling a process that enables digging into the surface of the sample. a cutting-edge FIB-SEM double beam equipment with a focus on ion beam techniques for nanofabrication. A liquid metal alloy ion source offers for versatility in ion species and beam conditions, opening up a wide range of activities. Direct writing by sputtering (milling) and ion beam implantation and production of defects to locally affect material properties are examples of potential ion beam operations.

The samples are put onto a stage that is controlled by a laser interferometer, allowing for nanometric step size in both the x and y directions and ensuring exact position control. This permits 'blind-navigation' or nanometric alignments to previously existing markers with outstanding stitching performance across various writing fields. This FIB system primary attributes are: Ion column (FIB) with oblique incidence electron column, normal to sample surface multi-species ion source that is innovative (liquid metal alloy source technology). Si^{++}, Au^{+}, and Au^{++} are predefined ion species. Ions with energies between 2 and 35 keV (70 keV for double-charged ions), with a column designed for ion acceleration at that energy.

The term calcination refers to the process of heating a substance in an environment and at a temperature that are both strictly regulated. This method is known to reorganize the crystal structure of materials in furnace shown in Fig.2.8.

Figure 2.7 Furnace Expertech CTR200 in CRM of FBK

2.2 Physical and Chemical Analysis Techniques

In order to characterize sensing materials properties, such as morphology, nanostructure, chemical composite and sensing ability, several techniques in FBK-MNF unit were applied during our work. Morphology and elemental composition were determined by the scanning electron microscope (SEM) and Energy Dispersive Spectrometer (EDS), and Thermo Fisher Scientific Helios 5 CXe with energy of 5 keV and current of 0.1 nA inside FBK. The SEM is a type of microscope that creates images by using a stream of electrons that collides directly with the specimen being examined. Electron beam in SEM is produced by the electron gun, and accelerated by high voltage. The impact of the electron beam on the specimen surface causes the surface to emit secondary electrons; this is the primary mechanism by which the SEM may produce images of three-dimensional objects. The secondary detector is just responsible for collecting secondary electrons. If the atomic number is higher, then the backscattering will be stronger and the electron transmission will be lower. In our case we used SEM system in Helios 5 PFIB Dual Beam, as shown in Fig.2.10.

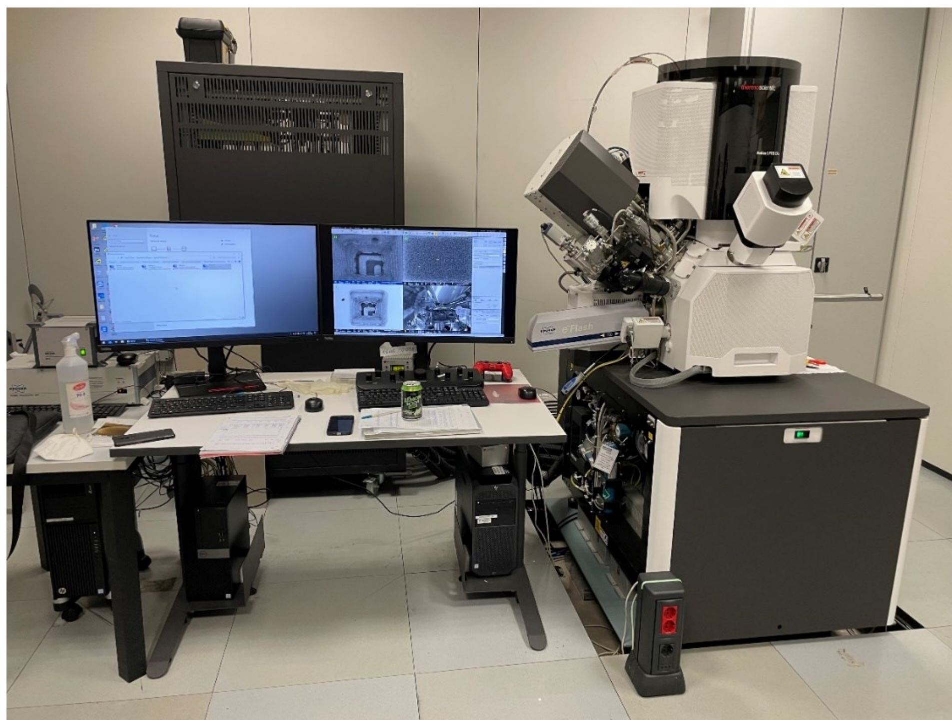

Figure 2.8 Helios 5 PFIB Dual Beam

Crystal phase, grain size, and cell parameters are estimated by X-ray Diffraction (XRD) through a PANalytical X'Pert PRO (PANalytical B.V., Almelo, Netherlands) instrument, equipped by X'Celerator detector based on RTMS (Real Time Multi Strip Technology) and optimized for Cu Kα1,2 radiation. X-ray tube is set at 40mA and 40kV and the data is collected at room temperature. X'Pert HighScore Plus version 2.0 program by PANalytical B.V., coupled with the Powder Diffraction File database (PDF), is utilized for phase identifications. Profex v. 4.2.1 fitting program is applied to estimate the cell parameters and the average crystallite size by Rietveld and Le Bail fits, which are carried out with the fundamental parameters approach [41]. X-ray diffraction (XRD) is widely considered to be the most effective technique for determining the structure of crystals as well as the phase of crystals in industries of inorganic chemistry, physics of solid states, and crystallography. Diffraction effects can be produced through the interaction of wavelengths with periodic structures if the periodicity of the crystals and the wavelengths themselves are of comparable magnitudes. X-rays can be easily generated with wavelengths that match the unit cell dimensions of crystals. When an X-ray primary beam is incident on a sample, scattering occurs in all directions regardless of whether or not diffraction effects are taken into account. The intensity of the scattered light is redistributed through diffraction into a variety of different directions. As a consequence of this, intensity peaks hike in certain directions, whereas the intensity significantly decreases in the regions that are located between peaks. It is possible that the peaks will go in different directions. The concept of scattering lattice planes and interference between the wavelets that are scattered by neighboring lattice planes is one way to describe these directions. As a result, a reflection will take place in accordance with the Bragg equation 2-6.

$$n\lambda = 2d * \sin \theta \qquad \textbf{2-2}$$

where λ denotes the length of the radiation's wavelength, n represents an integer number, θ stands for the angle formed by the lattice planes and the incident beam, and d is the distance between the lattice planes from which the peak originates. When an incident beam of monochromatic X-rays interacts with a target material, the X-ray diffraction effect occurs. The process of diffraction is applied to scattered X-rays when the scattering occurs in substances with regular structures, such as crystals. When the condition meets Bragg's law, the incident rays interaction with the sample results in the generation of constructive interference as well as a diffracted ray. The diffraction angle and the lattice spacing in a

crystalline sample are related to the wavelength of electromagnetic radiation by this law. X-rays that have been diffracted are, as a final step, subjected to additional analysis and quantification by detectors. Comparing the d-spacings to standard reference patterns is the typical method for converting diffraction peaks to d-spacings. This allows for the recognition of the minerals, as each mineral has its own set of distinctive d-spacings.

XRF analysis is conducted by HORIBA XGT-7200V with rhodium X-ray source. The work energy ranged from 15 to 30 keV, and the incident gun spot size changed between 10 and 100 μm to obtain reasonable results. X-ray fluorescence, also known as XRF, is a type of analysis that enables the detection of the emission of characteristic secondary X-rays from a substance after the substance has been excited by being subjected to high-energy X-rays. This analysis can be performed by bombarding the substance with high-energy rays. The phenomenon is utilized extensively in the field of elemental as well as chemical analysis. The apparatus ionizes substances by subjecting them to X-rays of a shorter wavelength. Ionization is the process by which an atom loses one or more electrons when it is subjected to radiation with an energy that is higher than the atom ionization energy. It is possible for X-rays to have enough energy to force electrons out of their securely held positions in the inner orbitals of an atom. When one electron is removed from an atom in this manner, the atom electronic structure becomes unstable, and electrons from higher orbitals fall into the lower orbital in order to fill the void that is created. When an object is allowed to fall, it will release energy in the form of a photon. The energy of this photon will be equal to the difference in energy that exists between the two orbitals that are involved. As a result, the substance gives off radiation, which has energy that is specific to the atoms that are there.

X-ray photoelectron spectroscopy (XPS) is a quantitative spectroscopic technique that enables measurements of the elemental composition, chemical state, and the electronic state of elements. For the purpose of recording XPS spectra, a Scienta Esca-200 system that is outfitted with a monochromatized Al Ka (1486.6 eV) source. A double-sided piece of carbon tape is utilized in order to secure the powders to the sample holder. A global energy resolution of 0.4 eV is typically employed for this purpose, performed in a high vacuum circumstance. The angle of emission between the axis of the analyzer and the normal to the surface of the sample is practically existed. Charge adjustment is accomplished for each sample by making use of an electron-flood cannon, and all core level peak energies are compared to the saturated hydrocarbon in C1 s at 284.8 eV as a point of reference.

Figure 2.9 Scienta Esca-200 XPS system at FBK

The XPS technique is based on the photoelectron effect induced by X-ray irradiation: when an X-ray photo is absorbed, the energy is transferred to a core electron of the target atoms, then the energy is transferred from the photon to a core electron of the target atoms. Photoelectron is thus emitted, resulting in the creation of an empty core state. After that, the photoelectron travels from the surface of the material to electron detector that measures the characteristic kinetic energy. In fact, the latter is linked to the photon energy and to the core level from where the photoelectron was emitted. As it can be seen from the Equation 2-3, where KE is the electron kinetic energy, BE is the binding energy of the core level of the photoelectron, Φ_{spec} is the work function of the spectrometer, where hv is the impinging photo energy.

$$hv = BE + KE + \Phi_{spec} \qquad \textbf{2-3}$$

A portion of the electrons that are located at the surface of the sample escape from the sample and travel to the vacuum chamber, where they are analyzed by the spectrometer analyzer slit. The plots of intensity versus energy can be seen in the XPS spectra. The saturated hydrocarbon in C 1 s at 285.0 eV serves as the reference point for all core level peak energies for each sample, and charge adjustment is accomplished using a flood cannon. The XPS instrument is utilized at FBK.

Secondary Ion Mass Spectrometry (SIMS), is a surface analysis technique that produces secondary ions by focusing a pulsed stream of primary ions onto a sample surface, as shown in Fig. 2.10. When these secondary ions are analyzed, information on the molecular, inorganic, and elemental species that are present on the surface can be determined. Due to the fact that SIMS is a survey approach, it is often possible to identify all of the elements included in the periodic table, including H element. In addition to that, the results of this analysis can include mass spectral information, information about an image in the XY plane that spans a sample, and information about a depth profile in the Z plane that extends into a sample.

SIMS has matured into a technique widely used in industrial laboratories to characterize elemental and molecular surfaces. The surface sensitivity of SIMS makes it an effective approach for guiding further analysis, in the same way that the binocular microscope can help in the decision-making process regarding subsequent analysis. SIMS is predicated on the largely unexpected observation that bombardment of surfaces with ions of some keV energy leads not only to the emission of elements, but also to the emission of intact involatile molecules that are characteristic of the chemical composition of the surface uppermost monolayer. The majority of secondary particles emitted are neutral, whereas only a small minority are positively or negatively charged (secondary ions). As the measurement of mass relies on charged particles, desorbed neutrals must be post ionized prior to mass determination; however, this is an inefficient procedure that reduces the number of secondary particles to the same order of magnitude as the number of primary particles. It is possible to collect not only spectroscopic information but also information on the lateral distribution of surface species (TOF-SIMS Imaging). Using contemporary liquid metal ion cannons, the lateral resolution for element identification exceeds 100 nanometers. For molecular species, however, the feasible lateral resolution depends not only on the performance of the instruments, but also on sample factors such as the generation of secondary ions and the sample area disturbed by a single source ion. Whereas the obtainable

resolution for bigger molecules can be many microns, imaging with sub-millimeter precision is conceivable when monitoring distinctive fragment ions. In our characterization process, we use cesium ions as the primary beam with the impact energy of 1 keV and beam intensity of 10 nA. The source potential is 8 kV, and the monitored species is Cs^+ (^{14}N, ^{28}Si, ^{48}Ti, ^{195}Pt, ^{197}Au). The sample raster size is 200 x 200 μm.

Figure 2.10 SIMS system in FBK.

AFM is a method that is developed for surface morphology, such as roughness and thickness. The tapping that takes place between the tip of AFM and a specimen surface during the AFM technique results in the production of a topographical recording of the sample surface. The interaction probe for the AFM apparatus is a pointed probe tip that is mounted on a microcantilever and serves as part of the AFM instrument itself. Monitoring variations in the microcantilever deflection is accomplished by tracking how the location of the laser spot on the photodetector moves in response to the microcantilever displacement. The deflection signal is computed by first finding the difference between the signal detected by the first and second quadrants, and the signal detected by the third and fourth quadrants, then subtracting that difference from the signal detected by the first and second quadrants. The signal strength that is detected by the second and third quadrants is compared to the signal strength that is

detected by the first and fourth quadrants in order to detect any lateral or torsional bending. The relative height information of the topographic features of the specimen can be obtained by the AFM apparatus through the scanning of the probe while it is in contact with the surface of the sample.

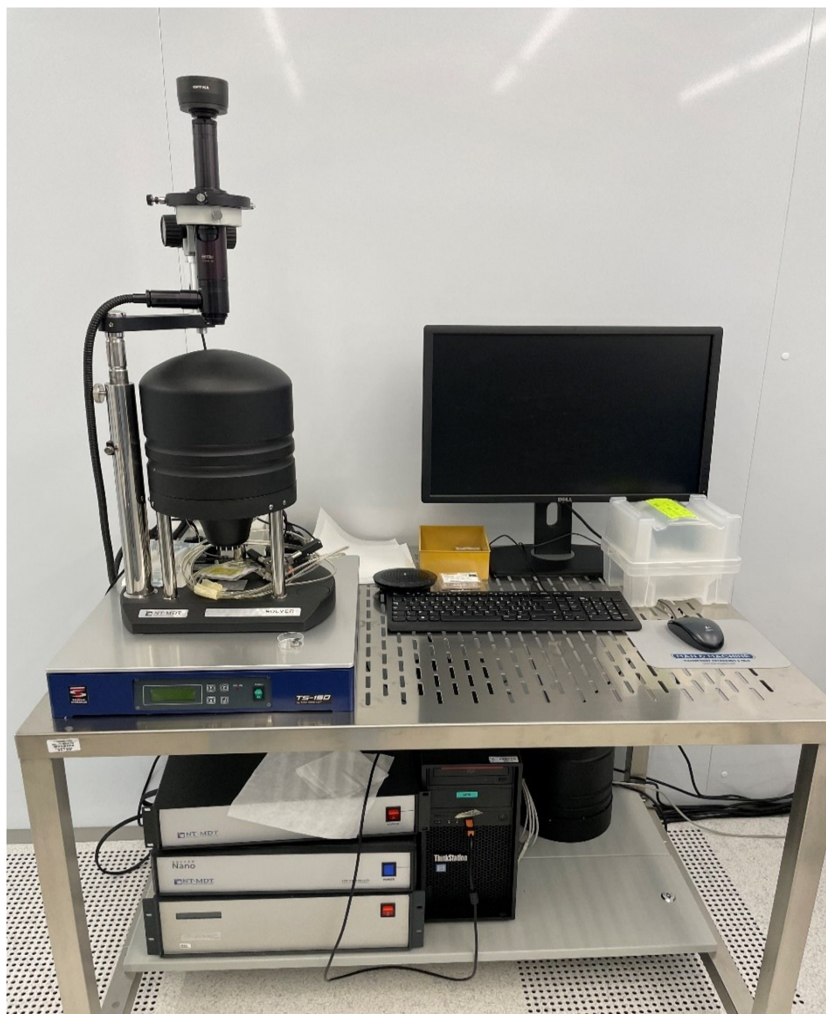

Figure 2. 11 AFM system at FBK.

UV/VIS Spectroscopy

The spectroscopy of photons in the ultraviolet–visible (UV/VIS) technique makes use of light in the visible spectrum as well as the nearby near-ultraviolet and near-infrared areas. Electronic transitions can be seen in molecules as they move across this portion of the electromagnetic spectrum. The quantitative analysis of solutions containing transition metal ions and highly conjugated organic molecules frequently makes use of UV/VIS spectroscopy as a method of investigation. Because the d electrons within the metal atoms can be stimulated from one electronic state to another, solutions of transition metal ions can have

color (that is, absorb visible light). This allows the solutions to be colored. The presence of additional species, such as certain anions, has a significant impact on the color of metal ion solutions. For example, a faint blue color can be seen in a solution of copper sulfate that has been diluted; but when ammonia is added to the solution, the color becomes more intense and the maximum wavelength of absorption shifts. Organic compounds, particularly those with a high degree of conjugation, absorb light in the ultraviolet or visible parts of the electromagnetic spectrum. Both the polarity of the solvent and the pH of the solution can have an effect on the absorption spectrum of an organic chemical. Even while charge transfer complexes can result in colors, those colors are frequently of an intensity that prevents them from being utilized in quantitative analysis.

According to the Beer–Lambert equation, the amount of light that can be absorbed by a solution is directly proportional to the concentration of the solution. Therefore, UV/VIS spectroscopy is a method that can be utilized in the process of determining the concentration of a solution. A UV/VIS spectrophotometer could be used in place of a detector in some situations. When an analyte is present, a response is elicited, the nature of which can be believed to be proportionate to the concentration of the analyte. The response factor can be thought of as the height of the peak for a certain concentration. The method is most frequently utilized in a quantitative fashion for the purpose of determining concentrations of an absorbing species in solution by the application of the Beer–Lambert law:

$$A = -\log10(I/I_0) = \varepsilon * c * L \qquad \text{2-4}$$

Where A is the absorbance that was measured, I_0 is the intensity of the light that was incident on a certain surface at a specific wavelength, I is the intensity of the signal that is delivered, and L is the path length across the sample, c represents the amount of the absorbing species in the sample. The molar absorptivity is denoted by the constant ε, and it varies depending on the species and the wavelength.

Figure. 2.12 The Manual Probe Station PM8 present at the FBK.

A Karl Suss Manual Probing Station PM8 (SUSS MicroTec Semiconductor, Garching, Germany), outfitted with an Agilent 4156C Precision Semiconductor Parameter Analyzer (Agilent Technologies, Santa Clara, CA, USA) with a nominal resolution of 1 fA and 2 uV, is used to make manual measurements. By using this machine, we can measure the resistance changing and current flowing though the electrode under a certain voltage. In our case, we measure the gas sensor device resistance including heater resistance changing and sensing material resistance changing with different voltage.

Figure 2.13 Binding machine of K&S Ball Analog Bonder Model 4014

Sensor bonding is essential to the packing of a gas sensor device. In fact, this procedure enables the sensor to be interfaced with the other electrical devices, making it helpful for reading the signal emanating from the transducer. A semi-automatic K&S Ball Analog Bonder Model 4014, located at the FBK, is employed for the bonding process when it comes to silicon and quartz devices. We use a gold wire with an 18 µm diameter in this apparatus. The ball bonding procedure is a special kind of wedge bonding that makes it possible to create a gold ball by applying a high-voltage electric charge to the wire using a capillary that resembles a needle. Then, using a combination of pressure, temperature, and ultrasonic energy, this ball is forced down and connected to the sample. Then, the machine passes over the area where the chip needs to be connected up after the wire has been sent out through the capillary. The second bonding is created when the machine returns to the surface and crushes the wire (without the ball) between the pad and the capillary tip.

2.3 Gas Sensor Test System

After we obtained the sensing materials on the substrate, the next step would be to bind the sensor device on T039 substrate by using gold wires with diameter of 0.06 mm in order to measure the resistance changing of the sensing materials.

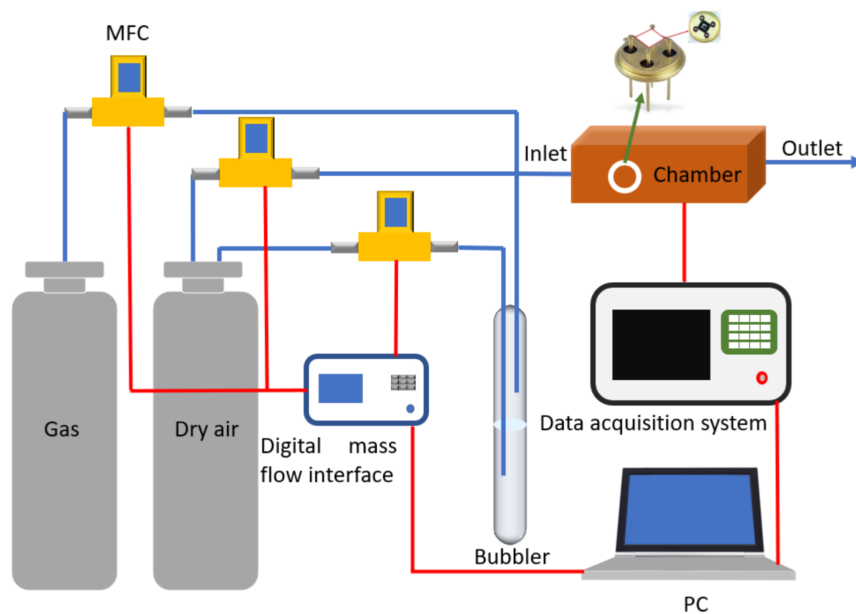

Figure 2.14 Scheme of the apparatus of the gas sensor characterization system.

The effectiveness of the gas sensing was then evaluated in a gas chamber with a volume by using homemade sensing test system. Gases were mixed and fluxed using MKF mass-flow controllers and came from certified bottles. The humidity environment control was achieved by sending a second dry air line through a deionized water bubbler and combining it with the gas lines. A digital humidity sensor (1.0% accuracy) placed close to the chamber exit managed the resulting relative humidity.

References

[1] K. Palka, M. Kurka, S. Slang, and M. Vlcek, "Utilization of As50Se50 thin films in electron beam lithography," *Materials Chemistry and Physics,* vol. 259, p. 124052, 2021.
[2] L. Bruchhaus, P. Mazarov, L. Bischoff, J. Gierak, A. D. Wieck, and H. Hövel, "Comparison of technologies for nano device prototyping with a special focus on ion beams: A review," *Applied Physics Reviews,* vol. 4, p. 011302, 2017.
[3] Toshihiko Tanaka, Mitsuaki Morigami and Nobufumi Atoda, "Mechanism of Resist Pattern Collapse during Development Process, " Jpn. J. Appl. Phys. vol. 32, p. 6059-6064, 1993.
[4] S. Okazaki, "High resolution optical lithography or high throughput electron beam lithography: The technical struggle from the micro to the nano-fabrication evolution," *Microelectronic Engineering,* vol. 133, pp. 23-35, 2015.

[5] Y. Chen, "Nanofabrication by electron beam lithography and its applications: A review," *Microelectronic Engineering,* vol. 135, pp. 57-72, 2015.
[6] A. A. Tseng, C. Kuan, C. D. Chen, and K. J. Ma, "Electron beam lithography in nanoscale fabrication: recent development," *IEEE Transactions on Electronics Packaging Manufacturing,* vol. 26, pp. 141-149, 2003.

3. Micro/Nano Hotplates Simulation and Fabrication

3.1 Hotplate Introduction

An SMO gas sensor is a device that identifies and communicates information regarding the ambient gas atmosphere, which contains numerous types of harmful and deadly gases. On top of the substrate, the device consists primarily of a sensing layer and a signal conditioning unit. By adjusting the sensor working temperature, a solid-state sensor can be used to detect a variety of gases in several ranges. A microelectromechanical system (MEMS) microheater (MHP) is one of the essential parts of an SMO gas sensor [1-3]. An MHP is typically made up of a resistor, which, as a result of Joule heating, can reach extremely high temperatures. The utilization of thermally insulating dielectric membranes results in a reduction in the amount of power that is consumed. On the MHP, the heating resistor depends on the type of sensor [4]. Deposited platinum (Pt) thin films are an ideal material for use as a functional electrode and heater layer because of their high temperature coefficient of resistance (TCR) and chemical inertness [5, 6]. Dielectric cover layers, such as silicon oxide and/or silicon nitride, serve for two purposes: they protect a device from the harmful effects of the environment and they passivate it electrically. However, adhesion problems might arise when platinum films are deposited on dielectric layers due to the poor adhesion between pure metal Pt and silicon compound materials. For the application of SMOs, the MHP is required to operate at high working temperature (generally above 300°C), which ultimately leads to significant power consumption [2]. A sensor system must have low power consumption in order to have an acceptable battery lifespan. It could be partially achieved by using silicon MEMS technology to optimize thermal mass, compactness, low power, repeatability, and low unit cost. Continuous research efforts are made to improve sensing materials, device design, and operating modes as a result of the need for sensors with better performances. A raised temperature with uniform temperature distribution throughout the detecting layer is also a significantly critical criterion for SMO gas sensors since it frequently increases the sensor sensitivity and response/recovery time. For this reason, one of the essential parts for the SMO in raising the necessary temperature with high temperature uniformity is the MEMS microheater. The membrane materials below the heater and the microheater geometry have the biggest impact on power efficiency and temperature uniformity.

To achieve these goals, it is necessary to understand and manage the thermal properties of the micro hotplate, particularly with regard to power consumption, transient responsiveness, and even temperature distribution, by managing heat losses, dielectric materials, and heater configuration [7-9]. In this chapter first we did simulation on the influence of the hotplate geometries size, heater circuit layout and substrate parameters on the temperature values and distribution. A bunch of simulation works have been done for the design and optimization of hotplate. For example, Avneet Singh et al. used ANSYS software to design and simulate single-cell microheater, they obtained platinum micro-heater by applying bulk micromachining technique on SiO_2 membrane with thickness of 1.5 µm, and the thermal isolation active area was 250 x 250 µm^2. The maximum temperature of 950°C at applied DC voltage of 2.5 V [5]. Mahanth Prasad et al used MEMS tool COVENTORWARE software to designed and simulated the micro-hotplate, which consisted of a 1.0 µm thick SnO_2 membrane of area 600 µm x 600 µm above the spiral Pt heater resistor deposited by DC sputtering technique. The micro-hotplate just consumed only 50 mW power at operational temperature of 500 °C with a TCR value 2.19 x 10^{-3}/°C [10]. S. Bedoui et al. optimized a meander-spiral by a Finite Element Method analysis, they found that by increasing the heater thickness, the temperature did not change too much. When the temperature was 300 °C, the power consumption was around 75 W. They also demonstrated that the temperature homogeneity could affected the power consumption reversely [11]. F. Samaeifar et al. used ANSYS finite element analysis software for thermal and mechanical simulations, and fabricated an suspended MHP devices by using back etch process, they found the temperature variation from 30 °C to 500 °C in the manufactured micro hotplate has a power consumption of 50 mW and a time constant of 4.23 ms, according to the results of an experiment [12].

All these above-mentioned hotplates, which exhibit super low power consumption (mW level), are based on suspended membrane structure. However, suspended-membrane structure of hotplate can be easily damaged during processing. A. Gaiardo et al. have tested the failure force of 900 nm thick closed-membrane-type hotplate with different planar sizes, identifying a strong correlation between the lateral size of the membrane and its mechanical strength and demonstrating that even at small lateral sizes the force needed to break the membrane is quite low (37 mN for 1.74x1.74 mm^2 membrane size) [25, 26]. The high fragility of the membranes precludes their further processability, including the thick film deposition of MOS. Therefore, particularly in some cases, bulk substrate with as much as

possible low power consumption has to be considered. For example, Y. Wang et al. had to sputter their heterostructure sensing material Au/SnO_2:NiO onto the self-assembled Au nanoparticles arrays, and they used Langmuir-Schaefer technique to transfer the Au nano particles to the solid-substrate hotplate [27]. Phung Thi Hong Van fabricated an effective networked nanowire sensors on Si/SiO_2 substrate via on-chip growth, the heater and electrodes were patterned by conventional lithography and loft-off techniques, and the sensing materials were grown by thermal evaporation at 1000 °C on the solid Si-based substrate [28]. Daihua Zhang et al. deposited In_2O_3 nanowires onto bulk Si wafer covered with 500 nm SiO_2, and patterned the finger-shaped metal electrodes by photolithography and electron beam evaporation on top the sensing material [29]. In term of this chance, the substrate cannot be suspended-membrane structure, hence the only approach to decrease the power consumption is miniaturization with high mechanical stability, which has been proved a valid way to improve the power efficiency due to small device area to be heated up, well-controlled temperature distribution and fast thermal response [30]. In this chapter, only solid-substrate hotplates were fabricated for following process.

3.2 Hotplate Design and General Fabrication Process

As we discussed in chapter 2, the processes were following the basic steps for the EBL steps. Firstly, we deposited the ONO layer on silicon wafer, the cross-section structure is shown in Fig. 3.1. In general, silicon wafer is electronically conductive, and cannot be used directly as devices substrate. In our work, we deposited SiO_2 and Si_3N_4 film above silicon wafer as insulating layer [2, 3]. The stack structure by combing SiO_2 and Si_3N_4 layers is not only electrically resist, but also exhibits 0 mechanical stress during high working time. The structure is shown in Fig. 3.1.

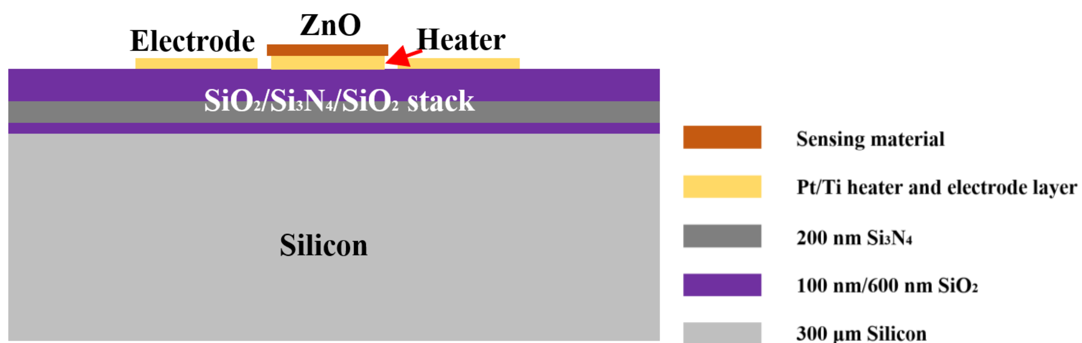

Figure 3.1 The cross-section structure of the sensor device on hotplate fabricated in this thesis.

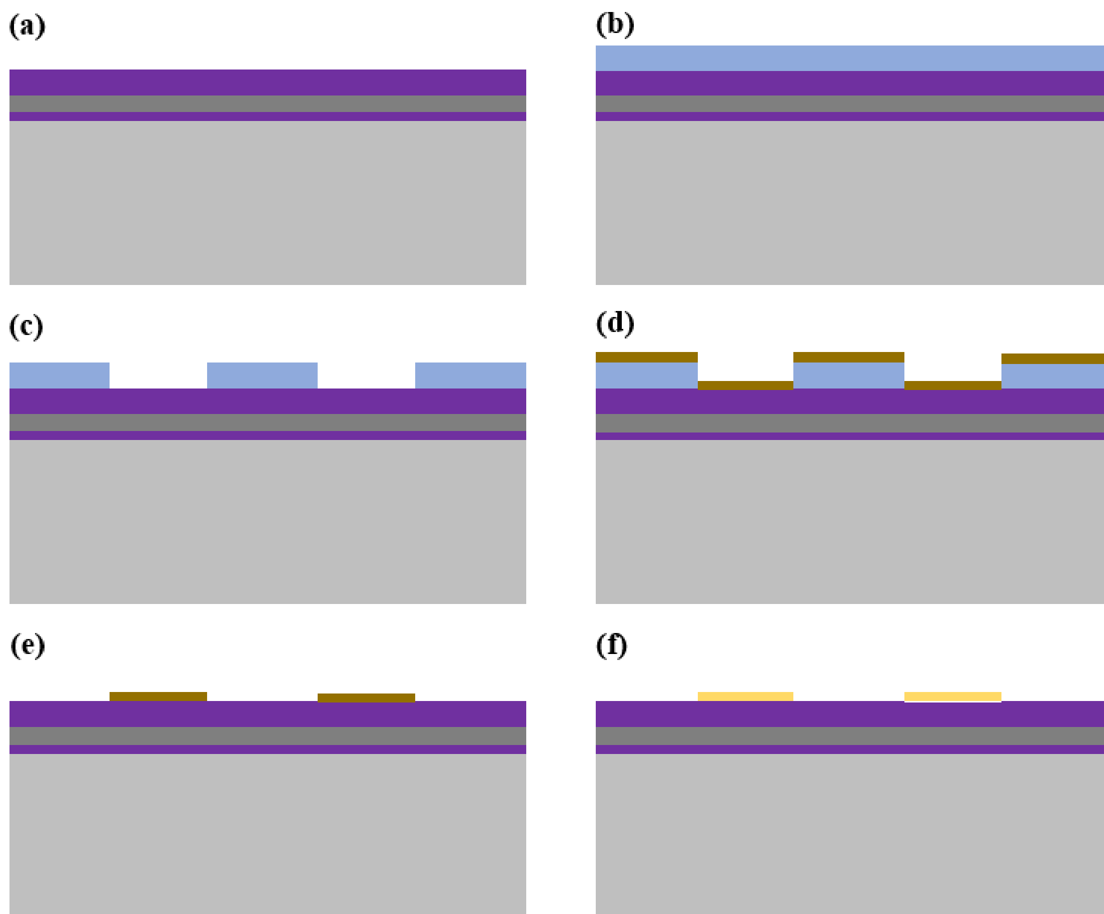

Figure 3.2 Fabrication process diagrammatic sketch: a). ONO stack structure deposition; b). PMMA resist spin coat; c). EBL exposure and develop; d). Pt heater and electrode deposition; e). Resist stripper; f). Calcination and metallization;

The first layer of SiO_2 was grown by thermal oxidation, which takes advantage of higher temperature of 800-1200°C and operates inside horizontal quartz tubes within a gas flow of O_2, H_2O or a mixed of them. The reaction formular is as followed:

$$Si + H_2O(g) \rightarrow SiO_2 + H_2(g) \quad 3\text{-}1$$

$$Si + O_2(g) \rightarrow SiO_2 \quad 3\text{-}2$$

The whole growth process is carried out for 40 minutes to obtain 200 nm thickness of SiO_2 at temperature of 975°C.

The second layer of Si_3N_4 and the third layer SiO_2 are formed by using LPCVD, which uses heat to initiate a rection of a precursor gas. Low pressure environment can ensure to avoid the unwanted gas phase reactions and increases the deposition uniformity. LPCVD reaction

temperature can be between 425 and 900 °C. The deposition process of Si_3N_4 layer is 42 minutes and the thickness is 100 nm. To deposit the top 600 nm SiO_2 layer, flowing gaseous tetraethyl orthosilicate (TEOS) is injected into the reaction oven at 720°C. The reaction is as shown in following:

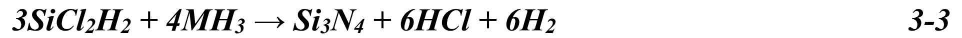

$$3SiCl_2H_2 + 4MH_3 \rightarrow Si_3N_4 + 6HCl + 6H_2 \qquad 3\text{-}3$$

$$Si(OC_2H_5)_4 \rightarrow SiO_2 + byproducts \qquad 3\text{-}4$$

After we obtained the substrate, then the PMMA resist A7 was spin coated following the isopropanol washing O_2 plasma cleaning process with oxygen flow of 10 sccm, pressure 800 mT, and RF set point 150W. In our case, the rotational speed was set as 4000 rpm/min, acceleration was 10000 rpm/s, and the duration time was 60s. Prebake is after the spin coating process to evaporate the coating agent and solidify the resist. Since A7 PMMA resist is purchased from Micro Chem, and the suggested prebake temperature is 180°C for 60-90 seconds on hot plate or 170°C for 30 min in convection oven.

To pattern the sensor devices by EBL machine, different acceleration voltages and doses were set for electron beam to optimize the exposure parameters. After exposure step by EBL, the developing process was conducted at room temperature, and the duration time was set as 30s, the stopper process time was 30s too. Then post bake was handled to eliminated the coating solvent, and the temperature was set as 120°C for 1 min. Pt/Ti was deposited by electron beam evaporation tool, and the thickness was set as 100nm/10nm. Then lift-off process was introduced to remove the resist residue. In the end, to metalize Pt and Ti, 650°C under N_2 gas environment was operated for 2h. These steps are standard steps for our micro hotplate fabrication.

For the hotplate layout design, three sizes of hotplate devices were developed, which were named as MHP1, MHP2, NHP1 and NHP2. MHP1 is the hotplate we are using in our lab, the layout design is referred to the work here [2]. MHP2 was obtained through downsizing MHP1 by 50 times, and two heater geometries for MHP2 were designed, one was rectangular shape named as MHP2_R, and another one was circular shape named as MHP2_C. The heater width of MHP2_R was 4 μm, and the heater circuit width of MHP2_C was 2 μm as shown in Fig.5.3a. The layouts of MHP2 were shown in Fig.5.3 (a). Two kinds of heater circuit width (1.1 μm and 0.6 μm) were designed for NHP1, and NHP2 heater circuit width was set as 1.1 μm. NHP1 and NHP2 heater circuit gap was 500 nm, these two layouts are shown in Fig.3.3b and c.

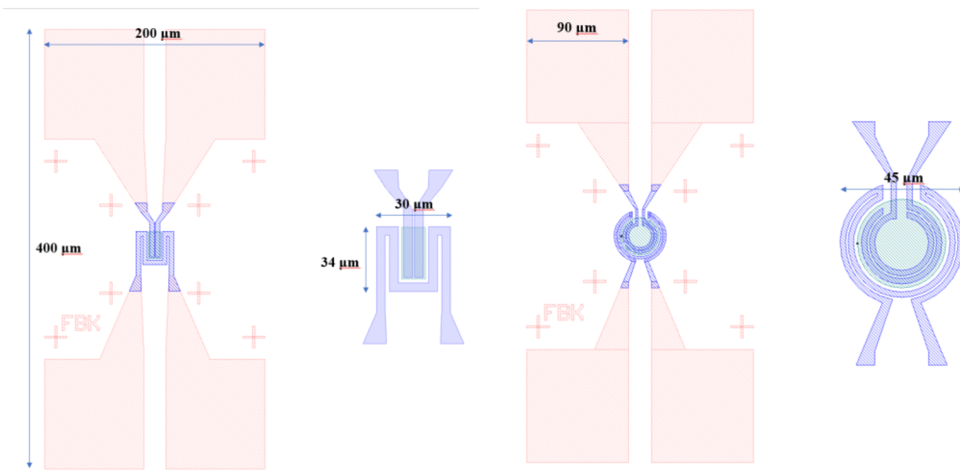

(a)

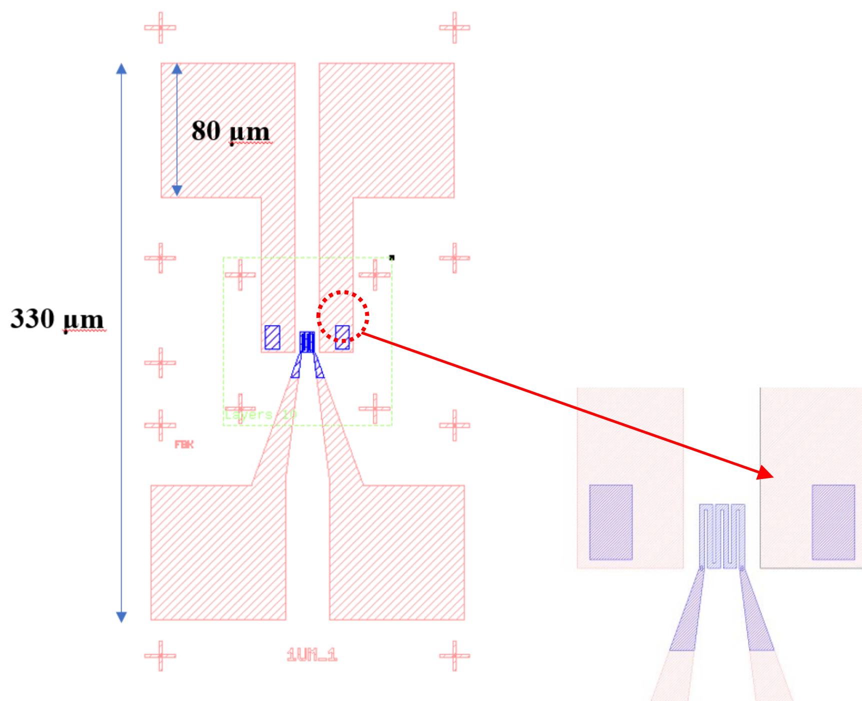

(b)

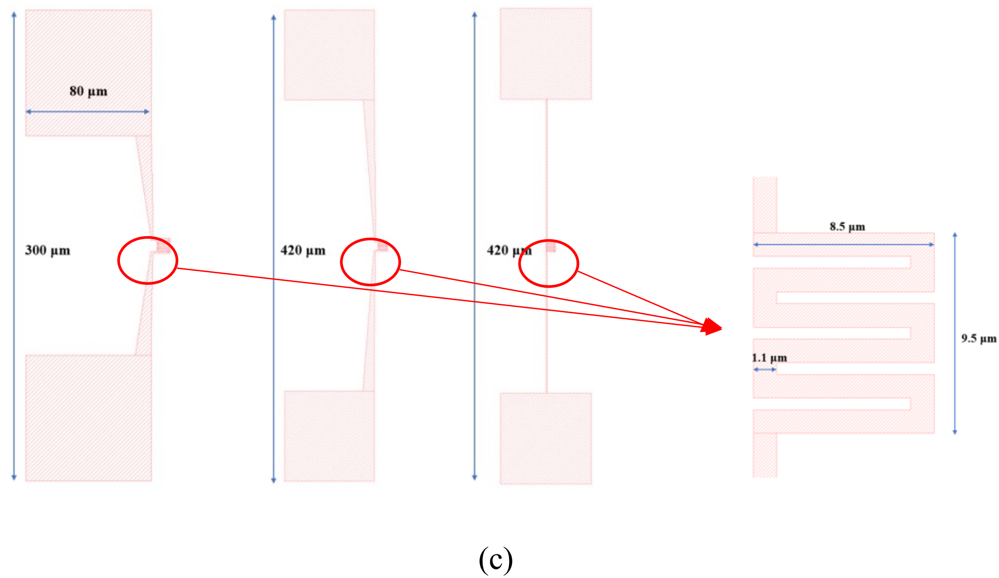

(c)

Figure 3.3 (a). Layouts of MHP2 with rectangular heater (MHP2_R) and circular heater (MHP2_C); (b). Layout of NHP1; (c). Layout of NHP2 (NHP2_1, NHP2_2 and NHP2_3)

3.3 Heat Dissipation Theory

After a basic model of hotplate is designed and the fabrication process is settled down, the next work will be optimization on the device geometry design and fabrication process investigation. If a micromachined gas sensor is going to be temperature modulated, the thermal parameters of the sensor need to be adjusted so that it has a low power consumption, a well-controlled temperature distribution over the sensing layer, and a quick transient response. Hence, first of all, the thermodynamics of the working hotplate should be basically understood.

Radiation, heat conduction, and heat convection are the three mechanisms that contribute to heat transmission, the pathway is shown in Fig.3.4. Heat conduction is something that must be dealt with along the membrane. Heat is transferred both above and below the membrane as a result of heat conduction and heat convection through the atmosphere that is around the membrane. Radiation is yet another factor that must be taken into consideration. The determination of total heat loss and temperature distribution is not simple due to the multiple channels of heat transmission. The measurement of total heat loss in vacuum is an experimental method that allows one to have a sense of the many channels of heat transfer. In vacuum, only heat loss due to conduction along the membrane and radiation must be considered. Utilizing the distinct temperature dependences of conduction (temperature-linear) and radiation, one may readily distinguish between these two components [13]. Thus,

both the heat loss due to conduction along the membrane and the heat loss owing to radiation can be determined. The total heat flow can be defined as:

$$Q_{tot} = \text{Conduction through membrane} + \text{conduction through air} + \text{radiation loss} + \text{convection loss} = G_m\lambda_m (T_{hot} - T_{amb}) + G_{air}\lambda_{air}(T_{hot} - T_{amb}) + G_{rad}\sigma\varepsilon (T_{hot}^4 - T_{amb}^4) + \Delta x \quad \textbf{3-5}$$

Where G_m, G_{air} and G_{rad} are geometry factors, mainly governed by membrane/device design; T_{hot} and T_{amb} stand for the temperature of the hot active area and the ambient, respectively, λ_m and λ_{air} are the thermal conductivity of the membrane and the surrounding atmosphere, ε is the emissivity and σ the Stefan-Boltzmann constant,

Thermal response is defined as the time to reach the steady state temperature from the time of starting heat. A simple expression for the thermal transient response can be obtained by

$$T(t) - T_{amb} = P_{el}R_{therm} (1 - e\text{-}t/\tau), \qquad \tau = R_{therm}C \quad \textbf{3-6}$$

where T(t) represents the temperature of the microheater, T_{amb} represents the temperature of the surrounding environment, P_{el} is the heating power, R_{therm} stands for the overall thermal resistance, and C represents the overall thermal capacity [14]. Hence to improve the thermal response, downsizing the microheater with high thermal conductivity are preferred. But on the other hand, high thermal conductivity can result in serious heat dissipation increasing the power consumption.

The power consumption of hotplate is caused by heat dissipation including conduction, convection and radiation [15]. The main heat loss is through the pillar and membrane conduction seen in Fig.3.4. One must solve a three-dimensional issue in order to calculate heat conduction. Due to the proportions of the membrane (thickness: several nanometers, edge length: roughly several micrometers), it is common practice to disregard the heat conduction perpendicular to the membrane in order to simplify matters. In the case of a suspended membrane, a reduction to a one-dimensional issue is straightforward, as heat conduction occurs mostly along the suspension beams of length l and cross-sectional area A_{beam}, which is:

$$Q_{membrane} = \frac{4(\lambda_m A_{beam})(T_{hot}-T_{amb})}{l} \quad \text{3-7}$$

$$G_m = \frac{4A_{beam}}{l} \quad \text{3-8}$$

In which r_a and r_i represent the width of the membrane and suspension beams [13]. Apparently to decrease the power consumption, it is better to design a small size of the heater beam part.

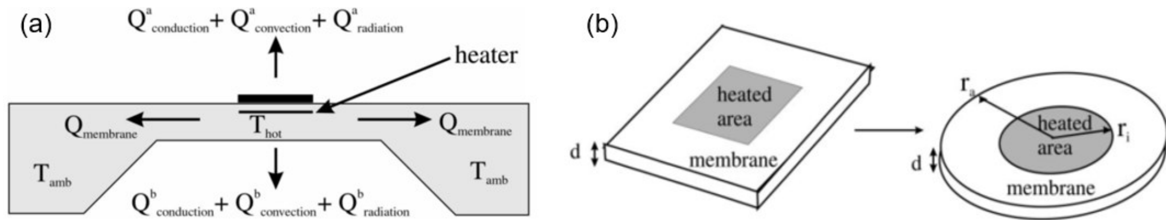

Figure 3.4 Heat flux of a micromachined gas sensor (a) and heat conduction model in one-dimensional. Reprinted with permission [13].

For closed membranes as shown in Fig.3.4 b, a simple model is derived by substituting a round membrane for a square one, which results in an easily solvable one-dimensional heat conduction problem in cylindrical coordinates.

$$Q_{membrane} = \frac{2\pi d\lambda_m(T_{hot}-T_{amb})}{ln(r_a-r_i)} \quad \text{3-9}$$

Two factors can contribute to heat loss to the surrounding air: fluid motion and conduction are examples of mechanisms. Fluid motion can be induced by either external forces or temperature differences, which cause density variations in the gravitational field and, consequently, buoyancy forces. The first situation results in heat transmission known as forced convection, whereas the latter is known as natural or free convection. When there is no fluid motion, only conduction transfers heat. Under this assumption, the following basic model can be used to predict heat losses to air. This model approximates the hot gas sensor and the cold ambient by spherical approximations with radii r_i and r_a, resulting in the expression:

$$Q_{conduction} = \frac{4\pi d\lambda_{air}(T_{hot}-T_{amb})}{1/r_i - 1/r_a} \approx 4\pi r_i\lambda_{air}\,(T_{hot} - T_{amb}) \quad \text{3-10}$$

On the assumption that the heated membrane area behaves as a gray emitter, i.e. the degree of emission of the heated membrane is set equal to the degree of absorption, radiation has

been calculated. In such case, the expression of heat dissipation through radiation is as followed:

$$Q_{radiation} = G_{rad}\sigma\varepsilon(T_{hot}^4 - T_{amb}^4) \quad \textbf{3-11}$$

But if the working temperature is less than 400°C, the radiation can be ignored for simplicity [2, 13].

3.4 Micro/Nano Hotplate Simulation

An MHP should have a low thermal mass, a low power consumption, and improved temperature uniformity. It is necessary for the temperature to be within the required temperature range over the heater area in order to detect any changes in the resistivity of the material. The temperature of MHP has an effect on the sensor performance in terms of both its sensitivity and its reaction time. It is of the utmost importance to make sure that the design of MHP can make the most of SMOs to perform efficiently. In this chapter, a Finite Element Analysis (FEA) program called COMSOL Multiphysics 5.0 is used to undertake an analysis of electro-thermal and mechanical model that helps create high temperature uniformity and power efficiency by geometric optimization of the heater structure and the substrate materials. Electro-Thermo-Mechanical study was carried out in order to investigate the temperature and stress distribution throughout the MHP. Simulations were run on a three-dimensional structure that compares the MHP temperature, power efficiency of suspended membrane and solid membrane in the first place based on Joule effect [15-18].

3.4.1 Model and Boundaries Setting for the Simulation

For the purpose of electrostatic modeling, the equation that follows will be used to compute the electrical field distribution across the MHP electrodes, denoted by the E:

$$E = -\nabla V \quad \textbf{3-12}$$

Where V represents the potential difference between the two sides of the micro heater. Following the completion of the solution for the electric field (E), the current density (J) and the Joule heating power (Q_j) can be calculated using the following equations:

$$J = \sigma E \qquad \textbf{3-13}$$

$$Q_j = \nabla \cdot J \qquad \textbf{3-14}$$

where σ is the electrical conductivity of the substance that makes up the heater. In addition, the temperature distribution can be computed by inputting the joule heating power Q_j, which can be determined by working through the following equation:

$$\rho C_p \cdot dT/dt = \nabla \cdot (k \nabla T) + Q_j \qquad \textbf{3-15}$$

Where ρ represents the density of the heater material, C_p means the heat capacity of the heater material at a constant pressure, k stands for the thermal conductivity of the heater material, Q_j is the heat source, and ∇T is the temperature differential across the heater material [8].

The boundary condition for this equation can be easily defined by setting the temperature at the base electrodes to be the same as the room temperature, i.e. $T_1 = T_2 = T_0$, where T_1 and T_2 are the temperatures at base electrode 1 and 2, respectively, $T_0 = 300$ K is the temperature of the substrate. This is a very straightforward way to define the boundary condition. The heat convection boundary condition is also accounted for in the simulation at this point in time. Simply solving the following equation will give the heat convection information:

$$(-k \nabla T) = h \cdot (T_0 - T) \qquad \textbf{3-16}$$

where h is the convective heat transfer coefficient of air.

The generated resistive heat Q_j is expressed as:

$$Q_j = \sigma \, |J^2| \qquad \textbf{3-17}$$

In which σ indicates electric conductivity and J represents current density, which is also the reciprocal of the temperature dependent electric conductivity.

$$\sigma = \sigma(T) \qquad \textbf{3-18}$$

By combining all these factors, we get:

$$Qj = 1/\sigma \cdot |J^2| = 1/\sigma \cdot |\sigma E|^2 = \sigma |\Delta V|^2 \qquad \textbf{3-19}$$

After determining the temperature distribution, the next step is to evaluate the displacement distribution based on the stress and the mechanical static equation, using the input thermal

strain obtained from the temperature distribution issue that is solved above, along with the thermal expansion coefficient, by using the equation:

$$\sigma = E\ (\varepsilon - \varepsilon_T) \quad \textbf{3-20}$$

$$\varepsilon = \alpha \Delta T \quad \textbf{3-21}$$

where in this equation ε, ε_T, E, α and T refer to the strain, initial thermal strain, Young's Modulus matrix, thermal expansion coefficient, and differential temperature, respectively. Additionally, the power consumption is characterized by equation [19, 20]:

$$P = V^2/R \quad \textbf{3-22}$$

The materials physical parameters we used in our simulation work are listed in Table 3-1 in appendix B.

3.4.2 Calibration of Simulation Results with the Experiment Data by Using MHP1 Model

In the first simulation part, we studied the MHP1 with comparison to the experiment data, which is the hotplate model with suspended membrane of our device in lab as shown in Fig.3.1 b [2]. Then we investigated the influence of the solid membrane and suspended membrane on the operational temperature and power efficiency, as shown in Fig.3.1. The size of the MHP1 was set in COMSOL as: silicon wafer substrate is 3000 µm*3000 µm * 300 µm, the ONO layer is 900nm thick, the width of the heater circuit is 100 µm, and the heat area is 1300 µm * 1300 µm, as shown in Fig.3.2.

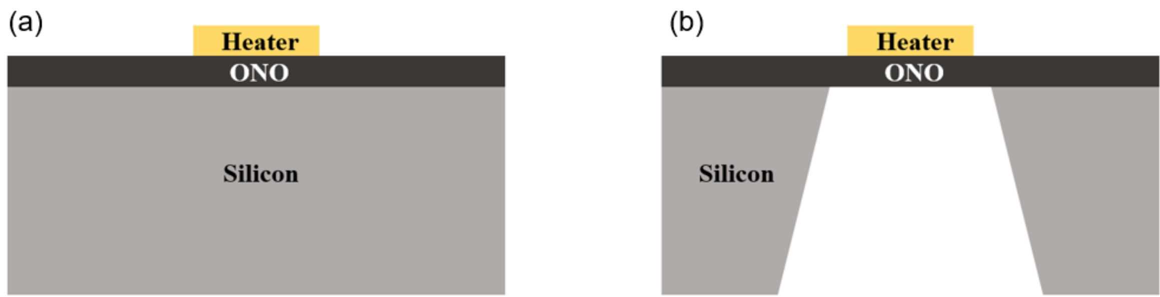

Figure 3.5 Model cross section structure of MHP1 with solid membrane (a) and suspended membrane (b).

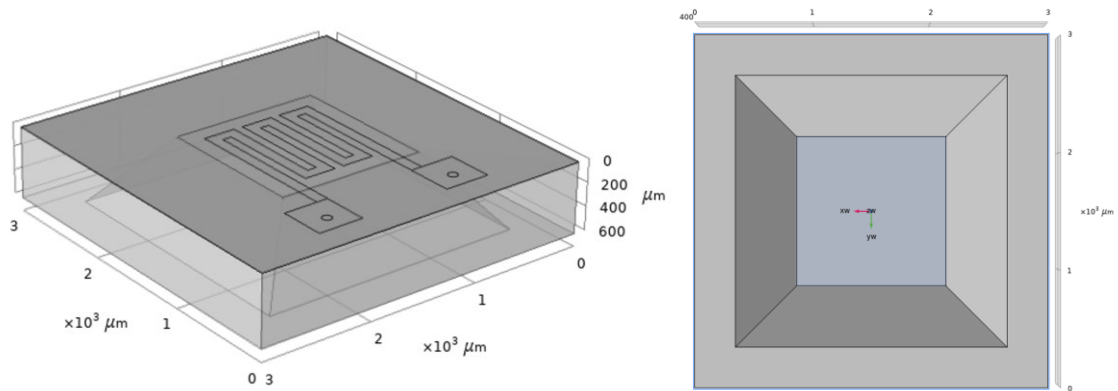

Figure 3.6 Model structure of MHP1 with suspended membrane in COMSOL.

The trench of the suspended membrane (fabricated by back etch) size is 1300 µm * 2300 µm * 300 µm. The simulation results are shown in Fig. 3.3

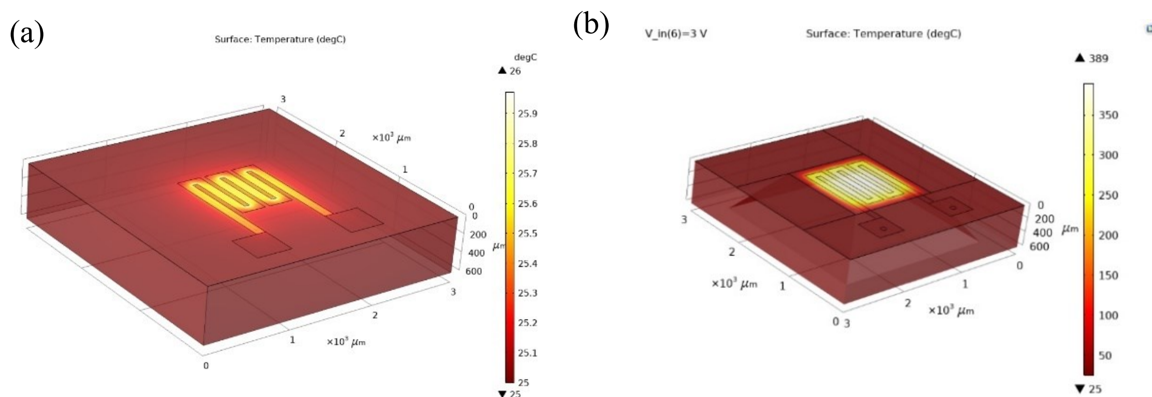

Figure 3.7 COMSOL simulation results of MHP1 with solid (a) and suspended membrane (b) at 3V.

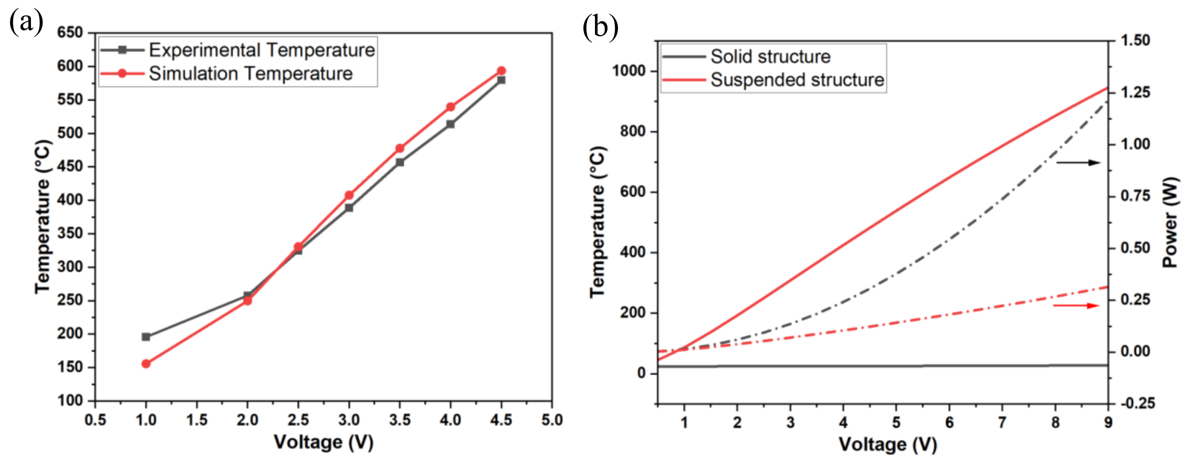

Figure 3.8 (a). Temperature comparison between experimental data and simulation data by using model MHP1; (b). Temperature and power consumption simulation results at different input voltage of MHP1 with solid membrane and suspended membrane.

Fig. 3.5 shows the cross-section structure of hotplate, and Fig. 3.6 shows the geometry model in COMSOL software. The simulated temperature of MHP1 at input voltage of 3V is shown in Fig. 3.7. Fig. 3.8a. shows that the simulation temperature result is quite closed to the experiment data, so in the next simulation work, we used the same boundary conditions parameters for the following model's simulation. It is distinct that the suspended structure has a huge effect on the temperature peak value and power efficiency from Fig.3.8b. With the solid membrane, it is impossible to heat it up by increasing the input voltage at this size mainly because of the heat conduction through silicon substrate, which accords with the general knowledge. Even when the voltage reached 9V, the temperature did not change too much. By designing a trench structure, the temperature increased a lot at the same input voltage compared to solid membrane structure, and the power consumption stayed very low. Since the trench is filled with air with thermal conductivity of 0.5 W/(m·K), which is much lower than silicon (230 W/(m·K)), and this could be the main reason that MHP1 with solid membrane cannot gain a high temperature due to the fast heat conduction through silicon substrate, and suspended membrane shows very high temperature and low power consumption because of the heat resist of the trench filled with air.

3.4.3 MHP2 Simulation Results

The smaller area to be heated up, the less power to be consumed. Therefore, to further decrease the power consumption, MHP2 is designed by downsizing 50 times compared to MHP1 size with the heater circuit width of 2 μm [13]. In this case, we also design two types of heater geometries, the rectangular shape and circular shape (MHP2_R and MHP2_C) to study the influence of the heater circuit geometry on the temperature distribution and power

efficiency, as shown in Fig.3.9. To further optimize the power efficiency, we investigate the effect of the insulating layer ONO thickness and Pt thickness on the temperature and power efficiency.

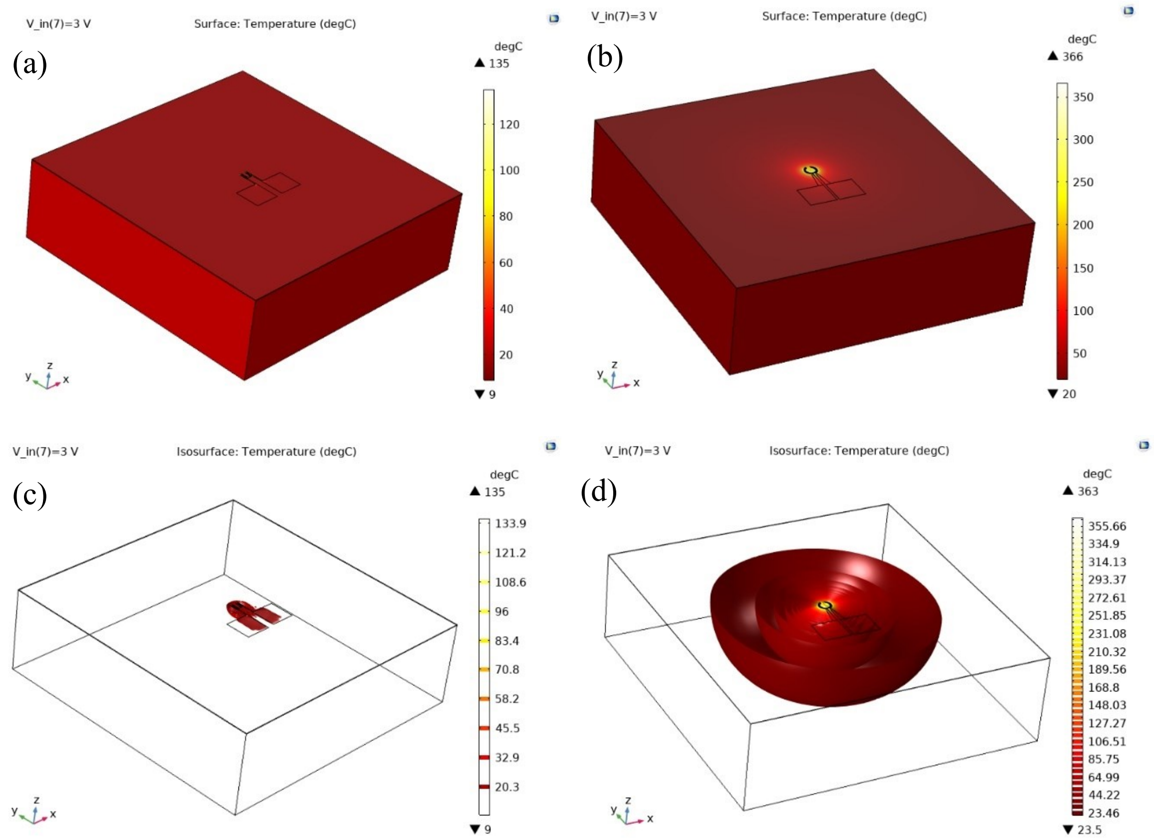

Figure 3.9 The model of MHP2_R (a) and MHP2_C (b) and the isothermal contours distribution (c) and (d) at 3V.

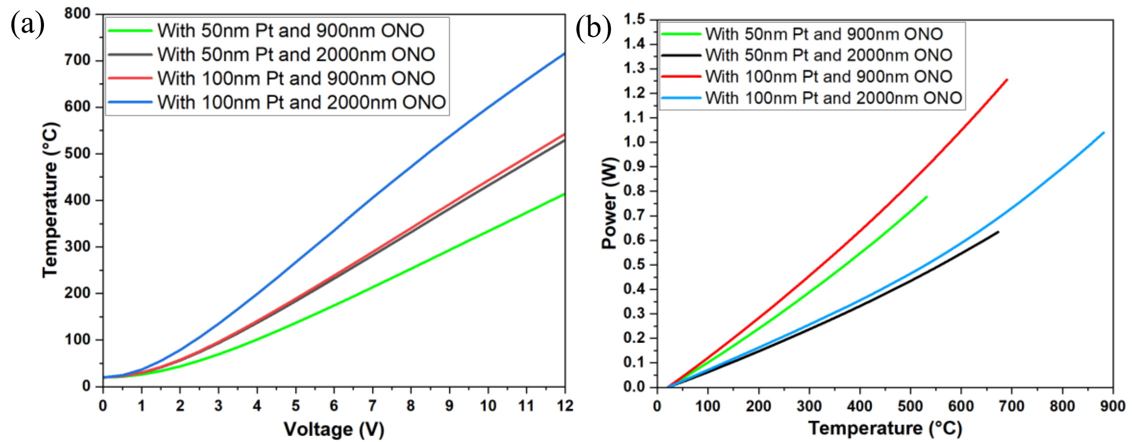

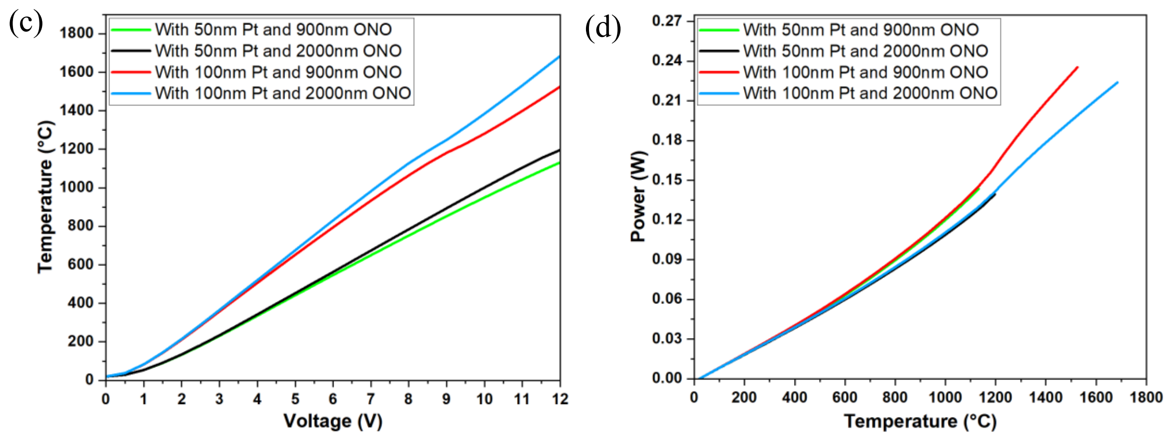

Figure 3.10 The temperature and power consumption of MHP2_R (a) and (b), and MHP2_C (c) and (d) at different input voltages with different thickness of Pt heater and ONO layer.

Fig. 3.9 c and d show the clear temperature distribution around the heater circuit at the same input voltage of 3V, which indicates the significate influence of different heater circuit geometries on the temperature peak and distribution. Circular-shape heater circuit owns more uniform and higher temperature peak comparing with rectangular shaper heater circuit at the same input voltage. In Fig. 3.10, the power consumption and temperature peak of the MHP2_R and MHP2_C are listed at different input voltages. It is easy to find out that when the insulating layer and Pt heater are thicker, the temperature of MHP2_R and MHP2_C is higher under the same input voltage. While the power consumption at the same temperature shows an interesting trend, thicker Pt heating circuits and thinner ONO layers showed higher power consumption. It could be because thicker ONO layer cause better heat resist, so higher temperature is obtained, or to achieve the same operation temperature, less power is needed. Thicker Pt electrode consumes more energy, and produces more heat resulting in higher temperature. This could explain why thicker Pt heater circuits and thinner ONO layers consume more power. Comparing the heat dissipation effect of MHP2_R and MHP2_C, it can be seen that MHP2_C obtains a higher temperature than MHP2_R under the same input voltage, and MHP2_C owns better power efficiency because of the different layouts of the heater. Thick ONO layer can both improve the temperature peak and the power efficiency. However, considering the requirements of temperature peak and power consumption, the choice of Pt electrode thickness is quite contradictory. It is because if higher temperature is the goal, we have to increase Pt heater. But if we want to decrease the power consumption, we have to do the opposite way. To balance these two requirements, more parameters should be considered [21].

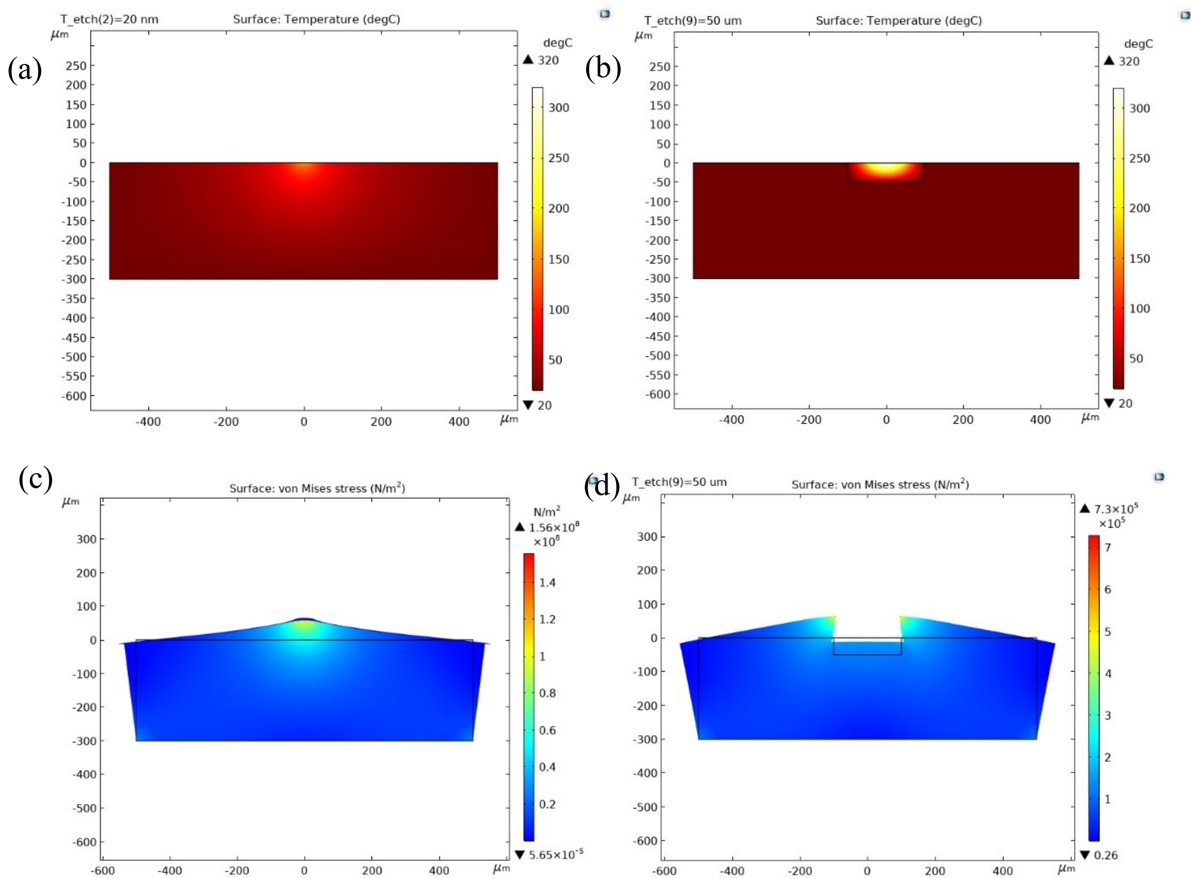

Figure 3.11 The influence of suspended structure on the heat conduction and mechanical property.

The suspended membrane affects not only the temperature distribution and power efficiency, and also the mechanical properties of the SMOs gas sensor devices. To simulate the heat conduction and mechanical performance inside the substrate, we used 2-D structure module, as shown in Fig.3.11, the heat source is on the top center of the substrate at 300°C. It can be seen that inside the solid membrane structure, the temperature distribution is radially dispersed, while from Fig. 3.11b it is clear that the suspended structure can block the temperature inside the air cavity, which is the suspended trench structure. To have a quantitative image, the temperature values under ONO layer were taken at different suspended structure thickness, as shown in Fig. 3.12. It shows that when the suspended structure thickness is above 1 um, the temperature did not change too much by increasing the power source temperature. At the same temperature of the power source, different structures also exhibit different stress results. The stress of the suspended membrane is distributed in the cross-section structure, while the solid structure stress is centralized around the heat source. That is, the stress of the solid structure is higher than that of the suspended structure, as compared in Fig.3.13.

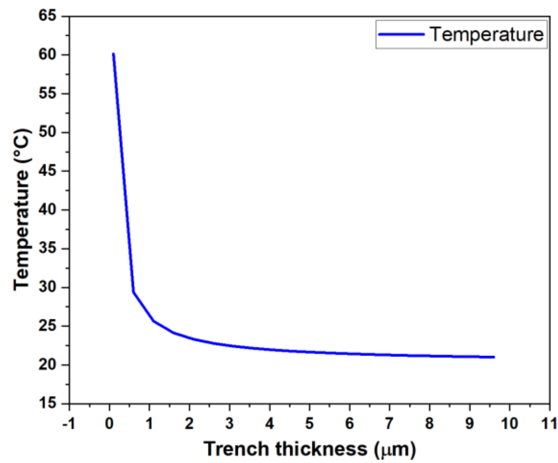

Figure 3.12 The temperature values under ONO layer changing the trench thickness.

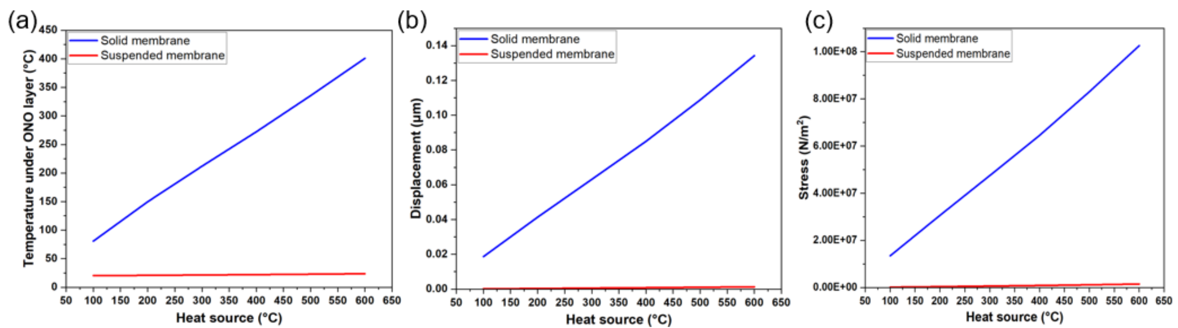

Figure 3.13 The comparison of temperature (a), displacement (b) and stress (c) of MHP with solid structure and suspended membrane at different temperature of the heat source.

To further study the influence of suspended structure on heat dissipation with the heat source temperature changing, the thickness of trench was fixed as 5 μm, and the results are shown in Fig.3.13. When the temperature of heat source increases, the temperature under ONO layer increases linearly with solid membrane structure. While for the suspended structure, the temperature does not change a lot. It is because the suspended structure obstructs the heat dissipation to the silicon substrate, and the heat can easily pass through the silicon material with the solid structure. In addition, the suspended structure can also enhance the mechanical performance of MHP from Fig.3.13 b and c by distributing the stress. Compared with the solid structure, the displacement and stress of the suspended membrane does not change too much when the heat source temperature is increasing.

3.4.4 NHP1 Simulation Results

By comparing MHP1 and MHP2, it proves that downsizing can increase the power efficiency. In this part, we kept decreasing the MHP size to obtain NHP1.

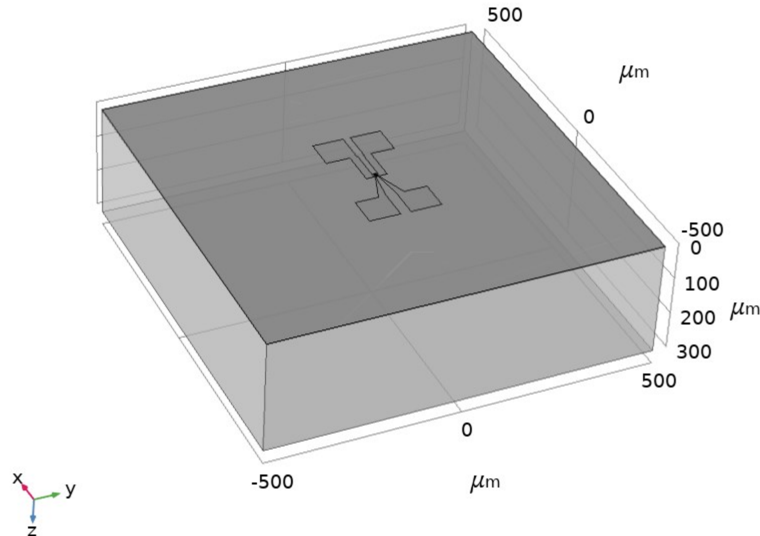

Figure 3.14 NHP1 model in COMSOL.

Since the temperature is the most concerned factor of hotplate, which is highly related to Pt heater circuit geometry size and the substrate material properties in this case. It is significantly vital to detect the exact temperature of hotplate. But when the heater size is very tiny as sub-micro or nano scale, it seems impossible to measure the temperature by infrared detector or thermal sensors. Since Pt has highly linear temperature resistance coefficient, in this condition, it is strongly suggested to obtain the temperature by calculation from the measured changing resistance of Pt heater based on TCR properties. Pt resistance can be obtained by using equation:

$$R_{Pt} = \rho(T)\, \ell / A \qquad \textbf{3-23}$$

In which, ρ(T) is the resistivity corresponding to the temperature changing, ℓ is the length of Pt circuit, and A is the cross-section area of heater circuit.

Based on the material properties in COMSOL, Pt material resistivity follows:

$$\rho(T) = -4.447775*10^{-19}*T^4+6.694129*10^{-16}*T^3-4.107885*10^{-13}*T^2+5.233699*10^{-10}*T-1.927892*10^{-08} / 0.668 \qquad (160T\text{-}600T)$$

$$\rho(T) = 2.814022*10^{-17}*T^{\wedge 3}-1.600249*10^{-13}*T^2+5.552497*10^{-10}*T-4.84357910*^{-08}/0.668 \qquad (600T\text{-}2000T)$$

3-24

Then we have resistance ratio:

$$R(T) / R(0) = \rho(T) / \rho(0) = r \quad \textbf{3-25}$$

In which R(T) and ρ(T) are the resistance and resistivity of Pt at temperature of T, and R(0) and ρ(0) are the resistance and resistivity at the temperature of 0°C. The equation 3-25 is shown in Fig. 3.15:

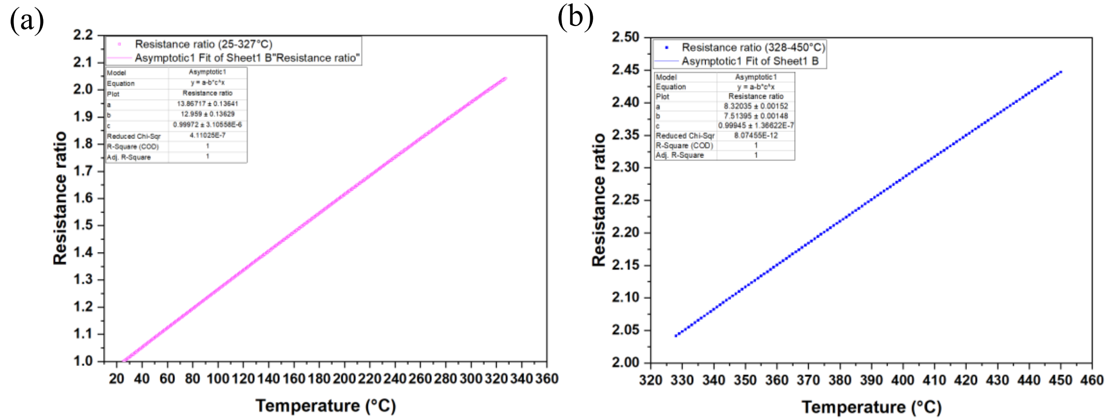

Figure 3.15 Resistance and temperature relationship in COMSOL.

By using this relation, we can calculate the operational temperature by considerinig r and the resistance value of Pt.

Additionally, if the operational temperature changes in a small range (under 450°C), we can use an experienced equation to calculate the Pt heater temperature:

$$R_T = R_0 (1+ 0.003 \cdot T) \quad \textbf{3-26}$$

In which, R_T denotes the resistance of the heater at working temperature, R_0 reprensents the resistance of Pt at 0 °C.

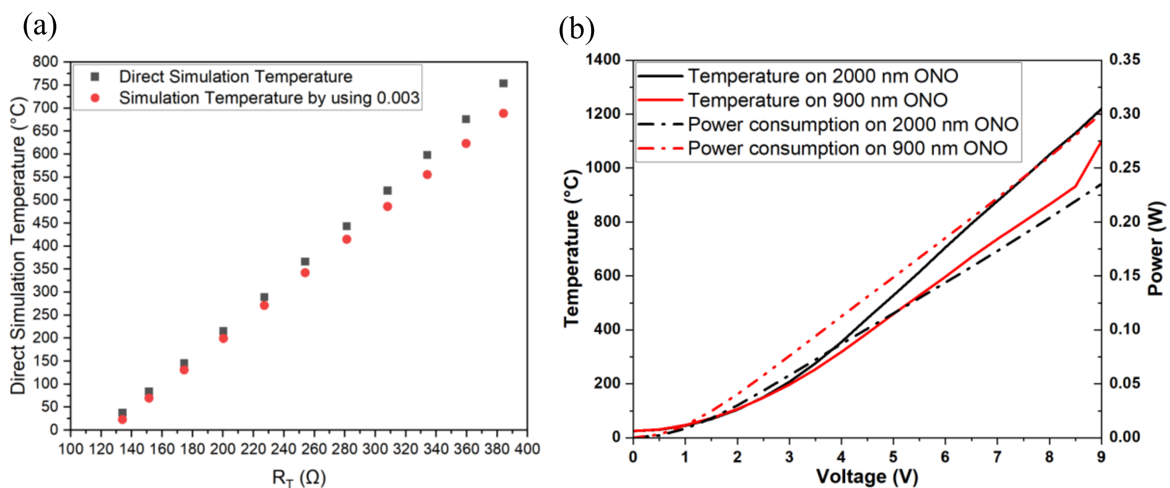

Figure 3.16 (a). Temperature comparison between COMSOL simulation and calculation by using TCR value; (b). Temperature simulation result affected by different insulation layer thickness at different input voltages.

Fig. 3.16a compares the temperature obtained by direct simulation on COMSOL software and calculation based on equation 3-26. In general, the SMOs gas sensor functions below 450 °C, so the temperature calculated by equation 3-26 is maximum around 25 °C lower than the simulation result in work condition. Fig. 3.16b reveals the influence of insulation layer thickness on the operational temperature and power consumption of NHP1. Because of the magnificent resist to the heat dissipation of ONO structure, higher working temperature and less power consumption can be obtained by thicker ONO layer at the same input voltage.

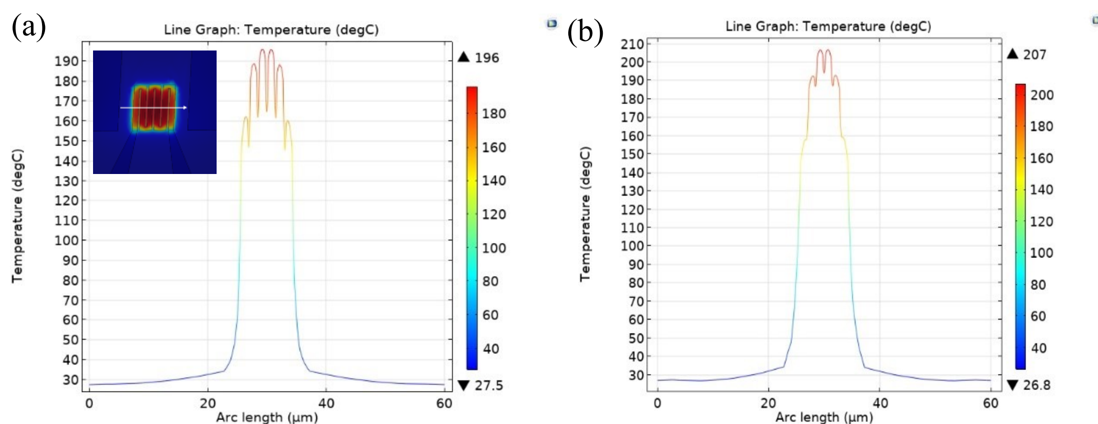

Figure 3.17 NHP1 model in COMSOL, and temperature uniformity on 900 nm ONO layer and 2000 nm ONO layer.

With comparison of Fig.3.17 b and c, it shows different temperature uniformity. For example, thinner ONO layer shows higher temperature drop than thicker ONO layer among the Pt heater circuit gap, which means larger heat dissipation by heat conduction along ONO stack structure. On one hand, it means thicker ONO layer can not only prevent the heat dissipation along the ONO layer longitudinally. On another hand, it can also promote the heat dissipation through the ONO stack structure horizontally. Alessio Giberti et al. also calculated the temperature profile in the non-heated zone of the membrane and along the z-direction under stationary conditions [17].

3.4.5 NHP2 Simulation Results

In the end, we designed another hotplate (NHP2) for normal usage, which has long electrodes to avoid any short circuit with suspended structure, the layout is shown in Fig.3.18.

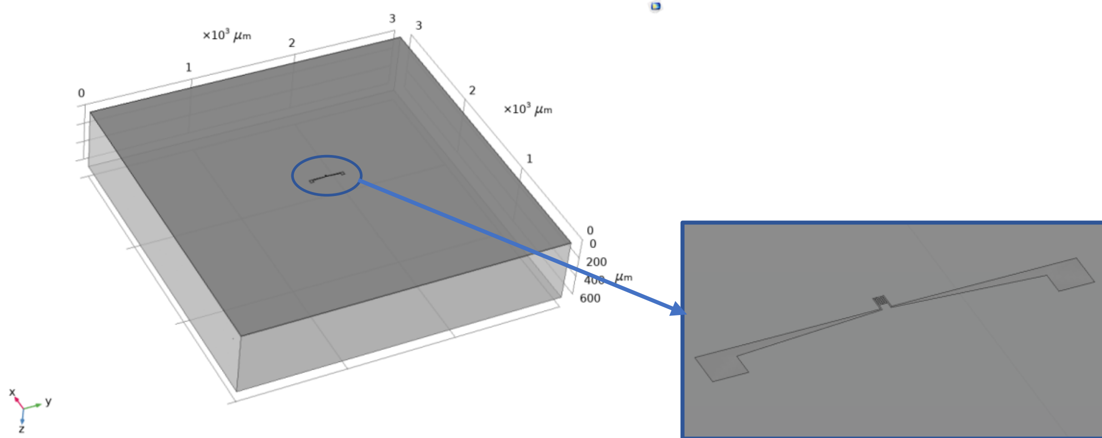

Figure 3.18 NHP2 model in COMSOL.

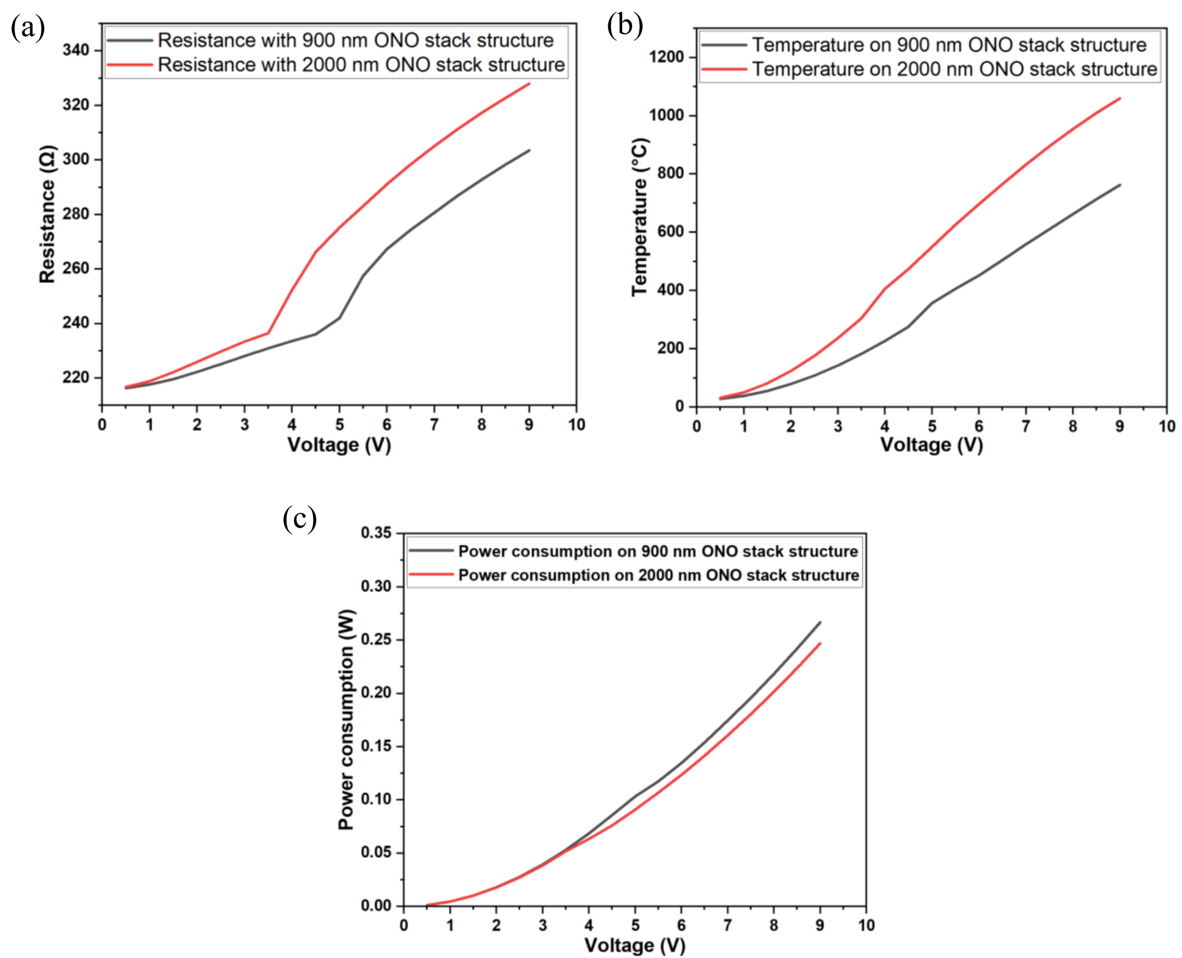

Figure 3.19 The resistance (a), operational temperature (b) and power consumption of NHP2 with different ONO layer thickness at different input voltages.

In this work, the influence of different thickness of ONO stack on the operational temperature and power consumption is compared. The temperature and power consumption are shown in Fig. 3.19. At voltage of 3V, the temperature is around 400°C, and the power

consumption is less than 0.1 W. NPH1 and NHP2 have the similar operation temperature and power consumption at the same input voltage due to the same heater circuit geometry, as compared between Fig 3.16b and Fig. 3.19.

In conclusion, firstly MHP1 model was simulated in order to calibrate the temperature and power consumption with the propriate boundary conditions. After the adjustment of the boundary conditions with the experimental data, the same boundary conditions are used to other different hotplate devices. The effect of suspended membrane and solid substrate structure on the operational temperature and power consumption at different input voltages is compared. It turns out suspended membrane structure significantly affects the operational temperature and power efficiency due to the high heat resist of the trench structure. However, the MHP1 cannot be heated above room temperature due to the huge heat dissipation. MHP2 is designed through downsizing MHP1 by 50 times. Less power is needed to achieve the same working temperature by heating up smaller hotplate, which also has higher thermal response. In the size of MHP2, even the heater on the solid substrate can be heated up above 500 °C. But the power consumption is still higher than MHP1 on suspended membrane structure, whose size is 50 times bigger than MHP2. The influence of the thickness of Pt circuit and insulating ONO stack structure on the highest obtained operating temperature is studied. Thicker ONO layer can cause higher temperature and power efficiency, thinner Pt circuit results in lower temperature and power consumption at the same input voltage. To optimize the best thickness for ONO layer and Pt heater, more parameters of the hotplate device should be considered. The suspended membrane structure effect on the mechanical properties of MHP2 is also investigated, which proves that the suspended membrane can inhabit the heat dissipation, and disperse the stress concentration around the heat source. NHP1 is obtained based on the miniaturization of MHP2, in this simulation example, the effect of ONO layer thickness on the temperature and power consumption is compared, NHP1 on solid substrate shows higher temperature and power efficiency than MHP2 on solid substrate. For example, at the input voltage, NHP1 exhibits 200 °C on 2000 nm ONO layer, and around 100 °C on 900 nm ONO layer. While MHP2 possesses 140 °C on 2000 nm ONO layer, and around 50 °C on 900 nm ONO layer. NHP2 is a common hotplate for wide application and for the fabrication process test, which shows similar operational temperature and power consumption to NHP1 at the same input voltage.

3.5 Hotplate Fabrication Process

Due to SMO materials stability, low cost, and ease of manufacture, it has been used for chemiresistive gas sensors for the longest and are currently used the most frequently [9–11]. Currently, SMO sensors are employed in a variety of applications, such as precision farming, disease screening, and air quality monitoring. SMO must be triggered at a specified operating temperature between 150°C to 450°C in order to function properly, providing for quick response and recovery duration as well as great sensitivity to target gases [14]. Typically, a heater built within the MOS sensors is used to generate heat. Therefore, one of the most important aspects to be taken into account is the power consumption of the hotplate on SMO gas sensor devices. For SMO gas sensor devices, high working temperatures are frequently provided using micro-hotplates (MHPs). MHPs are often heated via the Joule heating effect of a metal circuit (heater), which is powered with little power and has a very quick response time [15]. The portable application and operation at distant off-grid areas can be increased with the development of reduced power hotplate for SMO gas sensor devices [16]. Therefore, a key requirement for expanding the application of SMO sensors is to keep the hotplate operating temperature high while reducing power consumption.

MHP1 is the model of the hotplate that we are using in FBK laboratory. By comparing the experimental data of MHP1 with the results of the simulation, such as resistance and power consumption, we are able to alter the boundary conditions of the simulation until we get results that are as near as possible to the actual data. We built the MHP2 devices for the ZnO gas sensor using the specified layout, which is based on the modeling results discussed above. In addition, NHP1 and NHP2 devices are manufactured in an effort to improve the power efficiency even further. In this section, our work is presented in a chronological order; we begin with the most challenging aspect of the manufacturing process for NHP2 to get the fabrication experience, and then, using the knowledge and experience we gained from the beginning of the project, the fabrication procedure is optimized. Therefore, we began by fabricating the NHP2 device, followed by the NHP1 and MHP2 devices.

3.5.1 NHP2 Fabrication by Combining EBL and FIB Techniques.

Due to the rapidly advancing microelectromechanical systems (MEMS) technology, which enables specific geometric downsizing and structure bulk micromachining, silicon-based MHPs are now largely developed. By using MEMS techniques, the creation of closed-

membrane-type hotplates and suspended-membrane-type hotplates can produce microwatt-level power consumption. Additionally, MEMS exhibits outstanding benefits with the reduction of hotplate size into the micrometer range based on Si micromachining. For instance, H.R. Shwetha et al. used a suspended membrane etched from the silicon substrate's backside to obtain a power consumption of 5.85 mW at 300°C [20]. A. Bagolini et al. found that a 3 × 3 mm^2 heater made via photolithography could reach 450°C with rise and fall times of 1.06 and 1.14 seconds, respectively, from ambient temperature when powered by a maximum of 107 mW [21]. Through the use of the bulk micromachining technology, A. Singh et al. have created a microheater with a heating area of 250x250 μm^2 and a low power consumption (35mW) [22]. On a silicon platform, Jianwen Sun et al. examined a circular construction with an integrated micro-heater at input voltage of 2V, operating temperature of 100°C, and power consumption of 60 mW [23]. A platinum-resistor micro-hotplate with thermal long-term durability was presented by T. Schössler et al. [24]. Its operating temperature was about 250°C, and its power consumption was 50mW.

However, processing can easily destroy the hotplate suspended-membrane construction. The failure force of 900 nm thick closed-membrane-type hotplates with various planar sizes was tested by A. Gaiardo et al. They found a strong correlation between the membrane's lateral size and its mechanical strength and showed that, even at small lateral sizes, the force required to break the membrane is quite low (37 mN for 1.74x1.74 mm^2 membrane size) [25, 26]. The membranes cannot be further processed, including for the thick film deposition of MOS, because to their great fragility. Therefore, it is sometimes necessary to take into account bulk substrate with as little power usage as possible. For instance, Y. Wang et al. used the Langmuir-Schaefer approach to transfer the Au nanoparticles to the solid-substrate hotplate after having to spray their heterostructure sensing material Au/SnO_2:NiO onto the self-assembled Au nanoparticle arrays [27]. The heater and electrodes were printed using traditional lithography and loft-off procedures, the sensing materials were generated by thermal evaporation at 1000 °C on the solid Si-based substrate, and Phung Thi Hong Van successfully constructed networked nanowire sensors on Si/SiO_2 substrates [28]. On a bulk Si wafer covered in 500 nm SiO_2, Daihua Zhang et al. produced In2O3 nanowires before photolithography and electron beam evaporation were used to design the finger-shaped metal electrodes on top of the sensing material [29]. Given this possibility, the substrate cannot be a suspended-membrane structure. As a result, the only way to reduce power consumption is through miniaturization with high mechanical stability, which has been shown to be an

effective method for increasing power efficiency because it only requires a small portion of the device to be heated up, has a well-controlled temperature distribution, and responds quickly to thermal changes [30].

By downsizing the hotplate geometry, new MEMS production techniques are created to boost power efficiency. For micro- and nanofabrication in mass production, photolithography is a well-known ideal MEMS technique. However, because it requires mask designing and processing, often multiple masks are required, which results in high costs and lengthy processing times, it is not practical for making research prototypes. Additionally, photolithography equipment capable of lateral resolutions below 300 nm can be extremely expensive and unavailable to the majority of research labs. For making first prototypes, maskless approaches are appealing. Utilizing approaches for production without the use of masks is preferable when doing preliminary research activities. Modern electronics can swiftly design bespoke patterns on resist films thanks to the flexibility, masklessness, and direct writing of EBL. This allows the process to quickly inscribe patterns with individualized designs. Because the design and the substrate are so closely intertwined, it is necessary to do careful optimization of the processing parameters. However, in most cases it is extremely difficult or even impossible to establish the correct recipe for wide-size-varying patterns on the same layout that range from micro to nano level, particularly when dealing with uneven and dense pattern size distribution. When compared to the low-resolution areas, the dense patterns generally will be difficult to define due to undeveloped and underexposed or overdeveloped and overexposed effect. As a result, prior to constructing nano-size dense parts among micro-size patterns, it is imperative to investigate and consider all of the potential choices.

FIB instrument has been rapidly growing and is becoming an important tool in the micro and nano production industries because of its direct patterning capability, high resolution, precise control, and multi-role in the semiconductor industry. In spite of this, patterning with scanning FIB is a sequential process that is mostly dependent on the removal of material via ion sputtering at the micro-nano scale at the surface interface between the high-energy ion beam and the sample substrate. As a result, the fabrication of devices using ion beam lithography is a considerably slower process than using optical or EBL, but it does not require further steps after processing like developing and lift-off. This is due to the high ion doses that are required as well as the limited beam particle intensity.

Using a poorly focused/high intensity electron beam to create vast areas with low lateral resolution, such as pads for electrical contacts, EBL can be a faster maskless approach. FIB, on the other hand, can be used to shape the high-resolution structures. In order to create Pt hotplates for MOS gas sensors, the combination of EBL and FIB is investigated in this work: Prior to using FIB to specify the nano heater circuit components inside the hotplate, EBL is used to shape the micro pads for electrical contacts and the hotplate's main body. This hotplate is known as a nano hotplate since the heater's thickness is 120 nm and the device's minimum size is 550 nm (NHP).

The parameters have been established through testing and optimization for EBL, and the accelerated voltage and dose for FIB milling are based on calculations performed by the software SRIM (Stopping and Range of Ions in Matter) using the binary collision approximation Monte Carlo method, which can show the trajectories of the ions and the displaced atoms. The morphologies of NHP are then described using SEM, the milled surface and sputtering depth are investigated using AFM, and the SIMS result is examined to determine the distribution of cross-sectional ion implantation. Finally, electronic measurements are used to investigate how the resistance values and altering power consumption of NHP at various voltages change.

EBL experiment is operated in TESCAN machine, since PMMA A7 from MICRO CHEM company is used in the experiment, the resist exposure parameters of PMMA A7 are optimized based on the suggested recipe (E-beam dose: 5-50 μC/cm^2 depending on radiation source/equipment and developer used, Energy: 20-50 keV, higher energy for higher resolution). The exposure energy is set as 20 and 30 keV, and the current is set 1 nA and 500 pA depending on the layout structure. The EBL exposure doses are tested from a wide range in order to find the most appropriate one. For the FIB sputtering parameters, first we used the simulation software Stopping and Range of Ions in Matter (SRIM), which is used to simulate the ions interactions with the multilayer during ion beam sputtering. These simulations were essential to narrowing the range of beam parameters that were required to pattern the heating elements. After that, we attempted EBL to create the portion of the pads, and FIB to construct the part of the concentric center of the heater. For the result characterization, SEM was used to represent the morphologies, AFM was used to investigate the surface and the milling depth, and SIMS result was analyzed to detect the cross-section ion implantation distribution.

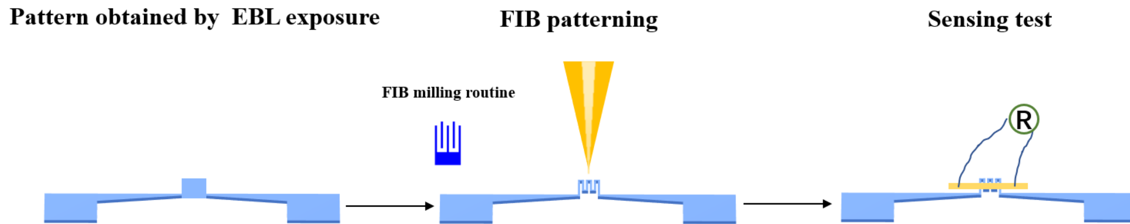

Figure 3.20. Heater circuit define by FIB.

The silicon-type substrate that is used in MEMS hotplates provides the mechanical support for the device. Since the hotplate operates at high temperatures, it must inevitably produce thermal stress, which might manifest as contraction and extension of the substrate. It is vital to integrate the layers that have a contraction force and the layers that have an extension force together so that the thermal stress is balanced. In addition, as silicon wafer is a highly conductive material both electrically and thermally, it is not acceptable to fabricate the NHP circuit directly on pure silicon wafer. Since heat dissipation can be accomplished through heat conduction, heat thermal diffusion and radiation, it is necessary to restrict the heat consumption from these orientations. Additionally, the power efficiency of the NHP is one of the most significant elements that should be considered. Therefore, the NHP should be built on an insulating wafer that has a high thermal resistance and is mechanically robust. Additionally, the thermal and electrical conductivity of the wafer surface should be tailored appropriately. Insulating materials such as SiO_2 and Si_3N_4 find widespread application in the MEMS industry. Since the SiO_2 layer possesses the extension force and the Si_3N_4 layer possesses the contraction force, combining these two layers and changing their thickness could result in a structure with zero stress. It has been demonstrated that a stack structure composed of $SiO_2/Si_3N_4/SiO_2$ known as an ONO stack may effectively support electrical devices. Because of their high resistance to electric conductivity and thermal conductance, SiO_2 and Si_3N_4 are both potential alternatives for the passivation layer that will support the heater circuit. The stack structure of (ONO) was realized by Plasma Enhanced Chemical Vapor Deposition (PECVD) on a SEMI 6 inch silicon wafer with crystal orientation <100> in the Micro-nano Characterization and Fabrication Laboratory of the Bruno Kessler Foundation (FBK-MNF), as discussed in the beginning of this chapter. This was done to compensate for the residual stress of SiO_2 and Si_3N_4 materials.

Controlling and measuring the operational temperature of the hotplate is the most crucial aspect of this appliance. Plenty of heater circuit materials have been widely investigated, such as SiC, Pt, poly-Si, and TiN [22-26]. Due to the fact that our dimensions are on the micron scale or smaller, it is highly improbable that the temperature can be measured using thermal meter equipment such as a thermal imaging camera or an infrared detector. Platinum was chosen as the material for the NHP circuit due to its remarkable chemical stability and perfect temperature coefficient of resistance (TCR). The TCR estimation appears to be a straightforward method for calculating the temperature based on the values of the input voltage and resistance. At high temperatures, the adhesion between the Pt layer and the SiO_2 or Si_3N_4 layer is ineffective. This is especially the case when the temperature is lower. The Pt layer and the ONO layer need an adhesive layer in order to achieve the desired level of adhesion. Several research works have studied the adhesion solutions by inserting an adhesive layer, such as Ti, SiO_2, and Ta [27, 28]. For example, Timo Schössler et al. sputtered 140 nm Pt thin film on SiO_2/Si_3N_4 and SiO_2 layer stack directly, and above the Pt film, it was covered by SiO_2 layer. After it annealed at different temperature of from 100°C to 800°C, it turned out that the TCR value increased with enlarging the calcination temperature. Wide range annealing temperature changing did not affect element composition distribution in the cross-section area. When the working temperature was 140°C, it could last for more than 1000 h duration time [6].

Before the Pt/Ti was deposited, one experiment was handled to test PtO adhesion layer between pure metal Pt and SiO_2 insulating layer in order to find another way for enhancing the adhesion between PtO and SiO_2. Sputtering machine was used to deposit PtO and Pt, and the parameters were set as: Ar flow 40 sccm, O_2 flow 10 sccm for PtO, holder rotate speed was 15 rpm, power generator was 500 V and current was 500 mA for Pt and 605 mA for PtO deposition. Deposited Pt thickness was 100 nm and PtO thickness was 20 nm. We compared three groups: 1. Pt on SiO_2 layer, PtO on SiO_2 layer and Pt/PtO on SiO_2 layer. These three groups of samples calcinated at 300°C, 450°C and 600°C in the air, and the results are shown below:

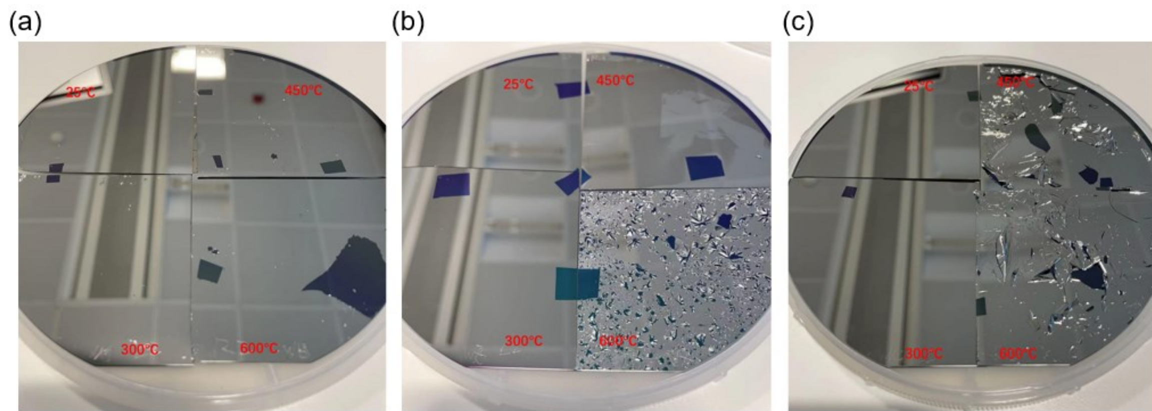

Figure 3.21 (a) Pt on SiO_2; (b) PtO on SiO_2; and (c) Pt/PtO on SiO_2 at different calcination temperature.

It is clear that when the calcination temperature is under 300 °C, the adhesion between Pt or PtO and SiO_2 was stable, but when the calcination temperature was above 450 °C, Pt/PtO sample showed very serious peeling effect, Pt and PtO could still be sticky onto SiO_2 layer. By increasing calcination temperature to 600 °C, PtO was also peeled off from SiO_2 surface. Even though Pt was held on the surface of SiO_2 after 600°C calcination, but it was easy to remove Pt from SiO_2 by tape. This experiment demonstrates that Pt/PtO system cannot work for our gas sensor heater system, so we selected Pt/Ti system as our heater and electrode system [29].

Since the hotplate size is very small, especially for the heater part, the structure is very dense. To define the structure fine, we fabricated the device in two steps: 1. The electrode part was defined, and Pt/Ti was deposited on this part; 2. The heater part was defined by FIB milling. Detailed fabrication process is shown in Fig 3.2.

Before resist was spin coated on the wafer, the surface of substrate should be cleaned. Acetone/isopropanol were used to remove the dust contamination and organic residue, and O_2 plasma was used to eliminate the polymer residue. After this clean process, the positive resist PMMA was spin coated at speed 4000 rpm/min using a coater machine (PMMA A7, Micro Chem) on the wafer substrate that was created in the first phase, and then a hard bake was performed at a temperature of 180 °C for 60 seconds. Second, in order to expose the architecture of hotplate device, this wafer was moved into an EBL machine of TESCAN. The exposure parameters (such as energy, step size and dwell time and doses) were optimized in FBK clean room CR D for PMMA A7, which called for an energy of 30 keV and doses of 750, 800, and 850 C/cm^2. Following this step of exposure, the wafer went through a soft bake at a temperature of 120 °C for 1 min, and then it was transferred to an

electron beam evaporation machine, where an adhesion layer of titanium with 10 nm thickness, and a heater layer of platinum with 100 nm thickness were deposited. The lift-off procedure was then carried out in an acetone solution at a temperature of 40 °C, and the treated wafer was afterwards washed in isopropanol. In the end, the wafer was placed through calcination and metallization in an oven (Expertech CTR 200, Expert Semiconductor Technology, Inc., Scotts Valley, California, USA) at a temperature of 650 °C for a period of two hours under a nitrogen atmosphere.

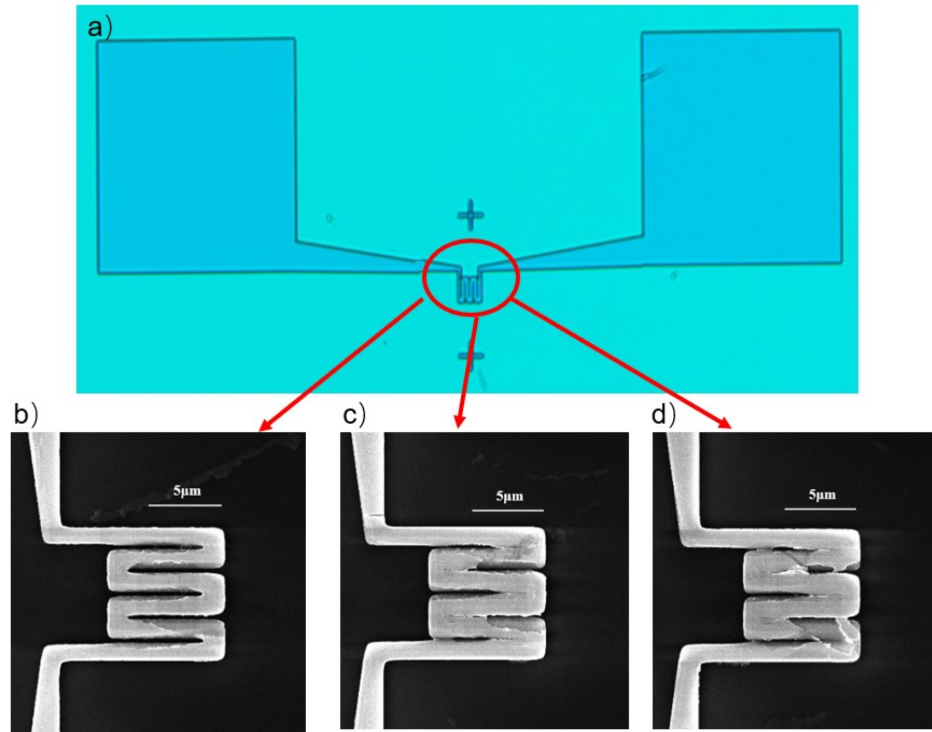

Figure 3.22 NHP2 heater part patterned by solo EBL technique with different doses of 750 μC/cm^2, 800 μC/cm^2, and 850 μC/cm^2.

We have designed three layouts for NHP2 hotplate device for different application purposes, but the heater part size is the same, as shown in Fig.3.20. To begin, we attempted to define the entire structure of NHP by just using the EBL technique. The results of this effort are displayed in Fig. 3.21, along with the NHP devices that we produced. We conducted experiments at 30 keV with dosages of 750 C/cm^2, 800 C/cm^2, and 850 C/cm^2 using PMMA that was acquired from Micro Chem and following the recipe for PMMA A7. It is abundantly obvious that the electrode parts were defined very clear, but a dose of 750 C/cm^2 was insufficient to completely define the NHP2 heater portion. Because of the proximity effect, the merge in the heater circuit occurred when the dose was increased to 800 and 850 C/cm^2. When higher doses administered, the gap distance became smaller, which increased the risk

of a short circuit. Additionally, the other components of the heater, such as the legs, were designed and perfected, which indicated that the required amount of energy and dose for the exposure of a structure with this size. On the other hand, the nanoscale heater part structure was not something that was anticipated. When working with an uneven pattern size and density, correction of the proximity effect is an absolute necessity for high-resolution e-beam lithography. This is especially true when the pattern size varies.

Then, in order to pattern the NHP2 structure clearly, we combined the EBL tool and the FIB machine together. Following the application of EBL to describe the electrode section and heater region, FIB was then utilized to design the heater circuit, as shown in Fig.3.18. Before beginning to mill the heater portion using FIB, SRIM simulation was conducted in order to determine the proper milling dosages and energies of FIB. The relationship between the milling depth and energy were explained as follows:

$$H = \frac{IF * SY * M}{N_A * \rho} \quad \textit{3-27}$$

H = Sputtered thickness;
IF = Ion fluence (ion numbers/cm^2) = 1* 10^{16};
SY = Sputtering yield = sputtered atom numbers/incident ion numbers;
M = 195.08 g/mol sputtered Pt atom molar mass (g/mol);
ρ = 21.45 g/cm^3 (Pt density);
N_A = Avogadro Constant = 6.02 * 10^{23} mol^{-1}.

Sputter yield SY is defined as the number of atoms expelled from the target surface per incident ion, and the factor sputtering yield takes into account the Coulomb force that exists among ions. It is clear from the equation that the ion fluence as well as the features of the target material have an effect on the sputtered thickness. The target layer of platinum has a thickness of 120 nm, and in order to sputter a film of that thickness, we need to determine the needed type of ion sources as well as the required ion dosages at a given input energy. Our research involves simulating the sputtering process, and we do it by employing a piece of software called SRIM, which is based on the Monte Carlo method. SRIM is a quantitative simulation of the process of ion beam sputtering. This simulation assures ion-solid interaction with aberrations and Coulomb repulsion forces in surface treatment and sculpting under a variety of input energies and beam currents. The results of the simulation of the link between the energy and the ion dosages of gold and silicon are depicted in Figure 3.19.

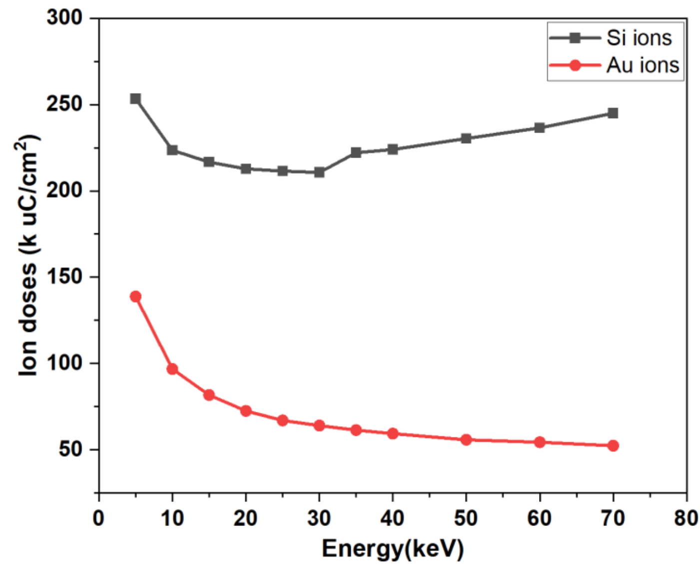

Figure. 3.23 Silicon and gold ion doses vs. ion energies for 100nm Pt layer milling

The amount of ion doses that are required to mill a platinum layer that is 120 nm thick varies depending on the energy. It is abundantly obvious that a greater ion energy calls for lower ion doses in order to remove a Pt layer with thickness of 100 nm. Due to the fact that silicon ions have a relatively low mass in comparison to gold ions, nearly twice as many silicon ions at the same energy level are required to bombard a target layer of platinum that is the same thickness. Because a higher ions dose milling contributes to a more severe proximity effect and redeposition, and a higher ion beam energy results in a smaller scattering angle, the end result is a more concentrated beam due to forward scattering at small angles, which has the additional benefit of reducing chromatic and space charge aberrations. For a more precise sputtering procedure, high energy and low dosage are typically used. Both the energy and ion fluence parameters of our apparatus are possible to be adjusted. Because of this condition, the source of the auger ions is favorably selected with a high energy. On the basis of the simulation result obtained from SRIM, Au ions with 60, 75, and 90 k μC/cm2 were finally tested at 70 keV at the beginning of this work. Many scans of an ion beam can lower the residence duration at each sputtering point. Additionally, multiple scans can sputter off those redeposited atoms from earlier sputtering, which results in significantly less redeposition of sputtering atoms compared to a slow and single scan. In addition to that, different loops milling (1, 10 and 100 loops scanning) was studied.

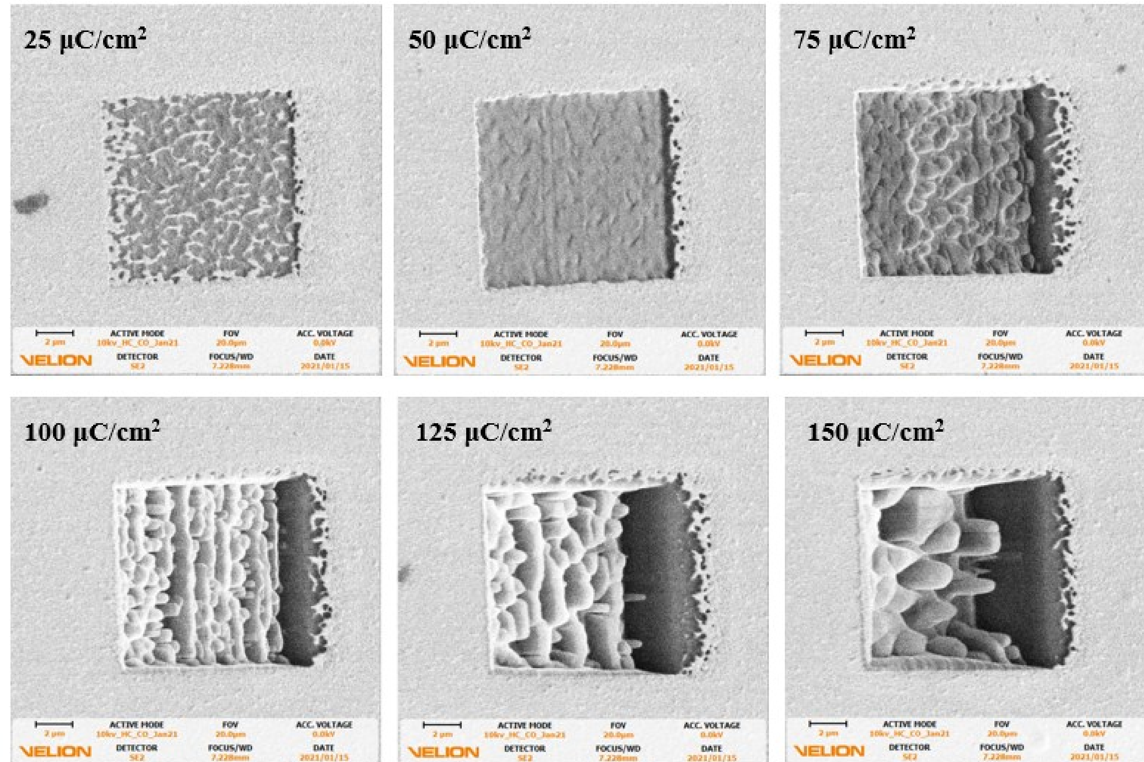
(a)
25 µC/cm²
50 µC/cm²
75 µC/cm²
100 µC/cm²
125 µC/cm²
150 µC/cm²

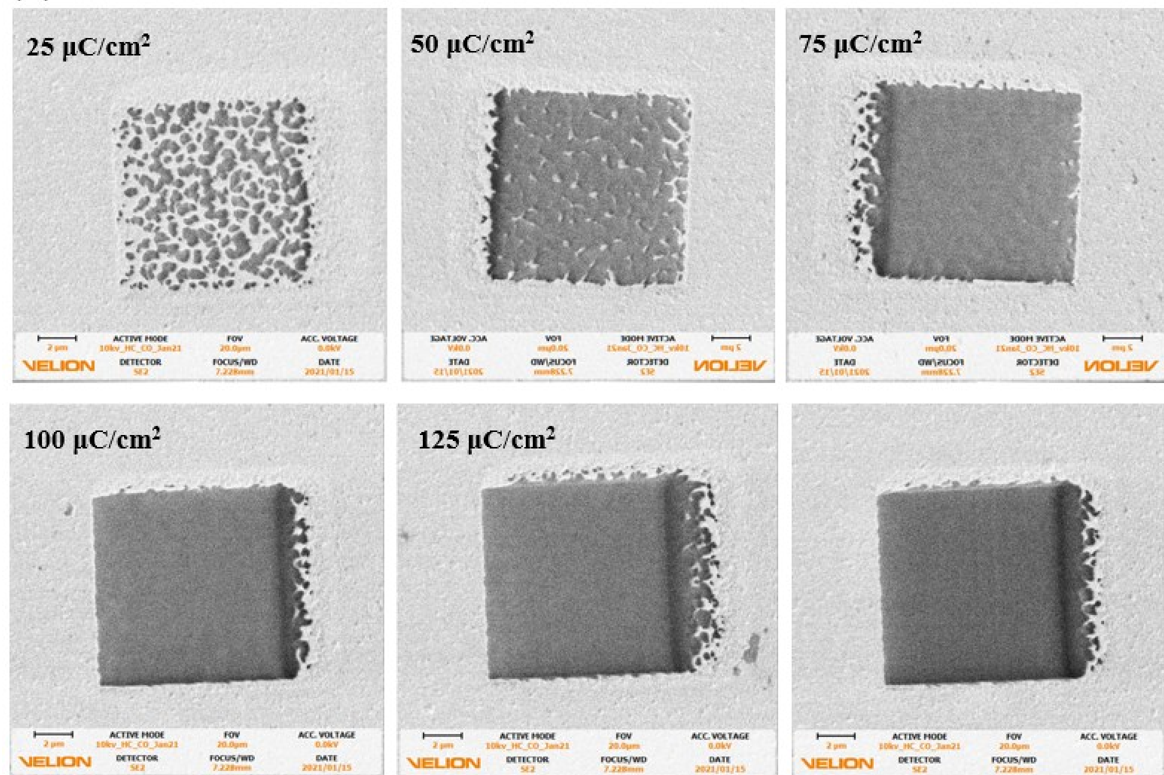
(b)
25 µC/cm²
50 µC/cm²
75 µC/cm²
100 µC/cm²
125 µC/cm²

(c)

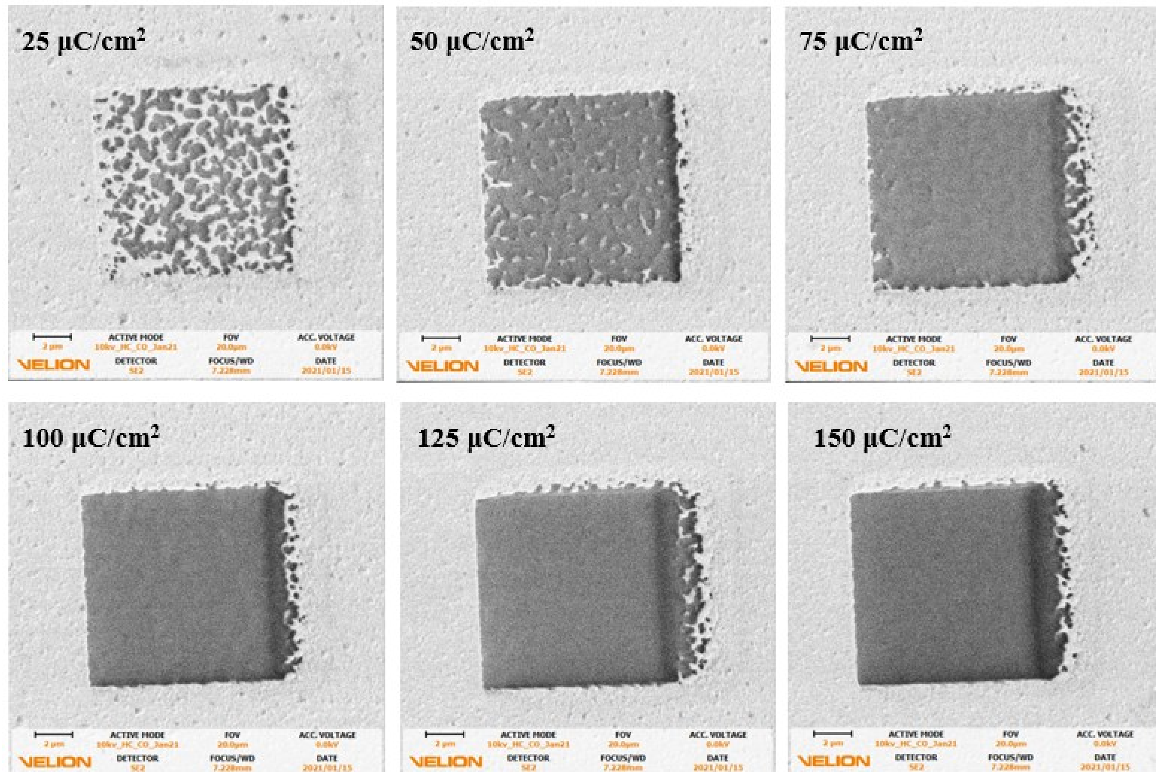

Figure 3.24 Au^{++} ions milling square by FIB on Pt film with doses of 25, 50, 75, 100, 125, 150 µC/cm^2 at one loop (a), 10 loops (b) and 100 loops (c).

After we set down the milling parameters of voltage and doses for Au^{++} ions by FIB, we tested the mill parameters on Pt film by milling a square of 10x10 µm^2. During the FIB sputtering process, the beam of Au ions that impacted the surface of Pt caused some of the Au ions to pass through the Pt layer and become trapped within the Pt layer. While other Au ions conveyed the kinetic energy, they also bombarded a significant number of regenerating platinum atoms. After receiving an adequate amount of energy close to the surface of the Pt film, the Pt atoms eventually became sputtering atoms because they detached themselves from the surface energy binding and entered free space. The Pt atoms that were sputtered landed in the area close to the milling area that generates the redeposition zone. Fig. 3.24 shows the Au^{++} ions milling result by FIB on Pt film. In one loop milling, the milling result can be seen from Fig.3.24a, the depth increased by increasing the milling doses. Same results happened in 10 and 100 loops scan milling. By comparing Fig. 3.24 (a), (b) and (c), it is clear that the roughness is totally different at the same doses but with different milling loops. More loops milling, smoother the surface is. Loop 10 and loop 100 milling results are quite similar to each other, hence, for the following work we only compared 1 loop milling and 10 loops milling results.

(a)

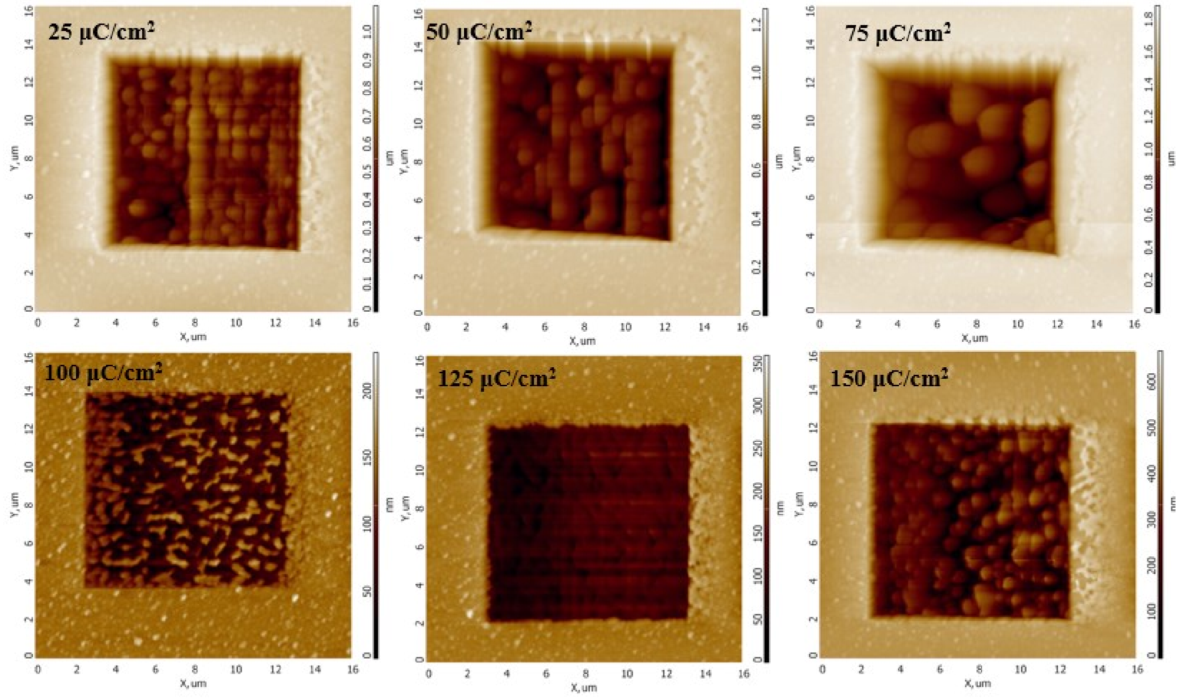

(b)

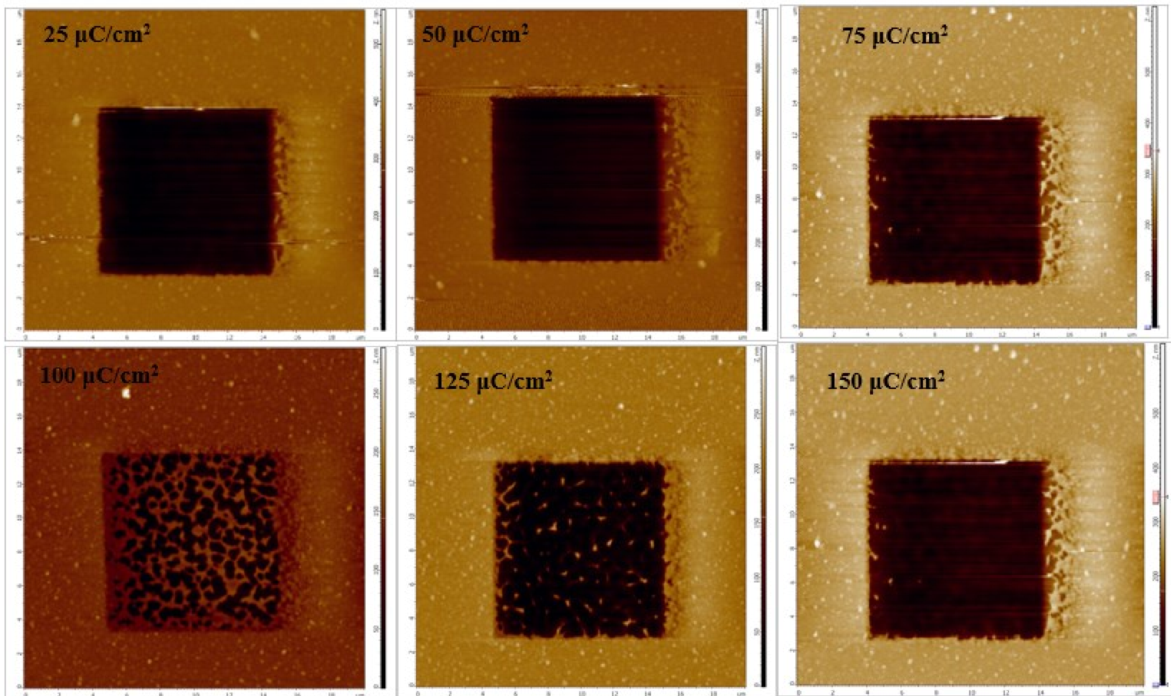

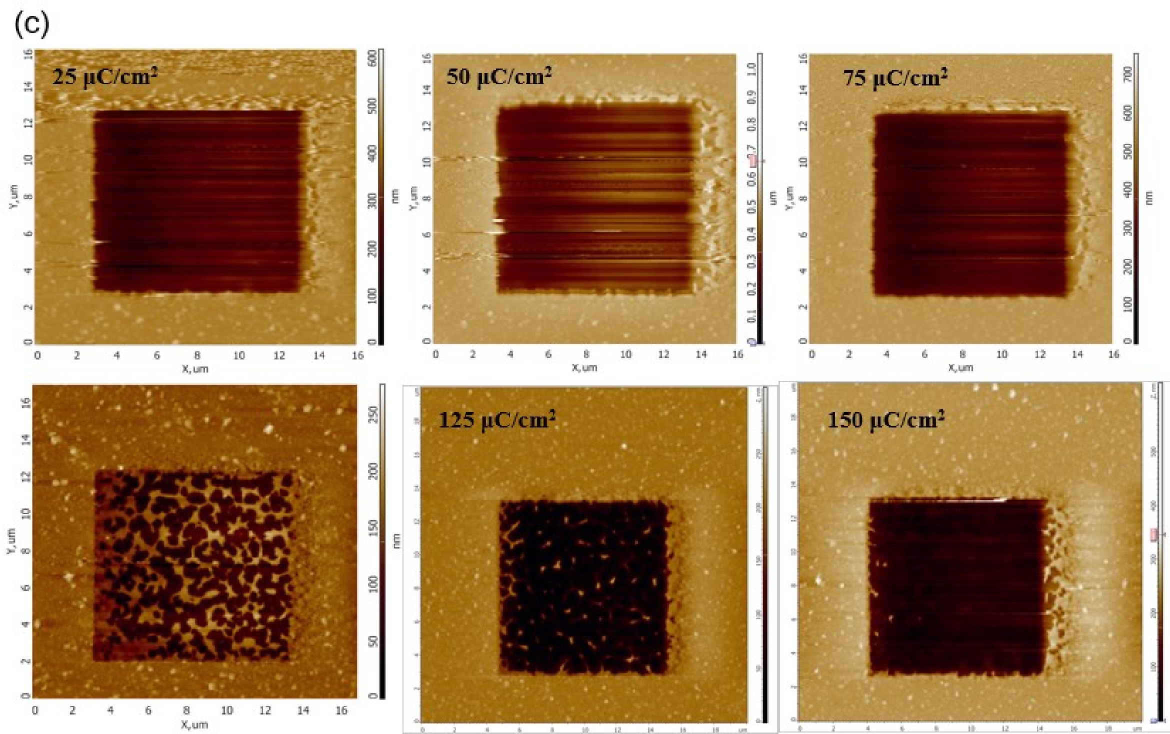

Figure 3.25 a) AFM result of Au^{++} ions milling squares by FIB on Pt film with doses of 25, 50, 75, 100, 125, 150 µC/cm^2 in 1 loop (a), 10 loops (b) and 100 loops (c) milling at energy of 70 keV.

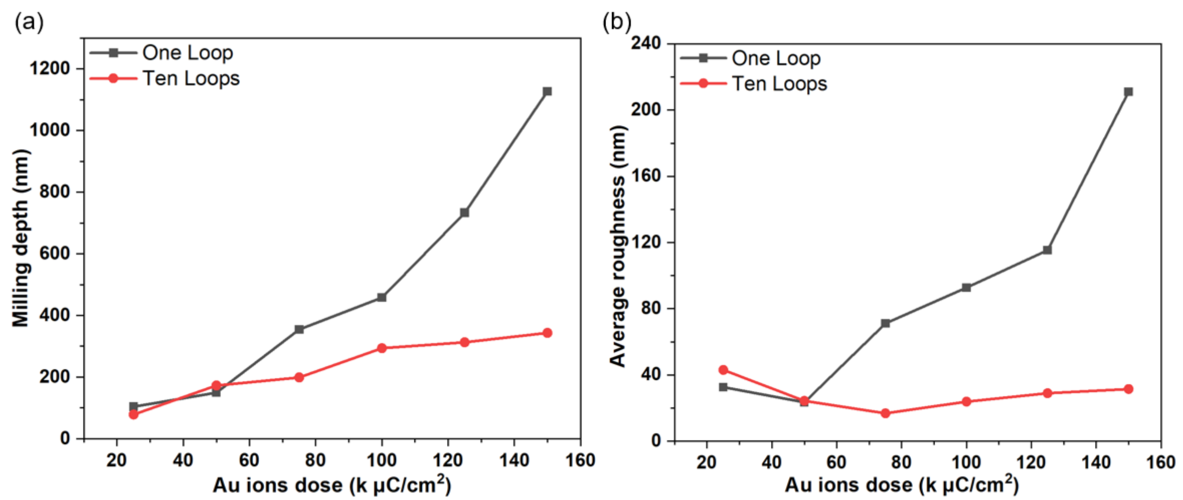

Figure 3.26. AFM results of milling depth (a) and roughness (b) of Au ions beam milling on Pt film with different doses and loops at energy of 70 keV.

Using AFM, we were able to characterize the surface topography of the milling area. AFM images revealed the results of the sputtering process, in which it was simple to observe that the sputtering area grew rougher as the dose was increased (seen in Fig. 3.25 a, b, and c). In addition, it was revealed among Fig.3.25 that increasing the milling doses resulted in an increase in the depth of the grinding zone. When the sputtering energy and dose are equal, it is clear that increasing the number of milling loops from one to ten results in a surface with

a smoother texture. This is due to the fact that the multi scan decreased the amount of time an ion beam spent dwelling at each sputtering location, which resulted in a significantly lower rate of redeposition of sputtering atoms. The precise milling depth and roughness of the region was illustrated in Fig. 3.26. According to Fig. 3.26, an increase in the ion dosage led to a linear rise in the milling depth, and higher doses combined with a single milling loop led to a deeper trench and a rougher surface while maintaining the same milling dose. A greater ion dose causes a slanted wall to form on the side of the beam movement that is opposite from it. It became increasingly difficult for atoms to escape the trench as the depth of the trench increased. It is impossible to remove the atoms that have been sputtered because they are not in a state of thermodynamic equilibrium, and they have a tendency to condense once more on the surface.

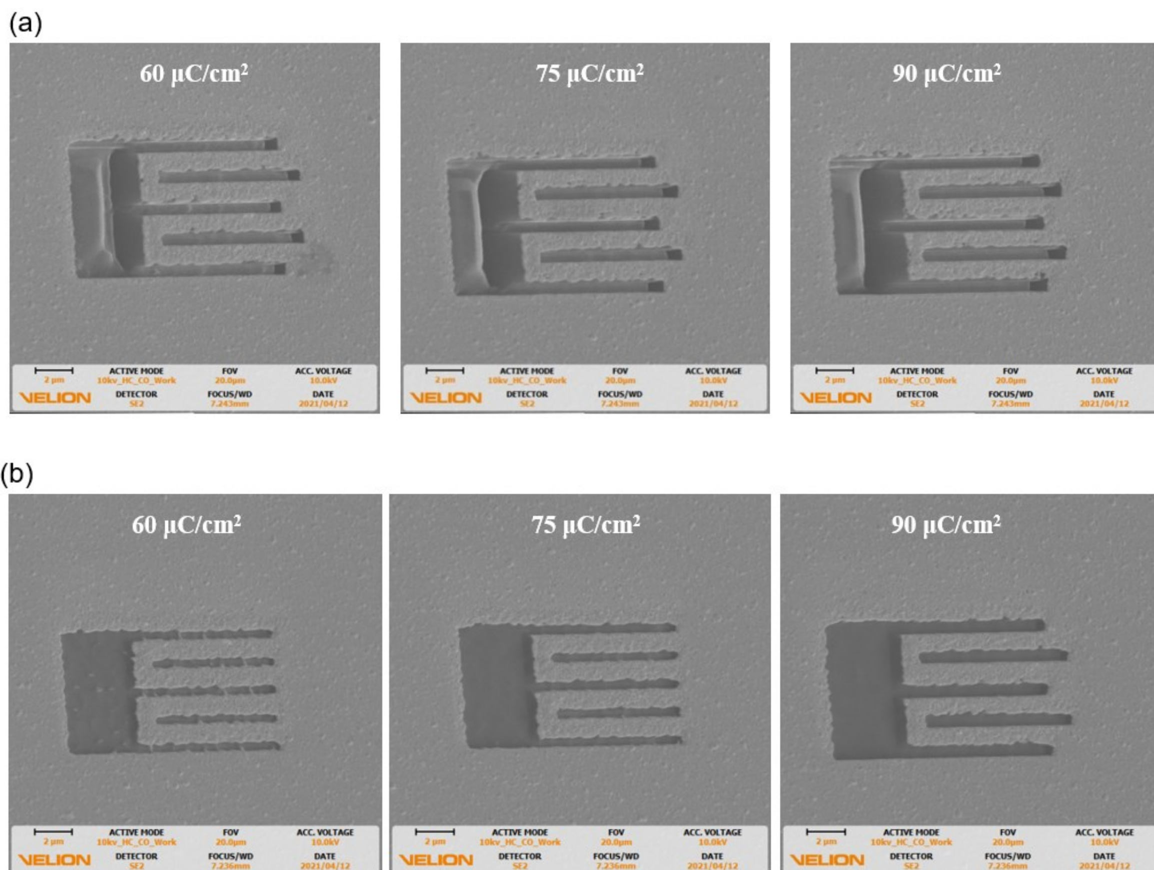

Figure 3.27 FIB milling routine at 60, 75 and 90 μC/cm^2 at one loop (a) and ten loops (b).

Finally based on the AFM results, we chose Au^{++} ions at 70 k eV with doses of 60, 75 and 90 μC/cm^2 to mill Pt layer by following the milling routine mentioned in Fig. 3.20. The milling routine results are shown in Fig. 3.27. The results are corresponded to the above-

mentioned milling results, 10 loops scan milling resulted in flatter surface than 1 loop scan milling.

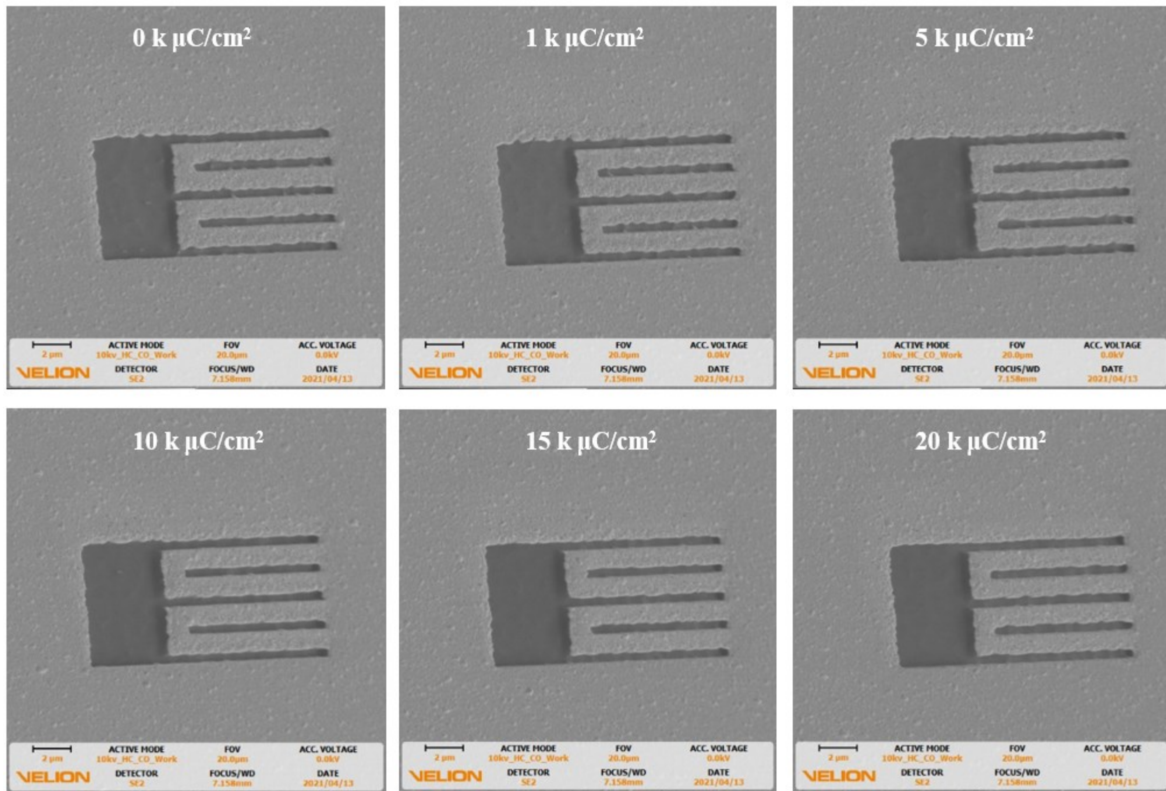

Figure 3.28. Si ions milling surface modification with doses of 0 k μC/cm^2,1 k μC/cm^2, 5 k μC/cm^2, 10 k μC/cm^2, 15 k μC/cm^2, 20 k μC/cm^2.

To flat the bombardment surface by Au^{++} ions milling, lighter ions of Si^{++} was used to smooth the surface with different doses of ranging from 1k μC/cm^2 to 20 k μC/cm^2. Fig. 3.28. represents the surface modification result by Si^{++} ions milling. Actually, when the milling dose of Si^{++} ions was higher than 15 k μC/cm^2, the surface roughness was quite stable.

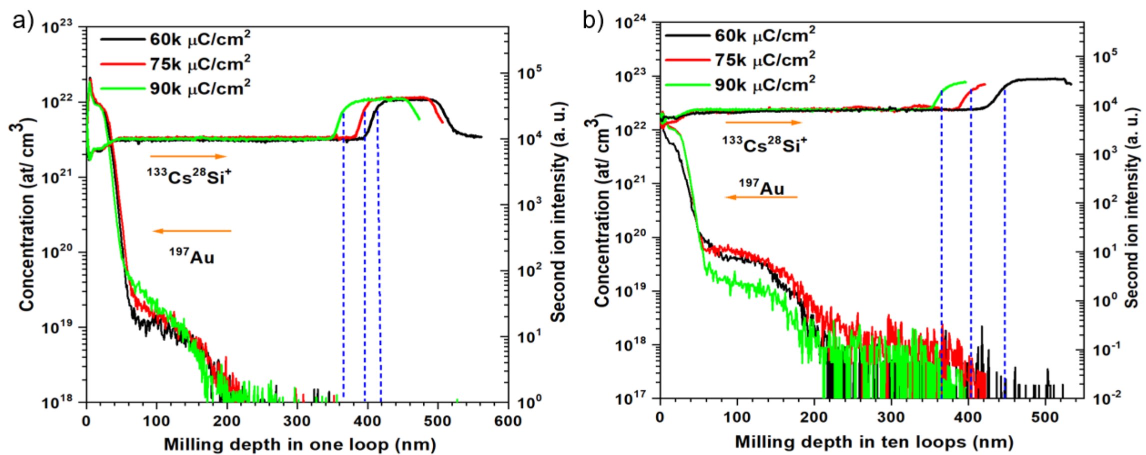

Figure 3.29. Au element distribution and Si ions intensities after Au++ milling on samples wafer with different doses at 1 (a) and 10 (b) loops.

It is possible for a large number of recoiling atoms, ions, and electrons to be produced concurrently when an ions beam is used to bombard a sheet of platinum target material. These recoiling atoms transfer their kinetic energy to the atoms around them, which in turn activates further atoms. After accumulating a sufficient amount of kinetic energy, it is possible that some of the recoiling Pt atoms will separate off the Pt target surface and enter the surrounding space. Some of the recoiling atoms that do not have enough kinetic energy will be redeposited on the surface. Secondary ions mass spectrometry, also known as SIMS, was applied during our work in order to investigate the atomic distribution on the target surface in the cross-sectional structure. Fig. 3.29 displays interlaced SIMS depth profiles of the deposited Pt film. First, in order to get samples ready for SIMS analysis, we milled a reference sample with Au^{++} ions source by FIB at a concentration of $5x10^{+16}$ at/cm^2 and 70 keV. After this step, we were able to make the necessary adjustments to the sensitivity factor RSF for the Au atomic concentration measurement on the samples. The same FIB parameters were used with doses of 60, 75, and 90 k μC/cm^2 at 70 keV in one and ten milling loops to create a milling crater that was 200 x 200 μm^2 in size. After the Pt material was removed with Au^{++} ions milling by FIB, the Au ions could be also implanted within the Pt layer as well as the substrate layer, if the Au^{++} ions energy was enough. The outcomes of milling were reflected in the thickness distribution of the Au. Cs^+ ions were blasted into this crater zone as part of SIMS in order to promote the formation of Au and Si secondary ions. In order to obtain the correct SIMS sputtered depth, the depth of each pristine crater was subtracted from the depth of the final matching crater. This was done after the Au milling process and prior to the SIMS sputtering process. The signal for $CsAu^+$, which represents secondary ions, has been translated to the signal for $CsSi^+$ point by point. All of the other ion species have been point-by-point standardized relative to the Cs^+ secondary ion signal (expressed as the number of secondary ion counts per second, or cts/s).

Figure 3.29 depicts the distribution of the Au element content as well as the intensity of the Si ions in samples with variable doses at one and ten loops. Based on the element concentration distribution curves of gold, it is simple to deduce that most of the gold is found on the surface of the crater at a thickness of less than 20 nanometers; this could be a layer of gold that has been redeposited. The resistance measurements provided evidence that a coating of gold with 20 nm thickness did not result in a short circuit under any circumstances. As it progressed deeper than 20 nm thick, the concentration of gold began to decline in a

significant way. The $CsSi^+$ intensity is constant in the beginning of the $CsSi^+$ curves, with the exception of the crater surface area; this indicates that the SIMS sputtering was performed in the same layer. After that, there is a bump, which indicates that SIMS sputtering was performed in a different layer. Given that the thickness of this layer is around 200 nm, it can be deduced that the milling depth reached the Si_3N_4 layer beneath the initial layer of SiO_2. It means that the Pt/Ti layer has been eliminated in its entirety. In the secondary ion intensity curve, the distance of the straight horizontal part actually corresponds to the thickness of the left top SiO_2 layer. Higher dosages of milling show less of the left SiO_2 layer, and the thickness changing of the left top SiO_2 layer for 75 and 60 k μC/cm^2 milling is approximately the same value of 36 nm when compared to 90 k μC/cm^2 for the 10 loops, but for one loop milling the change is smaller.

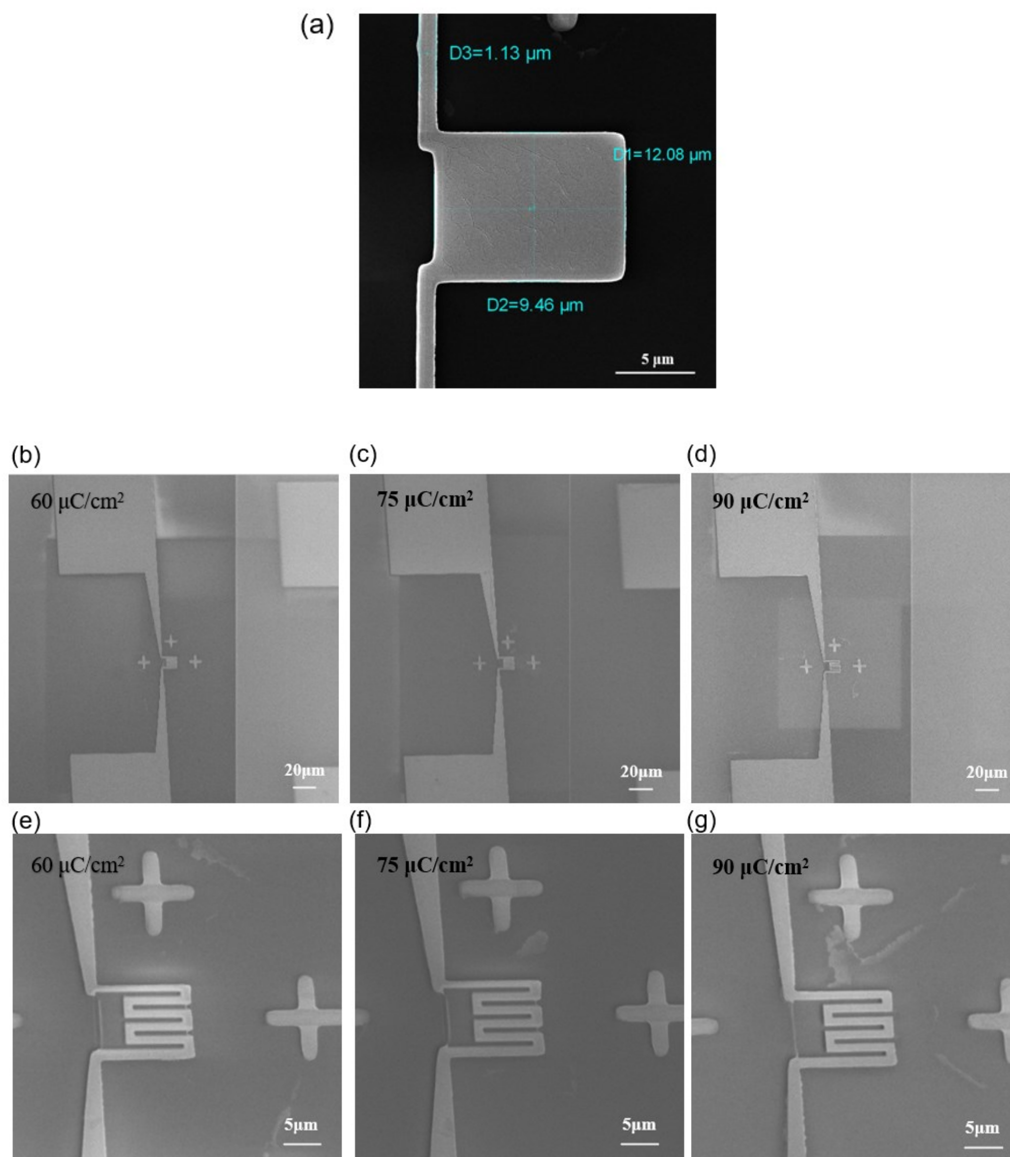

Figure 3.30. FIB-SEM images of the NHP2 fabricated by FIB Au ions milling at 60, 75 and 90 k μC/cm²

Au^{++} ion milling by FIB at dosages of 60, 75, and 90 k μC/cm² at 35 keV is effective for sputtering 120 nm Pt layer, according to the results of AFM and SIMS characterization. The circuit topology of the previously evaluated FIB milling technique featured a nanoscale gap, and this could have an impact on the redeposition effect [34]. After obtaining the heater area part using the EBL technique, the results are compared using Au^{++} ions with dose parameters of 60, 75, and 90 k μC/cm² at 35 keV in ten-loop mode milling. The results are then characterized using FIB-SEM, as shown in Fig. 3.30. In Fig. 3.30 a and b, there are still some small connections between the heater circuit gap with milling doses of 60 and 75 k μC/cm², which could lead to a short circuit. The appropriate structure in Fig. 10c demonstrates that the required ions dose is 90 k μC/cm².

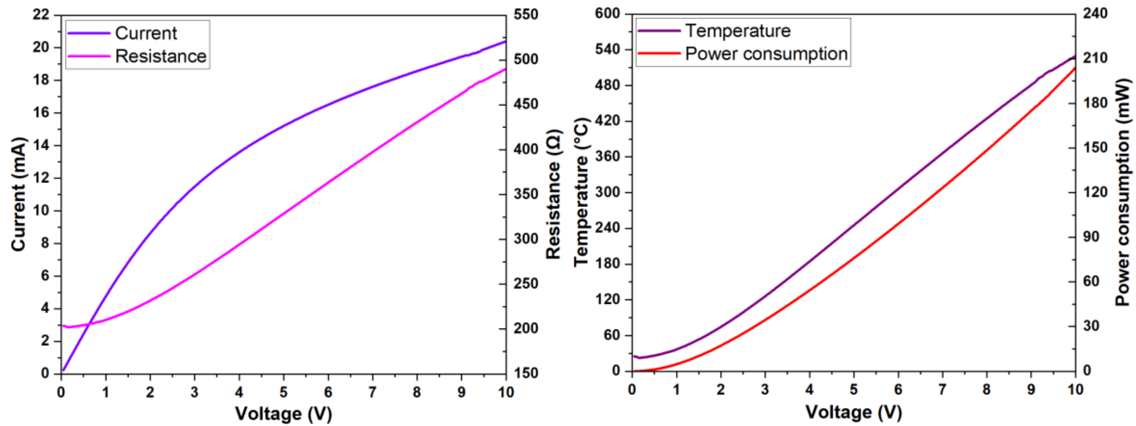

(a) (b)

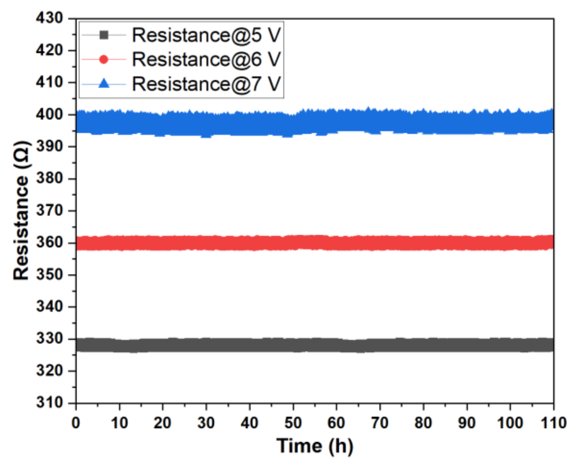

(c)

Figure 3.31. Electrical properties measurement a). The resistance and current of NHP device at different input voltages; b). Working temperature and power consumption of NHP devices at different input voltages; c). Resistance repeatability of NHP at high input voltages of 5 V, 6 V and 7V.

The Agilent 4156C-equipped Karl Suss Manual Probing Station PM8 was used to measure the resistance of the NHP2. To increase the power efficiency of NHP2, it has been scaled down and is intended for the application of MOS gas sensors. The resistivity of the NHP2 that was created utilizing FIB Au^{++} ion dosages of 90 k μC/cm^2 at 35 keV was eventually measured. The resistance and current of the NHP device were measured by using various voltages, as shown in Fig. 3.31a and b. Using the TCR measurement of Pt, which is as follows, one can determine the temperature of NHP induced by the Joule heating effect.

$$R_T = R_0 (1 + 0.003T) \qquad \textbf{3-28}$$

In which T is the current temperature, R_0 is the resistance at absolute zero, and R_T is the resistance at a specific voltage. The resistance of NHP2 is 203.57 Ω at 0.05V, which is regarded as being at room temperature. R_0 is calculated as follows: 203.57 / (1+0.003 x 25 °C), and is 189.36 Ω. This equation can be used to calculate the temperature, which is represented in Fig.3.31b from 0 V to 10 V. Due to their linear relationship, which is revealed by equation 3-28 by raising the input voltage, the resistance of NHP changing trend is compatible with the temperature changing trend.

The test environment is maintained at a constant relative humidity of 40% RH and room temperature of 25 °C with various input voltages (5V, 6V, and 7V) for 110 hours in order to measure resistance repeatability. Fig. 3.31c displays the resistance values of the NHP2 at various input voltages. When NHP2 is operating at 5 V, the resistance change range is 2Ω, indicating 0.6% resistance value drift and 3.5 °C in temperature inaccuracy. When the voltages are 6V and 7V, respectively, the temperature inaccuracies are 4.39 °C and 8.79 °C, while the resistance values are shifted by 0.7% and 1.4%.

3.5.2 NHP1 Fabrication in Two-step by EBL

FIB technique is a state-of-the-art process for defining the nano/micro structure, but it requires much time to finish one process. Hence, we attempted to develop the NHP with tiny structure by only using EBL tools. As we found out before, if we used the same exposure parameters of EBL to define the layout of NHP, the dense structure of heater part could not be patterned very well. For example, if we applied a low dose exposure, the heater part is not properly defined, but if a high dose is applied for the exposure, the heater part is emerged

at the same energy, as shown in Fig. 3.32. In this part, we used two-step process with different voltages and doses for electrode part and heater part separately to accomplish the whole NHP device fabrication. Low resolution exposure with a lower dose and large writing field (200 μm) at lower energy for the electrode part exposure, and higher resolution exposure with higher does and small writing field (100 μm) at higher energy for the heater part exposure. Since the connections between heater and electrodes are midways between the two situations, it is decided to extend the design of the heater to add some extra dose on these far ends, as shown in Fig. 3.33.

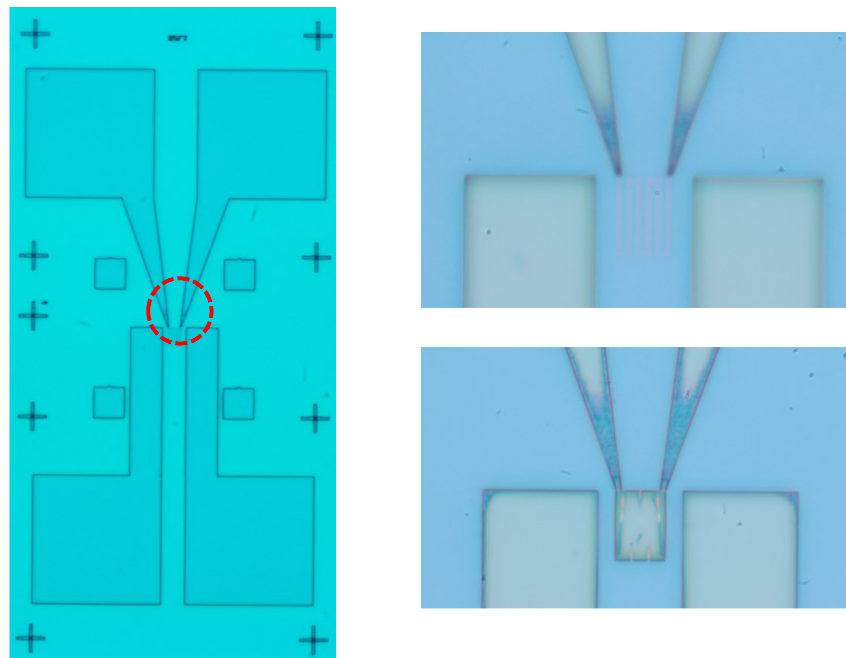

Figure 3.32 The layout of NHP1 images after EBL exposure with the same dose and energy in one step.

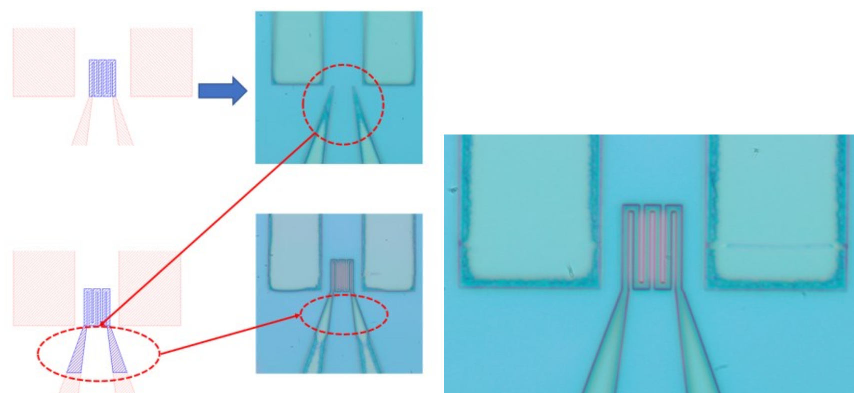

Figure 3.33 The layout of NHP1 images after EBL exposure in two-step.

The fabrication process is schematically shown in Fig 3.34. As it was talked before in Fig 3.2 in the beginning of this chapter, the insulating layer on the surface of the wafer is ONO layer, and the surface of the wafer was cleaned by acetone/isopropanol and oxygen plasma. After this clean process, the positive resist PMMA was spin coated at speed 4000 rpm/min using a coater machine on the wafer substrate, and then a hard bake was performed at a temperature of 180 °C for 60 seconds. To pattern the structure of hotplate device, this wafer was moved into the EBL machine of TESCAN. Following this step of exposure, the wafer went through a soft bake at a temperature of 120 °C, and then it was transferred to an electron beam evaporation machine to deposit an adhesion layer of titanium with 10 nm thickness, and a heater layer of platinum with 100 nm thickness. The lift-off procedure was then carried out in an acetone solution at a temperature of 40 °C, and the treated wafer was afterwards washed in isopropanol. The electrode part was defined by all these procedures, next we repeated these steps to pattern the dense heater part. In the end, the wafer was placed through calcination and metallization in an oven (Expertech CTR 200, Expert Semiconductor Technology, Inc., Scotts Valley, California, USA) at a temperature of 650 °C for a period of two hours in a nitrogen atmosphere.

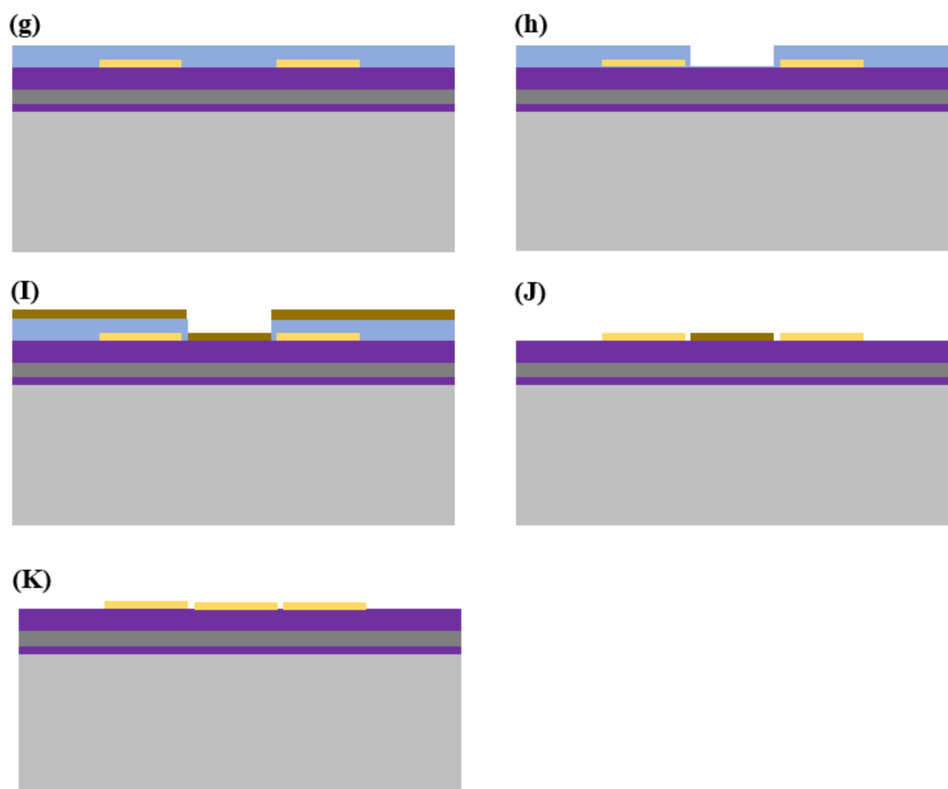

Figure 3.34 Diagrammatic sketch of the 2-step fabrication process for NHP1: (g). Resist deposit; (h). Resist exposure and development; (I). Pt/Ti deposition; (J). Lift-off process; (K). Calcination.

The layout of NHP1 is shown in Fig.3.34, and in our experiment work, we designed the heater width with 1 μm and 0.6 μm. To find the suitable exposure energy and does parameters of EBL for the electrode part and heater circuit part exposure, different energy and does were tested. There were two energy solutions, one was 20 keV with low dose, and another one was 30 keV with high dose. When the energy was set as 20 keV, the doses for the electrode part were set as 120 μC/cm^2, 140 μC/cm^2 and 160 μC/cm^2, and the doses for the heater part changed from 170 μC/cm^2 to 220 μC/cm^2. As shown in Fig.3.35.

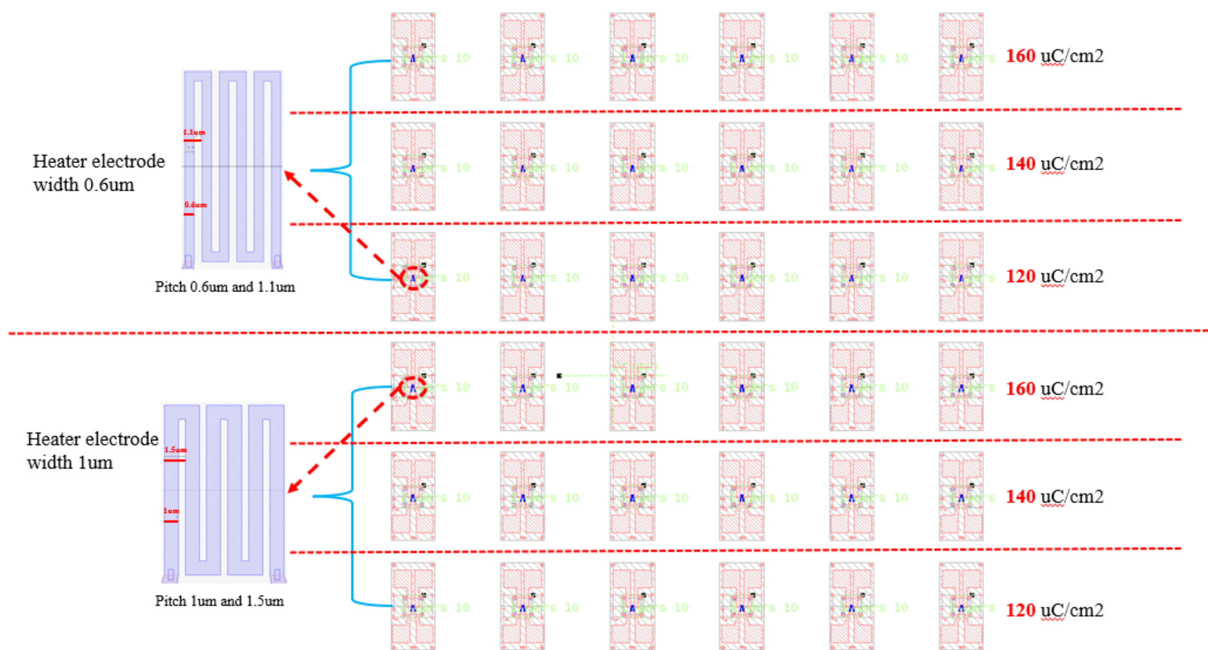

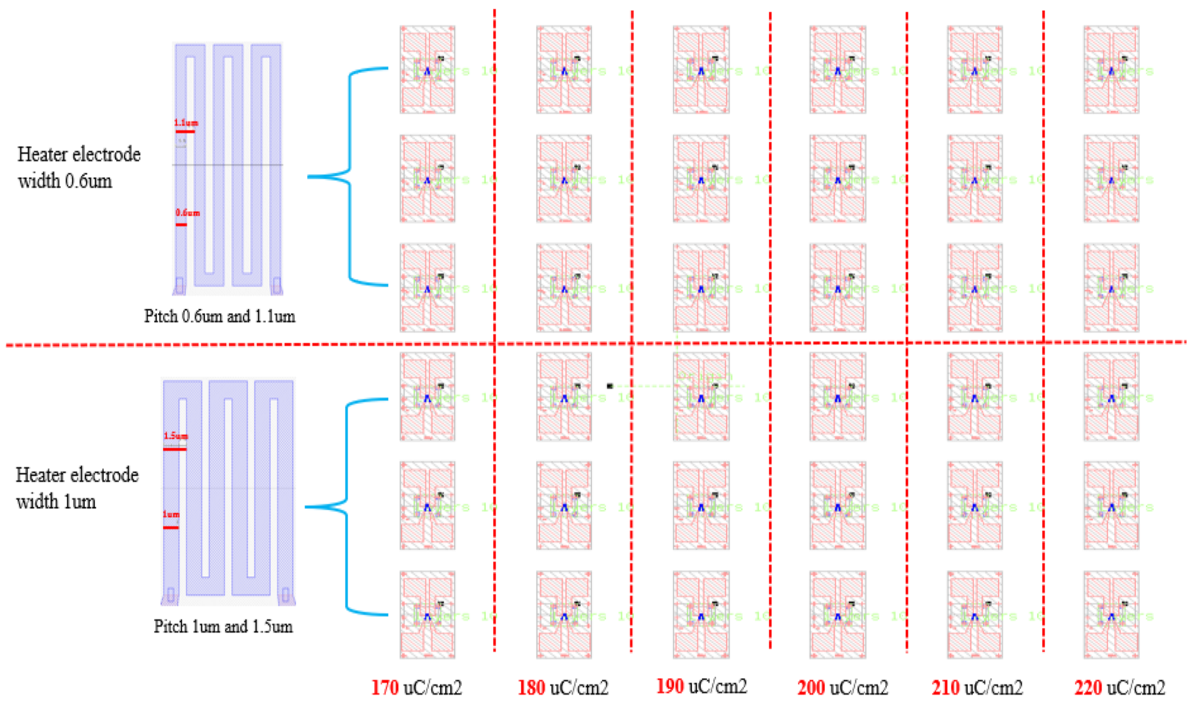

Figure 3.35 Doses set array for the electrode part and heater part.

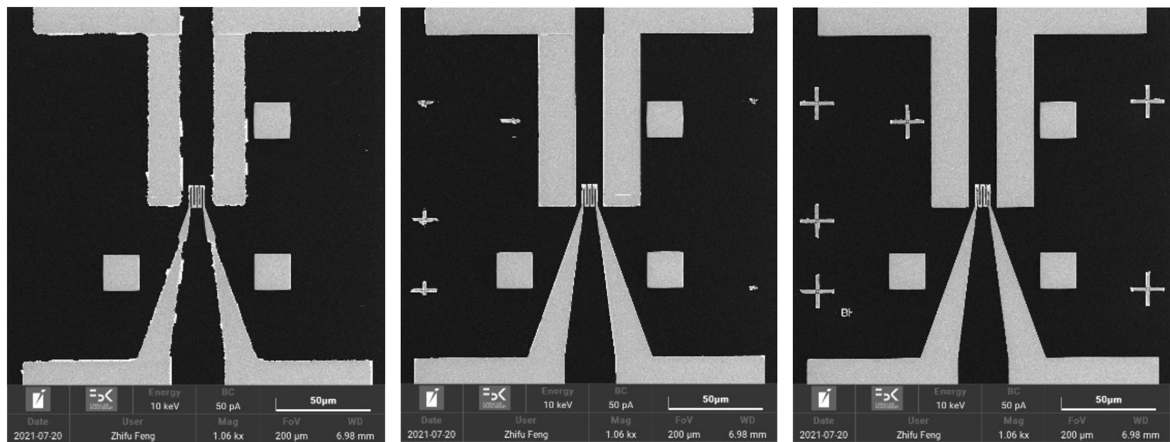

Figure 3.36 Electrode part exposed at doses of 120 μC/cm^2, 140 μC/cm^2 and 160 μC/cm^2 at 20 keV.

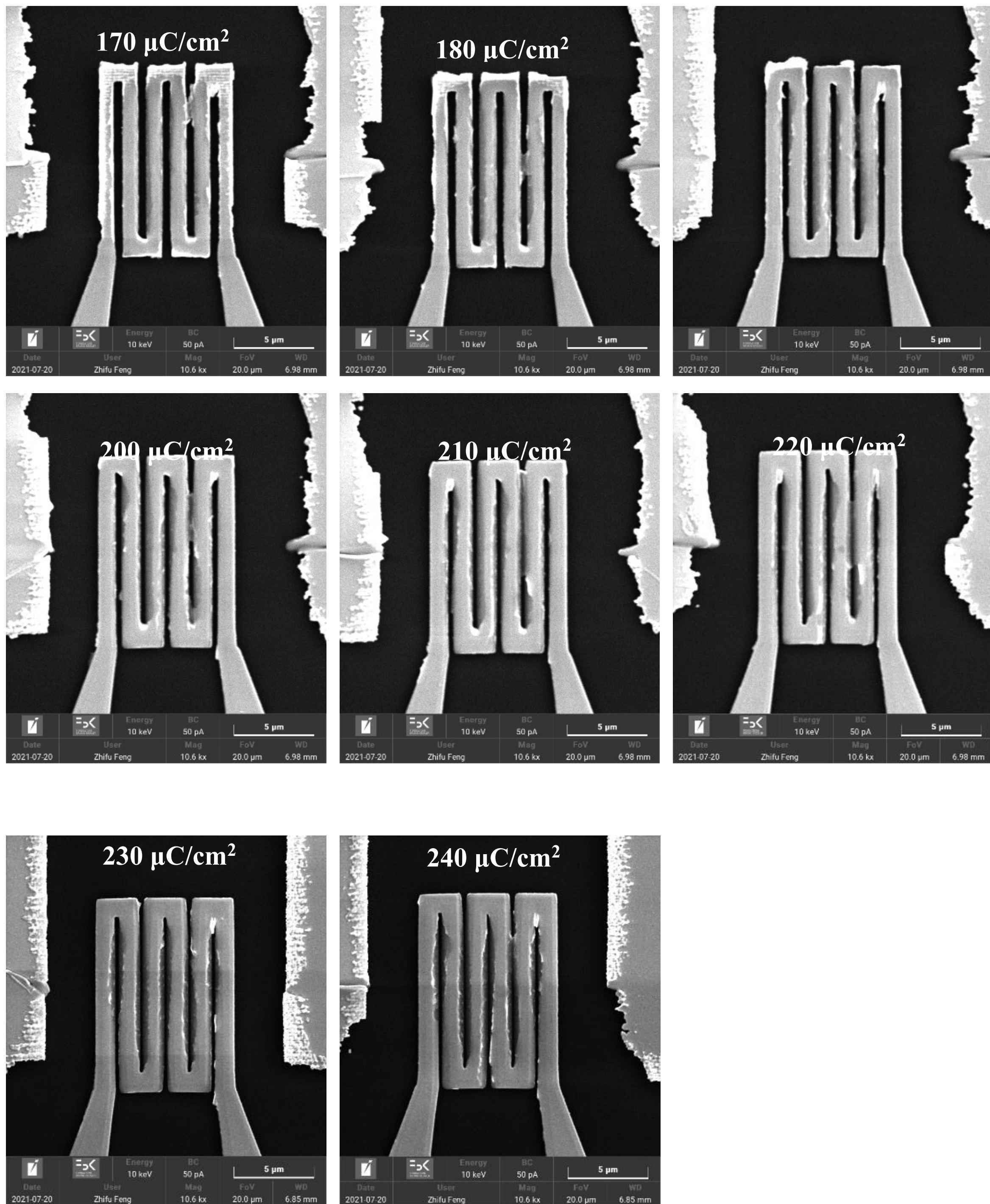

Figure 3.37 Heater part with 1 µm width circuit exposed at doses ranging from 170 µC/cm^2 to 240 µC/cm^2 at 20 keV.

When the exposure energy was set as 20 keV, does of 160 µC/cm^2 was the most suitable parameter for the electrode define, as shown in Fig 3.36. If the dose was lower than 160 µC/cm^2, the connection between different structures was not continues, and narrow part of the electrode risked because of low exposure dose, even the fringe was not lift-off very well. In conclusion, for the electrode part exposure, when the energy is at 20 keV, the exposure

dose should be over 160 μC/cm^2. It is clear that in Fig. 3.37 that the heating circuit with a width 1 μm merged together when the dose was higher than 190 μC/cm^2, which was caused by the proximity effect of electron beam passing through the photoresist. Therefore, the exposure dose should be lower than 190 μC/cm^2 for the heater circuit with the 1 μm width. But when the heating circuit's width was 0.6 μm (as shown in Figure 3.38), the exposure dose being lower than 190 μC/cm^2 was not enough to fully expose the dense structure, and the exposure should be higher than it. By comparing these experiment results, it indicates that the pattern structure also affected the exposure result and the dose should be lower, if the structure is denser.

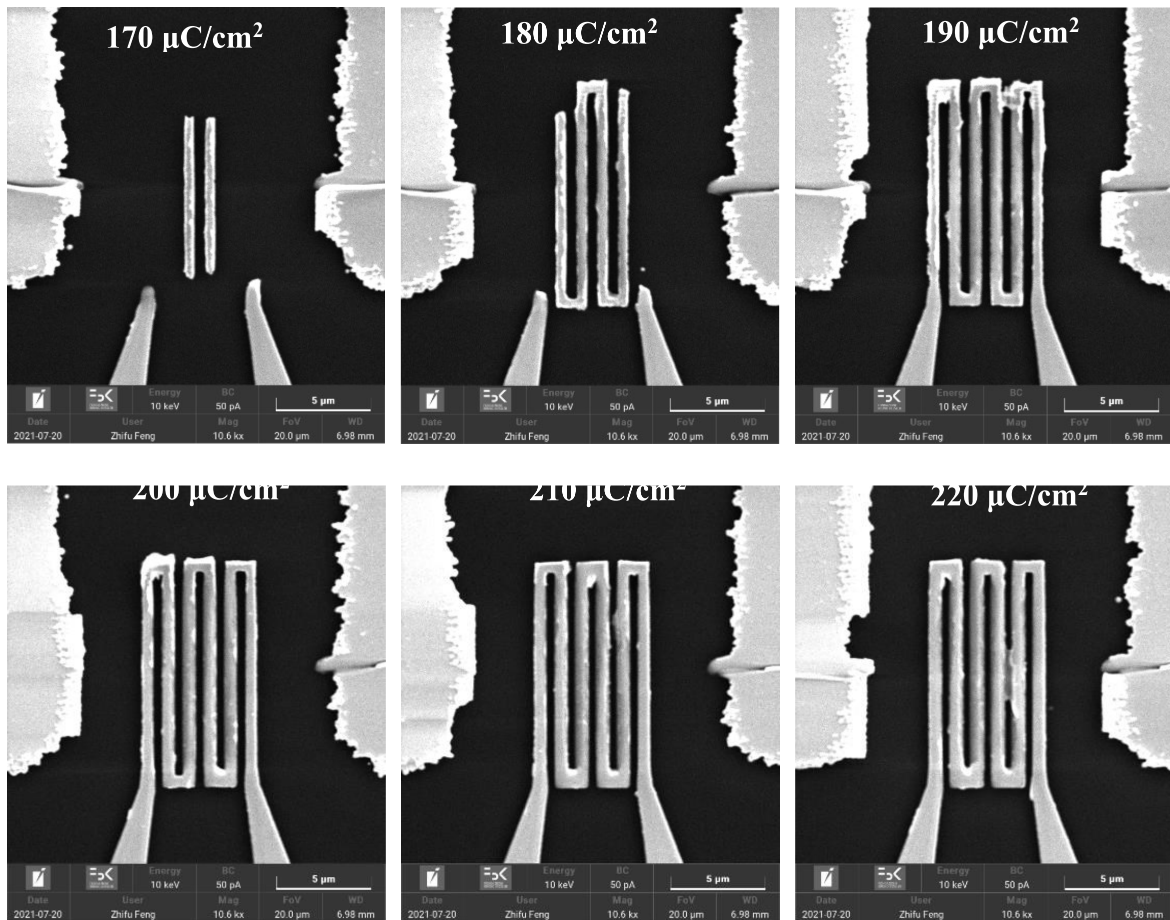

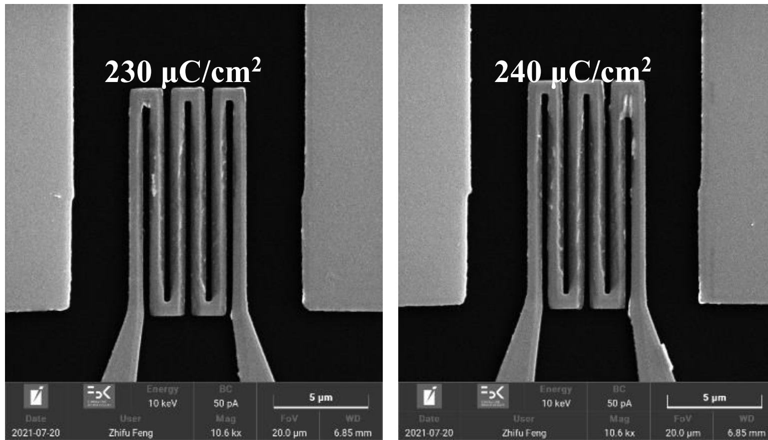

Figure 3.38 Heater part with 0.6 μm width circuit exposed at doses ranging from 170 μC/cm^2 to 240 μC/cm^2 at 20 keV.

It is clear that in Fig. 3.37 when the dose was higher than 190 μC/cm^2, the heater circuit with width 1 μm merged together, which was caused by proximity effect during electron beam passed through the resist. Hence, the exposure dose should be lower than 190 μC/cm^2 for the heater circuit with width of 1 μm. But when the heater circuit width was 0.6 μm, does lower than 190 μC/cm^2 was not enough to fully expose the dense structure, the exposure should be higher than it. By comparing these experiment results, it indicates that the pattern structure can also affect the exposure result, if the structure is denser, the dose should be lower.

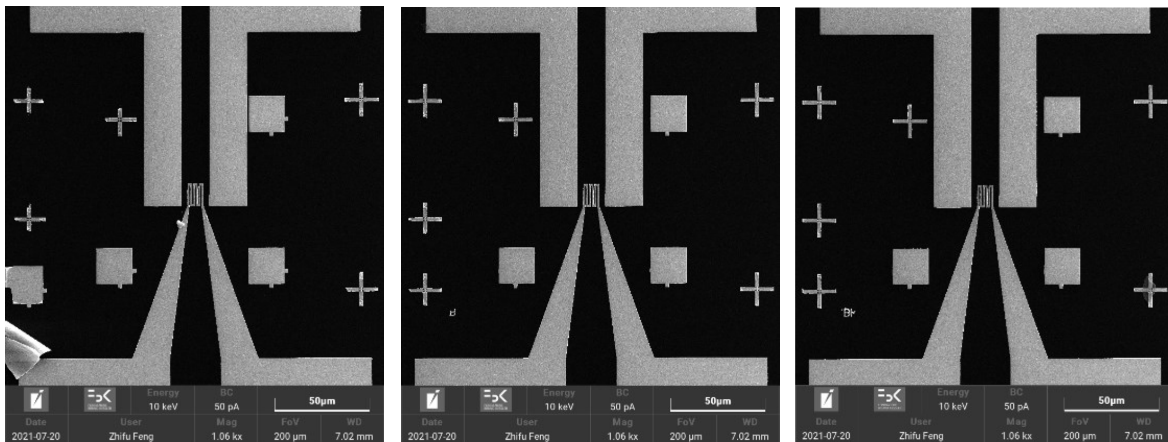

Figure 3.39 Electrode part exposed at doses of 230 μC/cm^2, 240 μC/cm^2 and 250 μC/cm^2 at 30 keV.

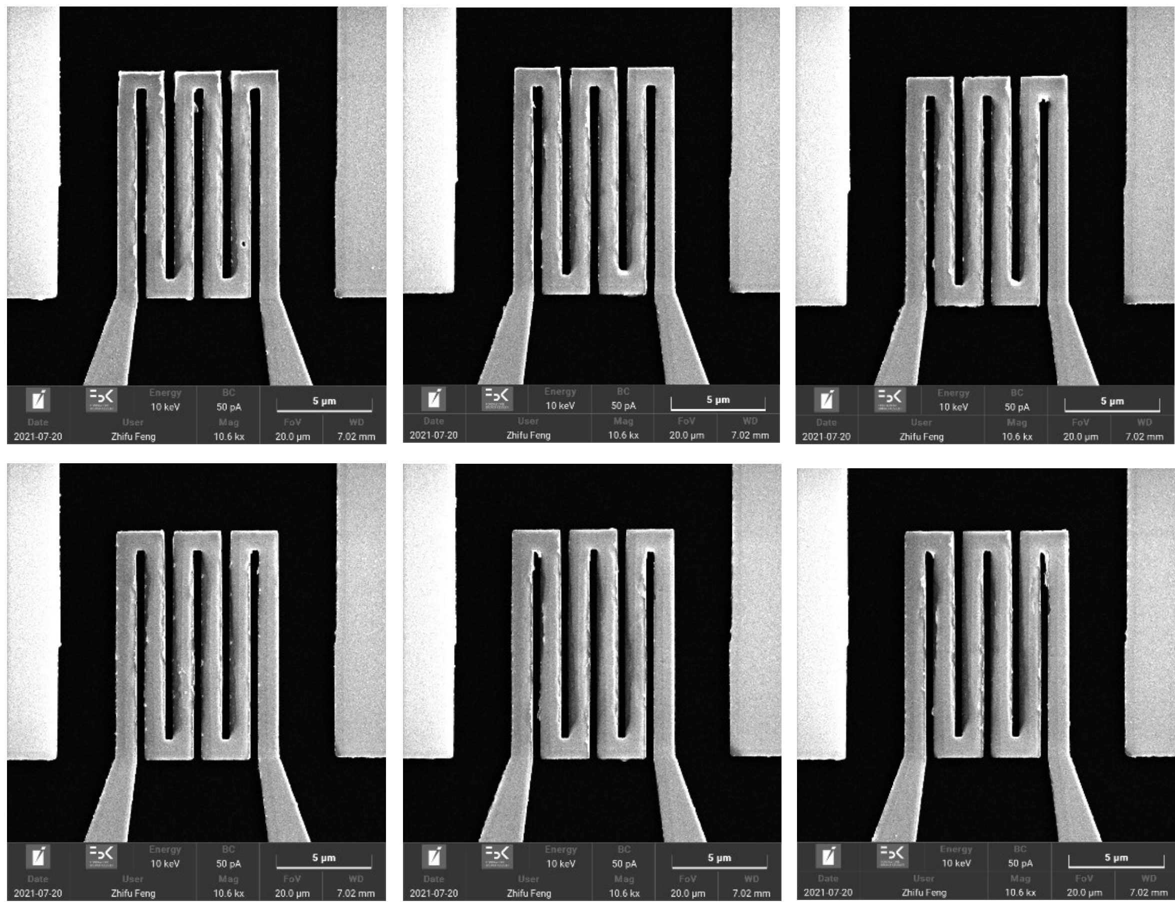

Figure 3.40 Heater part with 1 µm width circuit exposed at doses from 260 µC/cm² to 310 µC/cm² at 30 keV.

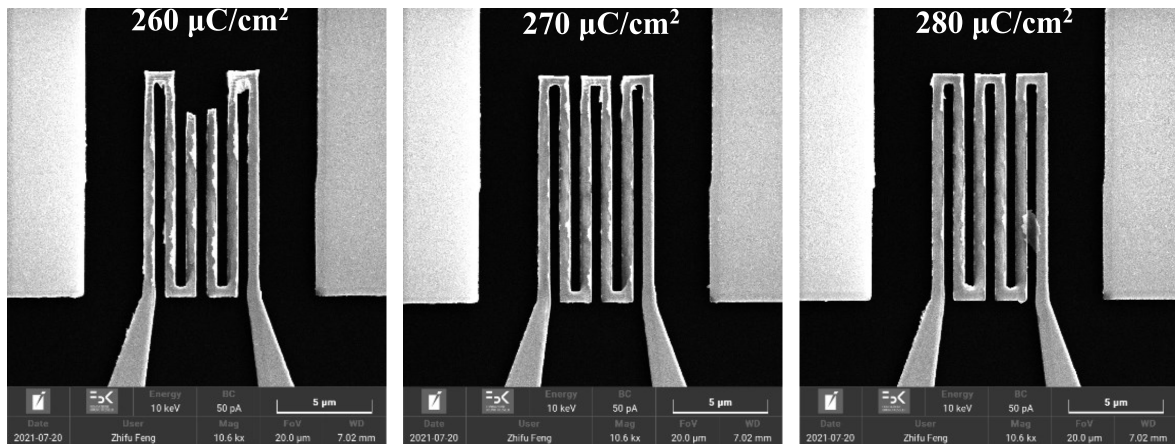

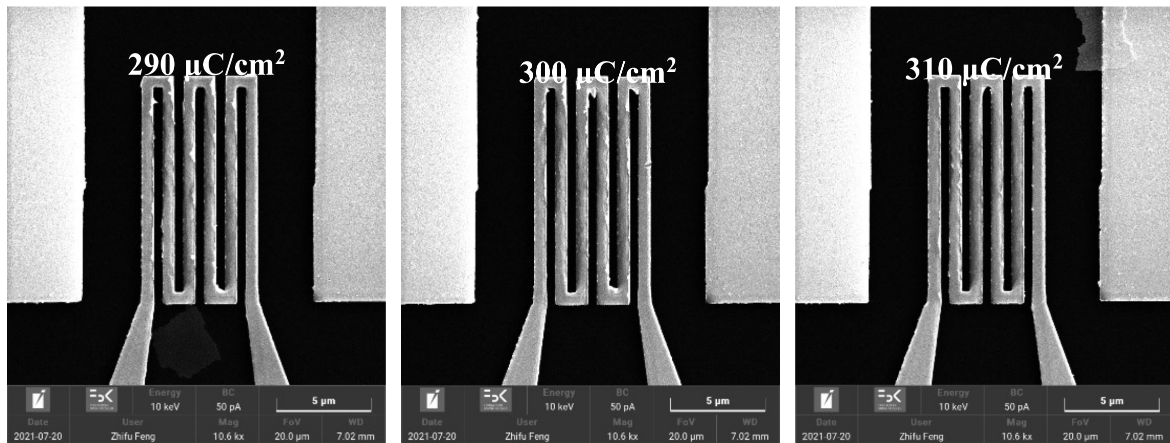

Figure 3.41 Heater part with 0.6 µm width circuit exposed at dose from 260 µC/cm^2 to 310 µC/cm^2 at 30 keV.

When the electron beam energy was set as 30 keV, for the electrode part, doses of 230 µC/cm^2, 240 µC/cm^2 and 250 µC/cm^2 were enough for the exposure, as shown in Fig.3.39. For 1 µm width heater circuit exposure, doses from 260 to 290 µC/cm^2 were propriate, but it was better to use dose of 280 to 310 µC/cm^2 to define the 0.6 µm width heater circuit. In comparison of 20 keV and 30 keV exposure results, it suggests low energy of electron beam should couple with low dose to define the same layout structure, and high voltage of the power source should combine with high dose. It is because high energy electron beam can travel deep inside the resist during exposure process, hence, it needs more electrons to react with resist near the surface of PMMA. Electrons with low energy stay near resist surface area, so it needs less dose of electrons.

In sum, for NHP1 layout patterning, proper exposure energy of electron beam and dose are needed. In our case, when the electron acceleration voltage is set 20 keV, the exposure dose is around 200 µC/cm^2, for both heater circuit and electrode part. Meanwhile, when the voltage is set as 30 keV, the exposure dose should be around 300 µC/cm^2 for the whole layout definition.

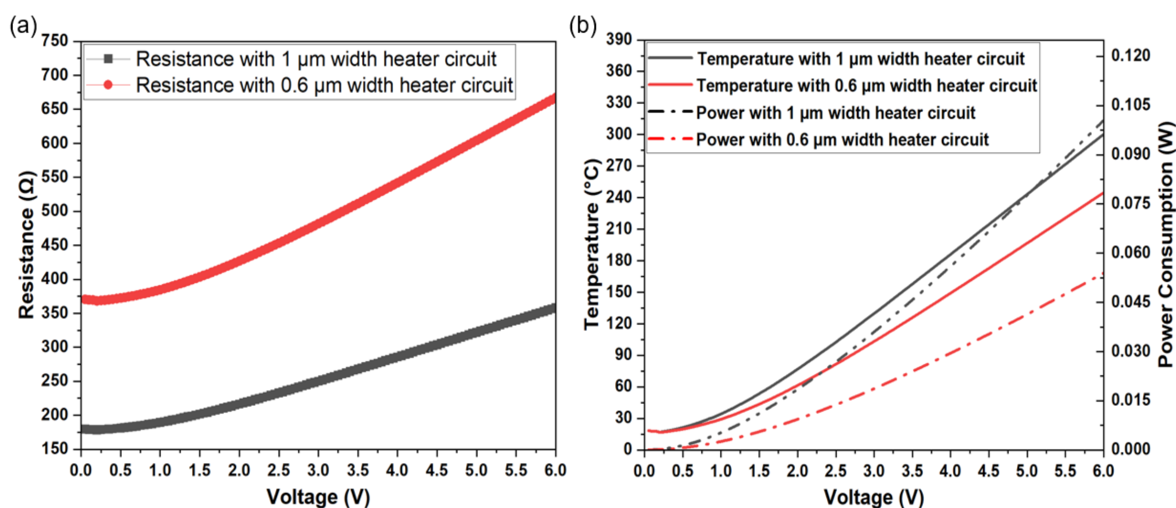

Figure 3.42 Resistance and temperature at different input voltages of NHP2 with different heater circuit width.

In the end, the resistance and work temperature at different voltages were measured, and the results are shown in Fig.3.42. Wider heater circuit with circuit width of 1 μm caused lower resistance value, but higher working temperature and power consumption compared to narrower heater circuit with circuit width of 0.6 μm. The experiment data of the resistance and temperature are much lower than the simulation results, it is because that the simulation temperature are recorded by the highest temperature value on the heater device on COMSOL, and our experiment data are based on the average value. For example, from the simulation images, it is obvious that the heater part shows a temperature-concentrated area at high voltage, where the temperature is much higher than the electrode part in such condition. The highest temperature appears on the heater surface, and is recorded for the simulation results. While the resistance we measured in the lab was about the whole device, and the temperature is calculated by using this average resistance value, which causes the lower operational temperature than the real temperature and the simulation results. It is well known that the heat part resistance changes a lot at high input voltage because of the high temperature on this part. However, the electrode part resistance barely changes because this part is almost at room temperature. Thus, if we want to calibrate the resistance measurement value, we have to eliminate the electrode resistance influence.

3.5.3 MHP2 Fabrication in Two-step by EBL

When the gas sensors are developed on MEMS hotplate, sometimes the deposited sensing material could not cover the heater part very well due to its high aspect ratio. For example, if the heater circuit gaps are very narrow and deep, the sensing materials cannot reach the

down corner of the heater circuit. To make sure that gas sensor can work very well, we increased the aspect ratio of heater circuit, and fabricated MPH2. In this case two kinds of heater circuit structures are designed. One is the rectangular shape, another one is circular shape, named as MHP2_R and MHP2_C shown in Fig.3.42, which affects the operational temperature and power consumption. The fabrication process is as the same as NPH2 above mentioned.

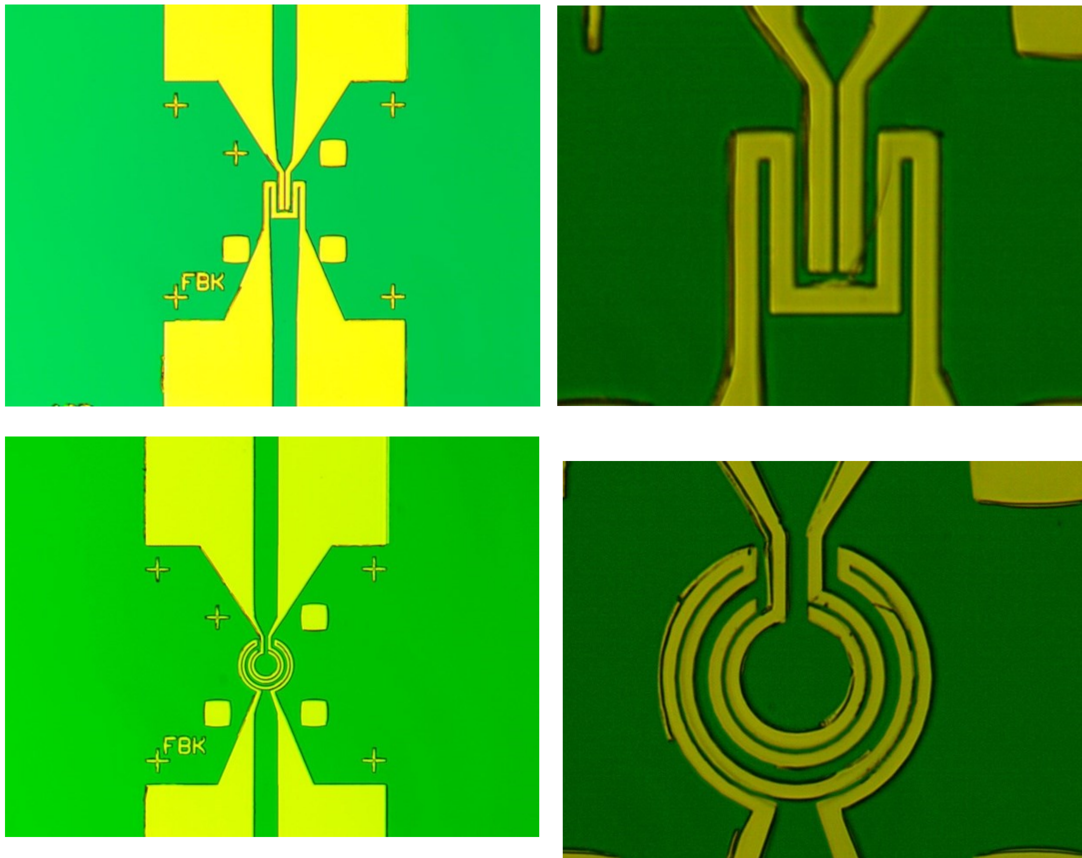

Figure 3.43 Optical microscope images of MHP2_R and MHP2_C.

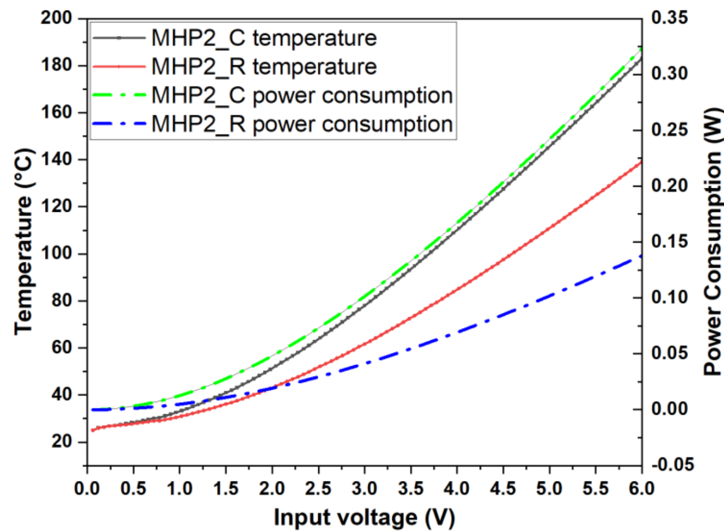

Figure 3.44 Resistance measurement and temperature at different input voltages of MHP2 with different heater geometries.

The temperature and power consumption of MHP2_R and MHP2_C are shown in Fig.3.44 at different input voltages. It reveals that at the same input voltage MHP2_C owns the higher working temperature and power consumption than MHP2_R. It could be because MHP2_C circuit is much longer than MHP2_R circuit, more Pt material to be heated up, higher temperature is obtained and more energy is consumed.

3.5.4 ZnO Self-heating Gas Sensor Fabrication by EBL

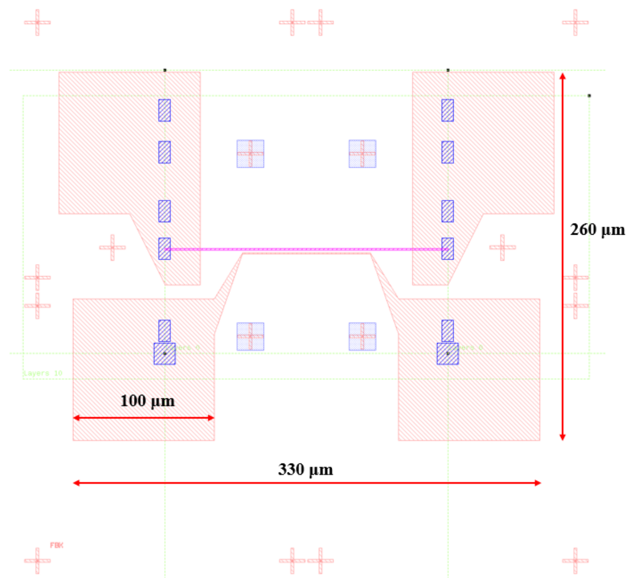

Figure 3.45 ZnO self-heating gas sensor layout.

Self-heating mode gas sensor can operate without any external power source, the sensing materials act as the heater and sensing part, which can simplify the structure of gas sensor

devices and fabrication processes. ZnO self-heating gas sensor device is total 330 µm x 260 µm area, and the ZnO nanowire (pink part in Fig.3.45) is 1000 nm wide and 200 µm long, and other part including electrode and pad parts are all Pt material, the Pt nano wire which is near ZnO is 600 nm wide. The fabrication process is above-mentioned as the same as NHP1.

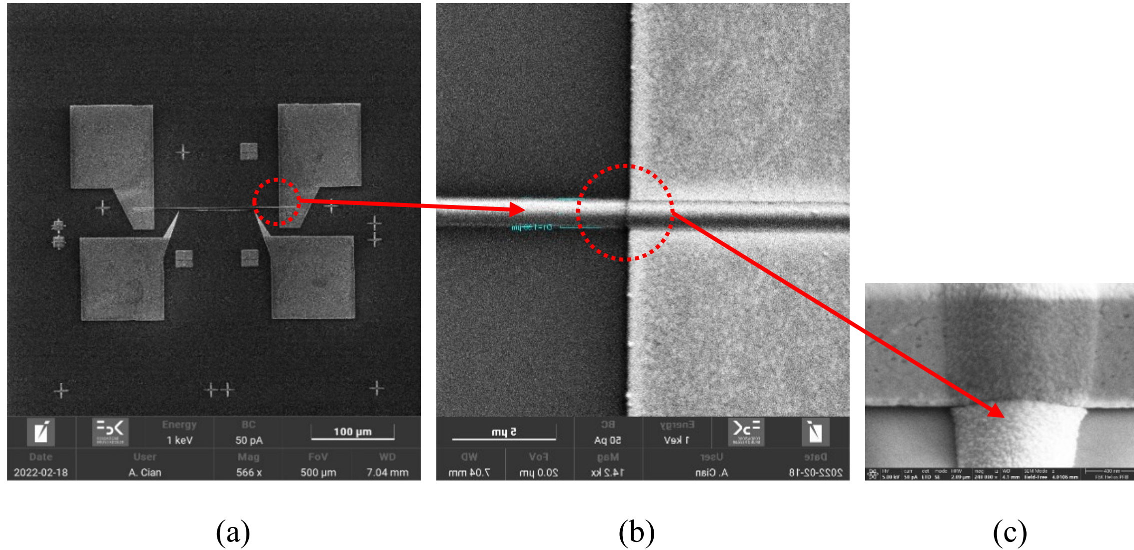

Figure 3.46 Resistance measurement and temperature at different input voltages of MHP2 with different heater geometries.

Fig. 3.46 shows self-heating ZnO layout SEM image. By applying a high voltage on ZnO nanowire, it will be heated up by Joule heating effect. The platinum nano wire which is near ZnO nano wire can be used as thermometer to detect the temperature of ZnO. From Fig. 3.46 c, it is clear that ZnO nano wire is connected well with Pt electrode, and the morphology of ZnO is nano size.

Conclusion

In this chapter, we mainly discussed about the hotplate simulation, design, fabrication and characterization used for SMO gas sensor devices. We totally designed three sizes (MHP2, NHP1 and NHP2) for the hotplate to satisfy different demands of the gas sensor devices. First, we calibrated our simulation model and boundary conditions by considering the experimental data of MHP1 in COMSOL, which is currently used in our lab for the gas sensor devices. For MHP1 model, we investigated the effect of suspended membrane on the temperature distribution and power consumption with comparison to the hotplate with solid membrane structure. It turns out that with solid membrane structure, the hotplate could not

be heated up even when the input voltage reached 9 V due to the heat conduction through the silicon wafer with high heat conductivity, but the power consumption increased from 0 to 1.25 W with input voltage ranging from 0 to 9 V. However, the hotplate with suspended membrane structure exhibited much more optimized power efficiency and higher operational temperature, when the input voltage was changing from 0 to 9 V, the temperature increased almost linearly from room temperature to around 900°C with power consumption of 0.35 W. Then based on MHP1 model, we downsized it by 50 times to get MHP2 device with 2 μm wide heater circuit. In this case, two heater circuit geometries were designed, one was rectangular shape (MHP2_R), and another one was circular oner (MHP2_C). We compared heater circuit thickness and insulating thickness influence on temperature distribution and power consumption on the hotplate with solid structure membrane. By using this size, the hotplate could be heated up even on solid membrane, and at the same input voltage on the heater circuit, MHP2_C showed higher working temperature than MHP_R geometry. Furthermore, the thickness of heater circuit and insulating layer could affect the temperature distribution and power consumption. For example, if the thickness of Pt heater is thicker, the temperature will get higher as well as power consumption. Meanwhile, if the insulating layer becomes thicker, the working temperature will be higher and the power consumption will be lower owing to its heat resist effect at the same input voltage on heater circuit. At the same time, the influence of a trench structure on the heat dissipation and the mechanical properties of MHP2 was studied in 2 D model. In this example, the heat source was fixed at 300°C, and the thickness of the trench beneath the heat source and insulating layer was parameter scanned from 0 to 10 μm. It was found that when the thickness of the trench was above 5 μm, the temperature under the insulting layer hardly changed. By this chance, we fixed the trench thickness as 5 μm, and we parameter scanned the heat source temperature from 100°C to 600°C. It presented that with the trench structure, the temperature, displacement and stress under the insulating layer barely changed compared the solid structure. In the end of this part, the thickness of insulating layer influence on the temperature uniformity was deliberated, the results stated that thicker insulating layer contributed to improve the temperature uniformity of hotplate. NHP2 is another hotplate which has the same heater circuit geometry size but with two longer electrode part compared to NHP1, because most of the hotplate resistance fell on the heater circuit part, and the electrode part owns pretty small resistance value, that is why the high temperature concentrates on the heater part. Hence, NHP2 exhibited almost the same temperature and power consumption at the same input voltage as compared to NHP1.

Considering horizontal comparison among MHP1, MHP2, NHP1 and NHP2 devices, it is discovered that through downsizing the geometry of the hotplate layout from MHP1 to MHP2 by 50 times, the operational temperature and power efficiency was enhanced significantly. For example, when the input voltage on heater circuit was set 3V, MHP1 showed the temperature of around 350°C with power consumption of 0.125 W on suspended membrane structure, and 25°C with power consumption of 0.24 W on solid membrane structure. MHP2_R exhibited around 100°C with power consumption of 0.1 W, and MHP2_C showed around 300°C with power consumption of 0.03 W both on solid membrane structure. NHP1 was evolved from MHP2_R through decreasing the size by 4 times, and when the input voltage was 3V, the temperature was around 150°C with a power consumption of 0.05 W.

To fabricate these three types of hotplates, we mainly used EBL machine in the clean room of FBK. First, we deposited ONO stack structure on silicon wafer, which was 100 nm SiO_2, 200 nm Si_3N_4 and another 600 nm SiO_2 layer. ONO stack structure acted as insulating layer with 0 stree. Since the geometry of these hotplates were not even, the electrode part was always micro-level, but the heater circuit was quite dense. In the begin, we attempted to only use EBL to define the pattern of the NHP in one step, for the electrode part, we found the optimized exposure parameters (20 keV with dose at least 160 $\mu C/cm^2$, or 30keV with does at least 230 $\mu C/cm^2$). But for the dense heater part, either the dose was too low or too high. We had to define the heater part by using different parameters. First, we tried to use FIB machine to mill the heater circuit after patterning the electrode part of hotplate by EBL. For the optimized FIB milling parameters, we used SRIM to simulate the relation between voltage and doses of Au ions beam, then we selected the most suitable doses of 60 75 and 90 $\mu C/cm^2$ for milling 100 nm Pt heater layer at 70 keV to do the experiment. SIMS results proved that the energy of 70 keV with dose of 60 75 and 90 $\mu C/cm^2$ was enough for milling 100 nm Pt layer. FIB is a super fine machine, which can define nm-size structures, but it consumes a lot of time. Next, we only used EBL tool to define the hotplate layout in two steps for NHP1 and MHP2 definition. We applied higher voltage and higher doses with smaller writing field for pattering the dense heater circuit part compared to the electrode part exposure. For instance, to expose the electrode part, 20 keV with dose of 200 $\mu C/cm^2$ was applied with 200 μm writing field in the first step, in the second step, 30 keV with dose of 300 $\mu C/cm^2$ and 100 writing field could finely define the heater circuit part.

Reference

[1] Z. E. Jeroish, K. S. Bhuvaneshwari, F. Samsuri, and V. Narayanamurthy, "Microheater: material, design, fabrication, temperature control, and applications-a role in COVID-19," *Biomed Microdevices,* vol. 24, p. 3, Dec 3 2021.

[2] A. Gaiardo, D. Novel, E. Scattolo, M. Crivellari, A. Picciotto, F. Ficorella*, et al.*, "Optimization of a Low-Power Chemoresistive Gas Sensor: Predictive Thermal Modelling and Mechanical Failure Analysis," *Sensors (Basel),* vol. 21, Jan 25 2021.

[3] A. Gaiardo, D. Novel, E. Scattolo, A. Bucciarelli, P. Bellutti, and G. Pepponi, "Dataset of the Optimization of a Low Power Chemoresistive Gas Sensor: Predictive Thermal Modelling and Mechanical Failure Analysis," *Data,* vol. 6, p. 30, 2021.

[4] D. Zappa, A. Bertuna, E. Comini, M. Herold, N. Poli, and G. Sberveglieri, "Tungsten Oxide Nanowires on Micro Hotplates for Gas Sensing Applications," *Procedia Engineering,* vol. 120, pp. 439-442, 2015.

[5] A. Singh, A. Sharma, N. Dhull, A. Arora, M. Tomar, and V. Gupta, "MEMS-based microheaters integrated gas sensors," *Integrated Ferroelectrics,* vol. 193, pp. 72-87, 2019.

[6] T. Schössler, F. Schön, C. Lemier, and G. Urban, "Reliability improvements of thin film platinum resistors on wafer-level and micro-hotplates at stress temperatures in the range of 140–290 °C," *Microelectronics Reliability,* vol. 104, p. 113557, 2020.

[7] Z. Zhang, C. Yin, C. Tao, B. Zhu, and N. Dong, "Design and optimization of planar structure micro-hotplate," *Procedia Engineering,* vol. 12, pp. 105-110, 2011.

[8] W. J. Hwang, K. S. Shin, J. H. Roh, D. S. Lee, and S. H. Choa, "Development of micro-heaters with optimized temperature compensation design for gas sensors," *Sensors (Basel),* vol. 11, pp. 2580-91, 2011.

[9] P. Kahroba, I. Mirzaee, P. Sharifi, and H. Shirvani, "The microcavity-based micro-heater: an optimum design for micro-heaters," *Microsystem Technologies,* vol. 14, pp. 705-710, 2007.

[10] M. Prasad and P. S. Dutta, "Development of micro-hotplate and its reliability for gas sensing applications," *Applied Physics A,* vol. 124, 2018.

[11] S. Bedoui, S. Gomri, and A. Kachouri, "Optimization of a Meander–Spiral Combination Micro Hotplate for Gas Sensors Based on Numerical Analysis," *Transactions on Electrical and Electronic Materials,* vol. 20, pp. 92-98, 2018.

[12] F. Samaeifar, A. Afifi, and H. Abdollahi, "Simple Fabrication and Characterization of a Platinum Microhotplate Based on Suspended Membrane Structure," *Experimental Techniques,* pp. n/a-n/a, 2014.

[13] Isolde Simon, Nicolae Barsan, Michael Bauer, and Udo Weimar, "Micromachined metal oxide gas sensors opportunities to improve sensor performance," *Sensors and Actuators B*, vol. 73, pp.1-26, 2001.

[14] P. Bhattacharyya, "Technological Journey Towards Reliable Microheater Development for MEMS Gas Sensors: A Review," *IEEE Transactions on Device and Materials Reliability,* vol. 14, pp. 589-599, 2014.

[15] K. L. Zhang, S. K. Chou, and S. S. Ang, "Fabrication, modeling and testing of a thin film Au/Ti microheater," *International Journal of Thermal Sciences,* vol. 46, pp. 580-588, 2007.

[16] S. Bedoui, S. Gomri, H. Charfeddine Samet, and A. Kachouri, "Design and Simulation of Microelectromechanical Systems (MEMS) for Ozone Gas Sensors," *Transactions on Electrical and Electronic Materials,* vol. 19, pp. 41-46, 2018.

[17] A. Giberti, V. Guidi, and D. Vincenzi, "A study of heat distribution and dissipation in a micromachined chemoresistive gas sensor," *Sensors and Actuators B: Chemical,* vol. 153, pp. 409-414, 2011.

[18] L.Sujath , V.S.Selvakumar, S.Aravind, R.Padamapriya, B.Preethi, " Design and Analysis of Micro-Heaters using COMSOL Multiphysics For MEMS Based Gas Sensor, " 2012 COMSOL Conference in Bangalore.

[19] S. Yu, S. Wang, M. Lu, and L. Zuo, "A novel polyimide based micro heater with high temperature uniformity," *Sensors and Actuators A: Physical,* vol. 257, pp. 58-64, 2017.

[20] D.Briand, J.Courbat, "Semiconductor Gas Sensors (Second Edition), " 2020, P. 413-464

[21] W. Jin, C. Xing, Y. Lu, S. Baoshou, and D. Li, "A novel method improving the temperature uniformity of hot-plate under induction heating," *Proceedings of the Institution of Mechanical Engineers, Part C: Journal of Mechanical Engineering Science,* vol. 235, pp. 190-201, 2020.

[22] W. Liu, Q. Su, Y. Xue, R. Z. Xie, X. M. Ren, and L. Liu, "Design and performance of NiCr-based micro-heater with lower excitation energy," *Journal of Physics: Conference Series,* vol. 1507, p. 022015, 2020.

[23] R. Xie, X. Ren, L. Liu, W. Liu, K. Yu, and Y. Xue, "Effect of sputtering on bridge region of thin film nichrome heater," *Journal of Physics: Conference Series,* vol. 2256, p. 012012, 2022.

[24] J. Park, G. Jung, S. Hong, Y. Jeong, W. Shin, D. Kim*, et al.*, "Analysis of Cr/Au contact reliability in embedded poly-Si micro-heater for FET-type gas sensor," *Sensors and Actuators B: Chemical,* vol. 360, p. 131673, 2022.

[25] G. Jung, Y. Hong, S. Hong, D. Jang, Y. Jeong, W. Shin*, et al.*, "A low-power embedded poly-Si micro-heater for gas sensor platform based on a FET transducer and its application for NO2 sensing," *Sensors and Actuators B: Chemical,* vol. 334, p. 129642, 2021.

[26] J. F. Creemer, D. Briand, H. W. Zandbergen, W. van der Vlist, C. R. de Boer, N. F. de Rooij*, et al.*, "Microhotplates with TiN heaters," *Sensors and Actuators A: Physical,* vol. 148, pp. 416-421, 2008.

[27] D. H. Olson, K. M. Freedy, S. J. McDonnell, and P. E. Hopkins, "The influence of titanium adhesion layer oxygen stoichiometry on thermal boundary conductance at gold contacts," *Applied Physics Letters,* vol. 112, p. 171602, 2018.

[28] X. Wang, Z. Jiang, J. Qin, H. Liu, G. Fan, and C. Hu, "Al/Ti-film-resistor based thermal heater with Zig-Zag configuration for MEMS application," *IOP Conference Series: Materials Science and Engineering,* vol. 892, p. 012063, 2020.
[29] N. H. Al-Hardan, M. J. Abdullah, A. Abdul Aziz, and Z. Hassan, "The effect of heat treatments on the properties of Ti/Pt heating elements for gas sensor applications," *Materials Science in Semiconductor Processing,* vol. 13, pp. 199-204, 2010.

4. MEMS-based Thin Film SMO ZnO Gas Sensor

4.1 Introduction

With the rapid expansion of the social economy and industrialization, a considerable number of waste gases such as nitrogen oxides, carbon monoxide, sulfur dioxide, and volatile organic compounds are emitted into the atmosphere. While most emitted gases are harmful to the human body and ecological system, which are produced by indoor decorating materials, outdoor industrial waste gases, life supplies, and building materials, since hazardous and dangerous gases have a significant impact on human existence, there is an urgent need to develop very sensitive technologies for identifying toxic and hazardous gases [1-3].

Zinc oxide (ZnO), is an extremely promising II–VI semiconductor with good chemical stability, high electron mobility, valid ability of gases both reductive and oxidative, and a broad band gap of 3.37 eV that can be used as transparent electrodes and active layers in a variety of devices, including solar cells, transistors, and gas sensors due to its low resistivity, abundance, and lack of toxicity [4]. ZnO high exciton binding energy of 60 meV ensures that effective excitonic emission can occur even at room temperature. ZnO crystallizes in the hexagonal P63mc space group and possesses a Wurtzite structure (a = 0.325 nm, c = 0.521 nm). Zn^{2+} is covalently linked to four O atoms to form corner-sharing ZnO_4 tetrahedra [5]. There are three shorter Zn–O bond lengths (0.2nm) and one larger Zn–O bond length (0.201nm). O atom is covalently linked to four Zn^{2+} atoms to form corner-sharing OZn_4 tetrahedra structure [6]. When it comes to metal oxide gas sensing materials, zinc oxide, as n-type semiconductor material was one of the first to be identified with high sensitivity to volatile and other radical gases, high chemical stability, suitability to doping, non-toxicity, and low preparation cost. ZnO possesses oxygen molecules that have been adsorbed onto its surface during gas sensing process at certain operational temperature. These oxygen molecules can be combined to generate ionized species that are able to grab electrons from the conducting band of the oxide, which results in the formation of a depletion layer at the surface of the oxide.

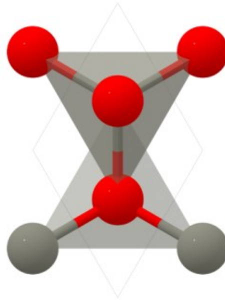

Figure 4.1 ZnO crystal structure (from The Materials Project).

For the ZnO gas sensing application, several approaches can improve the performance of ZnO, such as crystal adjustment, doping, morphologies changing and grain size controlling [7-11]. Additionally, the deposition parameters and post-deposition circumstances such as post-annealing can have a significant impact on the physical properties of ZnO films, which can also further affect the responsibility of ZnO because of its crystal structure adjustment during the calcination process. The grain-size impact results in unusually high sensitivity exhibited by nanostructured porous ZnO. In order to produce ZnO films with improved characteristics, numerous deposition methods have been implemented during the production process of these films. Sputtering is one of the most popular methods because of the relatively high deposition rates, as well as its good film characteristics and stable process. Recent studies have been concentrating on the association of surface and interface topology with deposition parameters and physical properties. This is because of the interest that is associated to the particular qualities of these metal oxide thin films. Therefore, it is absolutely necessary to make an effort to understand the association between the microstructure and the electrical properties of ZnO thin films. For example, Myung Sik Choi et al. synthesized porous ZnO nanosheets with porosity of 16%, pore size of 60 nm and thickness of 80 nm, to detect NO_2 gas via simple and scalable chemical-synthesis route, and they found that synergetic effects of the high surface area with ZnO/ZnO homojunctions and structural defects can enhance NO_2 gas response even in the presence of water vapor [12]. V. Paolucci et al. improved the sensitivity of ZnO toward ppb-level NO_2 by combining visible-light (red λ = 630 nm; green λ = 570 nm; purple-blue λ = 430 nm) at temperature of 25 °C-100 °C, ZnO nanocrystalline film doped by trivalent (Al-Ga) and tetravalent (Si-Ge) ions showed faster response/recovery behavior in visible light as respect to dark conditions [13]. K. Kasirajan et al. doped ZnO thin films by different rare-earth elements Gd, Nd and Sm to improve the responsibility of ZnO sensing material. They found that the band gap of

doping ZnO was increased comparing to pure ZnO, and the sensing response was enhanced under target gases of NO, NO_2, H_2, NH_3, CO and CO_2 [14].

MEMS based gas sensors have more advantages than conventional sensors, including small size, low power consumption, intrinsic safety, ease of fabrication and integration, high stability, high sensitivity and quick response and recovery time [15]. In our work, MEMS technology was applied to enhance the response and power efficiency of ZnO gas sensors by sputtering nanofilm of ZnO on miniaturized hotplate, which is fabricated due to the advantageous features such as higher sensitivity, lower power consumption, smaller designs, and a much lower fabrication cost, compared to the traditional gas sensors.

Sensor characterization is the process of comprehending the performance of a sensor towards different target gases at certain operational temperature. Sensitivity, selectivity, stability, detection limit, life cycle, response time, and recovery time are the primary properties of a gas sensor device. Typically, sensitivity measures the resistance ratio between the reference gas (usually in air) and target gases. Selectivity identifies the uniqueness of a device by measuring the target gas in the presence of other gases. The response time and recovery time of a gas sensor are defined as the time required to obtain 90% of the maximum response during gas injection and 10% of the maximum response after gas injection. To create a new, small, and low-cost gas sensor, these essential parameters must maintain a suitable range. Few strategies for enhancing sensor performance by altering the size, shape, porosity, thickness, doping, noble metal ornamentation, heterostructure, and composting architectures of 1D or 2D sensing materials have been deeply investigated.

In this chapter, to make the MEMS based gas sensor device, ZnO sensing thin film was deposited by magnetron sputtering on hotplate fabricated above-mentioned in Chapter 3. Then, the morphology and chemical composites of ZnO film was characterized, and the sensing ability of ZnO nano film was measured towards different target gases at dried and humid environments at certain operational temperatures.

4.2 Fabrication Process

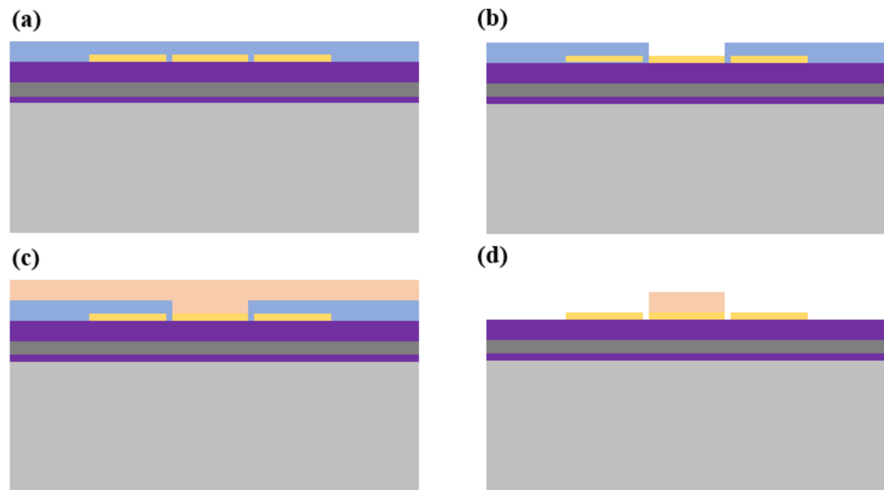

Figure 4.2 Fabrication process of ZnO micro gas sensor on MHP2 and NHP1: a). Spin coat resist on wafer; b). Exposure of resist by EBL; c). Sputtering of ZnO; d). Lift-off

To fabricate the ZnO gas sensor by MEMS techniques, here we used NHP2 and MHP2 hotplate fabricated above in Chapter 2 to support ZnO sensing nanofilm. The fabrication details are as follows: 1. Spin coating PMMA A7 on the wafer with MHP2 pattern array by applying the same parameters; 2. Soft bake at 180°C for 60s; 3. Then transfer the wafer to EBL machine, and implemented the exposure process by using 30 keV with 250 $\mu C/cm^2$ to define the ZnO sputtering area; 4. Development and hard bake; 5. Sputtering ZnO on this wafer, and the sputtering energy is 8 W, the gas condition is with 40 sccm Ar and 3 sccm O_2 flow; 5. Lift-off was conducted in acetone at 40°C until the resist was totally removed, after that the wafer was cleaned by isopropanol; 6. To metalize and calcinate ZnO (ZnO_P) nano film, the wafer was put inside the oven at 650°C for 2h, and the gas environment was pure N2 or air, finally we got the samples ZnO_N and ZnO_A; 7. The wafer was sliced into ZnO gas sensor units, and they were bonded by gold wire on TO support for resistance measurement of ZnO under different target gases.

4.3 Results and Discussion.

4.3.1 Morphological and Elemental Studies

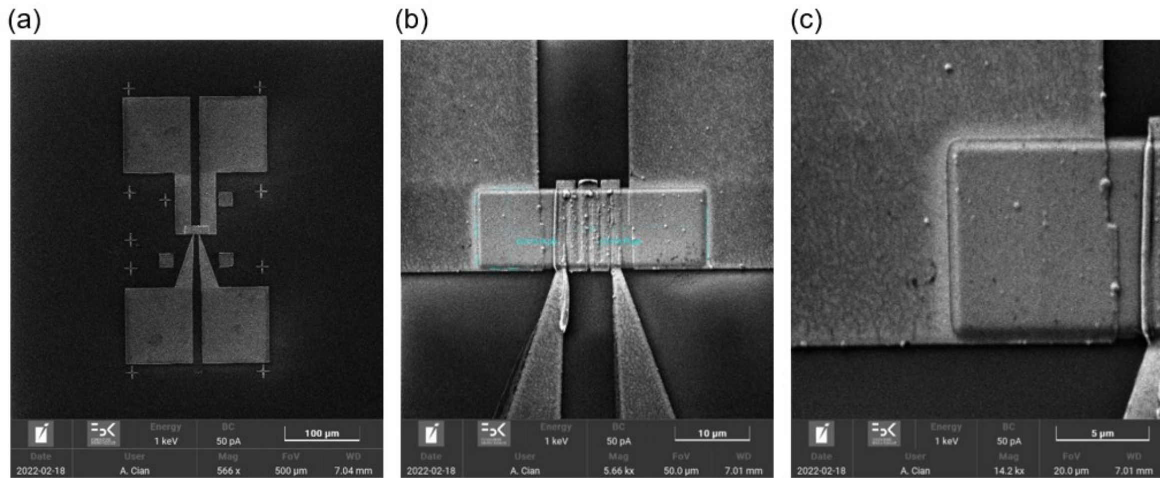

Figure 4.3 SEM images of ZnO gas sensor device deposition on NHP2 device (a), ZnO nanofilm on heater part (b) and the connection between ZnO and Pt electrode (c).

Fig.4.3 shows the ZnO sensing film on NHP2 device, the heater circuit was covered very well by ZnO film. But around the corner of the heater, especially the sharp part, it seemed that Pt circuit was peeled from the wafer substrate. Since other part of Pt circuit was fine, the peeling could be caused by sputtering process when the highly accelerated ZnO atoms hit on the surface of Pt circuit with high concentration of magnetic field around the sharp structure. Additionally, ZnO was also deposited thicker around the sharp structure than the flat part. There were big size particles on the flat part of ZnO film discretely, which could be that the thicker ZnO around the sharp structure was kicked off from the original position. To solve this problem, another insulation layer such as SiO_2 or Si_3N_4 should be deposited between Pt layer and ZnO material.

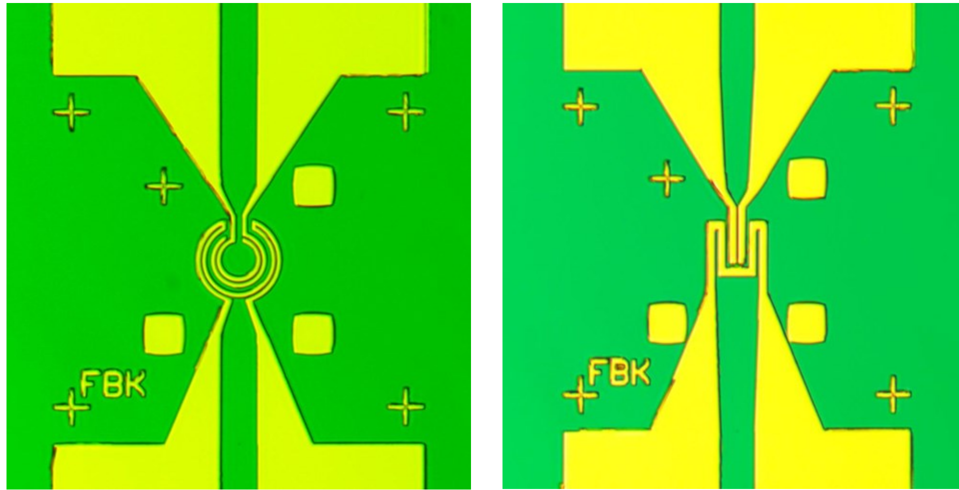

Before ZnO deposition on MHP2_C and MHP2_R

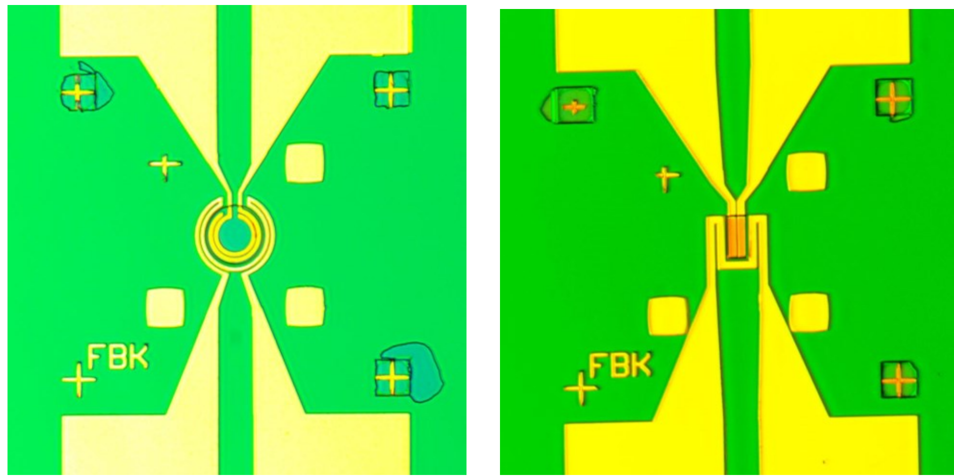

After ZnO deposition on MHP2_C and MHP2_R

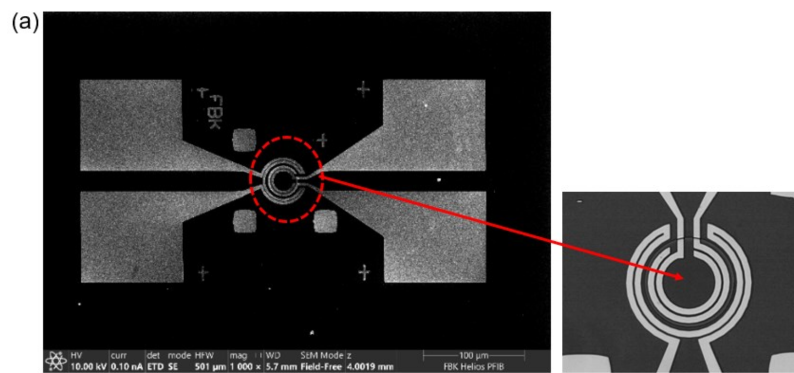

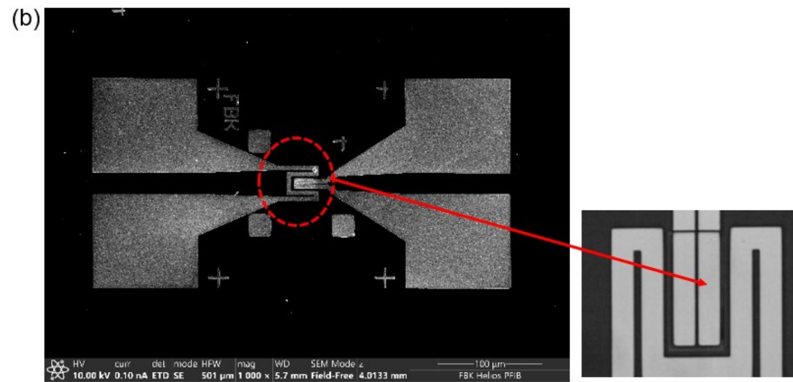

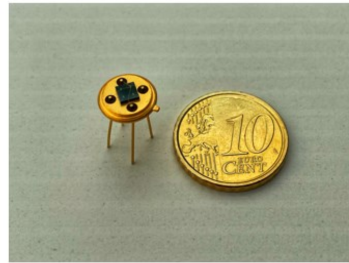

Figure 4.4 SEM images of ZnO on MHP2_C (a), MHP2_R (b) and ZnO sensor chip with four devices.

Fig. 4.4 a and b show the ZnO sensing film deposited on MHP2_C and MHP2_R, where ZnO fully covered the heater circuit. Fig. 4.4 c shows one gas sensor chip with four sensor device array after Au-wire bonding with TO substrate. Through applying an input voltage on heater circuit, heater is heated up to a certain temperature, and the resistance changing of sensing material ZnO is measured during different situations.

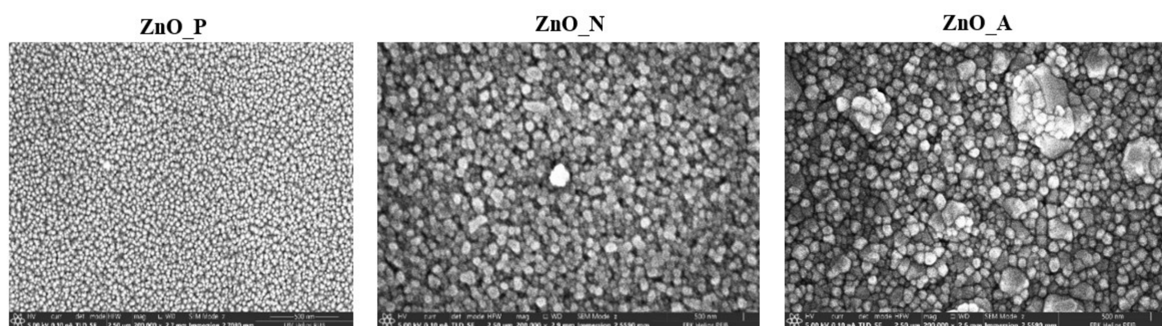

Figure 4.5 SEM images of ZnO_P, ZnO_N and ZnO_A materials.

The morphologies of the produced ZnO nanofilms were examined by SEM in order to investigate the impact of the synthesis routes on the morphology and diameter of ZnO nanofilm. The results are displayed in Fig. 4.5, which shows ZnO SEM images before and after different calcination environments. ZnO_P shows very even nano particles size with diameter of around 10 nm, but after calcination in pure N_2 environment, the particle grew to

around 100 nm. When the environment occurred to air, the particle size was not equal, with diameter ranging from 100 nm to 500 nm. Apparently, calcination temperature can help ZnO nano particles growth. Furthermore, the air environment can also significantly affect the size distribution of ZnO.

Table 4-1 Atom ratio of samples obtained from EDX results

Samples	Zn (% atom ratio)	O (% atom ratio)	C (% atom ratio)	Zn/O ratio
ZnO_P	31.87	33.56	34.56	0.94964243
ZnO_N	38.1	40.35	21.55	0.94423792
ZnO_A	32.45	33.71	33.83	0.96262237

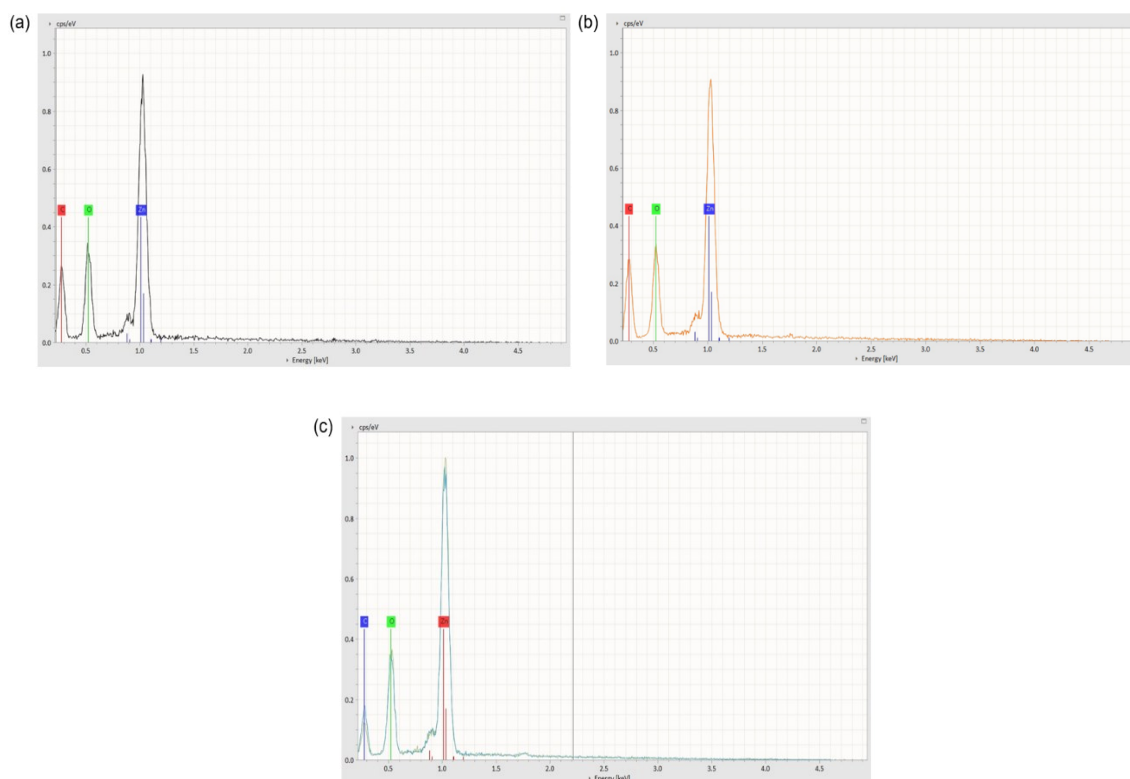

Figure 4.6 EDX of ZnO_P (a), ZnO_N (b) and ZnO_A (c).

Figure 4.6 and table 4-1 reveal the EDX results for samples ZnO_P, ZnO_N and ZnO_A, which proves the existence of Zn element. ZnO_A has the highest Zn/O atom ratio compared to ZnO_P and ZnO_N, it could be because calcination process at high temperature in air and pure N_2 changed the oxygen content. But the atoms ratio between Zn and O of these three samples are quite closed, which indicates that the calcination environment did not change too much the chemical compositions.

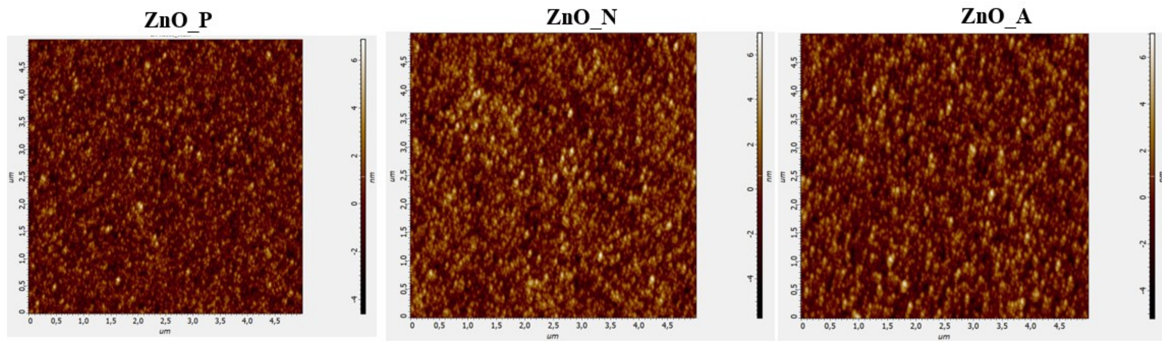

Figure 4.7 AFM of ZnO_P, ZnO_N and ZnO_A nano sensing films.

Fig. 4.7 reveals the surface roughness results of these three samples obtained by AFM tools, which also indicates no big change of the surface roughness after heat treatment in different environments. Table 4-2 shows the average roughness details about root mean square roughness (S_q) and average roughness (S_a) of ZnO_P, ZnO_N and ZnO_A. ZnO_P has the flattest surface among ZnO_N and ZnO_A, the result could be related to the particle size, since ZnO_P owns the smallest particles and most even size distribution.

Table 4-2 Roughness of ZnO_P, ZnO_N and ZnO_A sensing films

Materials	Sq (nm)	Sa (nm)
ZnO_P	1.321	1.051
ZnO_N	1.492	1.186
ZnO_A	1.593	1.269

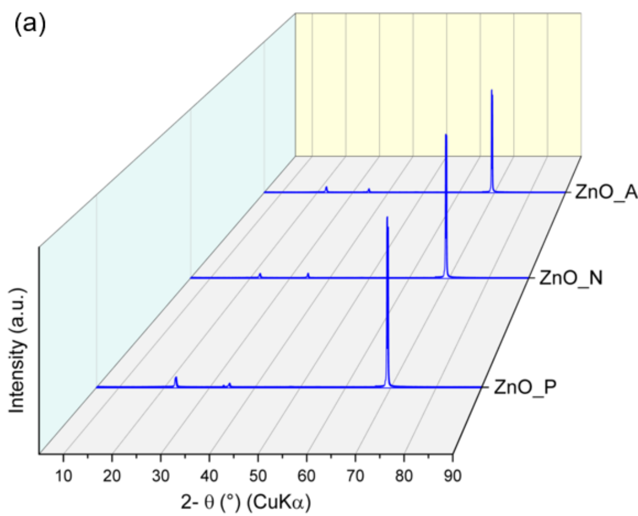

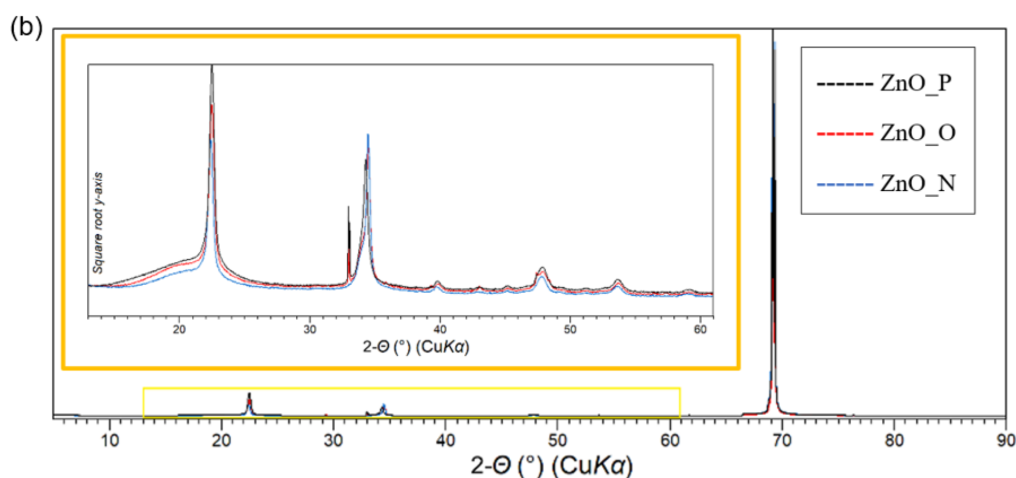

Figure 4.8 X-ray diffraction patterns collected at room-temperature for the as-prepared samples of ZnO_P, ZnO_O and ZnO_N (a); and a magnification of their comparison (square root of the y-axis) in the 13-61 °2θ angular range (b).

XRD was used to examine the crystalline structure and phase purity of the produced ZnO nanorods. The XRD data was gathered on a Bruker D8 Advance Da Vinci diffractometer with Bragg-Brentano geometry and a Cu-anode X-ray tube, Ni-filter to restrict contribution of the CuK component, and a LynxEye XE silicon strip detector (angular range covered by the detector = 2.585° 2), CuK radiation was distinguished. These samples under investigation were put in a height-adjustable poly (methyl methacrylate) specimen holder and scanned in a continuous mode from 5 to 90° 2 with a step size of 0.02° 2 and a counting duration of 2 s per step. A knife placed at a submillimeter distance from the sample and perpendicular to the specimen holder was utilized to reduce air-induced scattering at low angles. Figure 4.8 depicts X-ray powder diffraction patterns recorded at room temperature for the investigated substances and all demonstrates the ZnO nanofilm XRD pattern. The wurtzite hexagonal ZnO phase peaks were detected in the XRD spectrums of 31.77°, 34.44°, 36.26°, 47.56°, 56.60°, and 62.89°, respectively, reflecting (100), (001), (102), (110), and (103) [10]. The strongest peak (002) showed development of ZnO nanorods along the c-axis (JCPDS no. 036-1451). It tends to grow fastest in that direction because the (002) plane has the lowest surface energy with its c-axis perpendicular to the substrate [12]. The obtained XRD patterns are nearly identical. Thus, the heat treatment at 650 °C in varied atmospheres had no effect on the initial sample's phase composition. The ZnO sample's XRD pattern is dominated by Si 400 Bragg reflections belonging to the (100)-oriented Si substrate wafer. In addition, the appearance of the basis-prohibited Si 200 reflection at approximately 33° due to the multiple diffraction effect [16].

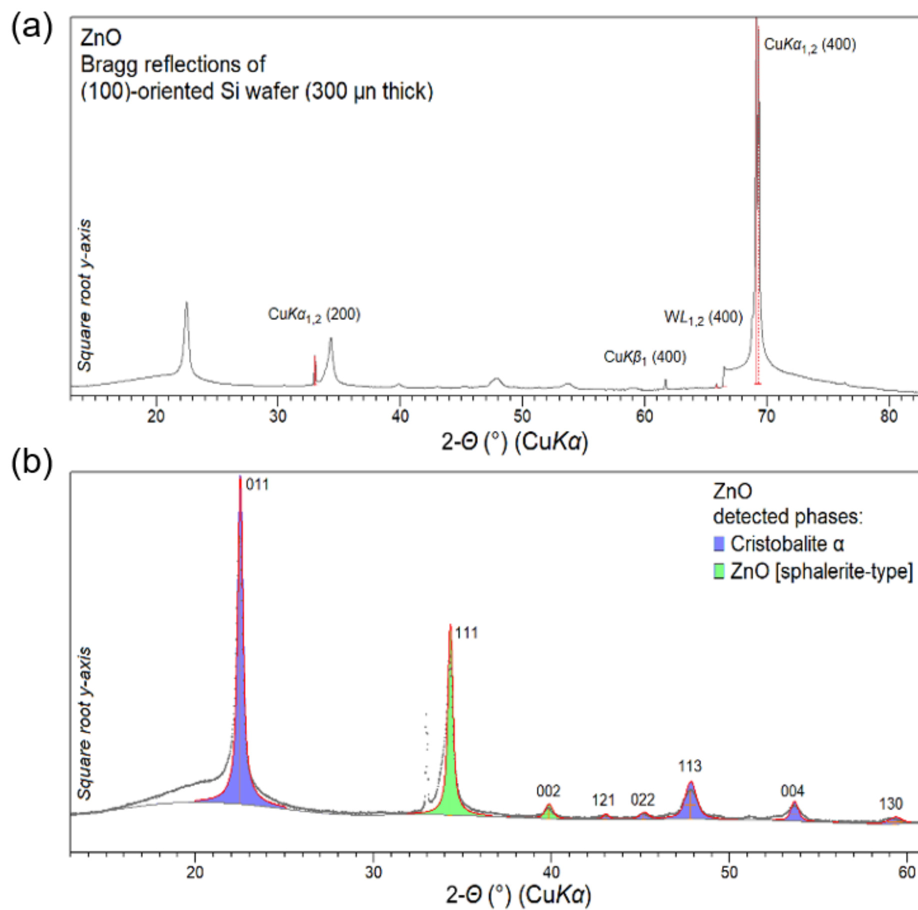

Figure 4.9 Assignment of diffraction peaks to the observed crystalline phases, namely -cristobalite and ZnO with sphalerite-type structure, and to those of the (100)-oriented Si wafer utilized as substrate (a) (b).

The XRD pattern for the sample ZnO is distinguished by a collection of diffraction peaks from various crystalline phases, but with a lesser intensity than that of the (100)-oriented Si support. In particular, hydration and heat treatment convert the tetraethoxysilane (TEOS) precursor into a SiO_2 crystalline phase having peaks that can be properly correlated with those of -cristobalite [17]. Other diffraction peaks, the most prominent of which is located at around 34.3 °2, are connected to those of a cubic sphalerite-type Zn oxide [18]. A line profile analysis of the diffraction peaks, which was used to determine the crystallite size of the latter phases, shows that the -cristobalite phase contains smaller crystallites than the ZnO sphalerite-type (on average, 17(2) vs. 29(4) nm, respectively) phase.

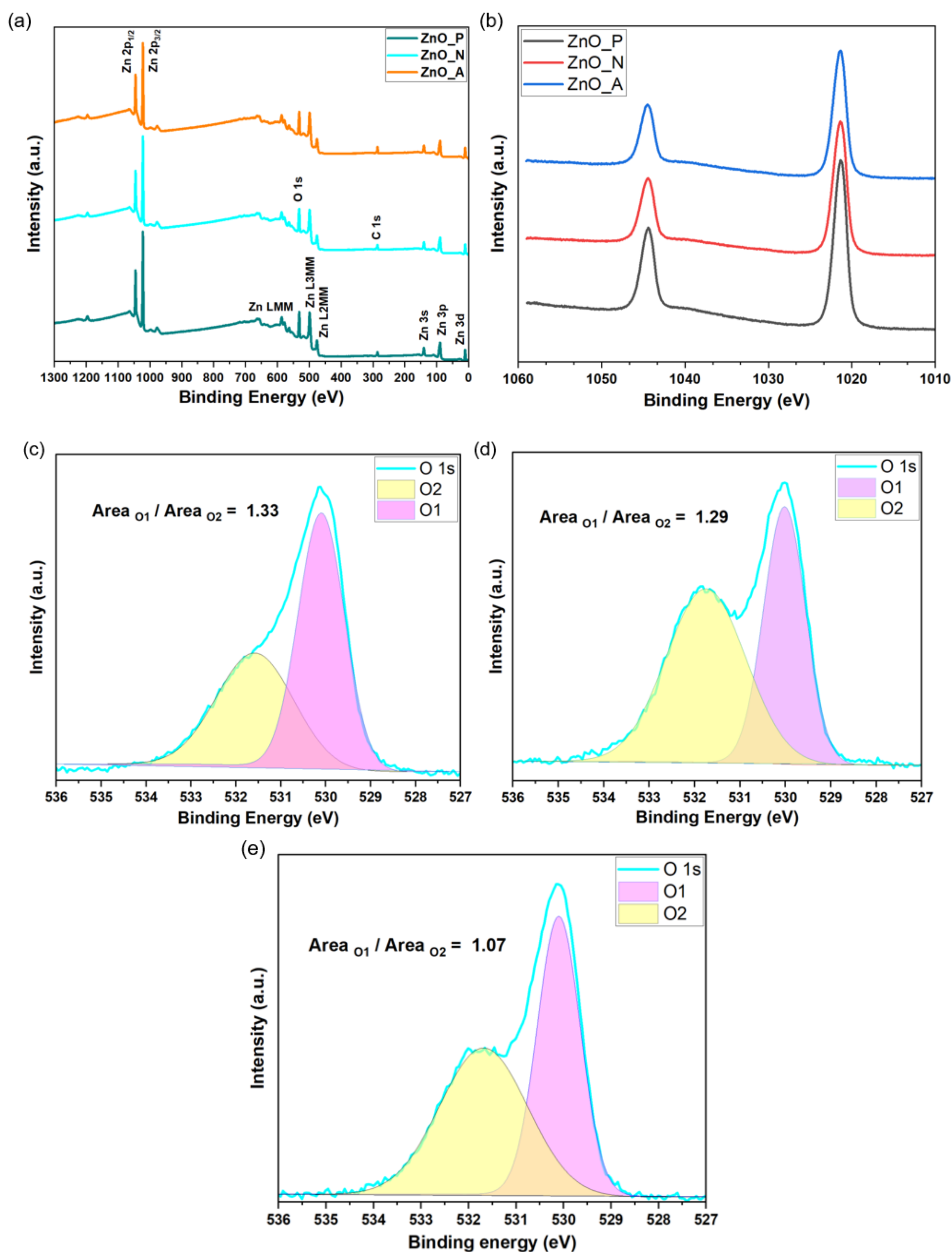

Figure 4.10 XPS of ZnO samples: a). Survey scan; b). Zn 2p region of samples; O 1s peak of c), ZnO_P, d). ZnO_N and e). ZnO_O.

The chemical constitutions and oxidation states of ZnO_P, ZnO_N and ZnO_A was conducted by XPS, which owned ZnO nano film before and after calcination under N_2 and O_2 at 650 °C. As displayed in Fig. 4.10a, the survey of XPS spectrum of ZnO samples is

exhibited, in which it manifests the existence of Zn, O elements, and trace amount of C in the sample. Fig. 4.10b shows Zn 2p including $2p_{3/2}$ and $2p_{1/2}$ states at binding energy of around 1044.4eV. From ZnO_P to ZnO_N and ZnO_A, Zn 2p peak faintly move to higher energy by 0.1 eV. Fig. 4.10 c, d and e show O 1s spectrum, which can be deconvoluted into two peaks, O1, and O2 corresponding to Zn-O, C-O and C=O at 530.6 eV and 532.7 eV separately [13, 19]. The first component O1 is associated to O^{2-} ions in the wurtzite structure of a hexagonal Zn^{2+} ion array, surrounded by Zn atoms with their full complement of nearest neighbor O^{2-} ions, while O2 can be ascribed both to hydroxide and to O atoms residing in oxygen-deficient environments within the ZnO matrix [20]. Zn and atoms ratio was calculated based on XPS data, ZnO_O has the highest oxygen atom density compared to ZnO_P and ZnO_N. The results are listed in table 4-5.

Table 4-5 Atoms ratio between Zn and O.

Samples	Zn	O	C	Zn/O
ZnO_P	39	41.7	19.4	1.8
ZnO_N	33	38.6	28.4	1.8
ZnO_A	33.7	41.4	24.9	1.9

4.3.2 Resistance Measurement

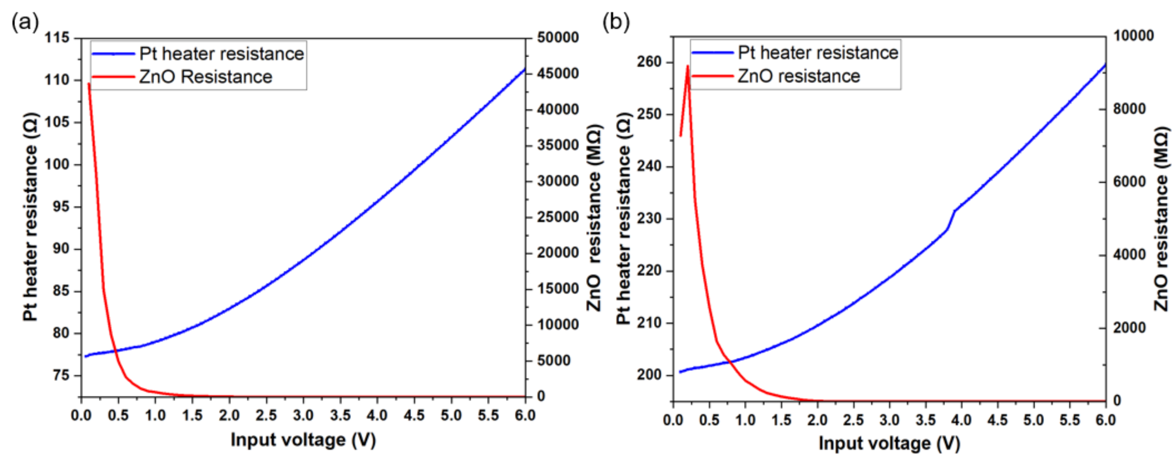

Figure. 4.11 The resistance of Pt heater and ZnO_A sensing film at different input voltage on MHP2_R and MHP2_C.

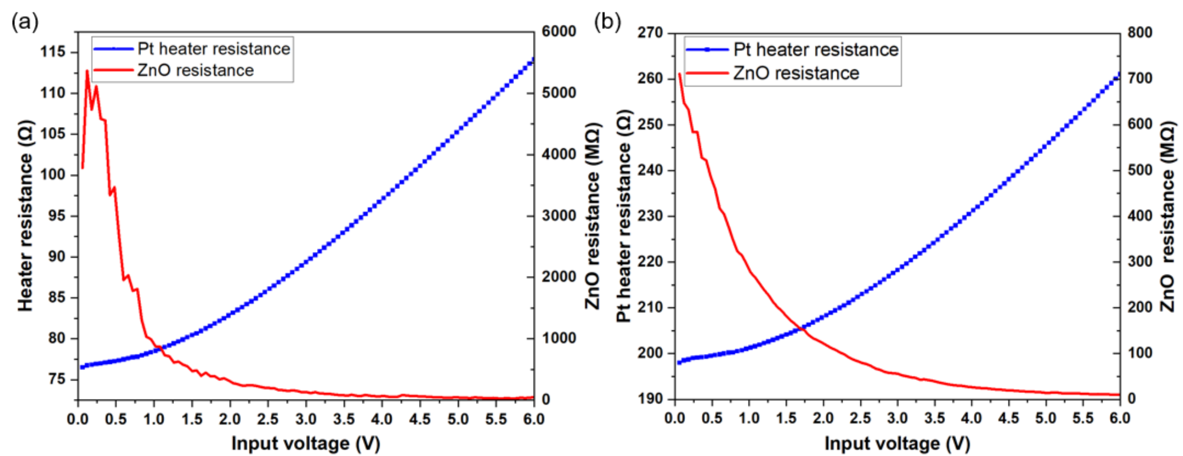

Figure. 4.11 The resistance of Pt heater and ZnO_N sensing film at different input voltage on MHP2_R and MHP2_C.

Fig. 4.11 reveals the resistance values changing of MHP2_R and MHP2_C with ZnO on them. Pt heater resistance value increased with increasing input voltage, and ZnO resistance changing trend was opposite way. That is the difference of resistance changing between the pure metal and semiconductor material of ZnO when they are heated up. Comparing MHP2_R and MHP2_C resistance values, MHP2_C resistance was almost three times bigger than MHP2_R at room temperature due to its longer circuit length. When the voltage was 6 V, the resistance of MHP_R was enlarged by 1.43 times, while MHP_R resistance was increased by 1.3 times, which means that MHP2_R achieved higher operational temperature than MHP2_C. ZnO resistance decreased fast when the voltage changing was below 1.5V, which means ZnO resistivity changed fast when the temperature was not very high. But when the input voltage on ZnO was higher than 1.5V, the resistance did not change too much.

Comparing ZnO_N and ZnO_P, it is easy to find that after calcination of 650°C in N_2 environment, the resistance was decreased by around 9 times for ZnO on MHP2_R and 10 times for ZnO on MHP2_C.

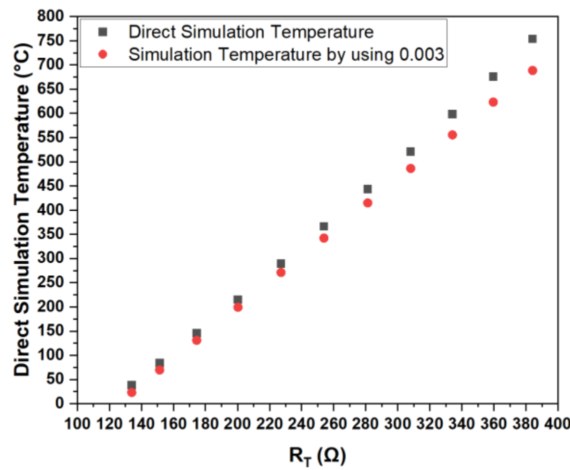

Figure 4.12 The difference of temperature obtained between COMSOL simulation results and calculation results (by using TCR of Pt α=0.003).

Fig. 4.12 compared the temperature difference between COMSOL simulation results and calculation results by using TCR coefficient of Pt (α = 0.003). The results are quite near to each other, especially at low temperature.

4.3.3 Gas Sensing Test

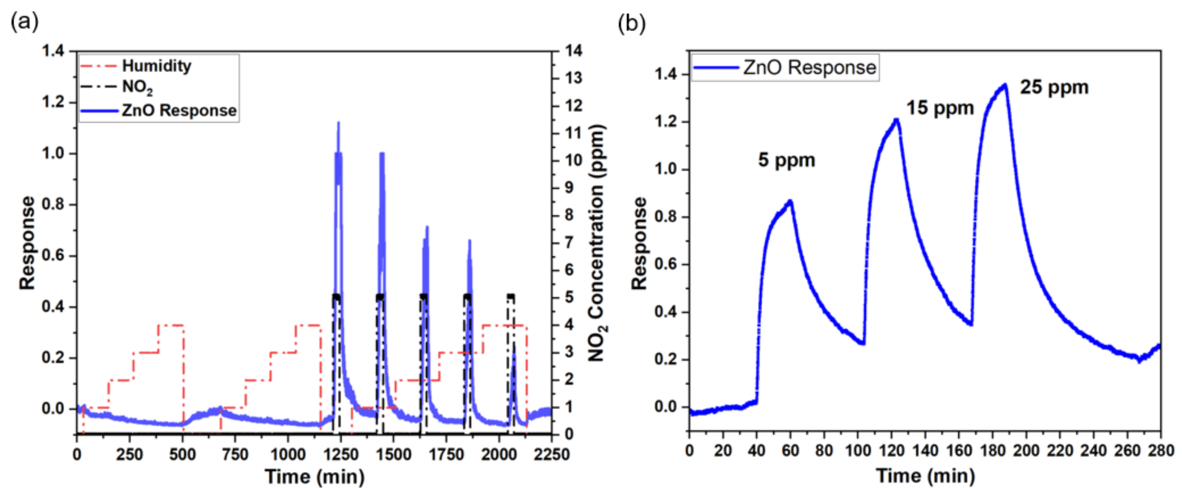

Figure 4.13 a). ZnO nanofilm response under 5 ppm NO_2 with different humidity; b). ZnO nanofilm response under NO_2 with different concentrations of 5ppm, 15ppm and 25ppm in dry air.

In this part we tested ZnO on MHP2_C sensing properties under different targeted gases of NO_2 and ethanol. Fig. 4.13 exhibits ZnO sensitivity under different humidity conditions and NO_2 target gases. In the beginning, when ZnO was exposed to humidity with different HR%, ZnO did not show related response, the resistance of ZnO gradually decreased. During the break, its resistance increased a little, and decreased again after the second loop of humidity injection. Then 5ppm NO_2 was inserted into the gas chamber under different humidity

conditions. In the first injection loop of NO_2 without humidity, the response of ZnO achieved the response of 1.1. After injecting humidity, the response of ZnO towards to NO_2 gradually decreased. Pure humidity environment did not cause huge response, but decreasing response towards NO_2 gas. It means that there was very weak chemical reaction between H_2O with ZnO, the reason why the response of ZnO towards NO_2 decreased under humidity could be H_2O molecules took up reaction sites, hence, less active spots on ZnO surface can react with NO_2.

This time we tested ZnO sensitivity under certain humidity of 40%RH towards different concentration of NO_2 (5ppm, 15ppm and 25ppm) at room temperature. Fig. 4.13b shows that with increasing NO_2 concentration, the response of NO_2 increased too.

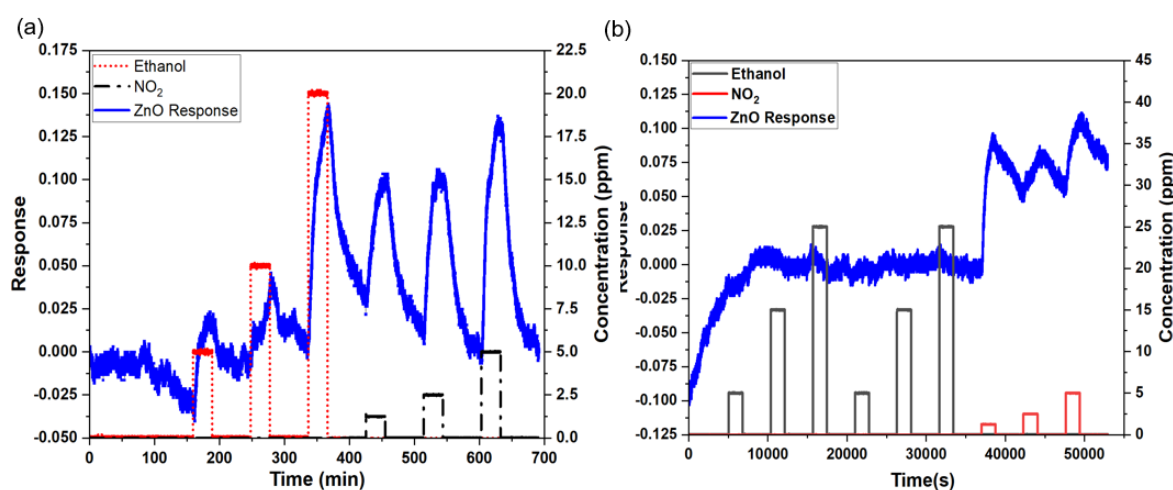

Figure 4.14 a). ZnO sensing film response under 5 ppm, 15 ppm and 25 ppm ethanol and 1.25 ppm, 2.5 ppm and 5 ppm NO_2 with 40 RH% humidity; b). ZnO nanofilm sensing response under ethanol and NO_2 with different concentration.

The response of ZnO towards ethanol with concentration of 5 ppm, 15 ppm and 25 ppm and NO_2 with concentration of 1.25 ppm, 2.5 ppm and 5 ppm was measured in 40% RH environment. In the test under ethanol, ZnO showed gradually increasing response. Specifically, when the concentration of ethanol was high (25 ppm), the response was decreased obviously. ZnO also shows gradually enlarged response towards increasing concentration of NO_2.

ZnO_R on MHP2_C then was tested under the same environment with ethanol and NO_2. In this case ZnO_R did not show apparent response towards ethanol, but very week response toward NO_2 gas.

4.4 Sensing Mechanism.

The adsorption, oxidation, and desorption of target gases on the surface can be summed up as the gas sensing mechanism for ZnO material during the sensing process. Adsorbed oxygen molecules from the atmosphere first attach to the surface of the ZnO material, where they subsequently capture electrons from the conduction band to form oxygen negative ions (O_2^-, O^-, O^{2-} formations depends on operational temperature listed below) [8, 10]. Consequently, electrons are produced throughout the process of a gas sensing mechanism when target gases interact with sensor materials. Both the sensing surface area and the electron properties influence the parameters of the gas sensor. Then, the sensing material with a larger specific surface area provides more active sites and boosts sensitivity, and these ions become surface acceptor states. As a result of the loss of electrons in the conduction band, a zone of electron depletion with a high potential barrier is formed on the surface of the ZnO material. This depletion zone hinders the free movement of electrons among the ZnO crystal grains.

$$O_{2\,gas} \leftrightarrow O_{2\,ads}$$

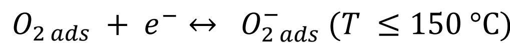

$$O_{2\,ads} + e^- \leftrightarrow O^-_{2\,ads}\ (T \leq 150\ °C)$$

$$O_{2\,ads} + e^- \leftrightarrow 2O^-_{ads}\ (150\ °C \leq T \leq 300\ °C)$$

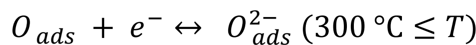

$$O_{ads} + e^- \leftrightarrow O^{2-}_{ads}\ (300\ °C \leq T)$$

$$NO_{2\,gas} + e^- \leftrightarrow NO^-_{2\,ads}\ (T \leq 150\ °C)$$

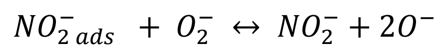

$$NO^-_{2\,ads} + O^-_2 \leftrightarrow NO^-_2 + 2O^-$$

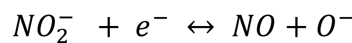

$$NO^-_2 + e^- \leftrightarrow NO + O^-$$

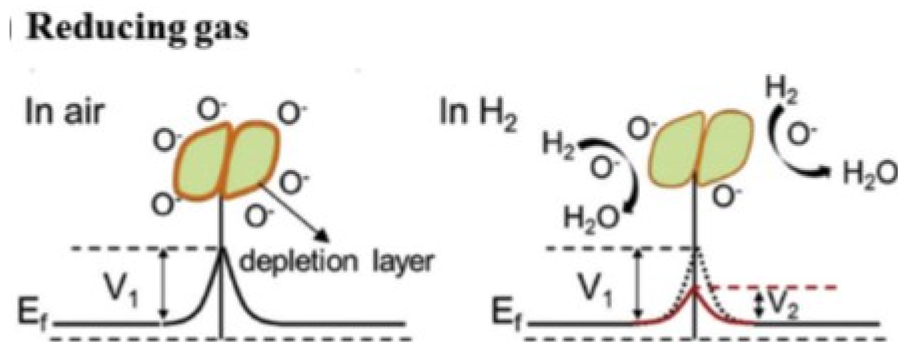

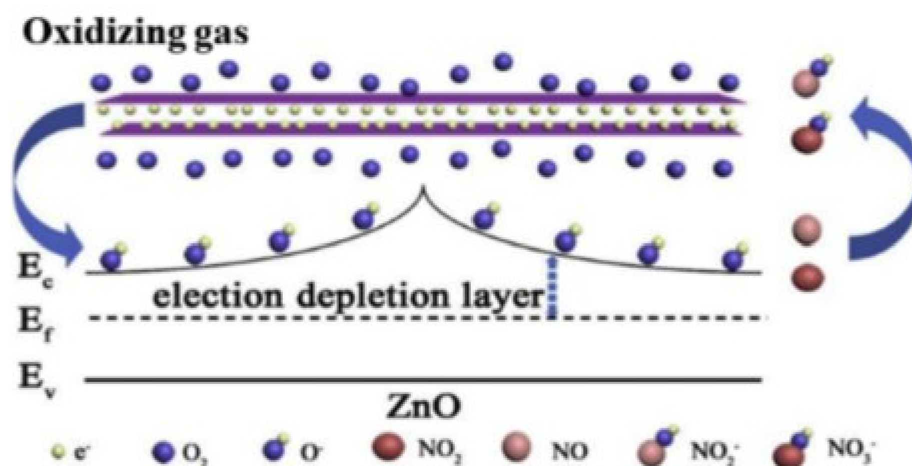

Figure 4.15 schematic representation of sensing mechanism for ZnO [8]. Reprinted from [8].

Once the chemical adsorption process reaches equilibrium, the resistance of ZnO remains constant. In the presence of ethanol reducing gas, oxygen anions are oxidized due to an interaction between the reducing gas and the oxygen anions. This occurrence initiates a charge transfer process in which extra free electrons return to the conduction band of ZnO. As a result, the electron depletion layer becomes thinner and the carrier density becomes more concentrated, causing the resistance value of ZnO to decrease until equilibrium is attained. When ZnO is exposed to the oxidizing gas NO_2, the oxidizing gas continues to grab electrons as O_2 does, resulting in a considerable drop in carrier density. In addition, the material resistance grows until it achieves a state of equilibrium. Fig. 4.15 depicts this gas sensitivity mechanism [8].

4.5 Chapter Summary

After we obtained NHP1 and MHP2 devices, we deposited n-type sensing material ZnO on them by magnetron sputtering with the thickness of 120 nm. Then deposited ZnO nano film (ZnO_P) was calcinated in air (ZnO_A) and N_2 (ZnO_N) and at 650°C. The calcination environments did change the particle size of ZnO, ZnO_P exhibited well-distributed size with diameter of 10 nm, after calcination in N2 gas environment, ZnO grew to around 100 nm, and around 120 nm in average with some big particle size of 500 nm in air environment. XRD revealed that the calcination environment did not change the crystal structure of ZnO. XPS proved the existence of ZnO, and calcination conditions did not change the atom ratio of Zn and O on the super facial surface, which was also supported by EDS results. ZnO deposited on SiO_2 layer showed great resist to TMAH etch, but poor resist to HF etch.

For the electrical performance test of ZnO, we inserted voltage on ZnO_A and ZnO_N materials. Both materials showed decreased resistance of ZnO, and ZnO_N owned much less resistance value than ZnO_A. ZnO_A resistance did not change too much after the voltage was above 2 V, while ZnO_N resistance gradually decreased at voltage ranging from 0 to 6 V.

In the end, we tested ZnO_N nano film sensing response. ZnO_N nano film did not show positively correlated response toward increasing humidity, but under 5 ppm NO_2 target gas, increasing humidity environment could decrease the response of ZnO_N nano film. In dry air, ZnO_N nano film showed enlarged response within increasing NO_2 target gas concentration from 5 ppm to 25 ppm. ZnO showed increased response under target gases of ethanol with concentration of 5 ppm, 15 ppm and 25 ppm, and NO2 with concentration of 1.25 ppm, 2.5 ppm ad 5 ppm under 40 RH% humidity. But when the environment switched to day air, ZnO_N did not show positively correlated response toward ethanol with increasing concentration.

References

[1] H. Nazemi, A. Joseph, J. Park, and A. Emadi, "Advanced Micro- and Nano-Gas Sensor Technology: A Review," *Sensors (Basel),* vol. 19, Mar 14 2019.

[2] L. Spinelle, M. Gerboles, G. Kok, S. Persijn, and T. Sauerwald, "Review of Portable and Low-Cost Sensors for the Ambient Air Monitoring of Benzene and Other Volatile Organic Compounds," *Sensors,* vol. 17, p. 1520, 2017.

[3] M. I. A. Asri, M. N. Hasan, M. R. A. Fuaad, Y. M. Yunos, and M. S. M. Ali, "MEMS Gas Sensors: A Review," *IEEE Sensors Journal,* vol. 21, pp. 18381-18397, 2021.

[4] M. A. Franco, P. P. Conti, R. S. Andre, and D. S. Correa, "A review on chemiresistive ZnO gas sensors," *Sensors and Actuators Reports,* vol. 4, p. 100100, 2022.

[5] T.-J. Hsueh, C.-H. Peng, and W.-S. Chen, "A transparent ZnO nanowire MEMS gas sensor prepared by an ITO micro-heater," *Sensors and Actuators B: Chemical,* vol. 304, p. 127319, 2020.

[6] L. Zhu and W. Zeng, "Room-temperature gas sensing of ZnO-based gas sensor: A review," *Sensors and Actuators A: Physical,* vol. 267, pp. 242-261, 2017.

[7] I. S. Jeon, G. Bae, M. Jang, Y. Yoon, S. Jang, W. Song*, et al.*, "Atomic-level mediation in structural interparameter tradeoff of zinc oxide nanowires-based gas sensors: ZnO nanofilm/ZnO nanowire homojunction array," *Applied Surface Science,* vol. 540, p. 148350, 2021.

[8] Y. Kang, F. Yu, L. Zhang, W. Wang, L. Chen, and Y. Li, "Review of ZnO-based nanomaterials in gas sensors," *Solid State Ionics,* vol. 360, p. 115544, 2021.

[9] A. A. Baharuddin, B. C. Ang, A. S. M. A. Haseeb, and Y. H. Wong, "Improvement of N-ZnO chemiresistive gas sensor toward lower detection limit of acetone and ethanol at low operating temperature," *Materials Letters,* vol. 303, p. 130562, 2021.

[10] V. T. Duoc, C. M. Hung, H. Nguyen, N. V. Duy, N. V. Hieu, and N. D. Hoa, "Room temperature highly toxic NO_2 gas sensors based on rootstock/scion nanowires of SnO_2/ZnO, ZnO/SnO_2, SnO_2/SnO_2 and, ZnO/ZnO," *Sensors and Actuators B: Chemical,* vol. 348, p. 130652, 2021.

[11] R. Kumar, O. Al-Dossary, G. Kumar, and A. Umar, "Zinc Oxide Nanostructures for NO_2 Gas-Sensor Applications: A Review," *Nanomicro Lett,* vol. 7, pp. 97-120, 2015.

[12] M. Sik Choi, M. Young Kim, A. Mirzaei, H.-S. Kim, S.-i. Kim, S.-H. Baek*, et al.*, "Selective, sensitive, and stable NO_2 gas sensor based on porous ZnO nanosheets," *Applied Surface Science,* vol. 568, p. 150910, 2021.

[13] V. Paolucci, J. De Santis, L. Lozzi, M. Rigon, A. Martucci, and C. Cantalini, "ZnO thin films containing aliovalent ions for NO_2 gas sensor activated by visible light," *Ceramics International,* vol. 47, pp. 25017-25028, 2021.

[14] K. Kasirajan, L. Bruno Chandrasekar, S. Maheswari, M. Karunakaran, and P. Shunmuga Sundaram, "A comparative study of different rare-earth (Gd, Nd, and Sm) metals doped ZnO thin films and its room temperature ammonia gas sensor activity: Synthesis, characterization, and investigation on the impact of dopant," *Optical Materials,* vol. 121, p. 111554, 2021.

[15] B. Sharma and J. S. Kim, "MEMS based highly sensitive dual FET gas sensor using graphene decorated Pd-Ag alloy nanoparticles for H_2 detection," *Sci Rep,* vol. 8, p. 5902, Apr 12 2018.

[16] P. Zaumseil, "High-resolution characterization of the forbidden Si 200 and Si 222 reflections," *J Appl Crystallogr,* vol. 48, pp. 528-532, Apr 1 2015.

[17] J. M. Ruso, A. N. Gravina, N. L. D'Elia, and P. V. Messina, "Highly efficient photoluminescence of SiO2 and Ce-SiO_2 microfibres and microspheres," *Dalton Trans,* vol. 42, pp. 7991-8000, Jun 14 2013.

[18] S. Cui, W. Feng, H. Hu, Z. Feng, and Y. Wang, "Structural and electronic properties of ZnO under high pressure," *Journal of Alloys and Compounds,* vol. 476, pp. 306-310, 2009.

[19] D. Yang, A. G. Ramu, Y. Lee, S. Kim, H. Jeon, S. V E*, et al.*, "Fabrication of ZnO nanorods based gas sensor pattern by photolithography and lift off techniques," *Journal of King Saud University - Science,* vol. 33, p. 101397, 2021.

[20] Chang Cao, Xinxin Xie, Yamei Zeng, Shaohua Shi, Guizhen Wang, Liang Yang, Cai-Zhuang Wang, Shiwei Lina, "Highly efficient and stable p-type ZnO nanowires with piezotronic effect for photoelectrochemical water spiltting," *Nano Energy*, vol. 61, July 2019, p. 550-558.

5. Thick Film Gas Sensor of SMO SnO_2 Doped by Antimony Deposited on MEMS-based MHP1

5.1 Introduction

In recent years, the air pollution problem has been gravely exacerbated and poses a threat to public health due to the growth of industry, the development automobiles, and the increasing population. Numerous toxic substances are released into the atmosphere by automotive and industrial exhaust, contributing to environmental pollution and air quality issues. On the one hand, they may pose environmental risks and emit hazardous contaminants [1-3]. After being absorbed by the human body, these dangerous gases will induce irreparable tissue damage. Concurrently, indoor air pollution has become a "silent killer" that impairs the health of individuals. Formaldehyde, benzene, and ammonia, which are present in new buildings and organic synthetic materials used for interior decorating, have carcinogenic effects on the human body and pose a grave threat to human health [4]. For example, the maximum concentration for SO_2 exposures of 30 minutes to one hour has been estimated to be between 50 and 100 ppm, the lethal concentration for 50% of those exposed to NO_2 for one hour in humans has been estimated to be 174 ppm, and the maximum concentration for H_2S exposure for one hour has been estimated to be between 170 and 300 ppm [3]. Because of the poor gas-surface interaction, only limited chemisorption and primarily physisorption are occurring, making it virtually impossible to detect it electronically. Therefore, the creation of a sensitive and effective gas sensor is absolutely necessary for the detection of dangerous gases. Gas sensor devices use SMO because of their chemical stability, rapid reaction, and affordable manufacturing [5-8]. These materials can be divided into two groups: p-type materials, such as Cr_2O_3, CuO, NiO, and Co_3O_4, whose resistance is easily changed by gas adsorption and desorption kinetics; and n-type materials include SnO_2, ZnO, WO_3, Fe_2O_3, and TiO_2 [2, 9-11]. According to the basic sensing mechanism, SMO gas sensor conductivity is regulated by the varying surface concentrations of unsaturated oxygen adsorption sites, which are determined by the equilibrium between oxygen adsorption and surface reactivity between the oxygen adsorbate and target gases [12].

Thanks to its steady-state chemical and physical properties at various temperatures, SnO_2, which has a broad band gap of roughly 3.6 eV at 300 K, is one of the most widely used semiconductor materials for gas sensors [13]. The high working temperature and low

selectivity of SnO_2-based gas sensors are still issues to be resolved [14-17]. The nanostructure alteration and metal element doping are two moderately successful methods for boosting the sensitivity and selectivity of SnO_2, according to the sensing mechanism model [18-20]. The synthesis of SnO_2 in a variety of nano-morphologies, such as thin films, nanowires, nanoflowers, nanofibers, nano hollow, 2D flakes, nanospheres, 3D mesoporous, and hollow spheres, has been investigated by research works [20-29]. Additionally, doping with noble elements such as S, Cu, Pd, Ru, Al, Pt, Sb, Ce, Ag, and Ti can alter the energy band structure of SnO_2 [14-16, 18-20, 30-36].

Doping is a more reliable and cost-effective method than modifying the nanostructure of a material to improve the efficacy of gas sensing [37]. Sb doped SnO_2 (ATO) can be used as a transparent conducting thin film for gas sensors, optoelectronic devices, and solar cells because of its quasi-metallic conductivity property [16]. Sb ions may occur in the crystal structure of SnO_2 as either Sb^{3+} or Sb^{5+}, depending on the circumstances of the synthesis (temperature, doping concentration, etc.) [19, 37-39]. Doping SnO_2 with Sb ions can significantly modify the electrical, electrochemical, and optical properties of the material [40, 41]. In point of fact, exchanging Sn^{4+} for Sb^{3+} results in the formation of a shallow acceptor level close to the valence band [16, 42, 43]. On the other hand, exchanging Sn^{4+} for Sb^{5+} results in the formation of a shallow donor level close to the SnO_2 conduction band. The kind of conductivity and the concentration of free carriers on doped materials are both determined by the ratio of Sb^{5+} sites to Sb^{3+} sites [25]. The introduction of Sb atoms into SnO_2 often results in the formation of oxygen vacancies, which act as donors in the compound. By contributing additional electrons to the conduction band, it is possible that a single or double ionization will emerge in the vacancies [44]. ATO, which possesses exceptional semiconducting characteristics, has attracted a lot of attention as a potential active material in gas sensors. In order to improve the material stability in an oxygen environment, Gayatri Joshi and colleagues doped SnO_2 with a maximum of 2 at.% of Sb. However, they found that 1 at.% Sb doped SnO_2 thin-film sample produced the best sensing results [45]. ATO nanowires were synthesized by Jae-Hun Kim and colleagues using an ion implanter with different Sb doses of $2x10^{13}$, $2x10^{14}$, and $2x10^{15}$ ions/cm^2. They then described the sensing properties under different target gases of NO_2, O_2, and SO_2, and found that the lowest dose gas sensor exhibited the best performance in this instance [37]. Formaldehyde gas in varying quantities was detected using a gas sensor that was developed by Qi Wei and colleagues [25]. This sensor was based on a 5 mol%

ratio of ATO. Another ATO nanoribbons sensing material was deposited by Jiang Ma et al. through the process of thermal evaporation. This material displayed an exceptionally high response to H_2S gas in comparison to other two toxic gases, namely NO_2 and CO. Even at room temperature, it exhibited relatively high sensitivity and good selectivity [46]. Kamalpreet Khun Khun et al. used a nonaqueous sol-gel process to generate ATO powder with concentrations ranging from 0 to 6 mol%. They next investigated the powder sensitivity to 50 ppm NH_3, acetone, and ethanol at room temperature. In their research, the ATO-based gas sensors demonstrated an exceptional selectivity to NH_3 with a response value of approximately 4316 % for the samples containing 4 mol% of Sb [47].

It is common knowledge, supported by the findings of research conducted by other groups, that increased doping levels can occasionally result in an enhancement in the sensing performance of active materials. For instance, M.C. Carotta et al. observed that increasing the titanium ratio in SnO_2 to a greater value (0.5 mol% compared to 0.1 mol% and 0 mol%) improved gas reactions under dry and wet CO at temperatures of 550 °C and 600 °C [48]. According to the findings of S. Morandi team, tungsten oxide with a higher tin atom ratio (Sn 0.12 mol% as opposed to 0 mol% and 0.0018 mol%) displayed a greater reactivity to NO_2 when heated to 250 °C [18]. Iron oxide that has been heavily doped with samarium and created by A. Gaiardo and colleagues ($SmFeO_3$) was capable of detecting carbon monoxide with great repeatability and was ultimately used as a sensing material in the SCENT prototype for the screening of cancer [49]. To the best of our knowledge, substantially Sb-doped SnO_2 has been examined as a gas sensor material, but the majority of doping levels that are used for gas sensing applications were under 5 wt% so far. Therefore, in this work, we have carried out an examination to compare the sensing capability of pure nanostructured SnO_2 (S1) and substantially Sb-doped SnO2 by employing two distinct concentrations of 10 wt% and 15 wt% Sb, named as ATO1 and ATO2, respectively.

5.2 Sensing Materials and Sensor Devices Preparation

S1, ATO1 and ATO2 pastes were obtained by gelation under hydrothermal conditions of the corresponding commercially available SnO_2 colloidal solutions (15% in water, Alfa Aesar, Ward Hill, MA, USA) and 10wt% Sb doped SnO_2 (50% in water, Alfa Aesar, Ward Hill, MA, USA). This process resulted in the formation of SnO_2 (S1) and 10 wt% in order to make a paste acceptable for screen printing. These powders were combined with the appropriate organics in a suitable ratio. To be more specific, powders was combined with ethyl cellulose

served as an organic binder, and α-terpineol served as a liquid phase. In order to achieve a stable, finely dispersed colloidal precursor, the resulting viscous pastes were subjected to additional homogenization in an ultrasonic bath for 30 min at 30℃. Then the colloidal pastes of S1, ATO1, and ATO2 were drop coat on MHP1.

MHP1 in this part was utilized to maintain a constant working temperature of up to 500℃ and to provide mechanical support for sensing materials. On top of the microheater, the sensing materials were applied using a drop-coating technique. The microheater is made up of Pt/Ti interdigitated electrodes and a heater that are 120/10 nm thick. Pt/Ti was deposited by electron beam evaporation on a 900 nm ONO stack layer ($SiO_2/Si_3N_4/SiO_2$) that was formed by thermal growth and low-pressure chemical vapor deposition processes above a 300 m thick silicon wafer with a crystal orientation of <100> and a resistivity of 10-20 Ω· m [50, 51].

After the drop coating, the gas sensing devices were subjected to a treatment at 220℃ for 30min in order to eliminate the organic medium, and then at 650℃ for two hours in order to stabilize the active material on the substrate in air. In the end, the devices were ball-bonded onto a typical TO39 support using gold wires, and then they were placed on our specialized sensing measuring equipment in order to undergo electrical characterizations [50, 51]. The sensor film resistance was measured in a home-made test system. Gas test chamber is connected to a peripheral pneumatic system that is made up of mass flow controllers and gas cylinders with authorized concentrations. Due to the fact that the temperature coefficient of resistance (TCR) of the heater was known, the microheater input voltage needed to be modified in order to achieve the correct working temperature for the sensing materials. The data-acquisition system continuously monitored and measured the film resistance [51]. In order to generate a controlled steady-state dried environment in the testing chamber, a total flow rate of 200 sccm worth of artificially produced dry air was pumped into the space for a period of two hours. In order to achieve temperatures of 200°C, 300°C, and 400°C, the input voltage of the microheater was adjusted until the surface of the sensing materials reached a state of thermodynamic stability. In order to acquire the expected values for the analyte concentration, tested gases were combined with dry air in a mixing chamber. After the baseline sensor signal had been stabilized, every target gas injection duration was 30 min. In this work, a number of different gases were tested in dry air to gain a deeper understanding of the selectivity of the sensing materials. These gases included acetaldehyde (2 ppm), ethanol (5 ppm), acetone (5 ppm), H_2S (5 ppm), CO (20 ppm), ethylene (50 ppm), CO2 (400

ppm), NH_3 (100 ppm), and NO_2 (10 ppm). The concentrations of the gases were determined according to the threshold limit values (TLV). After that, sensing characterizations were carried out at various relative humidity percentages (RH%) by utilizing a bubbler system filled with deionized (DI) water and connected to the pneumatic system. Temperature and relative humidity in the gas chamber were measured using a commercial HIH-4000 Honeywell sensor with an accuracy of 3.5%. This was done in order to explore the influence of humidity on the performance of the gas sensing device.

In order to accomplish an investigation into the relationship between the dynamical response and the concentration of various gases, the response value was specified by the following equations:

$$R = (R_{air} - R_{gas})/R_{air} \text{ (in reducing gases)} \quad (5\text{-}1)$$

$$R = (R_{gas} - R_{air})/R_{air} \text{ (in oxidizing gases)} \quad (5\text{-}2)$$

In which R_{gas} and R_{air} are the resistance values measured under target gases and air, respectively.

5.3. Results and Discussion

5.3.1 Morphological and Elemental Studies

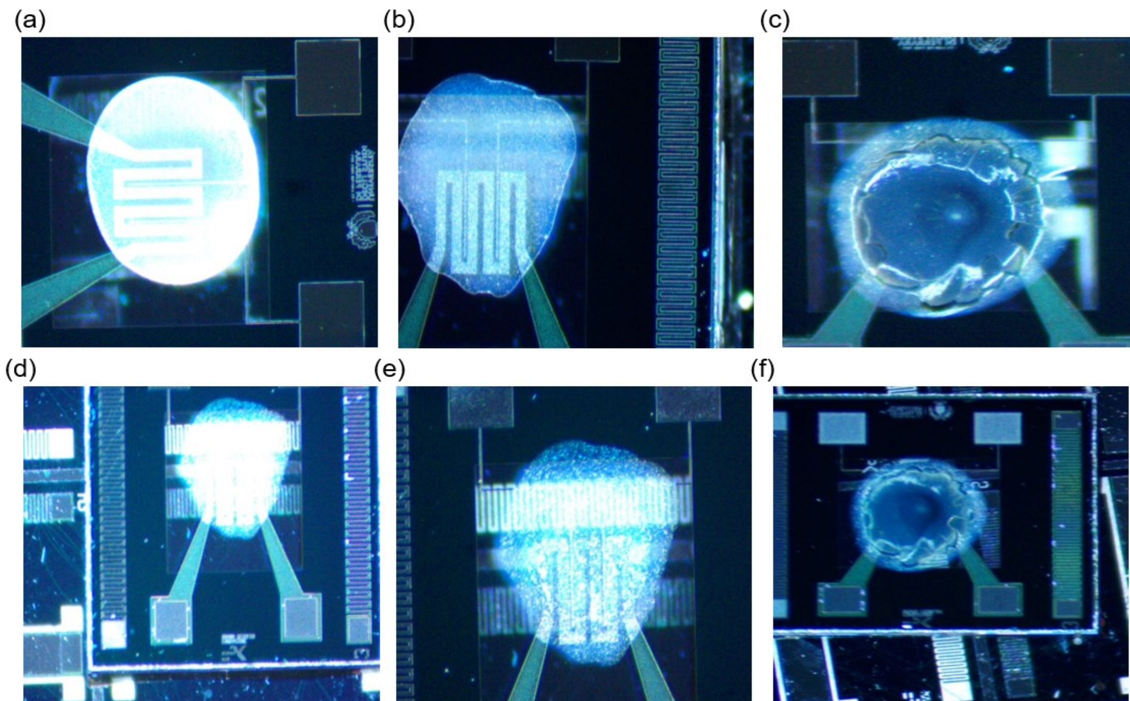

Figure 5.1 Optical microscope images of pastes coated on MHP1 of S1 (a and c), ATO1 (b and d) and ATO2 (c and e) before (a, b, and c) and after calcination (c, d and e).

Figure 5.1 showed the sensing paster dropped coated on MHP1 before and after calcination. The SEM was used to characterize the surface morphology of the samples. The particles in all of the samples presented sphere shape, as seen in Fig. 5.2. SnO_2 particles have an average diameter of 60 nm (as shown in Fig. 5.2a), but the incorporation of Sb into the SnO_2 lattice resulted in a reduction in the grain size of SnO_2, seen as ATO1 and ATO2 particles (ATO1 is less than 30 nm, and ATO2 is less than 10 nm). The particles size of ATO1 and ATO2 are as shown in Fig. 5.2b and Fig. 5.2c, respectively. It is important to note that increasing the level of antimony doping in SnO_2 typically resulted in a decreased particle diameter, which suggests that antimony doping inhibited the growth of the SnO_2-based particles during the powder calcination process. The increase in nanoparticle size that occurred after thermal treatment at high temperatures could be rationalized by referring to the surface energy [19]. In point of fact, smaller particle sizes produce higher surface energies, which could be conveniently minimized during the heat treatment by grain coalescence, and resulted in reduced surface area with a concomitant increase in particle size. When compared to pure SnO_2, the presence of Sb doping caused a decrease in the surface energy of SnO_2, which leaded to the development of smaller particle sizes during the process of nanoparticle synthesis [37].

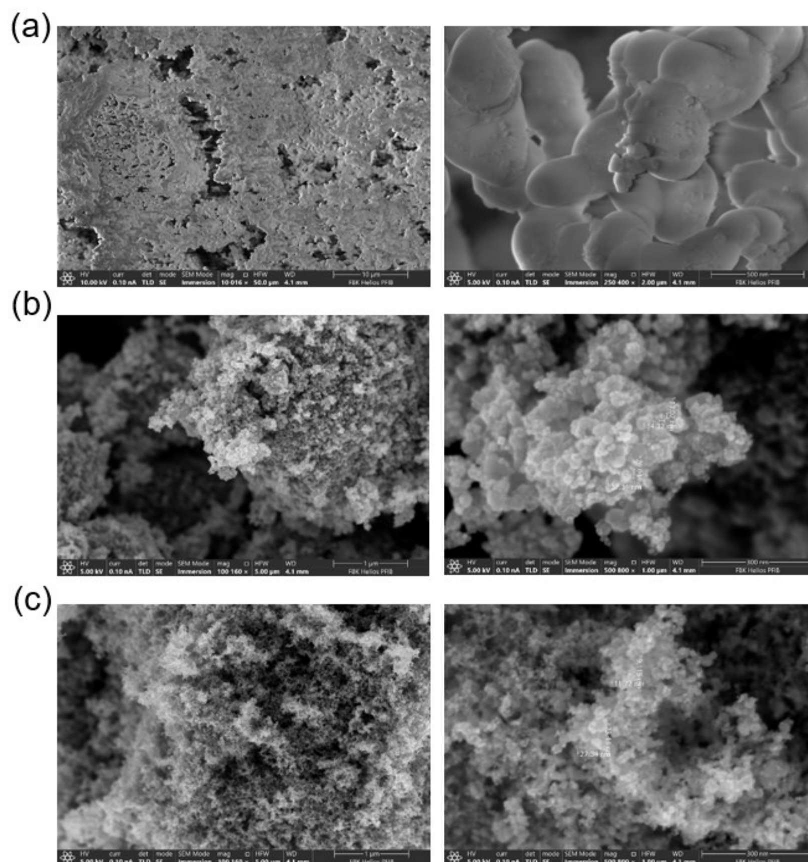

Figure 5.2. SEM images of a) S1; b) ATO1 and c) ATO2 at 250 kX magnification.

XRD analysis was used to investigate and assess the crystal structures of S1, ATO1, and ATO2. XRD patterns of the powders are shown in Figure 5.3a. All of the XRD diffraction peaks, as can be seen in this figure, are easily indexed to the tetragonal crystalline rutile structure of SnO_2, which corresponded to PDF 00-041-1445, P42/nmn. The characteristic peaks of the rutile crystal phase have been identified as (110), (101), (200), and (211), with their respective locations being 26.6°, 33.89°, 37.95°, and 51.78°. Table 5-1 displays the lattice parameters a and c estimated from XRD analysis. It can be seen that the parameters a and c increased slightly after doping, due to the larger radius of Sb ions replacing Sn ions in the lattice [38]. This can be explained by the fact that doping caused Sb ions to replace Sn ions in the lattice. However, Fig. 5.3a does not show peaks of Sb_2O_3 with a cubic structure (PDF 00-043-1071, 00-005-0534) or an orthorhombic structure (PDF 00-011-0689) or Sb_2O_5 with a monoclinic structure (PDF 00-033-0110) [24, 38]. This finding suggests that the Sb ions successfully took the place of Sn ions in the crystal structure without producing any additional Sb_yO_x phases [41]. In addition, it is clear to see the impacts of antimony doping on SnO_2 material from Fig. 3b, which shows that Full Width at Half Maximum (FWHM) peaks rose after antimony doping level enhancing. Because greater peaks indicate

a decreasing trend in crystallite size, this suggests that doping could inhibit the formation of crystallites. This can be seen from the various crystal orientations shown in Figure 5.3b, 5.3c, and 5.3d [25]. It is possible that the successful substitution of Sn ions with Sb (at least in the form of Sb^{3+}) into the SnO_2 lattice was the cause of this result [52].

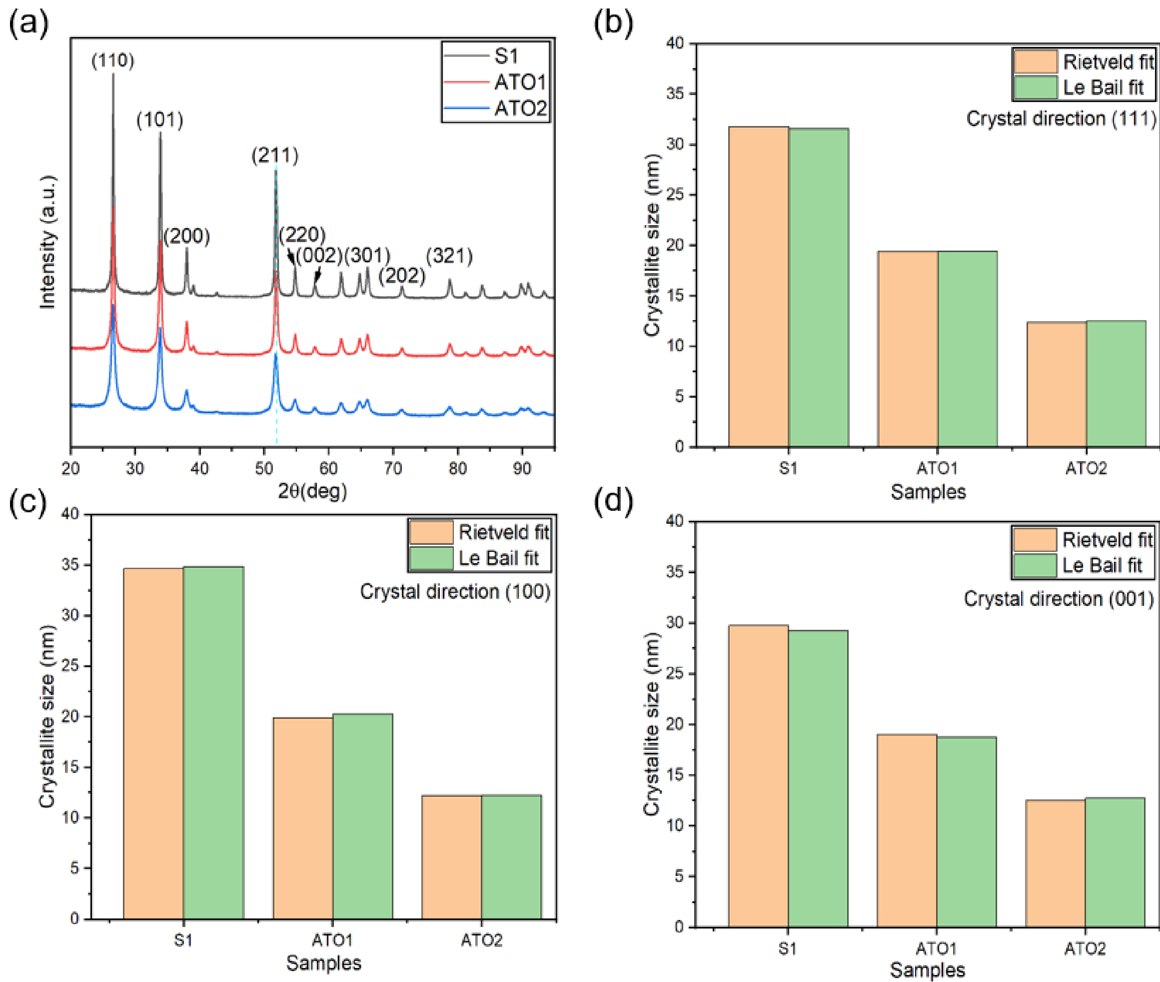

Figure 5.3. X-ray diffraction patterns(a) and crystallinity size (b, c and d) of S1, ATO1 and ATO2 estimated by Rietveld and LeBail approach from XRD data analysis, in three directions of (111), (100) and (001).

Table 5-1. Lattice parameters of S1, ATO1 and ATO2 samples estimated by Ritveld and LeBail approach from XRD data analysis.

Samples	Lattice parameter a (Å)		Lattice parameter c (Å)	
	Rietveld fit	LeBail fit	Rietveld fit	LeBail fit
S1	4.738377(60)	4.738349(60)	3.186908(57)	3.186859(56)

ATO1	4.73853(10)	4.73862(10)	3.188074(93)	3.188113(94)
ATO2	4.73991(14)	4.74024(15)	3.18913(12)	3.18917(13)

The techniques of XRF and EDS were utilized in order to conduct qualitative and quantitative studies of the composite material. Because oxygen cannot be detected by XRF, the elements Sn and Sb are the only ones that can be compared across various samples in this context. S1 includes 99.87% Sn element, and 0.13% impurities (mainly Al). ATO1 consists of 89.89 at% Sn and 10.12 at% Sb, making the ratio of Sb/Sn equal to 11.26%. Table 5-2 presents that ATO2 possesses 85.19 at% of Sn and 14.81 at% of Sb, with a ratio of 17.38% of Sb to Sn. Theoretically, the Sb concentrations indicated in the datasheets for commercial ATO powders were 10%wt and 15%wt, which corresponded to Sb/Sn ratios of 15.8% and 28%, respectively. These concentrations are based on the weight of the substance.

Table 5-2. Elemental composition of samples obtained from XRF analysis.

Samples	Sn(at%)	Sb(at%)	Sb/Sn (%)
S1	99.87	-	-
ATO1	89.88	10.12	11.26
ATO2	85.19	14.81	17.38

Table 5-3 shows the elemental composition in the obtained samples using EDS analysis. Atoms ratios between Sn and O are 50% and 44.96% for ATO1 and ATO2, respectively. These values are higher than the obtained ratio in S1, i.e. 41.6%. The atom ratios of Sb/Sn in ATO1 and ATO2 are 9.25% and 15.2%, that are close to the results from XRF.

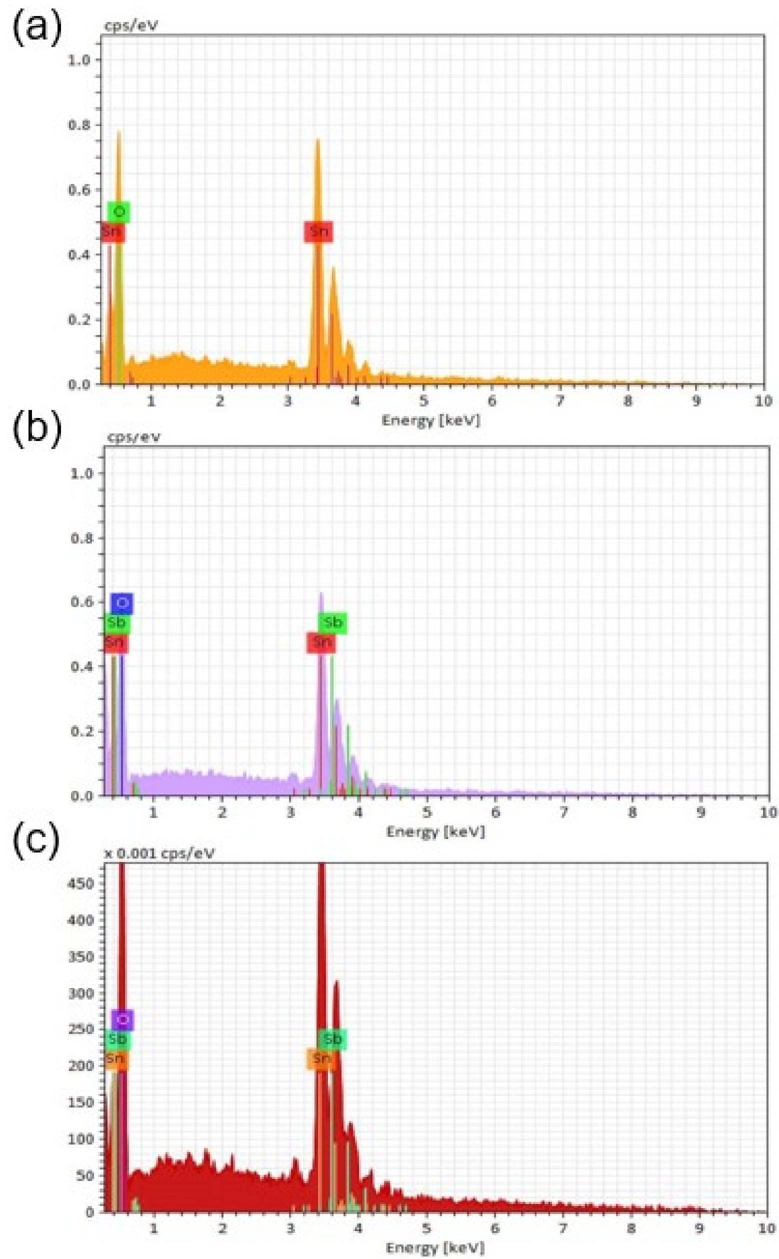

Figure 5.4 EDS results of samples S1, ATO1 and ATO2

Table 5-3. Elemental composition of samples obtained from EDS analysis.

Samples	Sn(at%)	Sb(at%)	O (at%)	Sn/O (%)	Sb/Sn (%)
S1	29.41	-	70.59	41.6	-
ATO1	32.34	2.99	64.67	50.00	9.25
ATO2	29.90	4.49	65.61	44.96	15.20

XPS was then used to detect the surface elemental compositions as well as the chemical states of the samples that were prepared. Fig. 5.4a depicts a wide scan spectrum of SnO_2 samples, which presents the peaks of Sb and Sn, in addition to the peaks of O and C. Since the peak separation was 8.5 eV and the binding energy of spin orbital states Sn $3d_{5/2}$ and Sn $3d_{3/2}$ were respectively referred to as 486.5 eV and 495.0 eV, this confirmed the presence of the Sn^{4+} oxidation state in samples, which could be seen in Fig. 5.4b. The doping element played a significant function in the chemical interaction, specifically in the shifting of covalency between the cation Sn5p state and the O2p state. In our samples, the incorporation of Sb into SnO_2 caused a little change in the binding energy of the Sn 3d peaks when compared to the undoped SnO_2 (Fig. 5.4b). It was important to fit the peaks in the O 1s/Sb 3d area in order to quantify both oxygen and antimony [53, 54]. This was because there was a partial overlap between the Sb $3d_{5/2}$ and O 1s regions. It has been determined that the binding energies of the Sb $3d_{5/2}$ and Sb 3d3/2 spin-orbital spectra were 530.3 eV and 540.2 eV respectively. Accurate deconvolution of Sb 3d peaks was necessary in order to identify the relative concentration of Sb^{3+} and Sb^{5+} in Sb/SnO_2 samples. This was because Sb^{3+} and Sb^{5+} had different ionic charges. The fact that it overlapped with the O1s core level, however, made it relatively difficult to distinguished. In spite of this, the binding energy of Sb $3d_{3/2}$ showed that the Sb^{3+} and Sb^{5+} oxidation states could coexist, which has consistently been seen in ATO materials (Fig. 5.4c) [53-55].

In order to proceed with the XPS analysis of these samples, it is essential to identify the relative amounts of tin and antimony that are present on the surface of the nanoparticles. In our samples, the obtained atom ratios between the elements Sb and Sn were, for ATO1 and ATO2, respectively, 50.79% and 42.93%. X-ray fluorescence and EDS methods could investigate a thickness of approximately 1um. When these two sets of findings were compared, it was clear that the concentration of antimony on the surface of the crystal was far higher than that found inside the crystal. It would appear that a segregation phenomenon happened as a result of high doping levels. This phenomenon may be induced by a difference in the ion geometric size or by a difference in the reactivity of Sn ions and Sb ions.

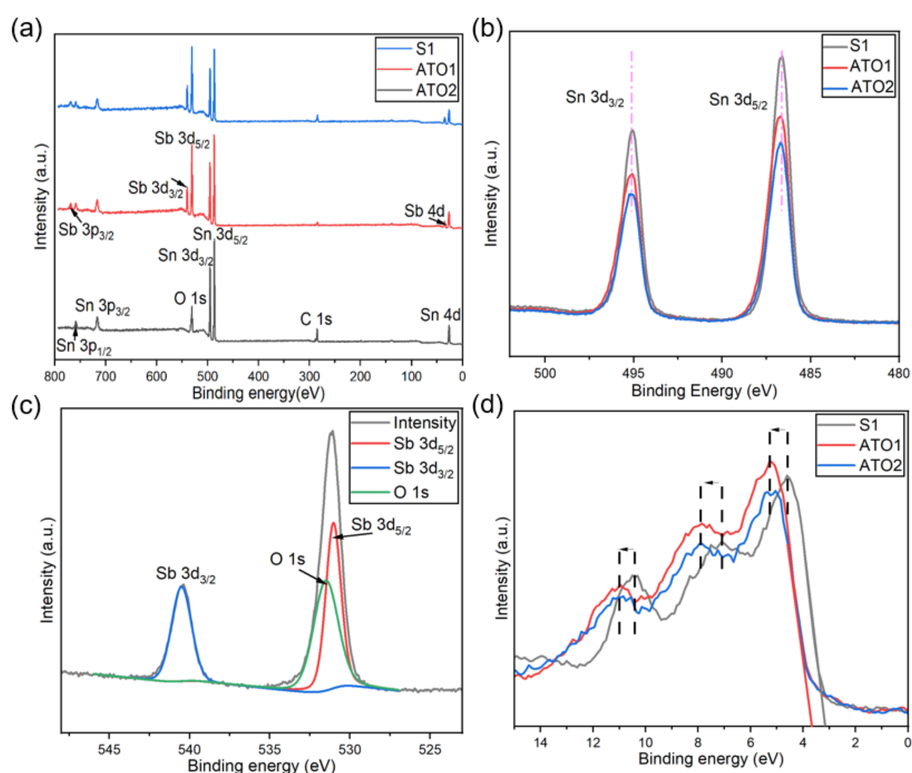

Figure 5.4. XPS spectra of S1 and ATO1 and ATO2: (a) survey spectrum, (b) Sn 3d spectrum, and (c) Sb 3d spectrum of ATO2, (d) XPS valence band of the three samples.

The information regarding the density and occupancy of electronic states in a material valence band that could be gleaned via XPS was provided by the valence band, also known as VB [37]. Figure 5.4d depicts the VB photoelectron spectra for all three samples taken from the experiment. It is clear that the spectrum exhibited the distinctive three-peaked pattern that was typical of SnO_2 when it originated from O2p states [56]. The onset of the valence band, as defined by linear extrapolation of the edge of the valence band, revealed a shift towards 3.697 eV upon doping with Sb, whereas it was at 3.140 eV for the sample that had not been doped at all. This shift occurred because Sb caused an increase in the valence band energy level. The occupation of conduction band states in degenerately doped SnO_2 was believed to be responsible for the shift of 0.557 eV. It has also been discovered that there were shifts in these three peaks that were indicative of the valence band, and this information was presented in figure 5.3d. In addition, the changes that were recorded provide evidence that the creation of Sb-O bonds made contributions to the valence band. This explained not only the energy gained by substituting Sn ions with Sb species at the surface, but also the decreased surface energy that was stated before as well as the greater surface concentration of Sb(V) species [57, 58].

5.3.2 Gas Sensing Characterization

Based on Morrison equation, the concentration of free carriers on the surface and in the bulk also varied when the resistance of functional materials shifts. This shift in concentration could be interpreted as a reflection of the height of the surface potential barrier shifting [47, 59]. At three distinct operating temperatures (200, 300, and 400 °C), these three samples resistance was measured. In Table 5-4, the baseline resistance values of the three devices are displayed. These values were measured in air, and it was clear that doped SnO_2 possesses a substantially lower resistance than pure SnO_2. This was due to the fact that doping with antimony introduced a new energy level, known as the donor level, into the energy band gap of SnO_2 near the conduction band. Because the donor level in SnO_2 was so high, it was simple for electrons that have enough energy to transition into the conduction band and contribute to the conductance mechanism [47, 60]. In addition to this, as the temperature rose, the resistances of S1 and ATO1 decreased, but the resistances of ATO2 increased. However, by comparing ATO1 and ATO2, it was evident that these two samples presented opposing resistance changing trends with increasing temperature, which could imply different conductivity mechanisms [47].

Table 5-4 Resistance (kΩ) of samples at different working temperatures in dry air.

Sample\Temperature	200 °C	300 °C	400 °C
S1	882.3	251.6	156.6
ATO1	242.2	106.2	78.2
ATO2	33.9	85	91.3

Fig.5.5a revealed that by increasing the Sb doping level onto SnO_2, enhanced response only occurred toward NO_2 gas. After the selectivity properties of the sensing films were evaluated, the sensors were put through a series of tests toward NO_2 at various temperatures ranging from 200 to 400 °C. Responses in dry air are displayed in Fig. 5.5b, and it can be seen that the maximum sensing response for ATO1 and ATO2 was obtained at a temperature of 300 °C. In addition, decreasing the operating temperature from 200 to 300 °C resulted in a significant decrease in the pure SnO_2 response, although the ATO1 and ATO2 responses exhibited just a modest decrease. Due to the fact that ATO and SnO_2 sensors behaved in opposing ways, the sensing response of ATO2 was found to be greater than that of SnO_2 at temperatures of 300°C and 400 °C, respectively.

In order to investigate response of samples to NO_2, the sensors were subjected to varying concentrations of NO_2 (1, 3, 5, and 10 ppm) at 300°C. Fig. 5.5c reveals that increasing the NO_2 concentrations caused the responses of S1 and ATO1 to increase almost linearly. However, Fig. 5.5d reveals that the sensor response of ATO2 increased exponentially, which indicated that ATO2 was more sensitive to NO_2 than S1 and ATO1.

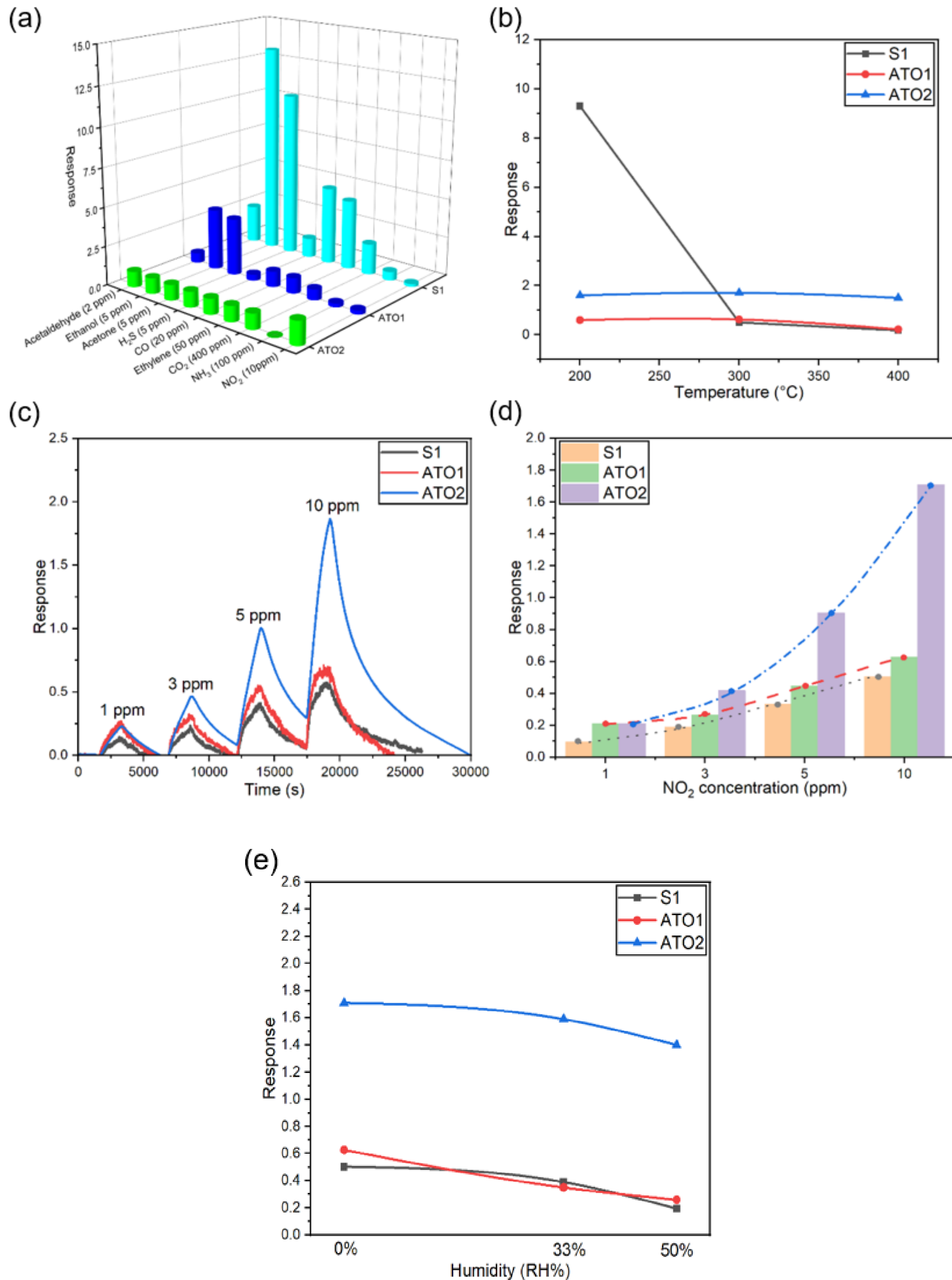

Figure 5.5. Electrical characterizations of the fabricated sensors: a) response to different gases at 400°C in dry air; b) response to 10 ppm of NO_2 at different operating temperatures in dry air; c) dynamical response of the three sensors towards 1, 3, 5, and 10 ppm NO_2 at 300°C; d) variation of the response vs. NO_2 concentrations for the three sensors in dry air at 300°C; e). response to different humidity at 300°C under 10 ppm NO_2.

The effect of relative humidity on the sensing response as well as the resistance of the materials was investigated, and the findings were presented in Figure 5.5e and Table 5-5 respectively. The sensors were injected to 10 ppm NO_2 at 300 °C with 33 RH% and 50 RH% humidity in order to monitor the behavior of the devices in a real-life environment as opposed to dry air. The presence of moisture in the gas chamber was shown to have a marginally negative impact on the sensing response of all three sensors to NO_2 as shown in Fig. 5.5e and Table 5-5. In addition, the response of ATO2 was approximately three times bigger than that of pristine SnO_2 and ATO1 in both dry and moist air conditions. It appears that an increase in humidity had a negative impact on the performance of the sensing materials because all of these samples showed a decrease in resistance values and response signals when the humidity level rose.

Table 5-5. Resistance (kΩ) of samples at different humidity at 300°C under 10 ppm NO_2.

Sample\Temperature	0 RH%	33 RH%	50 RH%
S1	378.15	106.20	78.23
ATO1	173.11	56.17	46.784
ATO2	229.50	39.54	41.51

5.4 Gas Sensing Mechanism Discussion

The suggested model demonstrates that the gas sensing mechanism of SMO can be summarized as adsorption-oxidation-desorption processes. At operating temperature above 100°C, the adsorbed oxygen molecules on the surface of the sensing material will be ionized by capturing electrons from the conduction band of materials [24, 61].

$$O_2\ (air) \rightarrow O_2\ (adsorbed) \rightarrow O_2^-\ (low\ temperature)\ or\ O_2^-\ (high\ temperature) \qquad (5\text{-}3)$$

In SnO_2 case, a depletion layer will be formed on the surface after oxygen adsorption, and when it is exposed to the gas target (NO_2 in this case), NO_2 will take electrons from the conduction band of sensing material (Eq. 5-4) [62].

$$NO_2(gas) \rightarrow e^- + NO_2^-(adsorbed) \quad (5\text{-}4)$$

Throughout the entirety of the sensing process, the resistance of the sensing material will fluctuate in response to the gas target, as well as in response to the material own inherent physical qualities. A new donor level was introduced into the conduction band of SnO_2 when it was doped by Sb, which was advantageous to electron transport and leaded to a reduction in the resistance of sensing materials. This happened after Sb doping. A higher concentration of Sb produced a layer that was more conductive in air and made it possible for extra carriers to be present. In addition, Sb doping may result in the formation of crystal defects, which in turn impacted the number of oxygen vacancies [19].

Amplification of reaction under NO_2 exposure was observed in ATO samples relative to pure SnO_2 when the samples were operated at temperatures of 300°C and 400°C. This observation suggested that increased Sb doping generated an improved response. Taking into account the high electron affinity of NO_2, as well as its oxidizing activity, there are two possible explanations for this phenomenon, which are as follows: a reduction in the band gap of ATO and an increase in the number of oxygen vacancies in ATO samples by Sb doping. Particularly, oxygen vacancies can enhance the chemisorption of oxidizing gases from ambient air and provide more surface adsorption sites. This is because oxygen vacancies provide more surface adsorption sites. A further benefit of using ATO powders is that they have a smaller particle size, which indicates a larger active surface area in comparison to that of pure SnO_2. This causes more adsorption sites being made available for interaction with the analyte gas. However, with the exception of NO_2, they did not exhibit any signs of an increased reaction in any of the gases listed above. Because the response was not only dependent on the geometry parameters, but also affected by the surface chemical processes, which was related to the donor-acceptor level of materials, and it caused the boundary barrier to change. During the entirety of the sensing process, it appeared to be abundantly clear that the surface chemical reaction dominated in our particular scenario [59].

It was possible that the collapse of faulty sites at high temperatures caused a reduction in the detecting response to NO_2 in both S1 and ATO sensors at 400℃. All of the samples exhibited a fading response pattern and lower resistance value when the environment was adjusted to simulate a real-world setting with a humidity of 33 RH% and 50 RH%. In this particular scenario, water molecules had the potential to occupy reactive sites on the surface of nanoparticles, which resulted in a diminished gas sensing response when NO_2 was injected

into the gas chamber. In addition, water molecules had the ability to provide H^+ and OH^- ions, which could affect the conductivity of the sensing materials.

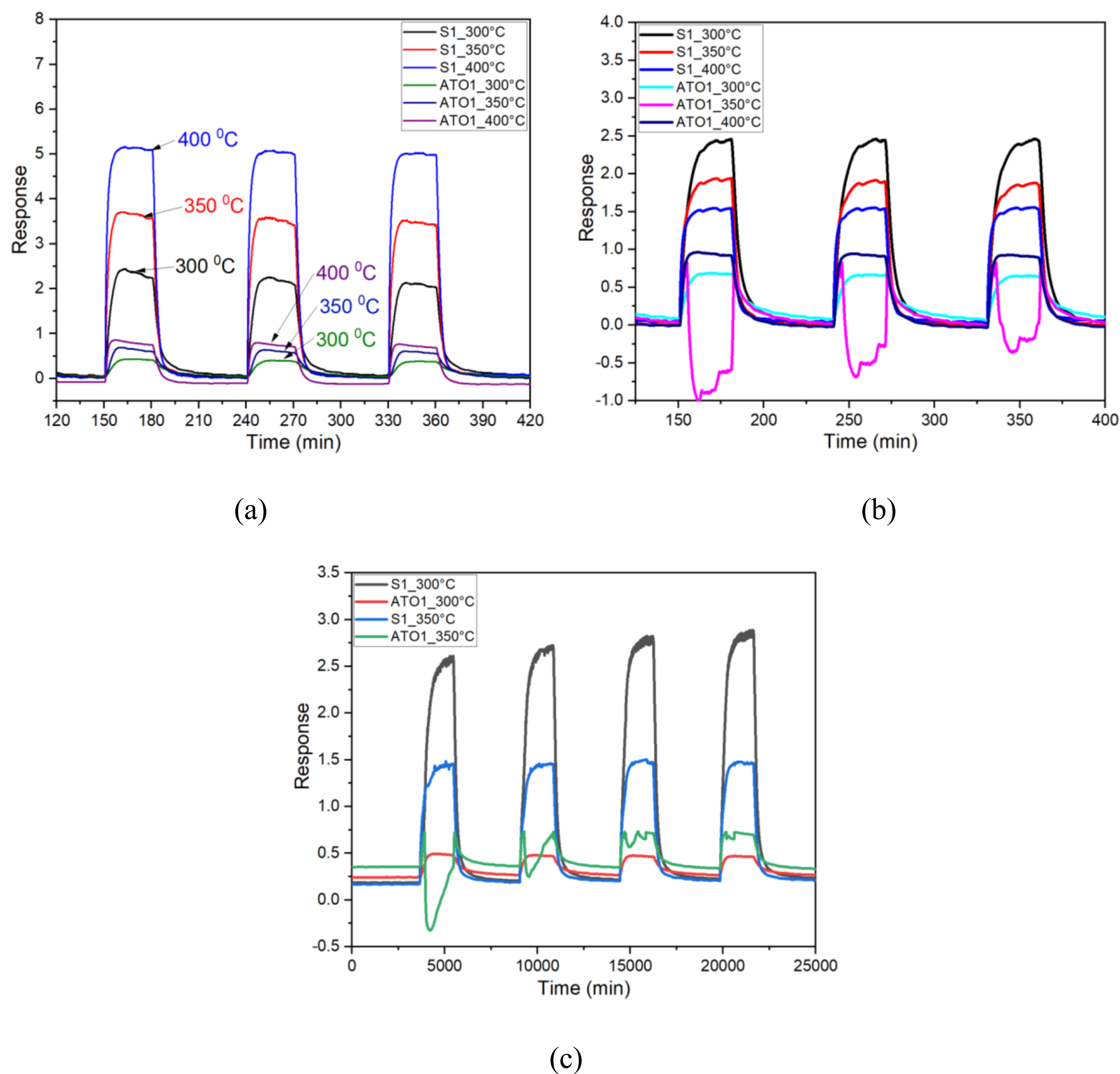

Figure 5.6. S1 and ATO1 samples sensing ability test at different temperatures toward 20 ppm CO (a), 5 ppm ethanol (b) and 0.5 ppm acetaldehyde (c).

To test ATO samples sensing response at different temperatures toward CO, ethanol and acetaldehyde gases, a group of experiments were conducted with temperatures of 300℃, 350℃ and 400℃. Fig.5.6a shows S1 and ATO1 response at temperatures of 300℃, 350℃ and 400℃ under 20 ppm CO gas, in which S1 at 400℃ shows the highest response, and by increasing the temperature from 300℃ to 400℃, the response of S1 also increased. While ATO1 shows lower response compared to S1 representing the same response changing trend under 20 ppm CO. When these two samples were exposed to 5 ppm ethanol, the response is shown in Fig.5.6. S1 still shows the highest response and the same response changing trend

with increasing temperature. But ATO1 shows the highest response at 350℃, and the response type even changed. Same results happened also to 0.5 ppm acetaldehyde.

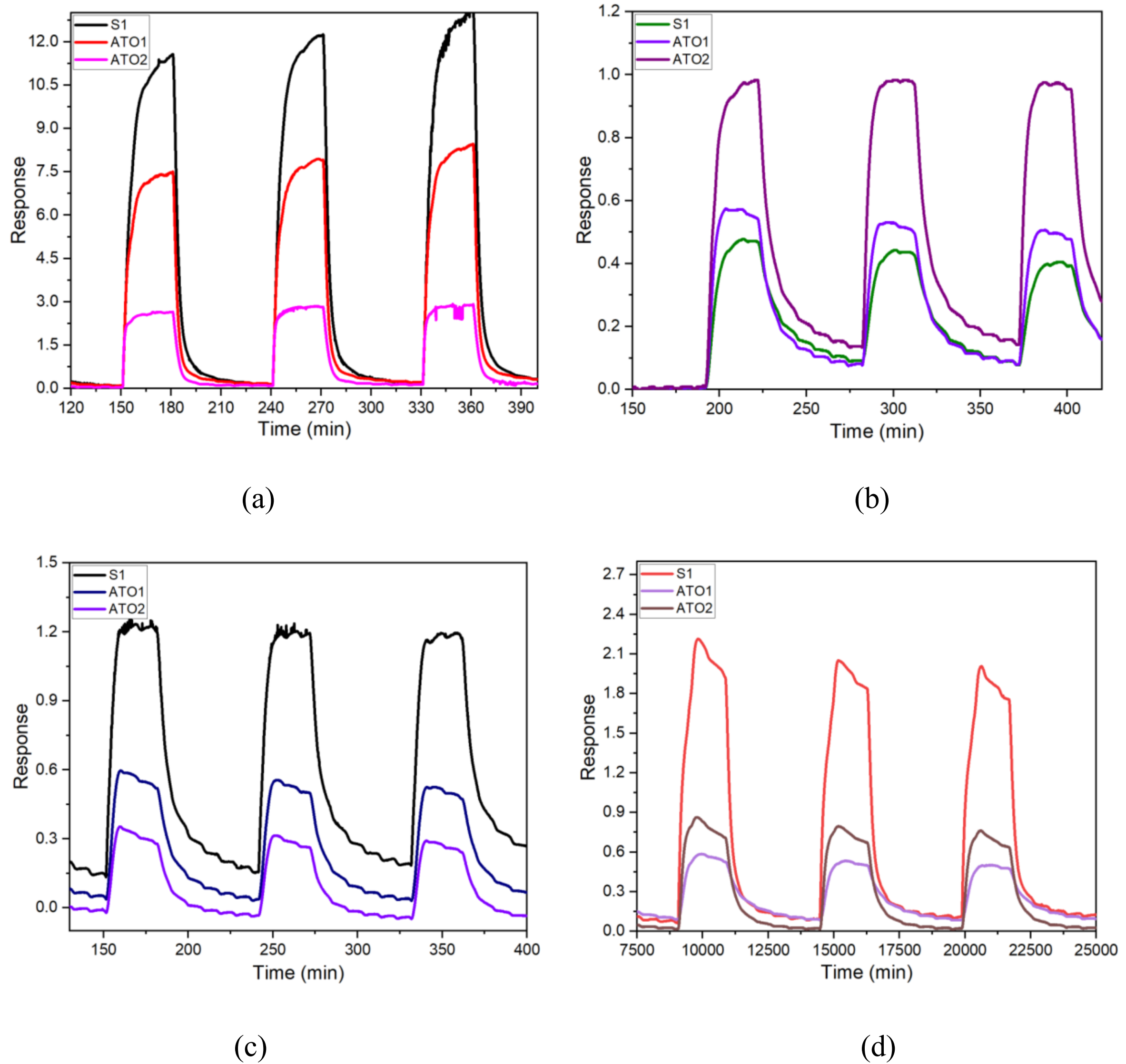

Figure 5.7 Samples sensing ability test toward 5 ppm acetone (a), 2 ppm SO_2 (b), and 5 ppm H_2S (c), 400 ppm CO_2 (d).

In this part, we compared S1, ATO1 and ATO2 gas sensing properties under acetone, SO_2, H_2S and CO_2 gases. S1 always shows highest response under these gases, then ATO1 shows higher response than ATO2 except for CO_2 gas, in which ATO2 response is higher than ATO1.

Conclusion

The sensing capability of highly doped Sb/SnO_2 nanoparticles was investigated and compared to that of unadulterated SnO_2 for the purpose of our study. Based on the findings

of the SEM, it has been established that antimony doping alters the morphology of SnO_2 powder by inhibiting the growth of powder particles. This was done in order to achieve this effect. In addition, the inclusion of antimony caused the crystallinity size, as measured by XRD, and the expanded lattice parameters to drop. This was caused by the insertion of Sb^{3+}. The appropriate level of doping was confirmed by XRF and EDS, and it was found that the concentration of oxygen vacancies increased as a result of the doping process. This may be advantageous for reducing the resistivity of SnO_2 in some applications. When taken together, the results from XPS show that the concentration of antimony is a little higher on the surface than it is in the depths of SnO_2, which corresponds to the partial saturation of antimony precipitation on the surface. The XPS results also indicated the normal chemical state of Sn^{4+}, as well as the ions Sb^{3+} and Sb^{5+}. As a result of the incorporation of Sb into the SnO_2 lattice, which causes the addition of a new band energy near to the conduction band, the electrical measurements revealed that ATO sensors possessed a resistance that was significantly lower than that of conventional sensors. Analysis of sensing data showed that ATO sensors led to a particularly high selectivity and sensitivity to NO_2 among the other gases that were examined at 400 °C in dry air. It appears that an increase in the percentage of Sb in the SnO_2 lattice leads to an improvement in the sensing performance because ATO2, which is the sample with the highest concentration of Sb, showed a higher response to NO_2 than both ATO1 and pure SnO_2. This suggests that increasing the percentage of Sb in the SnO_2 lattice leads to a higher response. In addition, the sensing response of ATO1 and ATO2 was only marginally impacted by humidity, making them ideal candidates for the development of sensitive materials that can detect NO_2 in the actual atmosphere.

References

[1] M. Della Ciana, M. Valt, B. Fabbri, P. Bernardoni, V. Guidi, and V. Morandi, "Development of a dedicated instrumentation for electrical and thermal characterization of chemiresistive gas sensors," *Rev Sci Instrum,* vol. 92, p. 074702, Jul 1 2021.

[2] S. Dhall, B. R. Mehta, A. K. Tyagi, and K. Sood, "A review on environmental gas sensors: Materials and technologies," *Sensors International,* vol. 2, p. 100116, 2021.

[3] M. A. H. Khan, M. V. Rao, and Q. Li, "Recent Advances in Electrochemical Sensors for Detecting Toxic Gases: NO(2), SO(2) and H(2)S," *Sensors (Basel),* vol. 19, Feb 21 2019.

[4] A. T. Guntner, S. Abegg, K. Konigstein, P. A. Gerber, A. Schmidt-Trucksass, and S. E. Pratsinis, "Breath Sensors for Health Monitoring," *ACS Sens,* vol. 4, pp. 268-280, Feb 22 2019.

[5] P. Raju and Q. Li, "Review—Semiconductor Materials and Devices for Gas Sensors," *Journal of The Electrochemical Society,* vol. 169, p. 057518, 2022.

[6] U. Yaqoob and M. I. Younis, "Chemical Gas Sensors: Recent Developments, Challenges, and the Potential of Machine Learning-A Review," *Sensors (Basel),* vol. 21, Apr 20 2021.

[7] D. Zappa, V. Galstyan, N. Kaur, H. M. M. Munasinghe Arachchige, O. Sisman, and E. Comini, ""Metal oxide -based heterostructures for gas sensors"- A review," *Anal Chim Acta,* vol. 1039, pp. 1-23, Dec 18 2018.

[8] G. Korotcenkov and B. K. Cho, "Metal oxide composites in conductometric gas sensors: Achievements and challenges," *Sensors and Actuators B: Chemical,* vol. 244, pp. 182-210, 2017.

[9] B. Bhowmik, N. K. Chowdhury, and A. K. Singh, "Efficiency Improvement in Metal Oxide Gas Sensor," p. 362, 2021.

[10] S. Nie, D. Dastan, J. Li, W.-D. Zhou, S.-S. Wu, Y.-W. Zhou*, et al.*, "Gas-sensing selectivity of n-ZnO/p-Co_3O_4 sensors for homogeneous reducing gas," *Journal of Physics and Chemistry of Solids,* vol. 150, p. 109864, 2021.

[11] A. Umar, A. A. Ibrahim, U. T. Nakate, H. Albargi, M. A. Alsaiari, F. Ahmed*, et al.*, "Fabrication and characterization of CuO nanoplates based sensor device for ethanol gas sensing application," *Chemical Physics Letters,* p. 138204, 2020.

[12] Z. Yuan, R. Li, F. Meng, J. Zhang, K. Zuo, and E. Han, "Approaches to Enhancing Gas Sensing Properties: A Review," *Sensors (Basel),* vol. 19, Mar 27 2019.

[13] Y. Kong, Y. Li, X. Cui, L. Su, D. Ma, T. Lai*, et al.*, "SnO_2 nanostructured materials used as gas sensors for the detection of hazardous and flammable gases: A review," *Nano Materials Science,* 2021.

[14] L. Yao, Y. Li, Y. Ran, Y. Yang, R. Zhao, L. Su*, et al.*, "Construction of novel Pd–SnO_2 composite nanoporous structure as a high-response sensor for methane gas," *Journal of Alloys and Compounds,* vol. 826, p. 154063, 2020.

[15] N. X. Thai, N. Van Duy, N. Van Toan, C. M. Hung, N. Van Hieu, and N. D. Hoa, "Effective monitoring and classification of hydrogen and ammonia gases with a bilayer Pt/SnO_2 thin film sensor," *International Journal of Hydrogen Energy,* vol. 45, pp. 2418-2428, 2020.

[16] M. Sun, J. Liu, and B. Dong, "Effects of Sb doping on the structure and properties of SnO_2 films," *Current Applied Physics,* vol. 20, pp. 462-469, 2020.

[17] M. Senapati and P. P. Sahu, "Meat quality assessment using Au patch electrode Ag-SnO_2/SiO_2/Si MIS capacitive gas sensor at room temperature," *Food Chem,* vol. 324, p. 126893, Sep 15 2020.

[18] S. Morandi, A. Amodio, A. Fioravanti, A. Giacomino, M. Mazzocchi, M. Sacerdoti, *et al.*, "Operational functionalities of air-quality WSn metal-oxide sensors correlating semiconductor defect levels and surface potential barriers," *Sci Total Environ,* vol. 706, p. 135731, Mar 1 2020.

[19] W. Li, C. Ding, J. Li, Q. Ren, G. Bai, and J. Xu, "Sensing mechanism of Sb, S doped SnO_2 (1 1 0) surface for CO," *Applied Surface Science,* vol. 502, p. 144140, 2020.

[20] X. Kou, F. Meng, K. Chen, T. Wang, P. Sun, F. Liu, *et al.*, "High-performance acetone gas sensor based on Ru-doped SnO_2 nanofibers," *Sensors and Actuators B: Chemical,* vol. 320, p. 128292, 2020.

[21] M. F. Hossain, M. A. H. Shah, M. A. Islam, and M. S. Hossain, "Transparent conducting SnO_2 thin films synthesized by nebulized spray pyrolysis technique: Impact of Sb doping on the different physical properties," *Materials Science in Semiconductor Processing,* vol. 121, p. 105346, 2021.

[22] P. Cheng, L. Lv, Y. Wang, B. Zhang, Y. Zhang, Y. Zhang, *et al.*, "SnO_2/$ZnSnO_3$ double-shelled hollow microspheres based high-performance acetone gas sensor," *Sensors and Actuators B: Chemical,* vol. 332, p. 129212, 2021.

[23] P. H. Phuoc, C. M. Hung, N. Van Toan, N. Van Duy, N. D. Hoa, and N. Van Hieu, "One-step fabrication of SnO_2 porous nanofiber gas sensors for sub-ppm H2S detection," *Sensors and Actuators A: Physical,* vol. 303, p. 111722, 2020.

[24] M. G. Masteghin and M. O. Orlandi, "A Gas Sensor Based on a Single SnO Micro-Disk," *Sensors (Basel),* vol. 18, Sep 25 2018.

[25] Q. Wei, P. Song, Z. Li, Z. Yang, and Q. Wang, "Hierarchical peony-like Sb-doped SnO_2 nanostructures: Synthesis, characterization and HCHO sensing properties," *Materials Letters,* vol. 191, pp. 173-177, 2017.

[26] A. Umar, H. Y. Ammar, R. Kumar, T. Almas, A. A. Ibrahim, M. S. AlAssiri, *et al.*, "Efficient H_2 gas sensor based on 2D SnO_2 disks: Experimental and theoretical studies," *International Journal of Hydrogen Energy,* vol. 45, pp. 26388-26401, 2020.

[27] A. Hermawan, Y. Asakura, M. Inada, and S. Yin, "One-step synthesis of micro-/mesoporous SnO_2 spheres by solvothermal method for toluene gas sensor," *Ceramics International,* vol. 45, pp. 15435-15444, 2019.

[28] J.-W. Yoon, S. H. Choi, J.-S. Kim, H. W. Jang, Y. C. Kang, and J.-H. Lee, "Trimodally porous SnO_2 nanospheres with three-dimensional interconnectivity and

size tunability: a one-pot synthetic route and potential application as an extremely sensitive ethanol detector," *NPG Asia Materials,* vol. 8, pp. e244-e244, 2016.

[29] Y. Wan, J. Liu, W. Li, F. Meng, Z. Jin, X. Yu*, et al.*, "Dense doping of indium to coral-like SnO_2 nanostructures through a plasma-assisted strategy for sensitive and selective detection of chlorobenzene," *Nanotechnology,* vol. 22, p. 315501, Aug 5 2011.

[30] D. Liu, Z. Tang, and Z. Zhang, "Visible light assisted room-temperature NO_2 gas sensor based on hollow SnO_2@SnS_2 nanostructures," *Sensors and Actuators B: Chemical,* vol. 324, p. 128754, 2020.

[31] S. Mohammad-Yousefi, S. Rahbarpour, and H. Ghafoorifard, "Describing the effect of Ag/Au modification on operating temperature and gas sensing properties of thick film SnO_2 gas sensors by gas diffusion theory," *Materials Chemistry and Physics,* vol. 227, pp. 148-156, 2019.

[32] N. L. Myadam, D. Y. Nadargi, J. D. Gurav Nadargi, F. I. Shaikh, S. S. Suryavanshi, and M. G. Chaskar, "A facile approach of developing Al/SnO_2 xerogels via epoxide assisted gelation: A highly versatile route for formaldehyde gas sensors," *Inorganic Chemistry Communications,* vol. 116, p. 107901, 2020.

[33] Z. Cai and S. Park, "Synthesis of Pd nanoparticle-decorated SnO_2 nanowires and determination of the optimum quantity of Pd nanoparticles for highly sensitive and selective hydrogen gas sensor," *Sensors and Actuators B: Chemical,* vol. 322, p. 128651, 2020.

[34] I. Ali, A. E.-H. B. Kashyout, M. Tayel, H. Shokry Hassan, and M. Rizk, "Ruthenium (Ru) doped zinc oxide nanostructure-based radio frequency identification (RFID) gas sensors for NH_3 detection," *Journal of Materials Research and Technology,* vol. 9, pp. 15693-15704, 2020.

[35] M. Yuasa, T. Masaki, T. Kida, K. Shimanoe, and N. Yamazoe, "Nano-sized PdO loaded SnO_2 nanoparticles by reverse micelle method for highly sensitive CO gas sensor," *Sensors and Actuators B: Chemical,* vol. 136, pp. 99-104, 2009.

[36] A. Hermawan, Y. Asakura, M. Inada, and S. Yin, "A facile method for preparation of uniformly decorated-spherical SnO_2 by CuO nanoparticles for highly responsive toluene detection at high temperature," *Journal of Materials Science & Technology,* vol. 51, pp. 119-129, 2020.

[37] J.-H. Kim, A. Mirzaei, J.-Y. Kim, J.-H. Lee, H. W. Kim, S. Hishita*, et al.*, "Enhancement of gas sensing by implantation of Sb-ions in SnO_2 nanowires," *Sensors and Actuators B: Chemical,* vol. 304, p. 127307, 2020.

[38] Y. Bouznit and A. Henni, "Characterization of Sb doped SnO_2 films prepared by spray technique and their application to photocurrent generation," *Materials Chemistry and Physics,* vol. 233, pp. 242-248, 2019.

[39] K. Großmann, K. E. Kovács, D. K. Pham, L. Mädler, N. Barsan, and U. Weimar, "Enhancing performance of FSP SnO_2-based gas sensors through Sb-doping and Pd-functionalization," *Sensors and Actuators B: Chemical,* vol. 158, pp. 388-392, 2011.

[40] I. M. Costa, Y. N. Colmenares, P. S. Pizani, E. R. Leite, and A. J. Chiquito, "Sb doping of VLS synthesized SnO_2 nanowires probed by Raman and XPS spectroscopy," *Chemical Physics Letters,* vol. 695, pp. 125-130, 2018.

[41] B. B. C, A. R. Varghese, A. G, and S. Hussain, "Sb:SnO_2 thin films-synthesis and characterization," vol. 1951, p. 030006, 2018.

[42] W. Zeng, Y. Liu, G. Chen, H. Zhan, J. Mei, N. Luo*, et al.*, "SnO–Sn_3O_4 heterostructural gas sensor with high response and selectivity to parts-per-billion-level NO_2 at low operating temperature," *RSC Advances,* vol. 10, pp. 29843-29854, 2020.

[43] S. Berardi, V. Cristino, M. Canton, R. Boaretto, R. Argazzi, E. Benazzi*, et al.*, "Perylene Diimide Aggregates on Sb-Doped SnO_2: Charge Transfer Dynamics Relevant to Solar Fuel Generation," *The Journal of Physical Chemistry C,* vol. 121, pp. 17737-17745, 2017.

[44] T. Abendroth, B. Schumm, S. A. Alajlan, A. M. Almogbel, G. Mäder, P. Härtel*, et al.*, "Optical and thermal properties of transparent infrared blocking antimony doped tin oxide thin films," *Thin Solid Films,* vol. 624, pp. 152-159, 2017.

[45] G. Joshi, J. K. Rajput, and L. P. Purohit, "Improved stability of gas sensor by inclusion of Sb in nanostructured SnO_2 thin films grown on sodalime," *Journal of Alloys and Compounds,* vol. 830, p. 154659, 2020.

[46] J. Ma, Y. Liu, H. Zhang, P. Ai, N. Gong, Y. Wu*, et al.*, "Room temperature ppb level H_2S detection of a single Sb-doped SnO_2 nanoribbon device," *Sensors and Actuators B: Chemical,* vol. 216, pp. 72-79, 2015.

[47] K. Khun Khun, A. Mahajan, and R. K. Bedi, "Nanostructured Sb doped SnO_2 thick films for room temperature NH3 sensing," *Chemical Physics Letters,* vol. 492, pp. 119-122, 2010.

[48] M. C. Carotta, A. Fioravanti, S. Gherardi, C. Malagù, M. Sacerdoti, G. Ghiotti*, et al.*, "(Ti,Sn) solid solutions as functional materials for gas sensing," *Sensors and Actuators B: Chemical,* vol. 194, pp. 195-205, 2014.

[49] A. Gaiardo, G. Zonta, S. Gherardi, C. Malagu, B. Fabbri, M. Valt*, et al.*, "Nanostructured $SmFeO_3$ Gas Sensors: Investigation of the Gas Sensing

Performance Reproducibility for Colorectal Cancer Screening," *Sensors (Basel),* vol. 20, Oct 19 2020.

[50] A. Gaiardo, D. Novel, E. Scattolo, M. Crivellari, A. Picciotto, F. Ficorella*, et al.*, "Optimization of a Low-Power Chemoresistive Gas Sensor: Predictive Thermal Modelling and Mechanical Failure Analysis," *Sensors (Basel),* vol. 21, Jan 25 2021.

[51] A. Gaiardo, D. Novel, E. Scattolo, A. Bucciarelli, P. Bellutti, and G. Pepponi, "Dataset of the Optimization of a Low Power Chemoresistive Gas Sensor: Predictive Thermal Modelling and Mechanical Failure Analysis," *Data,* vol. 6, p. 30, 2021.

[52] M. Wang, L. Zhu, C. Zhang, G. Gai, X. Ji, B. Li*, et al.*, "Lanthanum oxide @ antimony-doped tin oxide with high gas sensitivity and selectivity towards ethanol vapor," *Sensors and Actuators B: Chemical,* vol. 224, pp. 478-484, 2016.

[53] P. Y. Liu, J. F. Chen, and W. D. Sun, "Characterizations of SnO_2 and SnO_2:Sb thin films prepared by PECVD," *Vacuum,* vol. 76, pp. 7-11, 2004.

[54] Q. Wan and T. H. Wang, "Single-crystalline Sb-doped SnO2 nanowires: synthesis and gas sensor application," *Chem Commun (Camb),* pp. 3841-3, Aug 14 2005.

[55] X. Feng, J. Ma, F. Yang, F. Ji, F. Zong, C. Luan*, et al.*, "Highly thermal stable transparent conducting SnO_2:Sb epitaxial films prepared on α-Al_2O_3 (0001) by MOCVD," *Applied Surface Science,* vol. 254, pp. 6601-6604, 2008.

[56] Z. Wang, M. Zhi, M. Xu, C. Guo, Z. Man, Z. Zhang*, et al.*, "Ultrasensitive NO2 gas sensor based on Sb-doped SnO_2 covered ZnO nano-heterojunction," *Journal of Materials Science,* vol. 56, pp. 7348-7356, 2021.

[57] J. Rockenberger, U. zum Felde, M. Tischer, L. Tröger, M. Haase, and H. Weller, "Near edge X-ray absorption fine structure measurements (XANES) and extended x-ray absorption fine structure measurements (EXAFS) of the valence state and coordination of antimony in doped nanocrystalline SnO_2," *The Journal of Chemical Physics,* vol. 112, pp. 4296-4304, 2000.

[58] Z. Song, Z. Hu, J. Liu, J. Yan, H. Li, J. Jiang*, et al.*, "Metastable Antimony-Doped SnO_2 Quantum Wires for Ultrasensitive Gas Sensors," *Advanced Electronic Materials,* p. 2101049, 2021.

[59] J. Rebholz, P. Bonanati, C. Jaeschke, M. Hübner, L. Mädler, U. Weimar*, et al.*, "Conduction mechanism in undoped and antimony doped SnO_2 based FSP gas sensors," *Sensors and Actuators B: Chemical,* vol. 188, pp. 631-636, 2013.

[60] A. A. Zhukova, M. N. Rumyantseva, V. B. Zaytsev, A. V. Zaytseva, A. M. Abakumov, and A. M. Gaskov, "Pd nanoparticles on SnO_2(Sb) whiskers: Aggregation and reactivity in CO detection," *Journal of Alloys and Compounds,* vol. 565, pp. 6-10, 2013.

[61] N. B rsan and U. Weimar, "Understanding the fundamental principles of metal oxide based gas sensors; the example of CO sensing with SnO_2 sensors in the presence of humidity," *Journal of Physics: Condensed Matter,* vol. 15, pp. R813-R839, 2003/05/09 2003.

[62] M. Sik Choi, M. Young Kim, A. Mirzaei, H.-S. Kim, S.-i. Kim, S.-H. Baek*, et al.*, "Selective, sensitive, and stable NO_2 gas sensor based on porous ZnO nanosheets," *Applied Surface Science,* vol. 568, p. 150910, 2021.

6. Conclusion and Outlook

6.1 Conclusion

This PhD thesis is based on the collaboration between the Department of Physics and Earth Sciences of the University of Ferrara and the Micro-Nano Facilities group (MNF) of Bruno Kessler Foundation (FBK).

The dissertation work was focused mostly on the simulation, design, fabrication, and characterization of hotplates utilized for SMO gas sensor devices. As it is widely known that SMO gas sensors usually function at high temperature enabling a fast and reversible reaction between the target gas and sensing material surface, while recently the market demand for near-zero power consumption gas sensors device to integrate with other portable electronics. For this purpose, three sizes of hotplates with different heater circuit geometries were designed, simulated and fabricated for SMO gas sensor application. In the first case, micro size hotplate was designed and simulated with heater circuit width of 100 μm and heat area of 1300 μm, named as MHP1, then the geometry of MHP1 was downsized by 50 times into MHP2 device to decrease the power consumption. The power efficiency was enhanced a lot after downsizing, hence to further decrease the power consumption, NHP1 and NHP2 devices were obtained with 1 μm wide heater circuit and 500 nm wide heater circuit gap. NHP1 was applied for gas sensor hotplate, and NHP2 with longer electrode but the same heater part for general application.

In detail, to calibrate the simulation model and boundary conditions in COMSOL, the experimental data of MHP1 was referred, which is currently being used in FBK laboratory for the gas sensor devices. For the MHP1 model, the influence of suspended membrane on temperature distribution and power consumption was evaluated compared to the solid structure of the hotplate. Due to the heat conduction through the silicon wafer with high heat conductivity, the hotplate with a solid structure could not be heated up and stayed near room temperature no matter how big the input voltage was. But the power consumption increased from 0 to 1.25 W at such near room temperature with input voltage ranging from 0 to 9 V. However, the hotplate with a suspended membrane structure exhibited much more optimized power efficiency and a higher operational temperature compared to solid structure hotpate, when the input voltage increased. Based on the MHP1 model, a new micro heater layout MHP2 device with a 2 μm and 4 μm wide heating circuit was developed and simulated in

COMSOL. In this instance, two different heater circuit geometries were devised, one of which was rectangular shape (MHP2_R) and the other was circular shape (MHP2_C). The effect of heater circuit thickness and insulating thickness on temperature distribution and power consumption on a solid structure hotplate was compared. Using this size, the hotplate could be heated even on a solid structure substrate. At the same input voltage on the heater circuit, the MHP2_C geometry demonstrated a greater operating temperature than the MHP_R geometry. In addition, the thickness of the heater circuit and insulating layer impacted temperature distribution and power consumption. For instance, if the thickness of a Pt heater is thicker, the temperature and power consumption will be higher. At the same input voltage, if the insulating layer becomes thicker, the working temperature will increase and the power consumption will decrease due to its heat resisting effect on the heater circuit. Simultaneously, the impact of a trench structure (actually front etch suspended membrane) on the heat dissipation and mechanical properties of MHP2 size was studied. In this case, the temperature of the heat source was fixed constant at 300°C, while the thickness of the trench beneath the heat source and insulating layer was parametrically scanned from 0 and 10 μm in COMSOL. When the thickness of the trench exceeded 5 m, the temperature beneath the insulating layer barely altered. Afterwards, the trench depth was set as 5 μm and the heat source temperature was parameter-scanned from 100°C to 600°C. It was demonstrated that the temperature, displacement, and stress under the insulating layer were less altered with the trench structure compared to the solid structure. Moreover, the effect of insulating layer thickness on temperature uniformity was discussed, and the results indicated that a thicker insulating layer improved the temperature uniformity of the hotplate. Upon horizontal comparison of the MHP1, MHP2, NHP1, and NHP2 devices, it was determined that the operational temperature and power efficiency of the MHP2 device was greatly improved by reducing the geometry of the hotplate arrangement by a decreasing factor of 50 times from MHP1. When the input voltage on the heater circuit was set to 3V, for instance, MHP1 indicated a temperature of approximately 350°C with a power consumption of 0.125 W for a suspended membrane structure, and 25°C with a power expenditure of 0.24 W for a solid structure substrate. On a solid structure substrate, MHP2_R displayed around 100°C with a power consumption of 0.1 W, and MHP2_C exhibited approximately 300°C with a power usage of 0.03 W. NHP1 was created by reducing the size of MHP2_R by a factor of 4 times, and when the input voltage was 3V, the temperature was approximately 150°C with a power usage of 0.05 W. NHP2 has the same heater circuit part but longer electrode compared to

NHP1, the temperature reached 400°C with power consumption of 0.05 W at voltage of 3 V.

In FBK clean room, EBL machine was primarily utilized to fabricate these three types of hotplates. On a silicon wafer, an ONO stack structure was first deposited consisting of 100 nm SiO_2, 200 nm Si_3N_4, and another 600 nm SiO_2 layer. This ONO stack structure acted as an insulating layer with 0 strain. Due to the uneven design of these hotplates, the electrode portion was always micro-level size, but the heater circuit structure was quite dense and small. Initially, only EBL was applied to define the pattern of the NHP in a single step; for the electrode, the optimal exposure parameters (20 keV with a dose of at least 160 C/cm^2 or 30 keV with a dose of at least 230 C/cm^2) were determined. For the dense heater circuit structure exposure, the dose was either too low or too high due to proximity effect, and it was hard to find the right dose to define the heater circuit part. Hence, it was required to define the heating component using several different parameters compared to the electrode part exposure. There were two solutions for definition of the hotplate layout, one was to mill heater circuit using a FIB machine after EBL-patterning the electrode portion of the hotplate. For the purpose of optimizing the FIB milling parameters, SRIM was utilized to calculate the relationship between voltage and doses of Au ions beam at different energy, finally doses of 60, 75, and 90 C/cm^2 were selected for milling a 100 nm Pt heater layer at 70 keV based on the calculation result. SIMS studies demonstrated that 70 keV energy at doses of 60, 75, and 90 C/cm^2 was sufficient for milling a 100 nm Pt layer. For another solution to define the heater part by only using EBL, two-step exposure for NHP1 and MHP2 patterning with different exposure parameters was investigated. To expose the dense heater circuit component, a higher voltage, greater dosages, and a smaller writing field was applied as compared to the electrode part exposure. In the first stage, 20 keV with a dose of 200 C/cm^2 and a 200 m writing field were used to expose the electrode portion; in the second step, 30 keV with a dose of 300 C/cm^2 and a 100 m writing field were used to precisely define the heater circuit portion.

After the NHP1 and MHP2 devices were obtained, n-type sensing material ZnO was deposited by magnetron sputtering on each of them with thickness of 120 nm. Then the deposited ZnO nano film (ZnO_P) was calcinated at 650 °C in air (ZnO_A) and N_2 gas (ZnO_N). ZnO_P exhibited well-distributed size with diameter of 10 nm. After calcination in N_2 gas environment, ZnO grew to around 100 nm, and around 120 nm in average size with some big particle size of 500 nm in air environment. Calcination environments did

change the particle size of ZnO a lot. The results of the XRD analysis showed that the crystal structure of ZnO was unaffected by the calcination environment. The existence of zinc oxide was demonstrated by XPS, and the atom ratio of Zn to O on the super facial surface remained unaffected by the calcination conditions as well as demonstrated by the EDS results.

In order to evaluate the ZnO material electrical performance, we applied increasing voltage from 0 to 6 V on ZnO_A and ZnO_N nano films. Both of these materials displayed a decrease in the resistance of ZnO, and the resistivity of ZnO_N was significantly lower than that of ZnO_A. ZnO_A resistance did not vary significantly once the voltage was greater than 2 V, but ZnO_N resistance gradually dropped at voltages ranging from 0 to 6 V.

In the end, the sensing response of the ZnO nano film was measured. ZnO nano film did not show a positively linked relation toward increasing humidity; however, under an environment with 5 ppm NO_2 target gas and growing humidity, ZnO nano film response decreased due to the rising humidity. In dry air, the ZnO nano film demonstrated an increased sensitivity to an increasing NO_2 target gas concentration, which ranged from 5 to 25 ppm. ZnO had an increasing response under the target gases of ethanol with concentrations of 5 ppm, 15 ppm, and 25 ppm, as well as NO_2 with concentrations of 1.25 ppm, 2.5 ppm, and 5 ppm, all of which were conducted in an environment with a relative humidity of 40%RH. However, when the condition was changed to dry air, ZnO did not demonstrate a positively associated reaction toward rising concentrations of ethanol.

SnO_2 doped by antimony is widely used for gas sensor application, but to our best knowledge, the doping level generally is lower than 5wt%. In this part, highly doped SnO_2 by antimony with 10wt% and 15wt% thick films drop coated on MHP1, named as ATO1 and ATO2 separately were investigated. These materials were characterized by SEM, XRD, XPS, XRF and EDS. The sensing capacity of highly doped Sb/SnO_2 nanoparticles was analyzed and compared to that of pure SnO_2. It has been established, on the basis of the findings of the SEM, that antimony doping modified the morphology of SnO_2 powder by preventing the growth of powder particles. Additionally, the incorporation of antimony resulted in a reduction in both the crystallinity size (as assessed by XRD) and the parameters of the enlarged lattice. This was brought about as a result of the incorporation of Sb^{3+}. It was determined that there was an increase in the concentration of oxygen vacancies as a direct result of the doping process. This was discovered by XRF and EDS, which indicated reducing resistivity of SnO_2. The results of the XPS experiment demonstrate that the

concentration of antimony was higher on the surface of SnO_2 than it was in the depths of the compound. This difference in concentration corresponds to the partial saturation of antimony precipitation on the surface. The results of the XPS experiment also showed that the normal chemical state of Sn^{4+} was present, in addition to the ions Sb^{3+} and Sb^{5+}. Electrical studies revealed that ATO sensors possessed a resistance that was substantially lower than that of traditional pure SnO_2 sensors. This was as a result of the inclusion of Sb into the SnO_2 lattice, which caused the addition of a new band energy near to the conduction band. When the data from the sensors were analyzed, it was found that ATO sensors led to a particularly high selectivity and sensitivity to NO_2 when compared to the other gases that were tested at 400 °C in dry air. It would appear that an increase in the percentage of Sb present in the SnO_2 lattice results in an improvement in the sensing performance. This is supported by the fact that ATO2, the sample with the highest concentration of Sb, demonstrated a higher response to NO_2 in comparison to both ATO1 and pure SnO_2. According to this, increasing the amount of Sb that was contained within the SnO_2 lattice should result in a greater response. Additionally, the sensing response of ATO1 and ATO2 was only moderately affected by humidity, which made them ideal candidates for the development of sensitive materials that were capable of detecting NO_2 in the actual atmosphere.

6.2 Outlook

All the works we have done are good start for an in-depth development of SMO gas sensor devices. The aim of my PhD thesis is to optimize SMO gas sensor devices power efficiency by using MEMS technologies.

Even though micro and nano level hotplates for gas sensors have been obtained, but the power consumption can be further decreased by developing the suspend membrane structure based on the COMSOL simulation results. Hence, it will be prospective to fabricate the suspended membrane structure for hotplate to further improve the power efficiency. By this chance, the heater and electrode part will be super tiny and fragile, and it will be difficult to screen print or drop coat the sensing materials on the hotplate. Sputtering techniques are necessary to study to deposit different sensing materials on micro/nano-level size hotplate devices.

Since EBL and FIB process parameters have been optimized during the thesis works, which can be used to develop different size of hotplate and SMO sensor devices, it will be

promising to develop SMO sensor array on a tiny chip with super low power consumption and multiple sensing abilities. On the other hand, FIB technique could be used to decorate the sensing materials. By using FIB, the doping dose of noble metal can be exactly controlled, it could open a door to study the sensing mechanism of noble metal inside the sensing film.

ZnO nano film sensing unique results in dry air and humidity environment produce more ideas about the thin film sensing ability due to the Debye Length, the sensing response could be enlarged by depositing nano-thick sensing film, which is compatible to the geometric dimensions of Debye length. On the other hand, highly doped SnO_2 with high selectivity toward NO_2 gas could lead to investigate other highly doped SMO materials sensing abilities and mechanisms.

Appendix A: List of Figures and Tables

Figure 1.14 Gas interaction with n-type and p-type SMOs model. Reprinted with permission [30]. . 31

Figure 1.15 Models of (a) a traditional SMO gas sensor and (b) a micro hotplate SMO gas sensor. Reprinted with permission [69]. 33

Figure 1.17. Top view of hotplates with different geometry structures closed membrane, suspended membrane and bridge structure. Reprinted with permission [69]. 38

Figure 1.18 Different heater geometry: (a) Meander. (b) Meander with rounded corner. (c) S-shaped. (d) S-shaped rounded corner. (e) Double spiral. (f) Double spiral with rounded corner. (g) Double spiral with irregular spacings. (h) Plane plate with central square hole. (i) Circular. (j) Drive wheel. (k) Elliptical. (l) Honeycomb. (m) Irregular. Reprinted with permission [83]. 40

2. Fabrication Techniques and Characterization Methods 48

Figure 2.1 Chemical hood in FBK CRM clean room. 49

Figure. 2.2 Oxygen plasma dry etch machine in FBK........ 50

Fig. 2.3 SVG 8600 Photoresist Coating machine in FBK 51

Figure 2.4 Electron beam evaporation machine, PVD Ulvac model EBX-16C with e-gun Ferrotec EV S-6 in FBK........ 53

Figure 2.5 Magnetic sputtering machine KS 800C of Kenosistec........ 53

Figure 2.6 Raith focused ion beam system (a) and the LMIS (b)........ 54

Figure 2.7 Furnace Expertech CTR200 in CRM of FBK 55

Figure 2.8 Helios 5 PFIB Dual Beam 56

Figure 2.9 XPS system in FBK........ 59

Figure 2.10 SIMS system in FBK........ 60

Figure 2. 11 AFM system at FBK. 61

Figure. 2.12 The Manual Probe Station PM8 present at the FBK. 63

Figure 2.13 Binding machine of K&S Ball Analog Bonder Model 4014........ 63

Figure 2.14 Scheme of the apparatus of the gas sensor characterization system. 64

3. Micro/Nano Hotplates Simulation and Fabrication 66

Figure 3.1 The cross-section structure of substrate........ 68

Figure 3.2 Fabrication process diagrammatic sketch: a). ONO stack structure deposition; b). PMMA resist spin coat; c). EBL exposure and develop; d). Pt heater and electrode deposition; e). Resist stripper; f). Calcination and metallization; 68

Figure 3.3 (a). Layouts of MHP2 with rectangular heater (MHP2_R) and circular heater (MHP2_C); (b).

Layout of NHP1; (c). Layout of NHP2 (NHP2_1, NHP2_2 and NHP2_3) 70
Figure 3.4 Heat flux of a micromachined gas sensor (a) and heat conduction model in one-dimensional. Reprinted with permission [13]. 72
Figure 3.5 Model cross section structure of MHP1 with solid membrane (a) and suspended membrane (b). 75
Figure 3.6 Model structure of MHP1 with suspended membrane in COMSOL. 75
Figure 3.7 COMSOL simulation results of MHP1 with solid membrane and suspended membrane at 3V. 76
Figure 3.8 (a). Temperature comparison between experimental data and simulation data by using model MHP1; (b). Temperature and power consumption simulation results at different input voltage of MHP1 with solid membrane and suspended membrane. 76
Figure 3.9 The model of MHP2_R and MHP2_C and the isothermal contours distribution (at 3V). . 77
Figure 3.10 The temperature and power consumption of MHP2_R and MHP2_C at different input voltages with different thickness of Pt heater and ONO layer. 77
Figure 3.11 The influence of suspended structure on the heat conduction and mechanical property.. 78
Figure 3.12 The temperature values under ONO layer changing the trench thickness. 79
Figure 3.13 The temperature values under ONO layer during changing the trench thickness. 79
Figure 3.14 NHP1 model in COMSOL. 80
Figure 3.15 Resistance and temperature relationship in COMSOL 81
Figure 3.16 (a). Temperature comparison between COMSOL simulation and calculation by using TCR value; (b). Temperature simulation result affected by different insulation layer thickness. 82
Figure 3.17 NHP1 model in COMSOL, and temperature uniformity on 900 nm ONO layer and 2000 nm ONO layer. 82
Figure 3.18 NHP2 model in COMSOL. 83
Figure 3.19 NHP2 temperature and power consumption simulation results. 83
Figure 3.20. Heater circuit define by FIB. 85
Figure 3.21 a. Pt on SiO_2; b. PtO on SiO_2; and c. Pt/PtO on SiO_2 at different calcination temperature.86
Figure 3.22 NHP2 heater part patterned by solo EBL technique with different doses of 750 $\mu C/cm^2$, 800 $\mu C/cm^2$, and 850 $\mu C/cm^2$. 88
Figure. 3.23 Silicon and gold ion doses vs. ion energies for 100nm Pt layer milling 89
Figure 3.24 Au^{++} ions milling square by FIB on Pt film with doses of 25, 50, 75, 100, 125, 150 $\mu C/cm^2$ at one loop (a), 10 loops (b) and 100 loops (c). 91

Figure 3.25 a) AFM result of Au^{++} ions milling squares by FIB on Pt film with doses of 25, 50, 75, 100, 125, 150 μC/cm^2 in 1 loop (a), 10 loops (b) and 100 loops (c) milling at energy of 70 keV. 94

Figure 3.27 FIB milling routine at 60, 75 and 90 μC/cm^2 at one loop (a) and ten loops (b). 95

Figure 3.28. Si ions milling surface modification with doses of 0 k μC/cm^2,1 k μC/cm^2, 5 k μC/cm^2, 10 k μC/cm^2, 15 k μC/cm^2, 20 k μC/cm^2. 96

Figure 3.29. Au element distribution and Si ions intensities after Au++ milling on samples wafer with different doses at 1 and 10 loops. 96

Figure 3.30. FIB-SEM images of the NHP2 fabricated by FIB Au ions milling at 60, 75 and 90 k uC/cm^2 99

Figure 3.31. The relationship between input voltage with working temperature and power consumption of NHP2. 99

Figure 3.32 The layout of NHP1 images after EBL exposure in one step. 100

Figure 3.33 3.27 The layout of NHP1 images after EBL exposure in two-step. 100

Figure 3.34 Diagrammatic sketch of the 2-step fabrication process for NHP1 102

Figure 3.35 Does set array for the electrode part and heater part. 103

Figure 3.36 Electrode part exposed at doses of 120 μC/cm^2, 140 μC/cm^2 and 160 μC/cm^2 at 20 keV.104

Figure 3.37 Heater part with 1 μm width circuit exposed at doses ranging from 170 μC/cm^2 to 240 μC/cm^2 at 20 keV. 105

Figure 3.38 Heater part with 0.6 μm width circuit exposed at dose ranging from 170 μC/cm^2 to 240 μC/cm^2 at 20 keV. 105

Figure 3.39 Electrode part exposed at doses of 230 μC/cm^2, 240 μC/cm^2 and 250 μC/cm^2 at 30 keV.106

Figure 3.40 Heater part with 1 μm width circuit exposed at doses from 260 μC/cm^2 to 310 μC/cm^2 at 30 keV. 107

Figure 3.41 Heater part with 0.6 μm width circuit exposed at dose from 260 μC/cm2 to 310 μC/cm2 at 30 keV. 107

Figure 3.42 Resistance and temperature at different input voltages of NHP2 with different heater circuit width. 108

Figure 3.43 Optical microscope images of MHP2_R and MHP2_C. 109

Figure 3.44 Resistance measurement and temperature at different input voltages of MHP2 with different heater geometries. 110

Figure 3.45 ZnO self-heating gas sensor layout 110

Figure 3.46 Resistance measurement and temperature at different input voltages of MHP2 with different heater

geometries. 110

4. MEMS-based Thin Film SMO ZnO Gas Sensor 115

Figure 4.1 ZnO crystal structure (from The Materials Project). 115

Figure 4.2 Fabrication process of ZnO micro gas sensor: a). Spin coat resist on wafer; b). Exposure of resist by EBL; c). Sputtering of ZnO; d). Lift-off 117

Figure 4.3 ZnO deposition on NHP2 device 118

Figure 4.4 SEM images of ZnO on MHP2_C and MHP2_R. 119

Figure 4.5 SEM images of ZnO_P, ZnO_N and ZnO_A. 120

Figure 4.6 EDX of ZnO_P, ZnO_N and ZnO_A. 120

Table 4-1 120

Figure 4.7 AFM of ZnO_P, ZnO_N and ZnO_A sensing films. 121

Table 4-2 Roughness of ZnO_P, ZnO_N and ZnO_A sensing films 121

Figure 4.8 X-ray diffraction patterns collected at room-temperature for the as-prepared sample (a), that calcined at 650°C in air (b), that calcined at 650 °C in flux of N_2(c), their comparison (d), and a magnification of their comparison (square root of the y-axis) in the 13-61 °2θ angular range (e)......................... 122

Figure 4.9 Assignment of diffraction peaks to the observed crystalline phases, namely -cristobalite and ZnO with sphalerite-type structure, and to those of the (100)-oriented Si wafer utilized as substrate (a) (b).123

Figure 4.8 XPS of ZnO samples: a). Survey scan; b). Zn 2p region of samples; O 1s peak of c), ZnO_P, d). ZnO_N and e). ZnO_O. 124

Table 4-5 Atoms ratio between Zn and O. 124

Figure 4.9 The resistance values of Pt heater and ZnO_A sensing film at different input voltage on MHP2_R and MHP2_C 125

Fig . 4.9 The resistance of Pt heater and ZnO_N sensing film at different input voltage on MHP2_R and MHP2_C 125

Figure 4.10 The difference of temperature obtained between COMSOL simulation results and calculation results (by using TOC of Pt α=0.003). 126

Figure 4.11 a). ZnO nanofilm response under 5 ppm NO2 with different humidity; b). ZnO nanofilm response under NO2 with different concentrations of 5ppm, 15ppm and 25ppm in dry air. 126

Figure 4.12 a). ZnO sensing film response under 5 ppm, 15 ppm and 25 ppm ethanol and 1.25 ppm, 2.5 ppm and 5 ppm NO2 with 40 RH% humidity; b). ZnO nanofilm sensing response under ethanol and NO2 with different concentration. 127

Figure 13 schematic representation of sensing mechanism for ZnO [8]. Reprinted from [8]. 128

5. MEMS-based Thick Film SMO SnO_2 Doped by Antimony (ATO) Gas Sensor 132

Figure 5.1 Paste coated on micro hotplate images of S1 (a and c), ATO1 (b and d) and ATO2 (c and e) before (a, b, and c) and after calcination (c, d and e). 137

Figure 5.2. SEM images of a) S1; b) ATO1 and c) ATO2 at 250 kX magnification. 138

Figure 5.3. X-ray diffraction patterns(a) and crystallinity size (b, c and d) of S1, ATO1 and ATO2 estimated by Rietveld and LeBail approach from XRD data analysis, in three directions of (111), (100) and (001). 139

Table 5-1. Lattice parameters of S1, ATO1 and ATO2 samples estimated by Ritveld and LeBail approach from XRD data analysis. 139

Table 5-2. Elemental composition of samples obtained from XRF analysis. 140

Table 5-3. Elemental composition of samples obtained from EDS analysis. 141

Figure 5.4. XPS spectra of S1 and ATO1 and ATO2: (a) survey spectrum, (b) Sn 3d spectrum, and (c) Sb 3d spectrum of ATO2, (d) XPS valence band of the three samples. 142

Table 5-4 Resistance (kΩ) of samples at different working temperatures in dry air. 143

Figure 5.5. Electrical characterizations of the fabricated sensors: a) response to different gases at 400°C in dry air; b) response to 10 ppm of NO_2 at different operating temperatures in dry air; c) dynamical response of the three sensors towards 1, 3, 5, and 10 ppm NO_2 at 300°C; d) variation of the response vs. NO_2 concentrations for the three sensors in dry air at 300°C; e). response to different humidity at 300°C under 10 ppm NO_2. 145

Figure 5.6. S1 and ATO1 samples sensing ability test at different temperatures toward 20 ppm CO, 5ppm ethanol and 0.5ppm acetaldehyde. 147

Figure 5.7 Samples sensing ability test toward 5 ppm acetone, 2 ppm SO_2, and 5 ppm H_2S, 400 ppm CO_2, ... 148

Appendix B: Materials Properties Used in COMSOL Simulation.

Material	Thermal conductivity (W/(m·K))	Heat capacity (J/(kg·K))	Electrical conductivity	Density (kg/m³)	Relative permittivity	Young's modulus (Pa)
Silicon	230	63.0442191+3.7706731*T^1-0.00694853616*T^2+5.9532044E-6*T^3-1.91438418E-9*T^4		2332.565+0.003839515*T^1-5.433308E-5*T^2+4.287211E-8*T^3-1.366545E-11*T^4		1.310854E11+2223259.0*T^1-21955.19*T^2+16.60284*T^3-0.005400611*T^4
ONO	1.4	1000		2200		
Pt	73.99627-0.01557887*T^1+2.646931E-5*T^2-6.133801E-9*T^3	122.218657+0.0398634575*T^1-1.83617434E-5*T^2+7.55677261E-9*T^3	1/(2.814022E-17*T^3-1.600249E-13*T^2+5.552497E-10*T-4.843579E-08)	21557.19-0.5675783*T^1-1.7525E-5*T^2-3.171806E-8*T^3+4.698968E-12*T^4	2.76	1.68E11-3.38E7*T^1

Ti	15.13513+0.004158454*T^1+1.376649E-6*T^2	-33066.629+136.77383*T^1-0.204810858*T^2+1.3350416E-4*T^3-3.17182178E-8*T^4		4525.567-0.05296616*T^1-1.538843E-4*T^2+1.427212E-7*T^3-5.386443E-11*T^4		